UNIVERSITÉ DU LUXEMBOURG

PhD-FSTM-2026-017
The Faculty of Science, Technology and Medicine

DISSERTATION

Defence held on 11 March 2026 in Luxembourg

to obtain the degree of

DOCTEUR DE L'UNIVERSITÉ DU LUXEMBOURG

EN INFORMATIQUE

by

Almoatssimbillah SAIFALDAWLA AWAD HASSAN
Born on 12 December 1995 in Greater (Sudan)

ARTIFICIAL INTELLIGENCE-ENABLED INTERFERENCE MANAGEMENT FOR THE NEXT GENERATION OF SATELLITE COMMUNICATIONS

Dissertation defence committee

Dr Eva Lagunas, Dissertation Supervisor
Assistant Professor, Université du Luxembourg

Dr Bhavani Shankar Mysore Rama Rao, Chairman
Assistant Professor, Université du Luxembourg

Dr Symeon Chatzinotas, Member
Professor, Université du Luxembourg

Dr Miguel Angel Vazquez, Member
Senior Researcher, Centre Tecnològic de Telecomunicacions de Catalunya (CTTC), Spain

Dr Joel Grotz, Member
Senior Manager, Société Européenne des Satellites (SES), Luxembourg

Affidavit / Statement of originality

I declare that this thesis:

- is the result of my own work. Any contribution from any other party, and any use of generative artificial intelligence technologies have been duly cited and acknowledged;
- is not substantially the same as any other that I have submitted, and;
- is not being concurrently submitted for a degree, diploma or other qualification at the University of Luxembourg or any other University or similar institution except as specified in the text.

With my approval I furthermore confirm the following:

- I have adhered to the rules set out in the University of Luxembourg's Code of Conduct and the Doctoral Education Agreement (DEA)[1], in particular with regard to Research Integrity.
- I have documented all methods, data, and processes truthfully and fully.
- I have mentioned all the significant contributors to the work.
- I am aware that the work may be screened electronically for originality.

I acknowledge that if any issues are raised regarding good research practices based on the review of the thesis, the examination may be postponed pending the outcome of any investigation of such issues. If a degree was conferred, any such subsequently discovered issues may result in the cancellation of the degree.

Approved on 2026-01-21

[1] If applicable (DEA is compulsory since August 2020)

Artificial Intelligence-Enabled Interference Management for the Next Generation of Satellite Communications

Almoatssimbillah SAIFALDAWLA AWAD HASSAN

Abstract

The rapid deployment of ultra-dense non-geostationary satellite orbit (NGSO) constellations is fundamentally transforming satellite communication systems (SatComs) compared to legacy geostationary satellite orbit (GSO) architectures by enabling low-latency, high-capacity, and ubiquitous global connectivity. While these developments unlock new services and mission-critical applications worldwide, they also introduce complex interference challenges arising from spectrum scarcity, multi-constellation coexistence, and highly dynamic orbital motion. Conventional interference management techniques typically rely on accurate channel estimation and often fail in low signal-to-noise ratio (SNR) conditions and fast-varying NGSO environments, necessitating the adoption of more intelligent, adaptive, and data-driven solutions. This thesis investigates artificial intelligence (AI)–enabled interference management frameworks for next-generation SatComs, with a particular focus on downlink co-frequency interference (CFI) in multi-operator coexistence scenarios. Advanced AI-based interference detection and mitigation techniques are proposed to address the unique challenges imposed by NGSO system dynamics and large-scale deployments.

First, we tackled NGSO-to-GSO downlink interference detection at GSO ground stations (GGSs) by proposing advanced generative AI (GenAI)-based models, including variational autoencoders (VAEs) and transformer-based interference detector (TrID). These models are trained to generate samples of the expected interference-free GSO signal, then NGSO interference can be flagged by thresholding the generated samples' error with respect to the input signal. Realistic satellite characteristics, trajectories, and system parameters are used to emulate the interference scenarios and validate the proposed models. Numerical evaluation reveals that time-domain features exhibit higher accuracy for detecting interference compared to the frequency-domain features. Furthermore, the results demonstrate that TrID significantly outperforms other deep learning (DL)-based models as well as the traditional energy detector (ED) approach, showing an increase of up to 31.23% in interference detection accuracy.

We then introduce a novel attention-based blind adaptive beamforming model (AttBF) for NGSO-to-NGSO interference mitigation at NGSO user terminals (UTs). By leveraging estimation-free signal representations (e.g., received time-domain signals, frequency-domain representations, and sample covariance matrices (SCMs)), we evaluate the proposed AttBF model across various interference scenarios, encompassing both low spatial correlation (at UT's side-lobe) and high spatial correlation (at UT's main-lobe). Our findings highlight the enhanced spatial interference nulling capabilities of the AttBF-based approach, particularly when employing SCMs data, which offer near-optimal Signal-to-Interference-plus-Noise Ratio (SINR) performance with the fastest inference ($\sim 4.5\ \mu s$), compared to other DL-based beamforming models, such as convolutional neural networks (CNNs), and traditional methods, including zero forcing beamformer (ZFBF) and sample matrix inversion (SMI).

Finally, we propose a federated learning–enabled collaborative beamforming framework (Fed-SatBF) for NGSOs CFI interference mitigation in direct satellite-to-vehicle systems (DS2Vs). This work is also related to the previous second work by addressing the AttBF model generalization aspects and the various users' training capabilities. The proposed approach enables a serving satellite to aggregate locally trained attention-based beamforming models from a subset of vehicular user terminals (VUTs) using federated averaging, and broadcasts a global model that can be directly applied by both participating and non-participating VUTs experiencing similar CFI conditions. The proposed framework is explicitly designed to operate within the limited channel coherence time imposed by NGSO mobility. We investigate the impact of key FL hyperparameters, including per-coherent block communication rounds, per-round training data, per-VUT local epochs, VUT participation, and geographical VUT clustering, on convergence speed, interference nulling capability, and computational efficiency. Simulation results demonstrate near-optimal interference suppression performance, within 0.1 dB of optimal ZFBF, and strong generalization to non-participating users, highlighting the practicality of federated AI for large-scale NGSO deployments.

This thesis demonstrates that AI-driven interference management is a scalable and effective paradigm for enhancing the robustness, efficiency, and operational autonomy of next-generation satellite communication systems, while also contributing new open datasets enabled by realistic satellite orbit modeling.

Preface

This Ph.D. thesis was conducted from December 2022 to December 2025 at the Interdisciplinary Centre for Security, Reliability and Trust (SnT), University of Luxembourg, Luxembourg. It was carried out under the supervision of Prof. Eva Lagunas. The periodic evaluations of the thesis were performed by Prof. Symeon Chatzinotas, University of Luxembourg, Luxembourg, and Dr. Miguel Angel Vazquez, Telecommunications Technological Center of Catalonia (CTTC), Spain, who, along with Prof. Lagunas, constituted the thesis supervision committee (Comité d'encadrement de thèse, CET) at the University of Luxembourg.

Support of the Thesis

This work was supported by the Luxembourg National Research Fund (FNR) through **SmartSpace project**, with reference number (C21/IS/16193290), and with the support of SES S.A., Luxembourg, represented by Dr. Joel Grotz. Additionally, the support provided by the SIGCOM research group is gratefully acknowledged, contributing significantly to the research conducted in this thesis.

Use of Generative AI Tools

The scientific content, technical formulations, analyses, results, and interpretations presented in this thesis are the original work of the author. Any contribution from other parties has been duly acknowledged and/or credited. Generative AI tools were used solely for language refinement tasks such as improving grammar, clarity, and presentation, and all intellectual and scientific contributions remain solely attributable to the author.

Publications

As a result of the Ph.D. research, peer-reviewed journal and conference papers have been published or are under consideration for publication. These papers are listed below in the text under J $\equiv$ Journals, C $\equiv$ Conferences, M $\equiv$ Magazines,

[**J1**] **A. Saifaldawla**, F. Ortiz, E. Lagunas, A. B. M. Adam and S. Chatzinotas, "GenAI-Based Models for NGSO Satellites Interference Detection," in *IEEE Transactions on Machine Learning in Communications and Networking*, vol. 2, pp. 904-924, 2024, doi: 10.1109/TMLCN.2024.3418933.

[**J2**] **A. Saifaldawla**, F. Ortiz, E. Lagunas and S. Chatzinotas, "Attention-based Blind Adaptive Receive Beamforming for Interference Limited NGSO Satellite Systems," in *IEEE Open Journal of the Communications Society*, vol. 6, pp. 8946-8964, 2025, doi: 10.1109/OJCOMS.2025.3622661.

[**J3**] **A. Saifaldawla**, E. Lagunas, M. Alsenwi and S. Chatzinotas, "Federated Learning–Enabled Collaborative Beamforming for NGSO Direct-to-Vehicle Systems". *Under revision in IEEE Transactions on Machine Learning in Communications and Networking*.

[**C1**] **A. Saifaldawla**, F. Ortiz, E. Lagunas, S. Daoud and S. Chatzinotas, "NGSO-To-GSO Satellite Interference Detection Based on Autoencoder," *2023 IEEE 34th Annual International Symposium on Personal, Indoor and Mobile Radio Communications (PIMRC)*, Toronto, ON, Canada, 2023, pp. 1-7, doi: 10.1109/PIMRC56721.2023.10293839.

[**C2**] **A. Saifaldawla**, F. Ortiz, E. Lagunas and S. Chatzinotas, "Convolutional Autoencoders for Non-Geostationary Satellite Interference Detection," *2024 IEEE International Conference on Communications Workshops (ICC Workshops)*, Denver, CO, USA, 2024, pp. 1334-1339, doi: 10.1109/ICCWorkshops59551.2024.10615457.

[**C3**] **A. Saifaldawla**, E. Lagunas, F. Ortiz, A. B. M. Adam and S. Chatzinotas, "SmartUT: Receive Beamforming for Spectral Coexistence of NGSO Satellite Systems," *2025 28th International Workshop on Smart Antennas (WSA)*, Erlangen, Germany, 2025, pp. 195-200, doi: 10.1109/WSA65299.2025.11202840.

[**M1**] F. Ortiz, E. Lagunas, **A. Saifaldawla**, M. Jalali, L. Emiliani and S. Chatzinotas, "Emerging LEO constellations: Spectral Coexistence with Legacy GEO Satellite Communication Systems." *Frontiers in Communications and Networks*, vol.7, 2026.

[**M2**] A. Adam, E. Lagunas, M. Samy, **A. Saifaldawla**, and S. Chatzinotas, "Generative AI for Non-terrestrial Networks: Design, Applications, and Challenges," *EURASIP Journal on Wireless Communications and Networking*, 2025, doi: 10.1186/s13638-025-02549-7.

Acknowledgments

I would like to express my deep and sincere gratitude to all those who supported me throughout my doctoral studies. First and foremost, I am profoundly grateful to my supervisor, Prof. Eva Lagunas, for her continuous guidance, encouragement, dedication, and insightful feedback. Her support has been essential, and without her, this thesis would not have been possible. I extend my deepest appreciation to my mentors, Prof. Symeon Chatzinotas, Dr. Flor Ortiz, Dr. Abuzar Adam, Dr. Madyan Alsenwi, and Dr. Saed Daoud, for their invaluable technical guidance and constructive discussions throughout the years of my Ph.D. studies. I would also like to sincerely thank the members of my thesis committee, Dr. Miguel Angel Vazquez, Prof. Bhavani Shankar, and Dr. Joel Grotz for their time, feedback, and valuable insights. My sincere gratitude goes to my friends and colleagues in Luxembourg and abroad; it would be impossible to name everyone individually, but please know that your support is deeply appreciated. I owe a profound debt of gratitude to my family, especially my father *Saifaldawla*, my late mother (Rahimaha-allah), and my siblings; their love, prayers, care, and sacrifices have been the foundation of all my endeavors and achievements. I am forever grateful to my beloved wife, *Tasabih*, whose patience, support, and belief in me have been a constant source of strength and motivation throughout this journey. Finally, I would also like to thank Suzanne from the DSSE administration team, as well as the SigCom secretariat, Amélie and Corinne, for their assistance in facilitating my research activities.

Contents

1 Introduction **1**

1.1 Background . . . 2

1.1.1 SatComs Overview . . . 2

1.1.2 SatComs Link Budget . . . 5

1.1.3 SatComs Radio Spectrum . . . 6

1.1.4 Next Generation SatComs Applications . . . 7

1.1.5 AI-enabled SatComs . . . 8

1.2 SatComs Interference Problem . . . 9

1.3 SatComs Interference Management Strategies . . . 12

1.4 Research Motivation . . . 14

1.4.1 Research Questions . . . 16

1.4.2 Research Methodology . . . 17

1.5 Thesis Contributions and Related Publications . . . 18

1.5.1 Publication Not Included in the Thesis . . . 20

2 GenAI-based Models for NGSO Satellites Interference Detection **21**

2.1 Introduction . . . 22

2.1.1 Context and Motivation . . . 22

2.1.2 Related Work . . . 23

2.1.3 Contributions . . . 25

2.1.4 Chapter Organization . . . 26

2.2 System Model . . . 27

2.2.1 Link Budget Model . . . 27

2.2.2 Detailed Received Signal Model . . . 30

2.3 Data Preparation . . . 33

2.4 Interference Detection Models . . . 36
2.4.1 Notation and Assumptions . . . 36
2.4.2 Benchmark Models . . . 37
2.4.3 Proposed GenAI-based Models . . . 38
2.4.4 Interference Detection Performance Metrics . . . 43
2.5 Simulation Results . . . 45
2.5.1 Data Generation Phase . . . 45
2.5.2 Models Training Phase . . . 50
2.5.3 Models Evaluation Phase . . . 55
2.6 Comparison With Traditional Approach . . . 58
2.6.1 Generation of Comparative Datasets . . . 58
2.6.2 Energy Detector Approach . . . 60
2.6.3 Comparison Results . . . 61
2.7 Chapter Conclusion . . . 65

3 Attention-based Blind Adaptive Receive Beamforming for NGSO Satellite Systems 67
3.1 Introduction . . . 68
3.1.1 Context and Motivation . . . 68
3.1.2 Relevant Work . . . 69
3.1.3 Contribution . . . 70
3.1.4 Chapter Organization . . . 71
3.2 System Model . . . 72
3.2.1 Interference Scenario . . . 72
3.2.2 Channel Model . . . 72
3.2.3 Signal Model . . . 75
3.2.4 Traditional Receive Beamforming Techniques . . . 76
3.3 Proposed Attention-Based Beamforming . . . 80
3.3.1 Data Pre-processing . . . 81
3.3.2 AttBF Model Architecture . . . 82
3.3.3 AttBF Model Objective . . . 86
3.3.4 Benchmark Models . . . 88
3.3.5 AttBF Computational Time Complexity : . . . 89

3.4 Simulation Results . . . 90
3.4.1 Data and Simulation . . . 90
3.4.2 Training Phase Results . . . 93
3.4.3 Beamforming Performance Results . . . 95
3.5 Chapter Conclusion . . . 102

4 Federated Learning–Enabled Beamforming for NGSO Direct-to-Vehicle Systems 103
4.1 Introduction . . . 104
4.1.1 Context and Motivation . . . 104
4.1.2 Related Work . . . 107
4.1.3 Contribution . . . 108
4.1.4 Chapter Organization . . . 108
4.2 System Model . . . 109
4.2.1 Channel Model . . . 109
4.2.2 Signal Model . . . 112
4.3 Traditional ABF Techniques . . . 113
4.4 Proposed FedSatBF framework . . . 115
4.4.1 Base Model Architecture . . . 115
4.4.2 Learning Procedure . . . 117
4.4.3 Evaluation Protocol and Performance Metrics . . . 119
4.5 Simulation Results . . . 121
4.5.1 Data and Simulation . . . 121
4.5.2 FedSatBF Performance Analysis for $T_{\mathtt{COH}}$ . . . 122
4.5.3 FedSatBF Performance Analysis for $T_{\mathtt{VIS}}$ . . . 130
4.6 Chapter Conclusion . . . 133

5 Conclusions and Future Research 135
5.1 Main Conclusions . . . 135
5.2 Future Work . . . 136
5.2.1 Possible Extensions . . . 137
5.2.2 Open Research Directions . . . 139

Bibliography 141

List of Figures

1.1 An overview of basic SatComs components [11]. 2
1.2 Satellite Communications Radio spectrum 6
1.3 Next Generation SatComs ecosystem [11]. 8
1.4 Some satellite system interference scenarios: (a) SatCom IBI (i.e., intra-system IBI if both satellites belong to same operator, inter-system IBI if they are from separate operators (coexistence)); (b) SatComs-TN coexistence (i.e., CFI); (c) Intra-system interferences; (d) Jamming. 11
1.5 Summarized interference management techniques. 13
1.6 Satellites launched per year [82]. 15
1.7 CFI Scenarios of Interest. 16
1.8 Research methodology adopted in each chapter. 17

2.1 Proposed interference detection framework. 25
2.2 Simplified scenario scheme with a GGS pointing towards the desired GSO satellite and a potential interference from a NGSO system. 27
2.3 Overlap of GSO and LEO Bandwidths in Frequency Domain 32
2.4 Benchmark Models 37
2.5 Variational Autoencoder Interference Detection Model (VAE) 39
2.6 Transformer-based Interference Detector Model (TrID) 41
2.7 Schematic overview from data generation to models training and evaluation 45
2.8 Plot of numbers of LEO satellites interfering GGS (Top), and the received CNR and $\mathrm{INR}_{\mathrm{sum}}$ (Bottom), over the simulation period 48
2.9 Visualization of the GGS receiving gain of each satellite accessing to GGS at 30-07-2023 11:44:30 49
2.10 Training Phase Results 50

2.11 Model input (cyan color), reconstructed output (navy color), and error area (golden color) for an interference-free and interference Signal data (sub-left figures) and Spectrum data (sub-right figures) . . . 53
2.12 Threshold Selection Based On Optimal AUC Score Approach . . . 54
2.13 AUC_ROC plot per model for Signal data (left), and Spectrum data (right) . . . 55
2.14 Normalized Confusion Matrices per model for Signal data (sub-left figures), and Spectrum data (sub-right figures) . . . 56
2.15 LEO pass vs INR and off-axis angles . . . 60
2.16 Detection vs LEO off-axis Angles for Various GSO ModCods . . . 63
2.17 Detection vs LEO INR Values for Various GSO ModCods . . . 64

3.1 Considered scenario with a desired NGSO system (green) and an interfering NGSO system (red). . . . 73
3.2 Time frame of the simulation scenarios . . . 75
3.3 Typical structure of ABF . . . 77
3.4 Receive Beamforming Techniques: (a) sample matrix inversion (SMI), (b) Zero forcing beamforming (ZFBF), (c) Maximum ratio combining (MRC), and (d) The intended DL-based beamformer . . . 79
3.5 Illustration of the proposed AttBF beamformer. . . . 81
3.6 AttBF offline training, online deployment objectives. . . . 86
3.7 Proposed NGSO systems constellations . . . 91
3.8 A representation link status from the $L = 2M$ test data of a desired satellite pass with nearby interference satellites as received by UT during T_{Pass} . . . 94
3.9 Loss vs Training Epoch ($L = 2M$ test data) . . . 95
3.10 SINR distribution per beamforming method (when $L = M \mid 2M \mid 4M$) . . . 96
3.11 Case1: a main-lobe correlation ($\rho_{\max} = 0.67$) . . . 99
3.12 Case2 : a side-lobe correlation ($\rho_{\max} = 0.19$). . . . 100
3.13 SINR vs CSI estimation error ($\rho_{\max} = 0.78$) . . . 101

4.1 Illustration of the proposed FedSatBF Framework. . . . 109
4.2 An illustration of a Sat-VUTs link geometry. . . . 110
4.3 Per-VUT training time frame. . . . 117

4.4 FedSatBF leaning diagram and assessment strategies (pFL: personalized FL, gFL: global FL). 119
4.5 Impact of model initialization on $\Gamma^{\tau}_{\mathtt{gFL}}$ performance. 123
4.6 Impact of global model personalization on global SINR performance. 124
4.7 Generalization performance of FedSatBF on non-participating VUTs in terms of global SINR. 125
4.8 Impact of $N_{\mathtt{CRs}}$ on global SINR performance. The bars highlight the mean global SINR from all rounds ($\Gamma_{\mathtt{gFL}}$). 126
4.9 Effect of $K^{\mathtt{Fed}}$ on Global SINR. 127
4.10 Effect of R_{cluster} on Global SINR. 127
4.11 Comparison of different training parameters on the FedSatBF conformance: (a) Impact of the amount of training data per round; (b) Impact of the number of local epochs per round; (c) Impact of batch size. 128
4.12 Training parameters' performance bars ($N_{\mathtt{LEs}}, N^{\text{tr}}_{k,\tau}, B$). 129
4.13 Mean global SINR of $T_{\mathtt{VIS}}$ across coherent blocks under MRC and ZFBF, and highlighted representative windows of interest. 130
4.14 FedSatBF performance on $T_{\mathtt{VIS}}$ comparison within: (a) Window 1; (b) Window 2. . . 131
4.15 The effect of global model sharing (Memory: On) between Coherent-blocks: (a) Window 1; (b) Window 2. 132

List of Tables

1.1 Summary of Interference Classification in Satellite Communication Systems 10

2.1 Simulation Setup and Link Budget Parameters (Algorithm 1) 46
2.2 The visibility of GSO and LEOs to the GGS 47
2.3 Data Generation Parameters (Algorithm 2) 48
2.4 GSO ModCods 49
2.5 Models performance summary on Signal test data 57
2.6 Models performance summary on Spectrum test data 57
2.7 Overlapping Sets and Parameters 59
2.8 Performance Comparison of Models Across Bandwidth Overlap 61

3.1 Comparison between our proposed model and other benchmarks 89
3.2 Comparison of the End-to-end inference/latency time Complexity 89
3.3 Constellations parameters 92
3.4 UT Parameters 93
3.5 Satellite Link Budget Parameters 93
3.6 Comparison of models training (# $L = M \mid 2M \mid 4M$) 94
3.7 Comparison of models/methods beamforming performance (# $L = M \mid 2M \mid 4M$) . 96
3.8 Summary Comparison of Beamforming Methods for NGSOs Interference Mitigation 101

4.1 Key Notation of the FedSatBF Framework 115
4.2 Summary of the AttBF Model Architecture 116
4.3 Comparison of benchmarks Input type 116
4.4 Satellite Parameters 122
4.5 Per-VUT Parameters 122
4.6 FL Fixed Parameters 123

Abbreviations

3GPP	3rd Generation Partnership Project
6G	Sixth-generation of Mobile Communications
ABF	Adaptive Beamforming
AE	Autoencoder-Based Model
AI	Artificial Intelligence
AttBF	Attention-Based Beamforming
AWGN	Additive White Gaussian Noise
CAE	Convolutional Autoencoder
CFI	Co-Frequency Interference
CSI	Channel State Information
DS	Desired Satellite
DOA	Direction of Arrival
DS2V	Direct Satellite-to-Vehicle
ED	Energy Detector
EIRP	Equivalent Isotropic Radiated Power
FedAvg	Federated Averaging
FFT	Fast Fourier Transform
FL	Federated Learning
FSPL	Free-Space Path Loss
GenAI	Generative AI
GEO	Geostationary Earth Orbit
GSO	Geostationary Satellite Orbit
INR	Interference-to-Noise Ratio
IQ	In-phase and Quadrature
IS	Interfering Satellite

ITU	International Telecommunication Union
KPI	Key Performance Indicator
LEO	Low-Earth Orbit
LoS	Line-of-Sight
LSTM	Long Short-Term Memory Model
MAE	Mean Absolute Error
MEO	Medium-Earth Orbit
MHA	Multi-Head Attention
ModCod	Modulation and Coding
MRC	Maximum Ratio Combining
MVDR	Minimum Variance Distortionless Response
NGSO	Non-Geostationary Satellite Orbit
NLoS	Non-Line-of-Sight
NTN	Non-Terrestrial Network
PSD	Power Spectral Density
QoS	Quality of Service
SatComs	Satellite Communication Systems
SCM	Sample Covariance Matrix
SINR	Signal-to-Interference-plus-Noise Ratio
SMI	Sample Matrix Inversion
SNR	Signal-to-Noise Ratio
TLE	Two-Line Element
TN	Terrestrial Network
TrID	Transformer-Based Interference Detector
UPA	Uniform Planar Array
UT	User Terminal
VAE	Variational Autoencoder
VSAT	Very Small Aperture Terminal
VUT	Vehicular User Terminal
ZFBF	Zero-Forcing Beamforming

Notations

$\mathbf{X}$	Matrix, denoted by bold uppercase letters
$\mathbf{x}$	Column vector, denoted by bold lowercase letters
I_M	Identity matrix of size $M \times M$
I	Identity matrix with size inferred from context
$\lvert \cdot \rvert$	The absolute value of scalars
$\lVert \cdot \rVert$	Frobenius norm of a matrix
$(\cdot)^T$	Transpose of a matrix or vector
$(\cdot)^H$	Hermitian (conjugate) transpose
$(\cdot)^{-1}$	Inverse of a matrix
$\log_x(\cdot)$	The logarithm with base x
$\mathbb{R}^M$	M-dimensional real space
$\mathbb{C}^M$	M-dimensional complex space
$\mathrm{Re}(\cdot)$	Real part of a complex quantity
$\mathrm{Im}(\cdot)$	Imaginary part of a complex quantity
$\mathbb{E}_y(\mathbf{x})$	Expectation of $\mathbf{x}$ with respect to the distribution of y
$\odot$	The Hadamard (element-wise) product
∇f	Gradient of function f
$\mathcal{CN}(\mu, \sigma^2)$	Complex Gaussian distribution with mean μ and variance σ^2
$\mathcal{O}(\cdot)$	Big-O notation for computational complexity

Chapter 1

Introduction

Satellite communication systems (SatComs) are becoming a foundational component of future wireless ecosystems by complementing terrestrial networks (TNs) and enabling global, continuous, and resilient connectivity [1]. In the context of sixth-generation (6G) communication systems, SatComs are no longer isolated infrastructures but integral elements of heterogeneous non-terrestrial networks (NTNs) supporting broadband access, mobility, and mission-critical services worldwide [2]. The rapid deployment of non-geostationary satellite orbit (NGSO) constellations represents a paradigm shift in satellite communications [3, 4]. While these constellations significantly enhance capacity and latency performance, they also fundamentally alter the interference landscape [5]. Fast satellite motion, short channel coherence times, heterogeneous system deployments, and aggressive spectrum reuse introduce highly dynamic and non-stationary interference conditions that challenge existing conventional interference management techniques [6]. Artificial intelligence (AI) has recently emerged as a powerful enabler for addressing complex, dynamic, and high-dimensional problems in satellite communications [7–9]. By enabling data-driven modeling, adaptive decision-making, and estimation-free processing, AI-based techniques offer a promising pathway toward autonomous and scalable interference management [10]. However, designing AI frameworks that remain robust under realistic orbital dynamics, limited coherence time, and distributed deployment constraints remains an open research challenge. This thesis addresses this challenge by investigating AI-enabled interference detection and mitigation frameworks tailored to next-generation satellite systems.

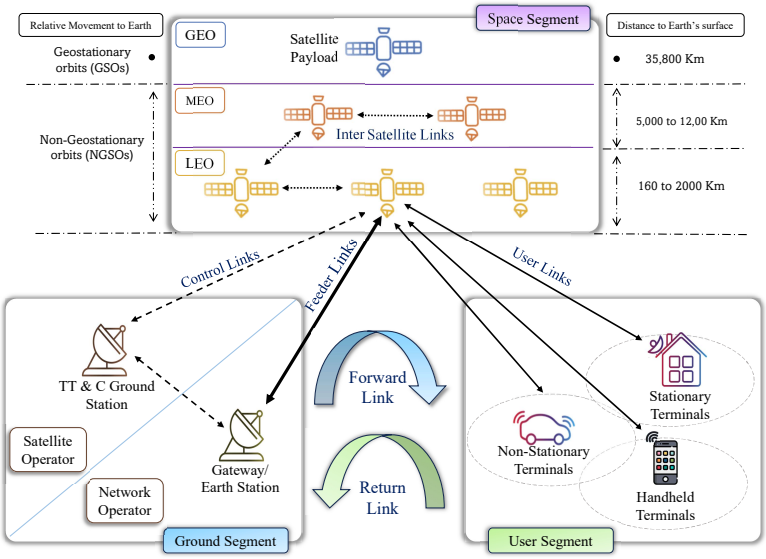


Figure 1.1: An overview of basic SatComs components [11].

1.1 Background

1.1.1 SatComs Overview

Fig. 1.1 provides a general overview of the main components of a satellite communication systems. The system is structured into three principal segments: space, ground, and user segments [11]. The space segment comprises satellites distinguished by their distance from the Earth's surface as, i) **Geostationary-Earth orbits (GEOs)**, or geostationary satellite orbits (GSOs)[1], operates at exactly 35,786 km and appears stationary to ground observers. Because of the advantages of fixed position relative to the Earth, wide coverage, and nearly constant latency, GEO becomes the most popular system deployed by satellite operators to implement their commercial applications. ii) **Medium-Earth orbits (MEOs)** operate at altitudes between roughly 5,000 km and 12,000 km, and iii) **low Earth orbit (LEOs)** operate at altitudes ranging from about 160 km to 2,000 km, both exhibiting rapid relative motion, thus known as non-geostationary satellite orbits (non-GSOs/NGSOs). NGSO systems, particularly those in LEO, provide significantly lower propagation delays (typically 20–50 ms) and higher data throughput. These constellations achieve global coverage by employing large fleets of satellites, making them essential for latency-sensitive 6G applications and high-speed mobile connectivity [12].

[1]GEO/GSO is a specific type of geosynchronous orbits: both have a 24-hour period matching Earth's rotation, but a geostationary orbit is perfectly circular, directly over the equator, making the satellite appear fixed in the sky; while a geosynchronous orbit can be inclined or elliptical, causing it to drift north/south daily in a figure-eight pattern.

The link direction from the gateway to user segment via satellites is called the *forward link*, while the opposite link direction is called the *return link*, these two links enables downlink and uplink satellite communications with both stationary terminals (e.g., fixed user terminals) and non-stationary terminals (e.g., vehicular and handheld devices) [3]. The *Feeder links* connect satellites to their gateways in the ground segment, which interface with the terrestrial core network and network operators. In addition, *control links* are shown to support satellite control and operation via telemetry, tracking, and command (TT&C), which refers to the downlinked platform data giving details of the satellite's status, determination of its location through tracking ranging signals, and the uplinked commands given to the platform. The *Inter-satellite links (ISLs)*, particularly relevant for NGSO constellations, enable direct communication among satellites (e.g., for routing, handover, and distributed processing) [5].

In SatComs, antennas play a fundamental role in shaping how radio frequency (RF) energy is radiated and received. The spatial distribution of this energy is referred to as the antenna beam [13]. The radiation pattern of an antenna beam contain of, i) *main lobe*: where the majority of the radiated power and defines the intended beam direction; ii) *side lobes*: of undesired secondary radiation peaks that can cause interference and reduce system efficiency [14]; and iii) the *nulls*, which are angular directions where the radiated power is ideally minimized or zero. Nulls are particularly important in interference management, as they can be deliberately steered toward strong interferers or protected users to suppress unwanted signals and enhance spatial isolation between co-channel links [15]. Beam shaping is essential to control coverage, improve link quality, reduce interference, and increase system capacity. In the following, we summarize some concepts that define the foundation of modern SatCom systems.

A. Antenna Types: Antennas in SatComs can be categorized based on where they are located,

- **Payload antennas:** These are mounted onboard the satellite responsible for illuminating the Earth or specific regions with RF signals. They determine the satellite footprint, beam geometry, and Effective Isotropic Radiated Power (EIRP) distribution. Depending on the mission requirements, some types include *Horn Antenna*: a flared metal waveguide, often used in GSO for "global beams" (covering 1/3 of Earth). *High-gain parabolic reflectors*: a large curved dish, very high gain and efficiency, ideal for "Spot-Beams" that target specific ground regions, but it often requires complex deployment mechanisms and mechanical tilting parts. *Phased array antennas*: a flat panel with many tiny elements that can change beam shape and direction "steer" instantly without moving parts "electronically", and can also create multiple beams simultaneously [16].

- **Ground station antennas:** Which are large, high-gain antennas used at gateway stations to communicate with satellites. They provide very narrow beams and high sensitivity, enabling reliable feeder links with high data rates. Their size and precision allow them to overcome the large free-space path losses (FSPL) of satellite links, but they are expensive and stationary [1].
- **User terminal antennas:** These antennas are deployed at the end users and are constrained by size, cost, and power consumption. *Traditional parabolic dishes* offer high gain at low cost for fixed users (e.g., Very-small-aperture terminal (VSAT)). *Phased-array antennas* enable mobility and seamless tracking of satellites (e.g., Starlink Dishy [17]), at the expense of higher complexity and power consumption. *Patch Antenna* are flat metal squares found inside smartphones, Global navigation systems (GPS) units, and Internet of Things (IoT) devices. They are extremely cheap, tiny, and can be integrated directly onto a circuit board, but have very low gain; they only work for low-data applications [18].

B. Satellite Footprint: These refers to the geographical area on the Earth's surface illuminated by a satellite beam. It defines the coverage region of the satellite, and it depends on the antenna radiation pattern, satellite altitude, and beam pointing direction. They can be classified based on their temporal and geographic stability into [19]: *Earth-Fixed Beams*: these beams ensure permanent and constant illumination of a specific geographic region (e.g., GSO Beams). *Quasi-Earth-Fixed Beams*: dynamically steered beams track a specific ground coordinate (fixed boresight) during the satellite's visibility window (pass-time), primarily utilized by NGSO satellites equipped with steerable antennas. While the geographic center remains fixed, the beam geometry may undergo deformation due to the changing slant range and incidence angle as the satellite moves. *Moving-Earth Beams*: here, the beam footprint sweeps across the Earth's surface (nadir boresight) following the satellite's orbital velocity, resulting in transient coverage areas, where ground users experience a sequence of rapid handovers as cells move across their location, typical for NGSO satellites with non-steerable antennas.

C. Spot-Beams: These are narrow and highly directive beams used to cover small geographical areas within the overall footprint. They enable frequency reuse (FR) across different regions, significantly increasing system capacity and spectral efficiency. Spot-beams are a key feature of modern high-throughput satellite (HTS) systems [20].

D. Beamforming: This refer to a signal processing technique used to shape and steer antenna beams by controlling the spatial direction of the transmitted or received RF energy. Beamforming architectures can be classified into analog, digital, and hybrid implementations. *Analog beamforming* relies

on phase shifters in the RF domain and offers low hardware complexity and power consumption but limited flexibility [21]. *Digital beamforming* is performed in baseband and provides fine-grained beam control and support for multiple simultaneous beams at the cost of higher computational complexity and power usage [22]. *Hybrid beamforming* combines both approaches to achieve a trade-off between performance and implementation complexity, and is widely considered a practical solution for large-scale antenna arrays in modern satellite payloads and user terminals [23]. In addition, *adaptive beamforming* techniques, usually employed at phased arrays receivers to adjust the antenna beamforming weights in response to variations in the propagation channel, user mobility, and interference conditions, enables real-time beam steering and interference suppression.

1.1.2 SatComs Link Budget

Satellite to user link budget calculations based on the well-known Friis propagation model[2], which characterizes the received signal power under ideal line-of-sight (LoS) conditions [24]. The signal strength collected at the user terminal can be expressed as,

$$S = P_{\text{tx}} \frac{G_{\text{tx}} G_{\text{rx}} \lambda^2}{(4\pi d)^2}, \tag{1.1}$$

where P_{tx} denotes the transmit power at the satellite antenna, G_{tx} and G_{rx} are the transmit and receive antenna gains of the satellite and user terminal, respectively, and d is the slant range between the satellite and the user. The carrier wavelength λ is related to the carrier frequency f through $\lambda = \frac{c}{f}$, where c is the speed of light. d are and slant range between the satellite and the user. In practical link budget formulations, the product $P_{\text{tx}}G_{\text{tx}}$ represents the EIRP. The inverse term $\frac{(4\pi d)^2}{\lambda^2}$ represents the FSPL, which is defined as the attenuation of signal strength as electromagnetic waves propagate through a LoS path [24]. However, the collected signal power S is corrupted by thermal noise N, mainly originating from the receiver electronics and the antenna noise temperature. The Signal-to-Noise Ratio (SNR) can be expressed as $\frac{S}{N}$, where the amount of noise collected N equals to $K_B T_A B_W$, where K_B is the Boltzmann constant (i.e., K_B in dB = $-228.6[\frac{\text{dBw/K}}{\text{Hz}}]$), T_A is the noise temperature and B_W is the bandwidth of the receiving filter. In the presence of an interference signal I, the SNR expression becomes known as Signal-to-Interference-plus-Noise Ratio (SINR), which can be expressed as $\frac{S+I}{N}$. The value of SNR or SINR is thus the main key performance indicators (KPIs) in SatComs, as they are directly associated with the achievable data rate, spectral efficiency,

[2]More elaborate models considering Rician fading are discussed in system model sections of Chapter 3 and Chapter 4.

and error performance of the adopted modulation and coding schemes (MODCOD). These KPIs highlight that higher-altitude constellations, such as GSO systems, experience significantly larger and essentially static path loss due to their large slant ranges. This typically requires higher transmit power, larger antenna apertures, or both, to achieve a target SNR/SINR. In contrast, NGSO systems benefit from substantially lower average path loss because of their shorter distances to the user, but the link attenuation becomes time-varying as the satellite moves, introducing additional challenges in power control, beam tracking, and adaptive MODCOD.

1.1.3 SatComs Radio Spectrum

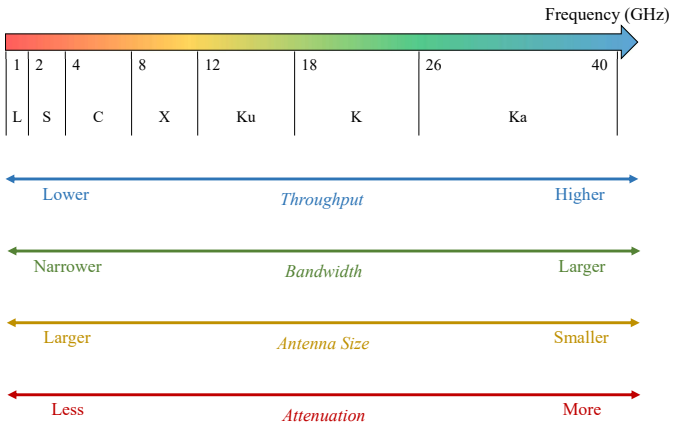


Figure 1.2: Satellite Communications Radio spectrum

Satellite communications operate in the Extremely High Frequency (EHF) band in the radio spectrum range, in particular between 1-50 GHz [25]. Different frequency bands are suitable for different climate conditions, types of service, and types of users. For simplicity, the frequency bands used for satellites are identified by simple letters: i) Lower frequencies (L, S, X, and C-bands), and ii) Higher frequencies (Ku, K, Ka, Q/V bands) [11]. Fig. 1.2, illustrate satellite spectrum bands, where lower-frequency bands offer reduced atmospheric attenuation and improved propagation robustness, but provide limited bandwidth and therefore lower achievable data rates. Conversely, higher-frequency bands enable substantially larger bandwidths and higher throughput, at the cost of increased susceptibility to atmospheric impairments such as rain fading. The figure also highlights the inverse relationship between operating frequency and antenna size, where higher frequencies allow for more compact antennas, facilitating multi-antenna systems.

GPS services primarily operate in the L-band, while the S-band is used for applications including weather radar, maritime radar, and satellite communications for space missions, as well as TT&C. These lower-frequency bands offer limited available bandwidth and are therefore highly congested and costly. Traditional SatCom services, particularly broadcasting, have predominantly operated in the C- and Ku-bands; however, increasing demand and fixed spectrum allocation policies have led to severe congestion in these bands. To improve spectral efficiency and support emerging broadband services, satellite systems have transitioned toward multi-beam architectures with aggressive frequency reuse [26]. Consequently, operators are increasingly exploiting higher-frequency bands, such as the Ka-band, which provide significantly larger bandwidth but are more susceptible to atmospheric impairments. The International Telecommunication Union (ITU) distinguishes between Fixed-Satellite Services (FSS), Mobile-Satellite Services (MSS), and Broadcast Satellite Services (BSS), in its Radio Regulations (RR) editions [27]. While FSS traditionally utilized legacy GSO systems, the modern trend utilizes both FSS and MSS spectrum allocations for stationary and non-stationary NGSO user terminals (UTs), creating a regulatory and technical overlap that exacerbates spectral congestion [28]. The emergence of large NGSO mega-constellations further intensifies spectrum-sharing challenges, particularly in the Ku- and Ka-bands, which are also used by legacy GSO systems. This coexistence raises critical interference concerns among NGSO systems and between NGSO and GSO networks, underscoring the need for enhanced coordination, interference awareness, and advanced spectrum-sharing mechanisms to ensure reliable and efficient satellite communication operations [29].

1.1.4 Next Generation SatComs Applications

Fig. 1.3 summarizes the next-generation of SatComs applications in the ”Network of Networks” vision [11]. It highlights the transition from satellites acting as isolated infrastructure to becoming a global ecosystem across diverse geographical topographies,

A. Geographical service segmentation: the figure shows three distinct operational domains, each presenting unique propagation and link-budget challenges, i) *Urban Area*: In high-density environments, the satellite functions primarily as a complementary layer to terrestrial network applications. ii) *Rural Area*: Here, satellites bridge the digital divide by providing Backhauling for isolated towers and Direct Connectivity for residential or agricultural IoT, where terrestrial fiber deployment is economically unfeasible. iii) *Remote Area*: In air, deserts, and oceanic zones, satellites are the exclusive providers of connectivity, supporting Maritime & M2M (Machine-to-Machine) communications and global logistics tracking.

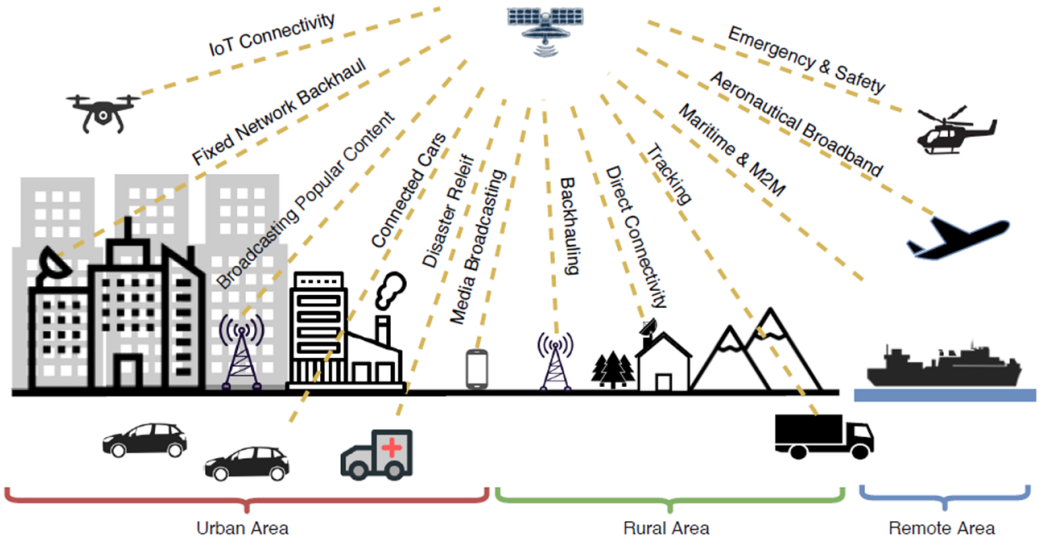


Figure 1.3: Next Generation SatComs ecosystem [11].

B. Vertical Market Applications: The figure delineates specific mission-critical and broadband use cases that motivate the shift toward low-latency NGSO constellations, i) *Mobility & Transport*: Supported by Connected Cars, Aeronautical Broadband, and maritime services, showcasing the need for robust beam-handover and Doppler shift compensation algorithms. ii) *Public Safety & Resilience*: Labeled under Disaster Relief, and iii) *Emergency & Safety*: satellites provide a "fail-safe" communication layer during terrestrial infrastructure outages caused by natural disasters. iii) *IoT & Massive Connectivity*: represents the integration of massive Machine-Type Communications (mMTC), requiring satellites to manage asynchronous access from millions of low-power devices.

1.1.5 AI-enabled SatComs

AI refers to a broad class of computational techniques that enable machines to perform tasks traditionally requiring human intelligence, such as learning from data, recognizing patterns, making decisions, and adapting to changing environments [30]. Modern AI, driven largely by machine learning (ML) and deep learning (DL), relies on data-driven optimization to approximate complex functional relationships that are difficult or impractical to model analytically [31]. As a result, AI has become particularly effective in high-dimensional, non-linear, and uncertain systems where explicit mathematical modeling is either inaccurate or computationally prohibitive [7]. AI encompasses multiple learning paradigms that differ in how models are trained and how supervision is provided. The most common learning types are,

- **Supervised learning (SL)**: relies on labeled data to learn mappings between inputs and desired outputs. In SatComs, supervised learning has been applied to classification tasks [32], anti-jamming [33], traffic forecasting [34], channel estimation [35], among others. While effective when labeled datasets are available, supervised approaches are often limited by the high cost of obtaining accurate data labels.

- **Unsupervised learning (USL)**: extracts patterns and structures from unlabeled data without explicit ground truth. In SatComs, this learning paradigm is particularly well suited for tasks such as user clustering [36], anomaly detection, and autoencoder-based (AE) tasks [37].

- **Reinforcement learning (RL)**: focuses on sequential decision-making through interaction with an environment, where actions are evaluated based on long-term rewards and decisions must account for time-varying channel conditions and system constraints [38]. In SatComs, RL has been explored for adaptive resource allocation [39], beam hopping [40], and task offloading [41].

Beyond typical SL, USL, and RL paradigms, **Self-supervised learning (SSL)** has emerged as a promising approach that bridges supervised and unsupervised learning by generating supervisory signals directly from the data itself [42]. This paradigm is particularly appealing for large-scale satellite systems, where labeled data is scarce but raw signal observations are abundant [43, 44]. Furthermore, the advent of distributed learning paradigms, e.g., **Federated learning (FL)**, enables collaborative model training across distributed nodes without centralizing raw data, thereby reducing communication overhead and preserving data privacy [45, 46]. The 3rd Generation Partnership Project (3GPP) in its release 18 and release 19, mainly discusses integrating AI into 5G/6G standards, including SatCom Systems [47–49]. This thesis leverages advanced paradigms, particularly USL, SSL, and FL, to design scalable and estimation-free interference management solutions tailored to satellites coexisting in dynamic NGSO environments.

1.2 SatComs Interference Problem

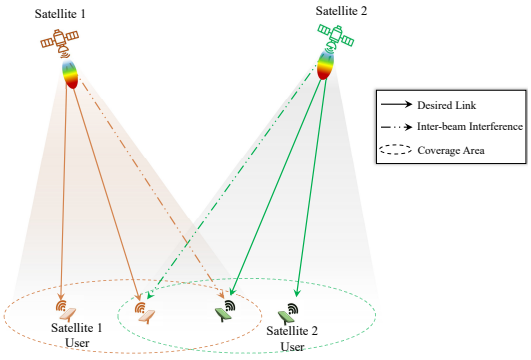
In physics, interference is known as the combination of two or more electromagnetic waveforms to form a resultant wave in which the displacement is either reinforced or cancelled. So, while constructive interference is useful in some applications (e.g., in array beamforming), it is considered a wide and multi-dimensional problem. Interference is formally defined by the ITU as "*The effect of unwanted energy due to one or a combination of emissions, radiations, or inductions upon reception*

in a radio-communication system, manifested by any performance degradation, misinterpretation, or loss of information which could be extracted in the absence of such unwanted energy" [50]. For wireless communication signals, which are basically electromagnetic waves, interference is known as electromagnetic interference (EMI) or radio-frequency interference (RFI). It arises when multiple transmissions overlap in time, frequency, and/or spatial domains, deteriorating the performance or even leading to a malfunction of the system or service unavailability [51]. Interference is a primary performance-limiting factor in SatComs, as it reduces signal quality, spectral efficiency, and quality of service (QoS). Eventually, it leads to user dissatisfaction and revenue losses for satellite operators. In modern satellite networks, the interference phenomenon is increasingly pronounced due to multi-beam payloads, aggressive frequency reuse, spectrum sharing, and the coexistence of heterogeneous space, air, and TNs [1].

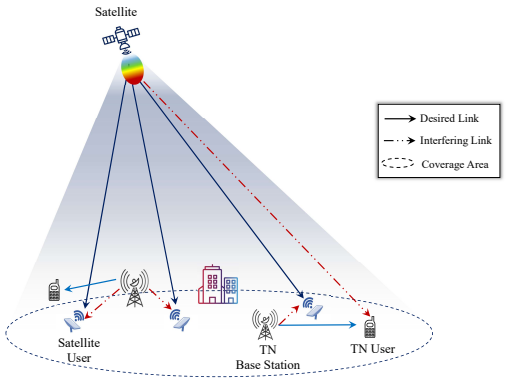
Table 1.1: Summary of Interference Classification in Satellite Communication Systems

Category	**Description**
Interference categories by severity of impact (ITU Classification [52]):	
Permissible interference	Occurs within predefined limits of duration and energy levels; short high levels or long low levels of such interference remain tolerable.
Acceptable interference	When interference exceeds permissible limits in duration or energy levels, yet not severe enough to significantly impair system performance or service quality.
Harmful interference	interference which seriously degrades, obstructs, or repeatedly interrupts a radio-communication service operating in accordance with the Radio Regulations (RR).
Interference categories by origin of source:	
Intentional interference	Deliberate interference (e.g., jamming) intended to deny or severely degrade communication, typically long-lasting and used in electronic warfare [53].
Unintentional interference	Usually short-term interference caused by operational errors or faults such as antenna misalignment, incorrect power settings, on-board/on-ground equipment failure, or satellite line-of-sight crossings [54].
Interference categories from operational perspective:	
Inter-system interference	Interference between different systems, including with NTNs/TNs coexistence (e.g., NGSOs-GSOs, NGSOs-NGSOs, SatComs-UAVs, SatComs-TNs), and SatComs-GNSS(Global Navigation Satellite Systems) used for Positioning, Navigation, and Timing (PNT). Also known as Cross-system interference [55].
Intra-system interference	Interference within the same system, such as multi-beam interference due to frequency reuse, adjacent-channel leakage, and imperfect filtering [56].
Interference categories by physical-layer effect:	
Co-frequency interference (CFI)	Occurs between transmitters operating on the same frequency channel, dominant in spectrum sharing scenarios, also known as Co-Channel Interference (CCI) [57].
Adjacent-channel interference(ACI)	Caused by spectral leakage from neighboring frequency channels due to imperfect filtering [58].
Multi-user interference (MUI)	Among users sharing common system resources such as time, frequency, code, or spatial beams, also known as co-user interference (CUI) [59].
Inter-symbol interference (ISI)	Where successive symbols overlap due to channel dispersion and filtering effects, degrading detection performance [60].
Inter-beam interference (IBI)	Between different beams of the same- or cross-satellites, mainly driven by aggressive frequency reuse and limited beam isolation [61].

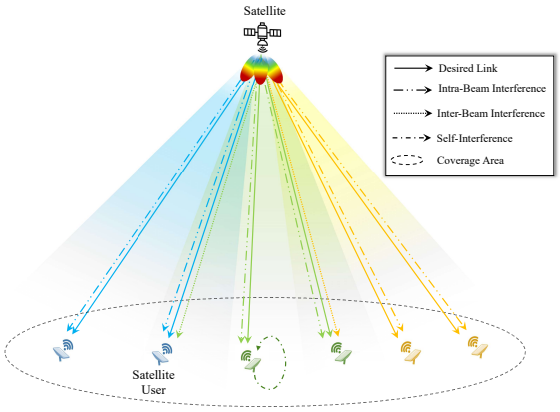
SatCom interference can generally be classified from many perspectives; we summarize some in Table 1.1. In Fig. 1.4 we showcase some SatCom interference Scenarios. The proliferation of NGSO constellations has further exacerbated the interference challenge. Unlike legacy GSO systems, NGSO satellites exhibit rapid orbital motion and highly time-varying link geometries, resulting in interference conditions that are inherently dynamic and difficult to predict [55]. Consequently, interference management strategies must operate under stringent latency, scalability, and robustness constraints that exceed the capabilities of conventional approaches. Moreover, the increasing reliance on aggressive frequency reuse, multi-beam architectures, and spectrum sharing needs has intensified CFI scenarios [57]. These effects are especially pronounced in the Ku- and Ka-bands, where spectrum scarcity, heterogeneous deployments, and regulatory permissiveness intersect.



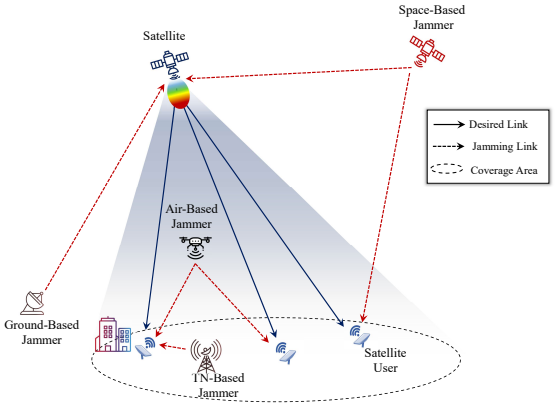
(a) SatCom-SatCom interference scenarios



(b) SatCom-TN interference scenarios



(c) Intra-system interference scenarios



(d) Intentional interference scenarios

Figure 1.4: Some satellite system interference scenarios: (a) SatCom IBI (i.e., intra-system IBI if both satellites belong to same operator, inter-system IBI if they are from separate operators (coexistence)); (b) SatComs-TN coexistence (i.e., CFI); (c) Intra-system interferences; (d) Jamming.

The development and operation of satellite communication systems are governed by a combination of regulatory and technical standardization frameworks. At the global level, the ITU is responsible for spectrum allocation, orbital resource management, and the definition of international coexistence rules, or radio regulations (RR), to ensure fair and interference-limited access among telecommunication systems [27]. For instance, Article 22 of ITU RR [52] enforces equivalent power flux density (EPFD) limits to protect GSO systems from harmful interference generated by NGSO constellations. However, NGSO operators, including major players like Amazon and SpaceX, requested increased flexibility in the EPFD limits to accommodate their evolving systems at the latest ITU's World Radiocommunication Conference 2023 (WRC-23) [62]. At the national level, regulatory authorities such as the U.S. Federal Communications Commission (FCC) implement and enforce licensing procedures, spectrum sharing policies that complement ITU methodologies, and operational constraints, which strongly influence the deployment and configuration of large NGSO constellations. Examples include the authorization of satellite operators to access specific frequency bands and orbital resources (e.g., STARLINK [63] and OneWeb [64]). In parallel, technical standardization bodies, such as the 3GPP, provide a common technological foundation for NTN deployment; they recently discussed the architectures, protocols, and system integration of NTNs (including satellite communications) within 5G and beyond standards through a series of technical specifications (TS) and technical reports (TR) [47, 48]. While these regulatory and standardization frameworks are essential for spectrum governance, system interoperability, and large-scale deployment, they remain policy-driven, and it is unclear whether current technical solutions and regulatory safeguards can be respected fully to ensure reliable coexistence under realistic operational conditions [65–67].

1.3 SatComs Interference Management Strategies

Due to the diversity of SatComs architectures, spectrum usage regulations, and deployment scenarios, interference management in SatComs cannot rely on a single mechanism. Instead, it is typically addressed through a hierarchy of complementary strategies operating at different layers of the system and across overlapping satellite networks (e.g., NGSO–GSO and NGSO–NGSO coexistence) [66, 67]. These strategies aim to prevent, detect, mitigate, or compensate for the detrimental impact of interference on communication performance and can be broadly classified according to their level of operation, degree of coordination, and reliance on system knowledge. *At a high level*, interference management strategies can be grouped into two main categories:

- **Proactive strategies**: aim to prevent harmful interference before it occurs, and they include, i) coordination procedures enforced by international and national regulatory, such as ITU radio regulations [27, 65], spectrum sharing frameworks [67], and the exclusion and protection zones between primary and secondary systems [68], ii) interference avoidance strategies through system planning, design, and pre-analysis [57], radio resource allocation (RRA) [69], iii) monitor possible interference events [70]. However, they operate on long time scales and cannot react alone to unexpected or rapidly varying interference conditions.

- **Reactive strategies**: operate once interference is observed and focus on managing interference at the physical layer using mathematical and analytical models, or signal processing techniques, and they include, i) interference detection techniques such as energy detection [71], ii) interference analysis techniques (e.g. interference type classification [72], interference localization [73]), iii) interference mitigation techniques (e.g., adaptive beamforming [15, 74], bandwidth filtering [75], precoding [76]). These methods usually rely on parameter estimation, or partial knowledge of the interference environment [77].

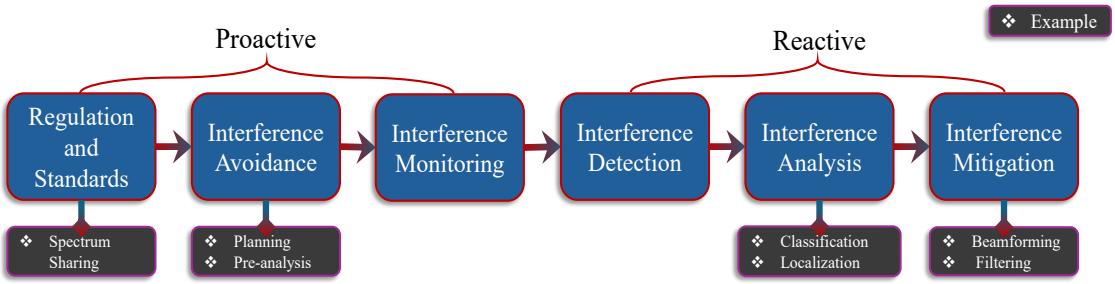


Figure 1.5: Summarized interference management techniques.

Fig. 1.5 provides a holistic view of interference management approaches in satellite communication systems by organizing the above strategies into six complementary stages. These stages span from long-term regulatory planning to real-time signal processing. This progressive and multi-stage structure is essential for coping with the dense, heterogeneous, and highly dynamic nature of emerging satellite networks. Despite extensive efforts, conventional interference management frameworks face fundamental limitations when applied to NGSO systems [78]. The high heterogeneity of NGSO constellations, combined with uncertainty in deployment parameters and fast orbital dynamics, significantly degrades the effectiveness of traditional approaches [5]. For instance, [66] evaluated three classical NGSO–to-GSO CFI mitigation strategies: i) *look-aside*, where the NGSOs user terminal

switches its pointing direction toward an alternative NGSO satellite within the visible region to avoid in-line interference with GSO satellites; ii) *band splitting*, in which the available spectrum is partitioned between systems, at the expense of reduced spectral efficiency; and iii) *exclusion zones*, where NGSO satellites operation is restricted or avoided in geographical areas in which GSO users experienced interference exceeds acceptable thresholds. The results demonstrated that existing frameworks may be insufficient to guarantee adequate protection of GSO systems against dense NGSO deployments. Similarly, the impact of NGSO-to–NGSO CFI was investigated in [67], where band-splitting techniques were studied for Ka- and V-band spectrum sharing. The analysis showed that the complex interactions among heterogeneous NGSO constellations make interference behavior highly scenario-dependent and difficult to control using static mitigation policies. These findings collectively indicate that NGSO interference requires more adaptive, intelligent, and scalable management mechanisms.

To comply with the efforts of integrating SatCom in future communication standards, a wide range of improved state-of-the-art (SoTA) interference management solutions has been actively investigated [20]. Consequently, the increasing complexity of satellite networks has driven a shift from traditional **model-based** methods, which rely on explicit mathematical descriptions, toward **data-driven** approaches [10]. Model-based methods rely on explicit mathematical descriptions of channel and interference dynamics, while data-driven methods, particularly those based on AI, learn to manage interference directly from observed data characteristics. The latter class is especially attractive for NGSO systems, where accurate modeling is difficult and real-time adaptability is essential. AI-based methods have been explored for SatComs interference detection [79], interference classification [80], preceding [76], and spectrum management [81]. Nevertheless, several challenges remain open when applying AI-based models, including models' robustness to unseen interference conditions, models' scalability to large constellations under strict latency and computational constraints, and models' generalization across heterogeneous satellite deployments. Addressing these limitations is essential for enabling practical and autonomous interference management in next-generation satellite networks, and forms the central focus of this thesis.

1.4 Research Motivation

The satellite communications landscape is undergoing rapid transformation driven by the deployment of large NGSO constellations, which significantly increases the density and heterogeneity of space-based systems as shown in Fig. 1.6.

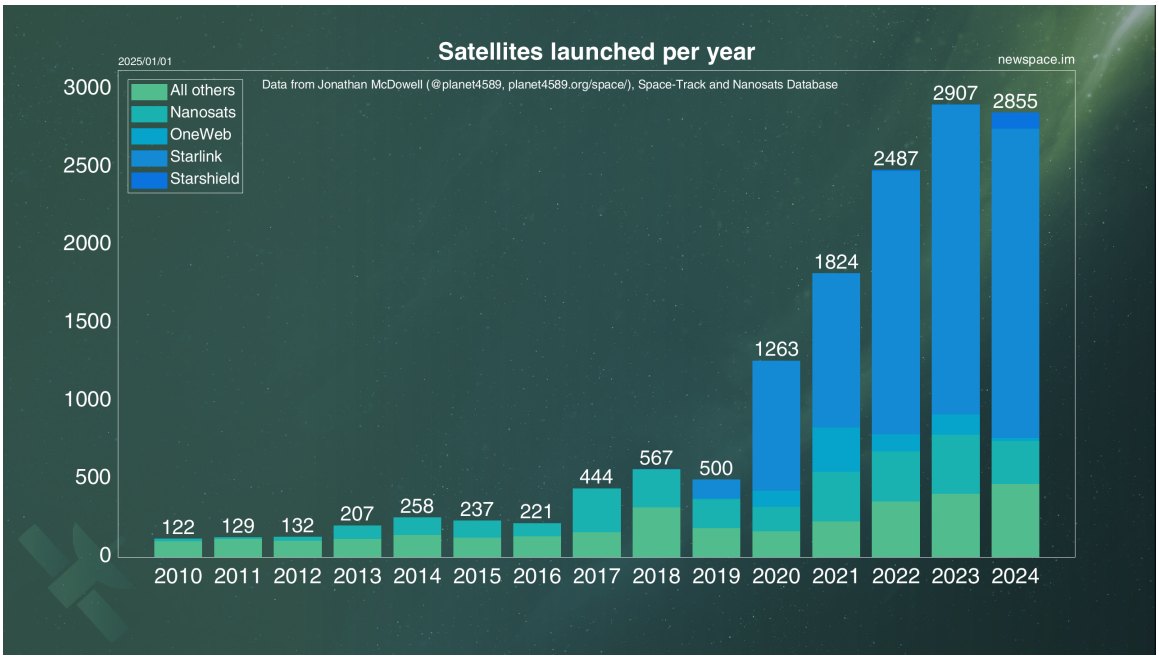


Figure 1.6: Satellites launched per year [82].

In this sense, it is estimated that approximately 10,000+ active satellites are currently orbiting the Earth, a number that is foreseen to grow to 40,000+ within the next ten years. This densification, combined with aggressive frequency reuse and spectrum sharing in Ku-/Ka-/V-bands, amplifies the likelihood of harmful CFI across NGSO-GSO, NGSO-NGSO coexistence scenarios. The most challenging inter-satellite coexistence CFI is expected to be in sharing the Ku-band, due to the very heterogeneous systems in terms of the number of NGSOs satellites (e.g., Starlink, OneWeb) and geometric orbit properties (e.g., circular, elliptical) that are set to operate in this band. Moreover, existing GSO systems also operate in the Ku-band (e.g., ASTRA [83]) and must be protected from interference by NGSO systems, as enforced by regulation, where applications for a license for these new systems have been initiated [27]. At the technical level, conventional interference management techniques often require accurate interference channel state information (CSI), direction-of-arrival (DoA) estimation, or large antenna signal realizations, which are difficult to obtain [12]. State-of-the-art optimization and coordination approaches can improve performance but may incur high computational complexity, substantial signaling overhead, and limited scalability in mega-constellation settings [20]. These limitations motivate the development of data-driven and estimation-free interference management frameworks capable of adapting to non-stationary interference dynamics and large-scale heterogeneous deployments. In particular, focusing on specific SatCom CFI scenarios, as illustrated in Fig. 1.7, this thesis addresses the following research gaps,

- Robust AI-based models for NGSO-to-GSO downlink CFI interference detection at GSO users' antennas without prior knowledge of interfering NGSO signal characteristics.
- AI-based models for NGSO-to-NGSO downlink CFI interference mitigation based on multi-antenna beamforming at the UTs, with no explicit interference sources' CSI/DoA estimation, while handling heterogeneous spatial correlation scenarios.
- Scalable and collaborative NGSO-to-NGSO downlink CFI interference mitigation for large-scale NGSO deployments, enabling distributed operation under communication, computation, and coherence-time constraints.

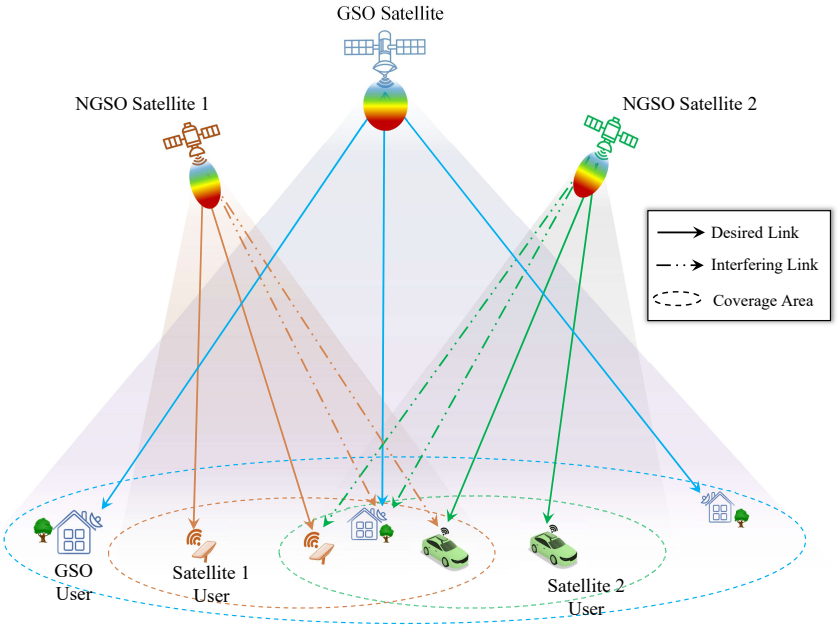


Figure 1.7: CFI Scenarios of Interest.

1.4.1 Research Questions

The overarching objective of this thesis is to design, evaluate, and validate AI-driven interference detection and mitigation frameworks that are robust, scalable, and suitable for the highly dynamic operating conditions of NGSO systems. In particular, the thesis aims to develop estimation-free and data-driven solutions capable of operating under realistic orbital dynamics, short channel coherence times, and large-scale heterogeneous deployments. In particular, this thesis investigates the following research questions (RQs),

RQ1

How can AI-based techniques assist in detecting NGSO-to-GSO downlink CFI events at GSO users terminals without prior knowledge of the NGSO interference characteristics?

RQ2

How can AI-based beamforming models enable fast mitigation of downlink CFI between NGSO systems at user terminals while relying solely on estimation-free data?

RQ3

How can federated learning paradigms, be leveraged to develop scalable AI-based beamforming model for CFI mitigation between NGSO systems at user terminals, in large-scale NGSO deployments, considering communication and computational constraints?

1.4.2 Research Methodology

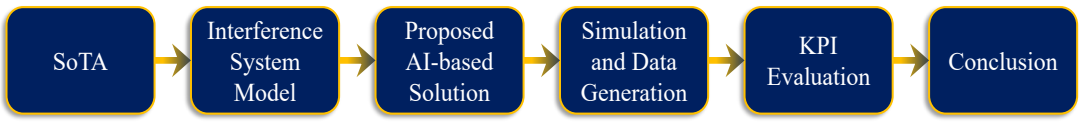


Figure 1.8: Research methodology adopted in each chapter.

This thesis adopts a data-driven research methodology, summarized in Fig. 1.8. First, the SoTA in conventional and learning-based interference management are reviewed to identify key limitations. Next, coexistence CFI scenarios and system models are formulated, including realistic orbital dynamics, channel, and signal representations. Building on this foundation, novel AI-based models for interference management are designed from scratch using Tensorflow and Keras frameworks in `Python`. Then, an extensive simulation and data-generation pipelines are conducted to create representative training datasets in `MATLAB`. All datasets are made publicly available through SmartSpace project webpage [84]. Finally, the proposed methods are rigorously evaluated using appropriate KPIs (e.g., probability of detection, SINR), and benchmarked against conventional other AI-based methods, leading to chapter-level conclusions and practical insights for next-generation SatCom systems.

1.5 Thesis Contributions and Related Publications

This section outlines the contributions of this thesis and provides an overview of its structure and related publications. This thesis addresses AI-enabled interference management for next-generation SatCom systems through three complementary contributions, corresponding to Chapters 2-4 and the associated publications as follows,

Chapter 2: GenAI-based Models for NGSO Satellites Interference Detection

This chapter investigates unsupervised learning techniques for NGSO-to-GSO downlink CFI detection at GSO user terminals, directly addressing **RQ1**. It proposes and evaluates generative AI-based (GenAI) detectors, including a variational autoencoder (VAE) and a transformer-based interference detector (TrID), using realistic orbital dynamics and system parameters. The proposed models learn to generate samples of the expected interference-free GSO signal, and the reconstruction error between the generated and the observed signals is exploited to flag interference events. The results demonstrate substantial performance gains over conventional energy detection methods (EDs) and classical autoencoder-based baselines. In addition, the chapter introduces extensive simulation and data generation pipelines and releases new open datasets to support reproducible research and future investigations in NGSO-to-GSO interference detection.

Related publications:

[**J1**] **A. Saifaldawla**, F. Ortiz, E. Lagunas, A. B. M. Adam and S. Chatzinotas, "GenAI-Based Models for NGSO Satellites Interference Detection," in *IEEE Transactions on Machine Learning in Communications and Networking*, vol. 2, pp. 904-924, 2024, doi: 10.1109/TMLCN.2024.3418933.

[**C1**] **A. Saifaldawla**, F. Ortiz, E. Lagunas, S. Daoud and S. Chatzinotas, "NGSO-To-GSO Satellite Interference Detection Based on Autoencoder," *2023 IEEE 34th Annual International Symposium on Personal, Indoor and Mobile Radio Communications (PIMRC)*, Toronto, ON, Canada, 2023, pp. 1-7, doi: 10.1109/PIMRC56721.2023.10293839.

[**C2**] **A. Saifaldawla**, F. Ortiz, E. Lagunas and S. Chatzinotas, "Convolutional Autoencoders for Non-Geostationary Satellite Interference Detection," *2024 IEEE International Conference on Communications Workshops (ICC Workshops)*, Denver, CO, USA, 2024, pp. 1334-1339, doi: 10.1109/ICCWorkshops59551.2024.10615457.

Chapter 3: Attention-based Blind Adaptive Receive Beamforming for NGSO Satellite Systems

To address **RQ2**, this chapter proposes an attention-based beamformer (AttBF) for NGSO systems coexistence, where an NGSO system user terminals face downlink CFI interference from another NGSO system. The proposed method performs blind adaptive beamforming using estimation-free sample covariance matrices (SCMs) as input data and employs self-supervision through SINR feedback, enabling instantaneous interference mitigation under short channel coherence time constraints. A comprehensive performance evaluation against classical beamforming techniques, such as zero-forcing beamforming (ZFBF) and sample matrix inversion (SMI), as well as deep learning–based baselines, demonstrates the superior interference nulling capability and robustness of the proposed approach. Similar to Chapter 2, this chapter introduces extensive simulation and data generation pipelines and releases open datasets to facilitate reproducible research and future investigations.

Related publications:

[**J2**] **A. Saifaldawla**, F. Ortiz, E. Lagunas and S. Chatzinotas, "Attention-based Blind Adaptive Receive Beamforming for Interference Limited NGSO Satellite Systems," in *IEEE Open Journal of the Communications Society*, vol. 6, pp. 8946-8964, 2025, doi: 10.1109/OJCOMS.2025.3622661.

[**C3**] **A. Saifaldawla**, E. Lagunas, F. Ortiz, A. B. M. Adam and S. Chatzinotas, "SmartUT: Receive Beamforming for Spectral Coexistence of NGSO Satellite Systems," *2025 28th International Workshop on Smart Antennas (WSA)*, Erlangen, Germany, 2025, pp. 195-200, doi: 10.1109/WSA65299.2025.11202840.

Chapter 4: Federated Learning–Enabled Beamforming for NGSO Direct-to-Vehicle Systems

This chapter addresses **RQ3** by introducing *FedSatBF*, a federated learning framework that enables collaborative receive beamforming among vehicular user terminals served by an NGSO satellite to mitigate downlink CFI imposed by nearby interfering NGSO systems. Building upon the AttBF architecture with SCMs inputs as the local model, FedSatBF performs distributed learning through federated averaging with considerations to channel coherence-time constraints. This design enables effective interference mitigation without sharing raw signal data or requiring explicit knowledge of the interference channels. Comprehensive evaluations demonstrate that the proposed framework achieves near-optimal SINR performance, exhibits strong generalization to non-participating users, and provides a favorable trade-off between performance and computational complexity, making it suitable for real-time and large-scale deployment in next-generation NGSO systems.

Related publications:

[**J3**] **A. Saifaldawla**, E. Lagunas, M. Alsenwi and S. Chatzinotas, "Federated Learning–Enabled Collaborative Beamforming for NGSO Direct-to-Vehicle Systems". *Under revision in IEEE Transactions on Machine Learning in Communications and Networking*.

Chapter 5: Conclusions and Future Research

This chapter provides a concise summary of the main findings, key insights, and overall conclusions of the thesis. It also discusses potential extensions of the proposed methodologies and identifies promising directions for future research, highlighting open challenges and opportunities for advancing AI-enabled interference management in next-generation satellite communication systems.

1.5.1 Publication Not Included in the Thesis

To maintain consistency, the following publications are not included in this thesis, even though they still pertain to the PhD work.

[**M1**] F. Ortiz, E. Lagunas, **A. Saifaldawla**, M. Jalali, L. Emiliani and S. Chatzinotas, "Emerging LEO constellations: Spectral Coexistence with Legacy GEO Satellite Communication Systems." *Frontiers in Communications and Networks*, vol.7, 2026.

[**M2**] A. Adam, E. Lagunas, M. Samy, **A. Saifaldawla**, and S. Chatzinotas, "Generative AI for Non-terrestrial Networks: Design, Applications, and Challenges," *EURASIP Journal on Wireless Communications and Networking*, 2025, doi: 10.1186/s13638-025-02549-7.

Chapter 2

GenAI-based Models for NGSO Satellites Interference Detection

RECENT advancements in satellite communications have highlighted the challenge of interference detection, especially with the new generation of non-geostationary orbit satellites (NGSOs) that share the same frequency bands as legacy geostationary orbit satellites (GSOs). Despite existing radio regulations during the filing stage, this heightened congestion in the spectrum is likely to lead to instances of interference during real-time operations. This chapter addresses the NGSO-to-GSO interference problem by proposing advanced artificial intelligence (AI) models to detect interference events. In particular, we focus on the downlink interference case, where signals from low-Earth orbit satellites (LEOs) potentially impact the signals received at the GSO ground stations (GGSs). In addition to the widely used autoencoder-based models (AEs), we design, develop, and train two generative AI-based models (GenAI), which are a variational autoencoder (VAE) and a transformer-based interference detector (TrID). These models generate samples of the expected GSO signal, whose error with respect to the input signal is used to flag interference. Actual satellite positions, trajectories, and realistic system parameters are used to emulate the interference scenarios and validate the proposed models. Numerical evaluation reveals that the models exhibit higher accuracy for detecting interference in the time-domain signal representations compared to the frequency-domain representations. Furthermore, the results demonstrate that TrID significantly outperforms the other models as well as the traditional energy detector (ED) approach, showing an increase of up to 31.23% in interference detection accuracy, offering an innovative and efficient solution to a pressing challenge in satellite communications.

2.1 Introduction

2.1.1 Context and Motivation

Among the dynamic field of satellite communications, the co-existence between non-geostationary (NGSO) and geostationary (GSO) satellite systems has become an increasingly important issue, this is due to the increasing number of satellites in NGSO, particularly in low-Earth orbit (LEO) [5]. This co-existence may lead to the possibility that NGSO satellites inadvertently degrade GSO communication with GSO ground stations (GGSs), which can severely impair the quality and reliability of vital communication services for many global applications [85]. To address this problem, the International Telecommunication Union (ITU) mandates a power radiation checkpoint whenever an NGSO operator files for a specific spectrum use, this is often referred to as the equivalent-power flux density (EPFD) limits [52]. This checkpoint is found to be too relaxed for GSO operators and too strict for NGSO operators [86]. Tackling interference effectively requires a multifaceted approach, encompassing several stages: monitoring of interference [70] [65], detection of interference [71], classification of interference types [72], pinpointing the location of interference [73], and finally, mitigating interference [87] [85]. In this chapter, we focus on the aspect of interference detection problem. Traditional interference detection methods, such as energy detectors (EDs), are increasingly inadequate in this evolving landscape [75]. EDs primarily measure the energy of a signal to determine the presence of an interference signal by thresholding over signal power. However, in a densely populated orbital environment, where there are many low-power signals, EDs may not have the sensitivity to detect weak or hidden interfering signals in the background noise. This lack of sensitivity can lead to missed detections.

The limitations of traditional interference detection techniques set the stage for exploring advanced machine learning (ML) techniques as possible solutions [80]. Consequently, various advents in generative artificial intelligence (GenAI), in which advanced algorithms are trained to create new original content [88], such as variational autoencoder models (VAEs) [89] and recent transformer-based models [90], could offer a new paradigm for complex interference detection tasks. Our research focuses on highlighting the promising benefits of GenAI in interference detection tasks for satellite communication systems. These benefits include improved accuracy, adaptability, and predictive capability, which help overcome the limitations of conventional methods.

2.1.2 Related Work

Interference detection based on traditional techniques

The current state of the art in interference detection within satellite communications predominantly revolves around traditional techniques that have been instrumental in interference detection problems [91]. The optimal detector depends on the amount of side-information that we have with respect to the signal to be detected. Since we generally do not have much information, the optimal detector (also known as the likelihood-ratio test) for stochastic signals in white Gaussian noise environments is the ED [91]. An ED essentially measures the energy of the received signals and compares it to a specific threshold, which makes a binary decision on the presence of interference. The simplicity and low computational requirements of EDs make them popular in scenarios where fast and direct detection is needed [75]. However, they have limitations in environments with complex signal characteristics or low signal-to-noise ratios (SNRs) [92]. In these cases, energy detectors can face difficulties in distinguishing between legitimate signals and interference, resulting in false positives or missed detections. Among the challenges of ED, the most relevant is the definition of the time window where the energy is calculated, as well as the establishment of an appropriate threshold [93].

Regarding the use of ED in space-based applications, Politis et al. [71] presented a novel two-step algorithm to detect interference in satellite communications using on-board spectrum monitoring units (SMUs). Focusing on the use of the DVB-S2X standard [94], [71] leverages pilot symbols for data transmission. The proposed method involves removing pilot signals from the received signal and applying an ED technique, showing superior performance to conventional ED, especially in low interference-to-signal and noise ratios (ISNRs). A significant limitation of this methodology is that the complexity and power consumption of on-board processing need to be optimized, as these are critical factors for in-orbit systems. Another popular technique is the detection of cyclostatinarity. For instance, Dimc et al. [95] examined cyclostationary feature detection for mobile satellite transmission. Although this technique overcomes the limitations of ED in low-SNR environments, it requires high computational complexity since all the cycle frequencies need to be calculated. Such complexity poses challenges in fast time-varying scenarios such as those included in this work, where the NGSO satellite(s) quick propagation results in a relatively short-time interference impact on the desired signal.

In general, key challenges faced by traditional techniques include their limited adaptability to rapidly changing and increasingly crowded satellite environments, the requirement for more sophisticated real-time processing and analysis capabilities, and dependence on external factors such as

signal strength and environmental conditions. These challenges highlight the need for more advanced, flexible, and robust interference detection methodologies as the satellite communications landscape evolves.

Machine learning for interference detection.

ML in satellite communication operations, particularly for interference detection, has seen remarkable advances in recent years. Machine learning models offer several advantages over traditional methods, such as improved accuracy, adaptability to complex signal environments, and the ability to learn and predict interference patterns [30] [96]. However, the integration of ML models into existing systems and the trade-off between computational efficiency and detection performance remain areas of ongoing research and development [39].

In this context, Pellaco et al. [79], presented an autoencoder-based long short-term memory model (LSTM), or LSTMAE, to identify both short-term and long-term interference within the spectrum of NGSO satellite signals at GSO ground stations, the goal was to detect deliberate interference or jamming, which was artificially created and added to the NGSO communication signal. Henarejos et al. [80], utilized a convolutional autoencoder (CAE) model to classify signals by processing in-phase and quadrature (IQ) samples directly. The primary signal considered is from a GSO satellite link, while interference is presumed to come from ground-based cellular networks. Saifaldawla et al. [97], proposed a conventional autoencoder model (AE) to detect interference from NGSO system to a GSO ground station in time and frequency domains data representations. The authors investigate the scenario of single NGSO satellite, and single modulation schemes (ModCods) for both GSO and NGSO. The aforementioned investigations [79, 80, 97] are limited to only high-level and simplified scenarios. Consequently, significant challenges remain in the application of ML for interference detection in satellite communication. In this chapter, we investigate the use of VAE and a transformer-based interference detector (TrID) models' capabilities for interference detection tasks in satellite communications, and we also address some of the existing interference detection challenges, which include the need for large and diverse datasets for training, the complexity of real-time processing, and adapting approaches to the dynamic nature of satellite communication environments. To the best of our knowledge, this is the first work to investigate the use of VAE and TrID for interference detection tasks in satellite communications.

2.1.3 Contributions

The key contributions of this work to the field of satellite communication, particularly in the area of interference detection between NGSOs and GSO satellite systems, can be stated as follows,

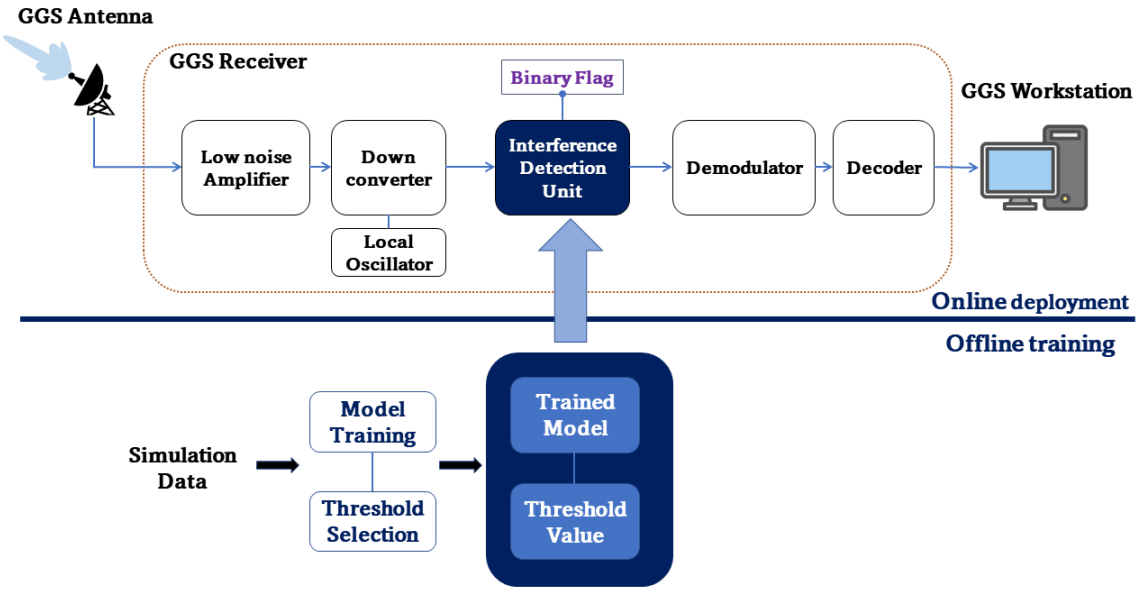


Figure 2.1: Proposed interference detection framework.

- The main contribution of this work is to design, develop, and investigate GenAI-based models (i.e., VAE and TrID models) capabilities for NGSOs-to-GSO interference detection tasks in satellite communications.
- We present a detailed evaluation of the proposed GenAI-based models against benchmark ML models, that is, AE, CAE, and LSTMAE, to detect interference instances in both time-domain and frequency-domain representations of the GGS received signal. This evaluation is one of the first to assess GenAI-based models in the context of satellite interference detection.
- We then provide a comparative analysis between the proposed GenAI-based models and a traditional detection methods, such as EDs, within the same NGSO interference conditions, to critically analyze their performance. This comparison highlights the strengths and limitations of both traditional and modern GenAI-based approaches in various satellite interference scenarios.
- Within this analysis, we explored the impact of varying GSO modulation schemes and bandwidth overlap scenarios on interference detection accuracy, along with the LEO off-axis arrival angles

and various interference power levels.

- We implement innovative and extensive simulation and data generation methodologies to facilitate and introduce new datasets for future investigation of NGSOs-GSO interference management techniques. In which we found that the proposed GenAI-based models reconstructing ability, especially TrID, can be used to generate new interference-free data samples to train future unsupervised learning models.

- By deploying an offline trained unsupervised ML-models, one aim of our study is to investigate the possibility of including ML-based interference detection unit into GGS receiver segment, as shown in Fig. 2.1, this will enable GGS receivers to perform automatic detection of interference signals within the desired GSO signal.

- The findings reveal that the proposed models exhibit higher accuracy in detecting interference in the time-domain signal representations compared to the frequency-domain representations. Moreover, our findings demonstrate the superior detection capabilities of GenAI-based models, with TrID outstanding from the VAE and other benchmark models over the ED approach. This highlights the potential of advanced GenAI-based techniques in improving the reliability and efficiency of satellite communication systems.

- We believe that this study lays the foundation for future research in this domain. The introduced datasts, the comparative analysis, and findings offer a baseline for further exploration and enhancement of ML models in the context of increasingly complex interference-limited satellite communication systems.

2.1.4 Chapter Organization

The rest of this chapter is structured as follows. Section 2.2. outlines the system model, focusing on the calculation of the link budget and the model for the received digital baseband signal. Section 2.3. discusses the simulation of NGSO-to-GSO interference scenarios and the generation of training data. Section 2.4. details the proposed GenAI-based models and the improved AEs models. Section 2.5. analysis the results obtained from training the models as well as the interference detection performance. Section 2.6. provide a comprehensive comparison of GenAI-based models and a traditional ED approach. The chapter concludes with Section 2.7, which provides a summary and concluding remarks.

2.2 System Model

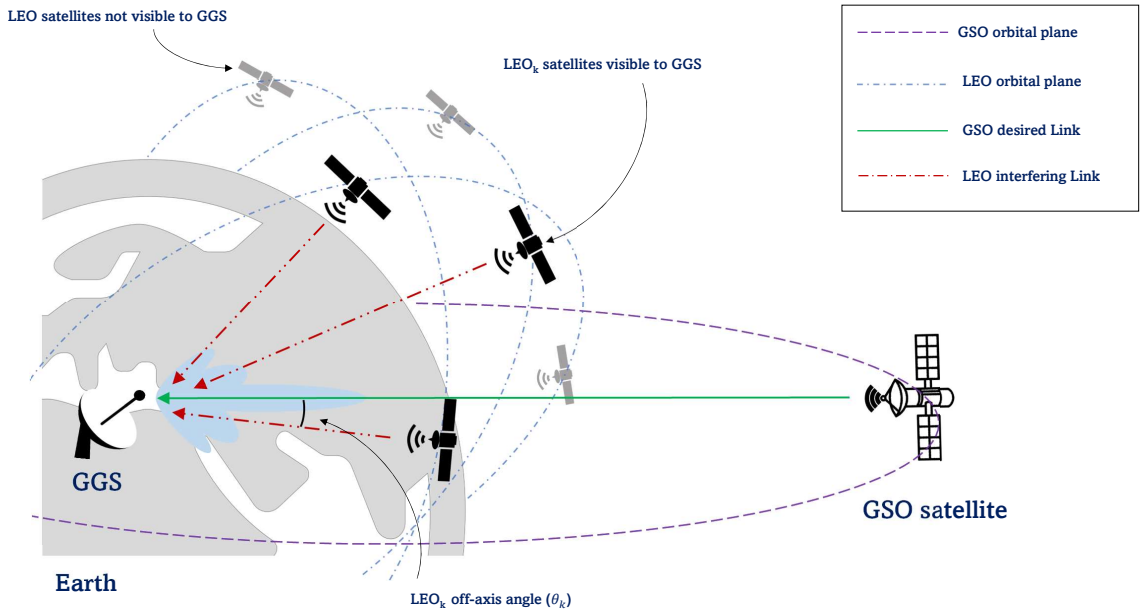


Figure 2.2: Simplified scenario scheme with a GGS pointing towards the desired GSO satellite and a potential interference from a NGSO system.

This research investigates the downlink dynamics of forward links originating from two distinct satellite constellations. Our main focus is on satellites in GSO orbits, as a primary system. We consider satellites in NGSO orbits, particularly those in LEO orbits, as potential sources of interference to a GGS[1]. In this section, a comprehensive description of the system model is presented, which includes aspects of link budget calculations and modeling of the received digital baseband signal.

2.2.1 Link Budget Model

In this context, we consider that both the GSO and LEO satellites are actively transmitting signals, with the primary lobe of the transmission consistently directed toward a GGS, as shown in Fig. 2.2. At the GGS receiver, the carrier power received, denoted as C, from the desired GSO satellite system, can be expressed as follows

$$C = \frac{EIRP_{\text{gso}} G_{r,\text{gso}}(\theta_0)}{L_{\text{FS, gso}} L_{\text{AD}}}, \tag{2.1}$$

[1]A general GSO ground station is assumed in the system model, which can represent either a gateway, a teleport or a user-terminal.

where $EIRP_{\text{gso}}$ is GSO satellite equivalent isotropic radiated power (EIRP), which quantifies the combination of the satellite antenna transmission power and its gain, $G_{r,\text{gso}}$ represents GGS maximum receiving antenna gain, θ_0 indicates the boresight angle, defining the alignment between the main lobe axis of GGS and GSO communication link, $L_{\text{FS, gso}}$ is the free space path loss (FSPL) at the GSO-GGS communication link with distance d_{gso}, signal wavelength λ_{gso} and carrier frequency $f_{c,\text{gso}}$. Lastly, L_{AD} correspond to the additional losses of the link (which include atmospheric, environmental, and external losses). With GGS being stationary on Earth, it consistently points towards its associated GSO satellite, which ensures optimal gain from its receiving antenna, As such, the value of (θ_0) is set to zero.

As LEO satellites traverse GGS visible sky, GGS may concurrently receive signals from one or more LEO satellites when they operate in the same frequency bands. These LEO signals primarily elevate the interference level within the primary signal. Consequently, the interference power I_k that GGS receives from an individual LEO satellite indexed as k is as follows

$$I_k = \frac{EIRP_k G_{r,k}(\theta_k) B_{\text{adj},k}}{L_{\text{FS},k} L_{\text{AD}}}, \quad k \in [1, \mathcal{K}] \tag{2.2}$$

where $\mathcal{K}$ represents the cumulative number of visible LEO satellites that can potentially affect the GGS at a particular time of day (time instant). $EIRP_k$ refers to the EIRP of k^{th} LEO satellite, $G_{r,k}$ denotes the GGS receiving antenna gain to k^{th} LEO satellite. Unlike (2.1), here θ_k represents the off-axis angle that aligns GGS beam primary lobe axis with the k^{th} LEO communication link as depicted in Fig. 2.2. The adjustment factor for bandwidth overlap, denoted as $B_{\text{adj},k} \in \mathbb{R}$, $B_{\text{adj},k} \in [0, 1]$, is constrained within the range [0,1], and it count for GSO and LEO bandwidth overlap, and can be calculated from the following formula

$$B_{\text{adj},k} = \frac{B_{\text{overlap},k}}{B_{i,k}}, \tag{2.3}$$

where $B_{\text{overlap},k}$ denotes the bandwidth overlap between the k^{th} LEO satellite bandwidth and GSO bandwidth, and $B_{i,k}$ is the bandwidth of the k^{th} LEO satellite. The value of $B_{\text{adj},k}$ adjusts the value of I_k according to the calculated ratio. Note that a full overlap of GSO and LEO bandwidths corresponds to a factor $B_{\text{adj},k} = 1$. $L_{\text{FS},k}$ convey the FSPL for the k^{th} LEO-GGS link. It should be noted that we have assumed a standardized value L_{AD} for both GSO and LEO connections, since they transmit under similar channel conditions. FSPL of the k^{th} LEO-GGS communication link with distance d_k, signal wavelength of λ_k and carrier frequency $f_{c,k}$.

The determination of the off-axis angle between GGS and the direction of the LEO satellite beam is based on the law of cosine. This relationship is expressed by the following formula

$$\theta_k = \arccos\left(\frac{d_{\text{gso}}^2 + d_k^2 - d_{\text{gso},k}}{2 d_{\text{gso}} d_k}\right), \tag{2.4}$$

where $d_{\text{gso},k}$ is represents the slant range between the GSO and the k^{th} LEO satellite.

In a context where transmission gain from both the GSO and LEO satellites is always at maximum, the impact of the receive antenna gain plays a pivotal role. Owing to the LEO satellite dynamic position, this receiving gain is subject to change and is influenced by the off-axis angle of the LEO satellite as observed from GGS. To make things more straightforward, we use a standard radiation pattern to determine the receiving gain of a generic ground station receiver equipped with a parabolic antenna [98]. This gain is associated with the first-order Bessel function $\mathcal{J}_1$ [99] and can be expressed as

$$G_{r,k}(\theta_k) = G_{r,\text{gso}}(\theta_0)\left[\frac{2\lambda_k}{\pi D_A}\frac{\mathcal{J}_1\left[(\pi D_{\text{A}}/\lambda_k)\sin(\theta_k)\right]}{\sin(\theta_k)}\right], \tag{2.5}$$

where D_A refers to GGS antenna aperture diameter. The GGS boresight receiving gain $G_{r,\text{gso}}(\theta_0)$ is given by

$$G_{r,\text{gso}}(\theta_0) = \eta_A\left[\frac{\pi D_A}{\lambda_{\text{gso}}}\right]^2, \tag{2.6}$$

where η_A indicates the efficiency of the receiver aperture. The downlink carrier-to-noise ratio (CNR) of the GSO satellite signal received by GGS can be calculated as

$$\text{CNR} = \frac{C}{\kappa_{\text{blz}} T_{\text{temp}} B_{\text{x}}}, \tag{2.7}$$

where κ_{blz} represents the Boltzmann constant (1.380649×10^{-23} J/K), T_{temp} stands for the receiver noise temperature, and B_{x} is the bandwidth of the GSO baseband signal.

For interference coming from the LEO satellite, the Interference-to-Noise Ratio (INR_k) received by GGS from an individual LEO satellite indexed as k is given as

$$\text{INR}_k = \frac{I_k}{\kappa_{\text{blz}} T_{\text{temp}} B_{\text{x}}}. \tag{2.8}$$

Furthermore, to gauge the effect of interference imparted by all LEO satellites on the GSO system,

we employ the carrier-to-interference plus noise natio (CINR) as an evaluation metric. It can be calculated as

$$\mathrm{CINR} = \frac{C}{\sum_{k=1}^{\mathcal{K}} I_k + \kappa_{\mathrm{blz}} T_{\mathrm{temp}} B_{\mathrm{x}}}. \tag{2.9}$$

In this context, we adopt the maximum bit error rate (BER) metric denoted by e_r and the corresponding minimum CINR denoted by $\mathrm{CINR}_{\min}$ that must be satisfied to meet the quality of service (QoS) of the desired signal [100]. For ease of exposition, despite the different possible modulation schemes, we show hereafter an example assuming that the modulation alphabet used by both the desired and interference signals is quadrature phase-shift keying (QPSK). The corresponding $\mathrm{CINR}_{\min}$ for QPSK is given as

$$\mathrm{CINR}_{\min} = \frac{\left[Q_{fun}^{-1}(e_r)\right]^2}{2} = \frac{\mathrm{CNR}}{\mathrm{INR}_{\max} + 1}, \tag{2.10}$$

where $Q_{fun}^{-1}(\cdot)$ is the inverse Q_{fun} function. The maximum allowed interference from LEOs at GGS receiver is denoted by $\mathrm{INR}_{\max}$ and can be found from (2.10) as

$$\mathrm{INR}_{\max} = \max\left(\frac{\mathrm{CNR}}{\mathrm{CINR}_{\min}} - 1, 0\right). \tag{2.11}$$

2.2.2 Detailed Received Signal Model

In the forward link of the GSO system transmits the baseband signal $x(t)$ [2], which we will refer to as the desired transmitted signal. It can be expressed as

$$x(t) = \sum_{v=0}^{V_x - 1} x[v] p_{RC_x}(t - vT_x), \quad t \in [0, V_x T_x] \tag{2.12}$$

where $x[v], v = 0, 1, ..., V_x - 1$ are modulated symbols sourced from a ModCod scheme in accordance with the DVB-S2X standard [94]. Each symbol holds an average power of P_x and lasts for a duration of T_x. The relationship between T_x and the baseband signal bandwidth B_x is given by $T_x = \frac{1}{B_x}$. Furthermore, V_x denotes the total number of symbols present in the desired signal. The function p_{RC_x} corresponds to a raised cosine filter with unit energy and duration T_x, and is incorporated with a roll-off factor between [0, 1] indicating how much power p_{RC_x} emits above a given bandwidth.

Simultaneously, one or several LEO satellites might transmit interfering signals towards the GGS.

[2] Up and down conversion impairments are considered ideally compensated through standard methods.

These signals can potentially cause interference with $x(t)$ in GGS. Consequently, the transmitted baseband signal $i_k(t)$ originating from the individual LEO satellite indexed as k to GGS can be expressed as

$$i_k(t) = \sum_{v=0}^{V_i-1} i_k[v] p_{RC_i}(t - vT_{i,k}), \quad t \in [0, V_i T_{i,k}] \tag{2.13}$$

where $i_k[v], v = 0, 1, , ..., V_i - 1$ are modulated symbols drawn from a ModCod scheme in accordance with the DVB-S2X standard. Each symbol holds an average power of $P_{i,k}$ and lasts for a duration of $T_{i,k}$. This duration $T_{i,k}$ correlates with the baseband signal bandwidth $B_{i,k}$ from the k^{th} LEO satellite, such that $T_{i,k} = \frac{1}{B_{i,k}}$. The function p_{RC_i} is indicative of a raised cosine filter with unit energy and duration $T_{i,k}$, and has a roll-off factor. For simplicity, we assume that $V_i T_{i,k} = V_x T_x$, that is, both the desired and interference signals blocks have the same total time duration.

In a time instant, the two signals components received by GGS are

$$y_x(t) = x(t)\sqrt{\text{CNR}} + \zeta(t), \tag{2.14a}$$

$$y_i(t) = \sum_{k=1}^{\mathcal{K}_t} \left(i_k(t) e^{j2\pi(f_{c,k} - f_{c,\text{gso}})t} \sqrt{\text{INR}_k} \right), \tag{2.14b}$$

Equation (2.14a) presents the desired signal components of GSO, where CNR as defined in (2.7), denotes the SNR of the GSO signal, and $\zeta(t)$ represents the complex-valued additive white Gaussian noise (AWGN) process, which has zero mean and maintains unity power throughout the bandwidth $2B_x$. Equation (2.14b) showing the components of the interference signals, where INR_k denotes the SNR of the k^{th} LEO signal. This equation aggregates the received interfering baseband signals at GGS originating from all visible LEO satellites at a time instant.In particular, the $i_k(t)$ signal is down-converted from its bandpass form using $f_{c,\text{gso}}$. Fig. 2.3 shows the overlapped bandwidth ($B_{\text{overlap},k}$) between GSO and LEO.

The complex-valued time domain received signal $y(t)$ at the GGS, which encompasses the desired signal, interference signal, and noise components is given by

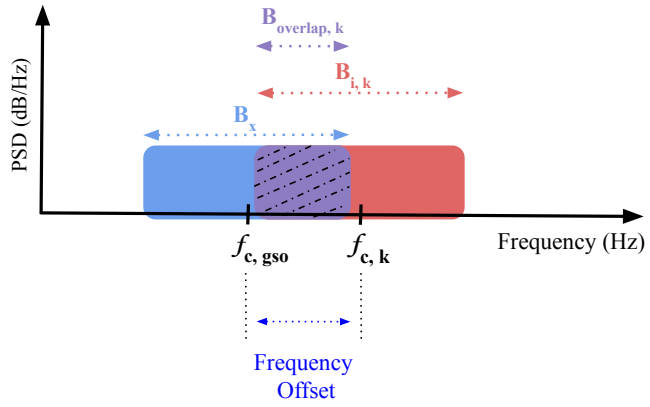


Figure 2.3: Overlap of GSO and LEO Bandwidths in Frequency Domain

$$\begin{aligned} y(t) &= y_x(t) + y_i(t) \\ &= x(t)\sqrt{\text{CNR}} \\ &+ \sum_{k=1}^{\mathcal{K}_t} \left(i_k(t) e^{j2\pi(f_{c,k} - f_{c,\text{gso}})t} \sqrt{\text{INR}_k} \right) \\ &+ \zeta(t). \end{aligned} \tag{16}$$

At the analog-to-digital (A/D) conversion process, the received baseband signal is sampled at a frequency $f_s = \frac{1}{T_s}$ Hz, where T_s denotes the sampling duration. The number of samples per symbol of the desired $x(t)$ signal is $s_1 = \text{ceil}(\frac{T_x}{T_s})$, and the number of samples per symbol of the interfering $i_k(t)$ signal is $s_2 = \text{ceil}(\frac{T_{i,k}}{T_s})$. To avoid a potentially high sampling rate and the corresponding large number of samples for each symbol, we assume that the signal is sampled in its baseband form. In particular, in our analysis, the bandwidths $B_{i,k}$ and B_x are similar, implying that both GSO and LEO employ an identical bandwidth value. When the received signal is shifted by $f_{c,\text{gso}}$ in the baseband, its highest frequency component is B_x. The minimum sampling frequency required to capture the entire subband spectrum is $f_{s,\text{min}} = 2B_x$.

Although (2.14) is a time-domain signal, our work will consider both time and frequency-domain input signals. Both the IQ time-domain and frequency-domain representation are of complex type, which is not accepted as input to ML models. Regarding the time-domain IQ samples of $y(t)$, we transform them into 1-dimensional (1D) data, or a sequence, which can be used for training and testing. In a time instant n a time-domain representation ($y_n^{\mathcal{A}}$) of the signal $y_n(t)$ can be generated by taking the magnitude[3] of the signal as follows

[3]Preliminary testing showed that the magnitude component was bringing good results and such results did not improved when adding the phase component [37]. Therefore, in this study, only the magnitude is considered.

$$y_n^{\mathcal{A}} = |y_n(t)|, \tag{2.15}$$

where $y_n^{\mathcal{A}} \in \mathbb{R}^{M_t}$ is a vector with M_t elements of amplitude (A) values and it represents the time-domain representation of the signal $y_n(t)$. For simplicity, we refer to the time-domain representation as $Signal$. The frequency-domain representation ($y_n^{\mathcal{F}}$) is based on the fast Fourier transform (FFT), and can be obtained by generating the estimated power spectral density (PSD) of $y_n(t)$ using the Welch method [101]. This step can be formulated as follows

$$y_n^{\mathcal{F}} = 10log_{10}(\varphi(y_n(t))), \tag{2.16}$$

where φ is the equivalent `pewlch` function in MATLAB, and $y_n^{\mathcal{F}} \in \mathbb{R}^{M_f}$ is the PSD estimation vector for the IQ samples of $y_n(t)$, with M_f elements of decibels per Hertz (dB/Hz) values. For simplicity, we refer to the frequency-domain representation as $Spectrum$.

2.3 Data Preparation

Before diving into the description of the proposed models for NGSO interference detection, in this section we present how the link budget and the received signal model presented in Section 2.2, are used to generate a realistic dataset for training and evaluation.

Due to the need to calculate realistic CNR and INR values for generating the training and evaluation data, we first run a satellite simulation scenario with one GSO and multiple LEOs using MATLAB satellite toolbox [102]. The real-time positions and trajectories information of the GSO and LEO satellites are based on Kepler's six orbital elements. These can be easily extracted from the corresponding satellite two-line element (TLE) information that is publicly available on the CELESTRAK website [103]. The corresponding orbit propagation of the selected LEO satellite has been calculated using MATLAB built-in functions, which provide estimates of latitude, longitude, and altitude over time according to the satellite trajectory. Using this setup in simulating satellites' interference scenarios where we consider the physical environment (distances, angles, satellites' orbit propagation, etc.), propagation conditions (path loss, weather, etc.), and the operational conditions (frequency, bandwidth), each element can drastically affect signal integrity and interference levels, altering CNR and INR values. Thus, considering all these factors allows us to generate more realistic link budget values and datasets, to fill the lack of real datasets in this specific domain [84], and which we believe are better than generating data from fixed CNR and INR values.

Algorithm 1: Computation of CNR and INR

Input: Link Budget Parameters
Output: $\mathbf{V}_{\mathrm{CNR}}$, $\mathcal{V}_{\mathrm{INR}}$
Initalize: $\mathbf{V}_{\mathrm{CNR}}$ as a vector, $\mathcal{V}_{\mathrm{INR}}$ as cell array
Create a satellite scenario object of period $\mathcal{T}$
Determine $\Delta(\tau)$ and N
Add GSO to the scenario using the TLE information.
Add all LEOs to the scenario using TLEs information
for $n \leftarrow 1$**to** N **do**
    Get GSO coordinations at n
    Calculate CNR_n from (2.7)
    Concatenate CNR_n to $\mathbf{V}_{\mathrm{CNR}}$
    Get $\mathcal{K}_n$, the number of LEOs that impact the GSO communication with GGS at n
    Initalize: $\mathbf{v}_{\mathrm{INR,n}}$ as an empty vector
    for $k \leftarrow 1$**to** $\mathcal{K}_n$ **do**
        Get the k^{th} LEO coordinations
        Calculate θ_k from (2.4)
        Calculate $G_{r,k}$ from (2.5)
        Calculate INR_k from (2.8)
        Concatenate INR_k to $\mathbf{v}_{\mathrm{INR,n}}$
    Compute $\mathrm{INR}_{\mathrm{sum,n}} = \sum_{k=1}^{\mathcal{K}_n} \mathrm{v}_{\mathrm{INR,n}}[k]$
    Calculate $\mathrm{CINR}_{\mathrm{min,n}}$ from (2.10)
    Calculate $\mathrm{INR}_{\mathrm{max,n}}$ using CNR_n from (2.11)
    if $\mathrm{INR}_{\mathrm{sum,n}} \geq \mathrm{INR}_{\mathrm{max,n}}$ **then**
        Concatenate $\mathbf{v}_{\mathrm{INR,n}}$ as cell to $\mathcal{V}_{\mathrm{INR}}$
        else
            Concatenate empty cell to $\mathcal{V}_{\mathrm{INR}}$
Return $\mathbf{V}_{\mathrm{CNR}}$, $\mathcal{V}_{\mathrm{INR}}$

The simulation runs for a period of $\mathcal{T}$, and at each simulation step $\Delta(\tau)$, a sample of CNR, INR_k values are calculated from (2.1) to (2.9), and only values that exceed the INR threshold $\mathrm{INR}_{\mathrm{max}}$ in (2.11) are saved. In general, we capture a total of N samples of CNR and INR values, within the time period $\mathcal{T}$. The overall data generation process is thus composed of two steps:

- CNR and INR values per-time instant calculation (see Algorithm 1).
- Detailed data generation of received signals (see Algorithm 2).

Algorithm 1. summarizes the calculations CNR and INR for each time instant. It outputs two vectors, the first $\mathbf{V}_{\mathrm{CNR}} \in \mathbb{R}^N$ is a vector consisting of all GSO CNR values calculated for each simulation step (time instant) indexed by n. The second output is a cell array $\mathcal{V}_{\mathrm{INR}}$, each nonempty cell can be denoted as $\mathcal{V}_{\mathrm{INR}}[n] \in \mathbb{R}^{\mathcal{K}_n}$, and it contains a vector $\mathbf{v}_{\mathrm{INR,n}}$ with $\mathcal{K}_n$ elements, each element

Algorithm 2: Generating the Datasets

Input: $\mathbf{V}_{\text{CNR}}$, $\mathcal{V}_{\text{INR}}$, $f_{\text{c,gso}}$, $f_{\text{c,k}}$, B_x, $B_{i,k}$, Data Generation Parameters, and GSO ModCods
Output: $\mathbf{Y}_{\mathcal{A}}$, $\mathbf{Y}_{\mathcal{F}}$
Initalize: $\mathbf{Y}_{\mathcal{A}}$, $\mathbf{Y}_{\mathcal{F}}$ as empty matrices
for $n \leftarrow 1$**to** N **do**
  Generate ζ_n, AWGN noise of length M_t
  Get CNR_n, the value of $\mathbf{V}_{\text{CNR}}[n]$
  Generate $x_n(t)$ from (2.12) at ModCod matching CNR_n
  Generate $y_{x,n}(t)$ from (2.14a)
  Get the $\mathbf{v}_{\text{INR},n}$ vector, the cell of $\mathcal{V}_{\text{INR}}[n]$
  if $\boldsymbol{v}_{\text{INR},n}$ *is an empty cell* **then**
    Set : α_n = 0 , interference-free label
    Set : $y_{i,n}(t)$ as zeros array
    else
      Set : α_n = 1, interference label
      Initialize : $y_{i,n}(t)$ as zeros array
      for $k \leftarrow 1$**to** $\mathcal{K}_n$ **do**
        Get INR_k, the value of $\text{v}_{\text{INR},n}[k]$
        Generate $i_k(t)$ from (2.13) at a defined LEO ModCod
        From (2.14b), $y_{i,n}(t) \leftarrow y_{i,n}(t) + \left(i_k(t)e^{j2\pi(f_{c,k}-f_{c,\text{gso}})t}\sqrt{\text{INR}_k}\right)$
  Get $y_n(t)$ from (2.14)
  Get $y_n^{\mathcal{A}}$ of length M_t from (2.15)
  Concatenate $[y_n^{\mathcal{A}}, \alpha_n]$ to $\mathbf{Y}_{\mathcal{A}}$
  Get $y_n^{\mathcal{F}}$ of length M_f from (2.16)
  Concatenate $[y_n^{\mathcal{F}}, \alpha_n]$ to $\mathbf{Y}_{\mathcal{F}}$
Return $\mathbf{Y}_{\mathcal{A}}$, $\mathbf{Y}_{\mathcal{F}}$

representing a INR_k value of the k^{th} LEO that affects GSO communication with GGS at the n^{th} time instant.

The Algorithm 2 expresses the data generation steps of the received signals. It outputs two separate datasets generated for N samples, which are: 1) The dataset of the received signals in time-domain representation (Signal dataset) $\mathbf{Y}_{\mathcal{A}} \in \mathbb{R}^{N\times M_t+1}$, and 2) The dataset of the received signals in frequency-domain representation (Spectrum dataset) $\mathbf{Y}_{\mathcal{F}} \in \mathbb{R}^{N\times M_f+1}$. The additional variable $\alpha_N \in \mathbb{Z}_2$ is a binary indicator for when GGS receives an interference signal, in particular when GGS receives an interference-free signal α_n takes a value of 0. In contrast, when interference is present within the signal, α_n takes 1. Please note that α_n is not needed for the interference detection per-se but it is required for the evaluation of the different models (i.e., ground truth).

2.4 Interference Detection Models

The proposed models process 1D data based on the concepts of unsupervised learning. In this section, the models details are presented and discussed.

2.4.1 Notation and Assumptions

For readability purposes, we denote a single 1D input data (vector of length M) to the models as

$$\mathbf{y}_n = \begin{cases} y_n^{\mathcal{A}}, & \text{for a time-domain (Signal) data} \\ y_n^{\mathcal{F}}, & \text{for a frequency-domain (Spectrum) data} \end{cases}$$

where $\mathbf{y}_n \in \mathbb{R}^M$, $n \in [1, N]$, and $M \in \{M_t, M_f\}$. Furthermore, an element-wise normalization is performed on the input before it is fed to the models; this can be expressed as follow

$$\mathbf{y}_{n,\mathrm{norm}} = \frac{\mathbf{y}_n - \mathrm{a}}{\mathrm{b} - \mathrm{a}}, \tag{2.17}$$

where $\mathbf{y}_{n,\mathrm{norm}}$ is the normalized version of $\mathbf{y}_n$ of scale ranging from 0 to 1, a and b are the minimum and maximum values in the processed data representation, respectively. The subscript "norm" will be removed for readability, but the input $\mathbf{y}_n$ from now onwards is assumed to be normalized.

The goal of the proposed interference detection models is to learn an efficient and meaningful representation of the input data by minimizing the reconstruction error between the original input ($\mathbf{y}_n$) and a reconstructed output ($\hat{\mathbf{y}}_n \in \mathbb{R}^M$). The interference detection problem is performed as an anomaly detection task [104]. An interference-free (anomaly-free) data consist of a GSO signal and noise only. A signal containing an anomaly (interference) from LEO consists of a GSO signal, noise, and LEO signals as interference. The mean absolute error (MAE) is the loss function that is used to evaluate the performance of all proposed models. In a noisy and interference data, the MAE loss function is robust to outliers and treats all errors with equal importance, this uniform treatment helps ensure that no single large error (outlier) can dominate the loss calculation, which is particularly beneficial in the context of interference detection where the goal is to identify all instances that deviate from the normal pattern of the data. MAE loss is calculated as the average of the absolute differences between the predicted values and the actual values and is given by the formula

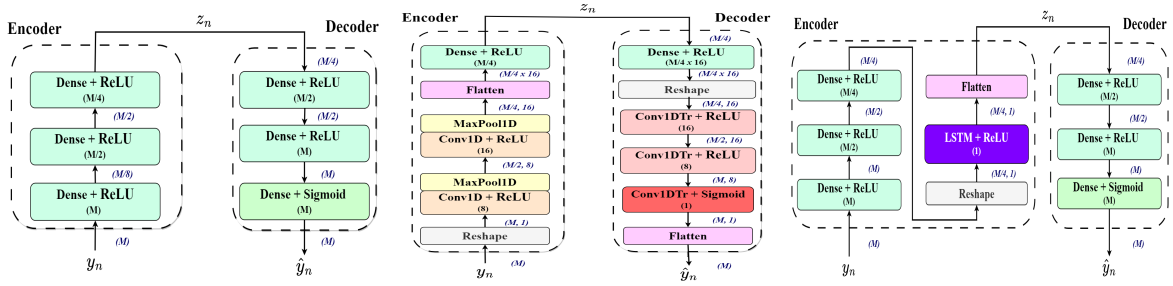
$$\mathcal{L}_{\mathrm{MAE}} = \frac{1}{N} \sum_{n=1}^{N} |\hat{\mathbf{y}}_n - \mathbf{y}_n|. \tag{2.18}$$

The expectation is that the proposed models will reconstruct interference-free sequences with a low MAE, and when interference data is received, this will be compared with the expected one and that would raise higher MAE. By setting a threshold β on the MAE loss, it is possible to differentiate between normal and interference observations, thus β serves as the interference score, and so on.

$$d_n = \begin{cases} 1 & \text{Interference}, \quad \text{if} \quad \mathcal{L}_{\text{MAE}} > \beta \\ 0 & \text{Interference-free}, \quad \text{otherwise} \end{cases} \tag{2.19}$$

where d_n is the model predication decision of the input $\mathbf{y}_n$ after being judged by the thresholding process.

2.4.2 Benchmark Models



(a) AE Model (b) CAE Model (c) LSTMAE Model

Figure 2.4: Benchmark Models

Here we present and redesign three AE-based interference detection models, which are AE [97], CAE [80], and LSTMAE [79], as shown in Fig. 2.4, and will serve as a benchmark models to compare with our proposed models.

An AE-based model takes any input $\mathbf{y}_n$ and compresses it into a lower-dimensional representation vector $\mathbf{z}_n \in \mathbb{R}^{M_z}$ $(M_z = \frac{M}{4})$ using an Encoder $\mathcal{E}(\cdot)$ as

$$\mathbf{z}_n = \mathcal{E}(\mathbf{y}_n). \tag{2.20}$$

A reconstructed version of $\mathbf{y}_n$ can be found by decoding the representation vector back to the original dimension by the Decoder $\mathcal{D}(\cdot)$ as

$$\hat{\mathbf{y}}_n = \mathcal{D}(\mathbf{z}_n). \tag{2.21}$$

Fig. 2.4a shows a standard AE architecture, with a modified architecture compared to the one proposed in [97]. Excluding the input layer, the model comprises a total of five fully connected dense layers with a rectified linear unit (ReLU), and a final dense layer with a Sigmoid functions to ensure the output values fall between 0 and 1, this is useful for the normalized input data. The dense layers are adept at capturing linear relationships and basic patterns within the interference-free signal signal. By learning to compress and accurately reconstruct the typical GSO signal, the AE model can be used to establish a baseline of interference-free signal behavior.

Fig. 2.4b illustrates a modified architecture of the CAE model proposed by [80]. CAE adapts convolutional ability to the AE architecture, which leverages feature extraction from input data with spatial or temporal structures. The encoder's convolutional (Conv1D) and max pooling (MaxPool1D) layers first perform dimensional reduction to encode the input sequence into the representation vector dimensions. The decoder layers then use conventional transpose layers (Conv1DTr) to up-sample the sequence dimensions, and the last Conv1DTr layer with M filters and a single kernel produces a single feature map, which then flattened to produce the reconstructed output. All layers use ReLU activation, except the last one with Sigmoid activation. The CAE can capture local patterns with shared weights (kernels), making it more efficient than dense layers for high-dimensional GSO signals that may have inherent spatial correlations due to modulation techniques. NGSO interference would likely disrupt these spatial correlations, which the CAE would manifest as increased reconstruction errors.

Fig. 2.4c illustrates the architecture of the LSTMAE model, it combines dense layers with an LSTM unit on the encoder to process the representation vector of the input sequence, which is suitable for learning order dependence in sequence data prediction problems, and it is an improved architecture from that of [79]. The LSTM unit, a type of recurrent neural networks (RNNs), is particularly useful for sequence data where the current sequence is dependent on the previous sequence. This is particularly appealing for NGSO-to-GSO interference detection, where the expected GSO signal has a strong correlation with the previous GSO signal instance.

2.4.3 Proposed GenAI-based Models

Variational Autoencoder Model (VAE)

Our first proposed GenAI-based model is the VAE model, its architecture illustrated in Fig. 2.5. VAE learns not only the encoding of the data, but also the underlying probability distribution [89].

As an architecture, VAE consists of similar hyperparameters in the encoder and decoder parts as in the standard AE. The major difference lies in the encoder and the representation vector part.

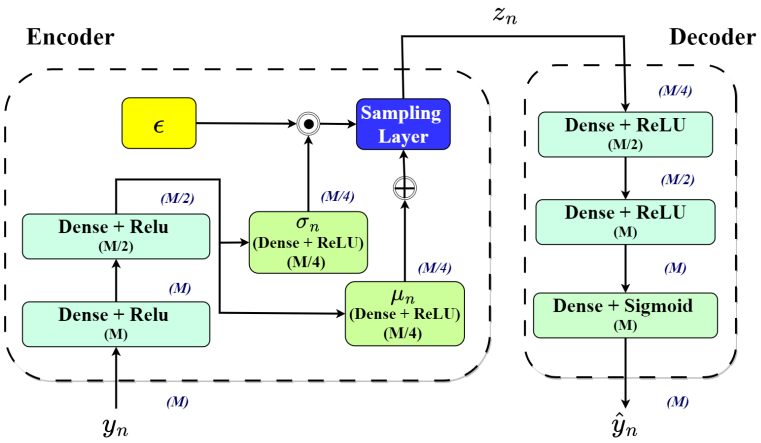


Figure 2.5: Variational Autoencoder Interference Detection Model (VAE)

Here, VAE learns to generate new sequences that are similar to the input sequence by enforcing a distribution on the representation vector. This is achieved by introducing a sampling layer instead of a typical neural layer. This layer samples from the distribution defined by the mean (μ_n) and standard deviation (σ_n) dense layers. Furthermore, the reparameterization trick is utilized in VAE, which entails expressing the representation vector as a deterministic function of learnable parameters and a fixed distribution sample. This technique effectively decouples the stochastic element from the parameters optimization process. The reparameterization trick is represented by the equation

$$\mathbf{z}_n = \mu_n + \sigma_n \odot \varepsilon, \tag{2.22}$$

where μ_n and σ_n are learnable parameters, and ε is a sample of a standard Gaussian distribution. The symbol $\odot$ represents the Hadamard product, or element-wise multiplication, which facilitates the combination of the variability introduced by ε with the scaled parameter σ_n. The form in (2.22) of $\mathbf{z}_n$ allows differentiation with respect to the parameters μ_n and σ_n while incorporating randomness, thereby allowing the loss gradient to be backpropagated through the stochastic sampling process.

Let $p(y)$ denote the actual training data distribution, $p(z)$ express the distribution of the representation vector, and $p(\hat{y}|z)$ indicate the conditional distribution of data reconstruction -generation- given the representation vector. The goal of VAE is to infer $p(z)$ from $p(z|y)$. The distribution $p(z|y)$ is a complex probability distribution that positions the input data in a representation vector, which is typically a standard Gaussian distribution $\mathcal{N}(0, 1)$. However, lacking the actual distribution $p(z|y)$, we approximate it through a more tractable distribution $q(z|y)$, in this case as an approximation of

the Gaussian distribution $\mathcal{N}(\mu, \sigma^2)$. During the VAE training process, the encoder is tasked with assimilating the approximate distribution $\mathcal{N}(\mu, \sigma^2)$ so that it closely resembles the true distribution $\mathcal{N}(0, 1)$. This resemblance is quantified using the Kullback-Leibler (KL) divergence [105], as a metric of disparity between two probability distributions. The loss function for the VAE inherently incorporates this KL divergence term, which it strives to minimize as

$$\mathrm{D}_{\mathrm{KL}}\left[q(z|y)||p(z|y)\right] = \int q(z|y) \log \frac{q(z|y)}{p(z|y)}\, dz. \tag{2.23}$$

In this case, D_{KL} can be derived as [89]

$$\mathrm{D}_{\mathrm{KL}} = -\frac{1}{2}\left(1 - \mu^2 - \sigma^2 + \log\left(\sigma^2\right)\right). \tag{2.24}$$

VAE probabilistic approach allows it to generate new sequences that are variations of the input data, potentially offering a more robust detection of NGSO interference by evaluating how likely a new signal instance could have been generated by the same distribution as the GSO signal. Diffrent from the benchmark models, the loss function of the VAE incorporate the KL divergence D_{KL} term, or the similarlty loss as follows

$$\mathcal{L}_{\mathrm{VAE}} = \frac{1}{N}\sum_{n=1}^{N} |\hat{\mathbf{y}}_n - \mathbf{y}_n| + \mathrm{D}_{\mathrm{KL}}, \tag{2.25}$$

The loss function of the VAE is composed of two main components: the reconstruction error, using $\mathcal{L}_{\mathrm{MAE}}$, and a regularization term D_{KL}, which accounts for the divergence in the representation vector distribution approximations. The integration of D_{KL} within the VAE loss function can be interpreted as a measure of how well the representation vector matches the desired standard normal distribution, ensuring that the model generates meaningful and diverse data samples. Additionally, this regularization aids in curbing overfitting throughout the model training process.

Transformer-based Interference Detector Model (TrID)

Inspired by transformer models [90], we propose the TrID model as illustrated in Fig. 2.6. Unlike VAEs, which sample probability distributions to generate new data, transformer models are particularly adapted for GenAI applications because of two mechanisms: self-attention and positional encodings. Both of these technologies allow the model to focus on how sequences are related to each other over a long time [90].

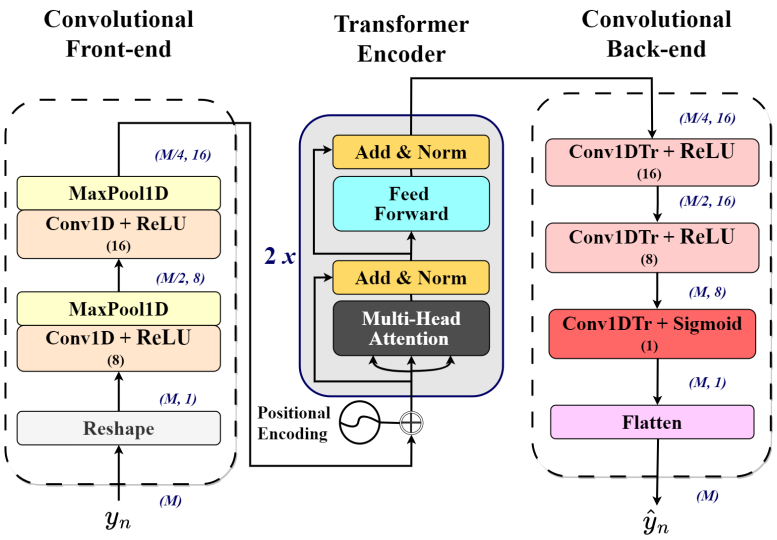


Figure 2.6: Transformer-based Interference Detector Model (TrID)

Our proposed TrID model consists of three main blocks. At the beginning, the input signal is passed through Convolutional Front-end where two conv1D layers with ReLU activation and each is followed by MaxPool1D. The Convolutional Front-end primarily serves to extract meaningful features from the raw input signal, reducing dimensionality while reducing the computational load, and helping in bridging the local features with the global context needed for the transformer layers. This is very important for understanding the underlying structure of the data. This setup ensures that the transformers are not merely processing raw data but rather more abstract representations of the input signal.

The second block is Transformer Encoder, which consists of a sinusoidal positional encoding followed by two standard transformer encoder layers [90]. The abstract representation, which has the dimensions $\frac{M}{4} \times 16$, of the input signal is treated as a sequence of embeddings (sequence length $\times$ embedding size), a Positional Encoding is applied before the first transformer layer to encode the embedding order of the input sequence and get,

$$PE_{(pos,2i)} = \sin\Big(pos/1000^{2i/d_{TrID}}\Big), \tag{2.26}$$

$$PE_{(pos,2i+1)} = cos(pos/1000^{2i/d_{TrID}}), \tag{2.27}$$

where pos is the embedding position in the sequence, i is the dimension in the embedding space

and d_{TrID} is the dimensionality of the embedding or the embedding size. That is, each dimension of the positional encoding corresponds to a sinusoid. Next, the first transformer's multi-head attention is applied on the positional encoding output. Toward that, we consider the linear projections of the queries Q, the keys K, and the values V, then we obtain the attention matrix as

$$\mathrm{Att}\left(Q,K,V\right)=\mathrm{softmax}\left(\frac{QK^{T}}{\sqrt{d_{k}}}\right)V, \tag{2.28}$$

where d_k represents the dimension of the keys. If the number of attention heads is h, and the output weight matrix is denoted as W_{out}^{l}, the output of the multi-head attention is given as

$$\mathrm{MH}\left(Q,K,V\right)=\mathrm{Concat}\left(H_{1},...,H_{h}\right)W_{\mathrm{out}}, \tag{2.29}$$

where

$$H_{i}=\left(QW_{i}^{Q},KW_{i}^{K},VW_{i}^{V}\right), \tag{2.30}$$

where W_i^Q, W_i^K, W_i^V are the weight matrices of each head's inner dense layers, and W_{out} is the final dense layer weight matrix. In this chapter, $W_i^Q \in \mathbb{R}^{d_{TrID}\times d_k}$, $W_i^K \in \mathbb{R}^{d_{TrID}\times d_k}$, $W_i^V \in \mathbb{R}^{d_{TrID}\times d_v}$, where $d_v = d_k = \frac{d_{TrID}}{h}$.

In the self-attention mechanism of a transformer, the internal relationships within an input sequence are comprehensively learned. Essentially, attention weights are calculated at each sequence position by comparing a given position with every other position in the sequence. This process allows the model to capture the overall sequence information, enhancing the representation of each observation by focusing on the contributions of all other positions. Consequently, the hidden state of each point in the sequence emphasizes the contextual significance of the surrounding regions to that specific point.

The output of the multi-head attention are added and normalized before process by a feed forward network (FFN) with residual connection, followed by addition and normalization once again in order to obtain the final output of the first transformer encoder layer. This layer processes the embedding sequence input to create a unified hidden representation for each position within the sequence. Subsequently, these representations are fed into a second transformer encoder layer, which iteratively helps generate more sophisticated, higher-level representations during training. This hierarchical processing enhances the model's ability to discern more complex patterns and relationships within the data.

The extracted features of the Transformer Encoder block are further processed with the third block, namely Convolutional Back-end. The Convolutional Back-end is consisting of transposed

convolutional layers (two conv1D layers with ReLU, and a third conv1D layer with Sigmoid), and serves to up-sample these features back to the original dimensionality of the input in $\hat{y}_n$. The output of the convolutional layer is fed into the flattening layer where the final reconstructed signal $\hat{y}_n$ is conveyed. The Convolutional Back-end not only reconstructs the signal from the abstracted and generated representations from the Transformer Encoder block but also refines this reconstruction to ensure that the output is detailed and accurate. It effectively translates the global contextual understanding of the transformer back into a high-resolution space. TrID utilized the MAE loss function defined in (2.18).

2.4.4 Interference Detection Performance Metrics

Performance metrics provide quantitative measures that help to understand how well the model performs, particularly in distinguishing between different classes [106]. Here we introduce some of the selected metrics that will be used in this work to evaluate the performance of the models, listed in Section 2.4.2, for the interference detection task.

Let us first introduce the basic key performance indicators: 1) **True Positives** (TP): The number of interference (positive) instances correctly identified by the model, 2) **True Negatives** (TN): The number of interference-free (negative) data correctly identified by the model, **False Positives** (FP): The number of interference-free data incorrectly identified as interference, and 4) **False Negatives** (FN): The number of interference data incorrectly identified as interference-free observations. The derived metrics includes

- True Positive Rate (TPR): Also known as Recall, or the probability of detection ($\mathrm{P_D}$). This metric measures the proportion of actual interference instances that are correctly identified by the model.

$$\mathrm{TPR} = \frac{\mathrm{TP}}{\mathrm{TP} + \mathrm{FN}}. \tag{2.31}$$

- False Negative Rate (FNR): It indicates the proportion of actual interference instances that are missed identified by the model as interference-free instances. Is the complement of the TPR.

$$\mathrm{FNR} = \frac{\mathrm{FN}}{\mathrm{TP} + \mathrm{FN}}. \tag{2.32}$$

- True Negative Rate (TNR): This metric measures the proportion of actual interference-free

instances that are correctly identified as such by the model.

$$\mathrm{TNR} = \frac{\mathrm{TN}}{\mathrm{TN} + \mathrm{FP}}. \tag{2.33}$$

- False Positive Rate (FPR): This metric measures the proportion of actual interference-free instances that are incorrectly identified by the model, in other words it indicates the probability of false alarms. Is the complement of the TNR.

$$\mathrm{FPR} = \frac{\mathrm{FP}}{\mathrm{TN} + \mathrm{FP}}. \tag{2.34}$$

- Normalized-valued Confusion Matrix (NCM): NCM is a tabular representation of TNR, FPR, and FNR and TPR, widely used in classification problems [106].

- Accuracy score : It represents the overall proportion of correct predictions (both TP and TN) relative to the total number of cases examined.

$$\mathrm{Accuracy} = \frac{\mathrm{TP} + \mathrm{TN}}{\mathrm{TP} + \mathrm{TN} + \mathrm{FP} + \mathrm{FN}}. \tag{2.35}$$

- Precision score : This metric measures the proportion of predicted interference that are actually TP. It focuses on the purity of interference identifications. Precision is particularly important in contexts where the cost of false alarm is high.

$$\mathrm{Precision} = \frac{\mathrm{TP}}{\mathrm{TP} + \mathrm{FP}}. \tag{2.36}$$

- F1 Score: F1 score is the harmonic mean of precision and recall. This score is a robust metric for evaluating interference detection models because it accounts for both the model's ability to correctly identify interference and its efficiency in not misclassifying interference-free signals as interference.

$$\mathrm{F1} = 2 \times \frac{\mathrm{Precision} \times \mathrm{Recall}}{\mathrm{Precision} + \mathrm{Recall}}. \tag{2.37}$$

- Receiver Operating Characteristic Curve (ROC): ROC is a graphical representation that plots TPR against FPR at various threshold settings.

- Area Under the ROC Curve (AUC): AUC score is a scalar value summarizing the ROC curve.

AUC is a valuable metric for evaluating the performance of interference detection models [107], it gives a sense of how well the model can be tuned to balance the detection of interference (TPR) against mistakenly flagging interference-free instances as interference or false alarms (FPR).

2.5 Simulation Results

In this section, we present the simulation setup, including details on the data generation, model training phase, as well as validating and comparison of the different ML models proposed in Section 2.4. The workflow logic is shown in Fig. 2.7. In this approach, data labeling (interference and interference-free) is only used to calculate the key performance metrics described in Section 2.4.4.

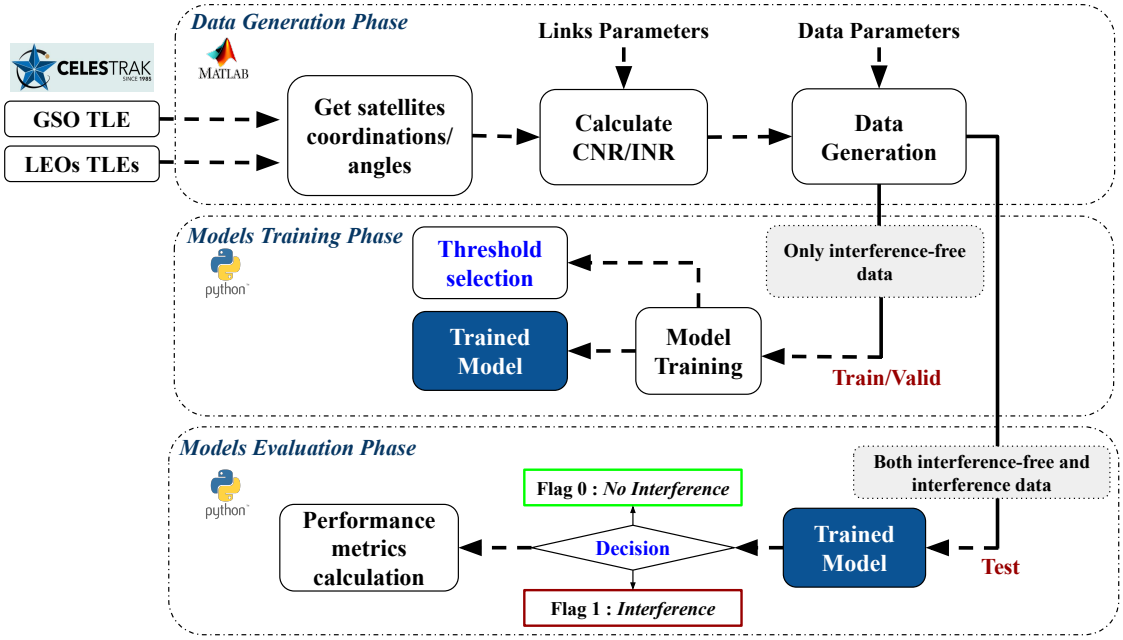


Figure 2.7: Schematic overview from data generation to models training and evaluation

2.5.1 Data Generation Phase

We initialize our simulation in MATLAB by selecting one GSO satellite from the SES fleet, the ASTRA 28.2E system [108].The GGS is assumed to be a VSAT dish located in Luxembourg City, Luxembourg, Coordinates: $(49.6257\text{N}, 6.1598\text{E}, 300\,\text{m})$. The GSO system corresponds to an European broadcasting system operating at 10.7-12.7 GHz [109]. The potential NGSO interference is emulated by selecting 20 LEO satellites that eventually fly in the neighboring area of the GSO line

of sight. These correspond to 10 LEO satellites from SpaceX Starlink constellation, and 10 LEO satellites from Eutelsat-OneWeb constellation. Note that the altitudes of these LEO satellites are between 550 and 1,200 Km. Starlink and OneWeb constellations are deployed to provide broadband connectivity worldwide, and according to recent filings with the Federal Communications Commission (FCC), Starlink OneWeb satellites are operating in the same Ku frequency bands 10.7–12.7 GHz as ASTRA [63] [64].

Simulation setup and link budget calculation

Table 2.1: Simulation Setup and Link Budget Parameters (Algorithm 1)

Parameters	Names	**Values**
-	Simulation UTC startTime	30-Jul-2023 00:00:00
-	Simulation UTC stopTime	01-Aug-2023 00:00:00
$\mathcal{T}$	Simulation period	48 Hours
$\Delta\tau$	sampleTime	10 Seconds
N	Simulation samples	17281
-	GSO satellite TLE	1 TLE
-	LEO satellites TLEs	20 TLEs
L_{AD}	Link additional losses	0 to 9 dB
GSO satellite Parameters		
$EIRP_{\text{gso}}$	Transmitted EIRP	52.2 dBW
B_x	Signal bandwidth	50 MHz
$f_{c,\text{gso}}$	Carrier frequency	11.750 GHz
e_r	maximum BER allowed [110]	10^{-5}
LEO satellites Parameters (Per Satellite)		
$EIRP_k$	Transmitted EIRP	44.7 dBW
$B_{i,k}$	Signal bandwidth	50 MHz
$f_{c,k}$	Carrier frequency of LEO	11.750 GHz
B_{overlap}, k	Overlapping bandwidth	50 MHz
B_{adj}, k	Adjustment factor	1
GGS Parameters		
D_A	Antenna diameter	1.2 m
η_A	Antenna efficiency	0.6
λ_{gso}	Wavelength	0.0255 m
T_{temp}	Noise temperature	250° K
$G_{r,\text{gso}}(\theta_0)$	GSO recivng gain, from (2.6)	42.2 dBi

Table 2.1 describes the simulation setup and link budget parameters used in Algorithm 1 for the computation of CNR and INR values. Satellite communications implement the air interface defined in the DVB-S2X standard for downlink transmission. The DVB standard defines a set of ModCod

schemes that adapt the transmission mode depending on the link characteristics. In our simulation, the value of the link losses (L_{AD}) is intentionally varied over time within the range of [0,9] dB to emulate different ModCod schemes for both GSO and LEO links independently.

A representation part of the visibility intervals of GSO and LEOs satellites to the GGS during the simulation is shown in Table 2.2. It can be observed that the selected GSO satellite (ASTRA 2F) is visible to GGS all the time with a total duration of 48 hours (172800 seconds, which corresponds to the overall simulation period), while the selected LEO satellites have discrete visibility to GGS occurring 296 times during the whole simulation period, with varying visibility duration (190 to 1190 seconds).

Table 2.2: The visibility of GSO and LEOs to the GGS

Source	Target	IntervalNumber	StartTime	EndTime	Duration
ASTRA 2F	GGS	1	30-Jul-2023 00:00:00	01-Aug-2023 00:00:00	172800
STARLINK-2734	GGS	1	30-Jul-2023 09:02:20	30-Jul-2023 09:05:30	190
STARLINK-2734	GGS	2	30-Jul-2023 10:36:20	30-Jul-2023 10:47:40	680
...	...	...	...	...	...
ONEWEB-0101	GGS	19	31-Jul-2023 18:03:00	31-Jul-2023 18:09:50	410
ONEWEB-0101	GGS	20	31-Jul-2023 23:45:40	01-Aug-2023 00:00:00	860

With this setup, Algorithm 1 generates a total of $N = \frac{48\times60\times60}{10} = \mathbf{17281}$ simulation samples. We recorded 2218 data points whose aggregated interference over noise ratio exceeds the INR threshold INR_{max} defined in (2.11). The maximum aggregated interference over noise ratio is $\text{INR}_{\text{sum}}[\text{dB}] = 32.47$ and the minimum is $\text{INR}_{\text{sum}}[\text{dB}] = 4.49$. Regarding individual interference over noise ratio (INR per LEO satellite), we obtain maximum $\text{INR}_k[\text{dB}]$ value of 32.47 [4], and the minimum $\text{INR}_k[\text{dB}]$ value is -31.03. For the GSO satellite link, the maximum $\text{CNR}[\text{dB}]$ value is 15.40, and the minimum $\text{CNR}[\text{dB}]$ is 6.40.

Fig. 2.8 illustrates how the simulation and the calculation of CNR, INR are performed in parallel. The top plot visualizes the varying number of LEO satellites received as interference at GGS for each time instant n. The bottom plot illustrates $\text{CNR}[\text{dB}]$ and $\text{INR}_{\text{sum}}[\text{dB}]$ that exceed the INR threshold INR_{max} mentioned above in (2.11).

Fig. 2.9 shows the GGS radiation pattern described in (2.5) and the gain of each satellite access to it at the 4227^{th} time instant (i.e., at 30-07-2023 11:44:30). It can be seen that satellite LEO_1 is received with a significantly higher gain than the rest of the LEO satellites.

[4] During the simulation, the maximum aggregated interference at the GSO ground station was primarily caused by significant in-line interference from a LEO satellite, while another LEO contributed with a close-to-negligible interference power.

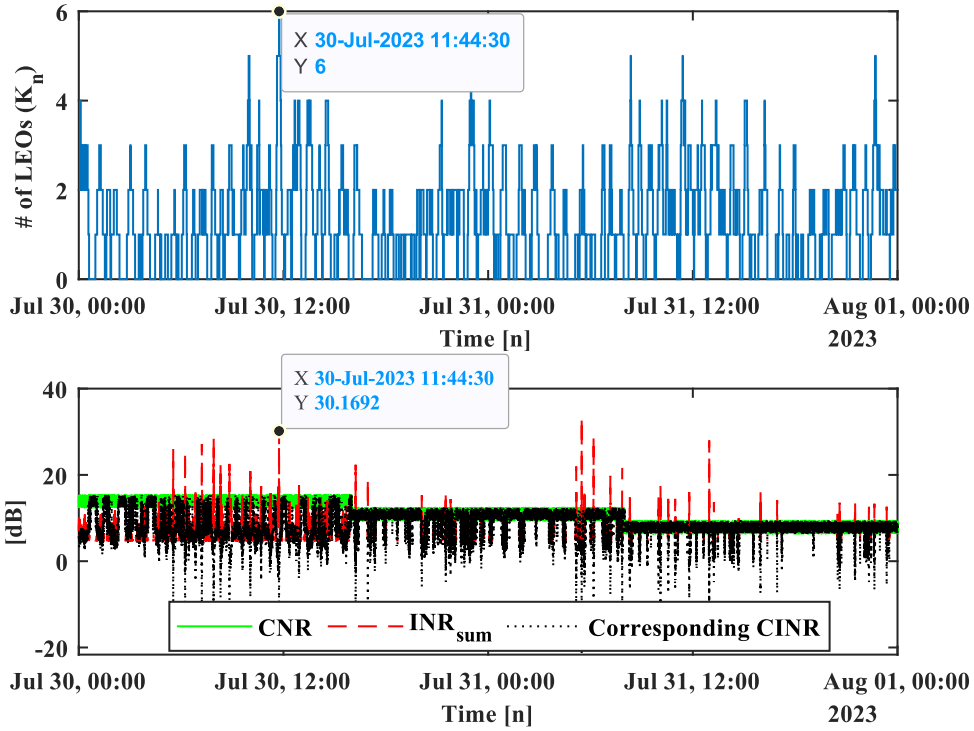


Figure 2.8: Plot of numbers of LEO satellites interfering GGS (Top), and the received CNR and $\mathrm{INR}_{\mathrm{sum}}$ (Bottom), over the simulation period

Received signals data generation

To generate data from the received signals for training and evaluation as described in Algorithm 2, we implement the parameters shown in Table 2.3, and the table of simplified modulation schemes from [94] as in Table 2.4.

Table 2.3: Data Generation Parameters (Algorithm 2)

Parameters	Names	**Values**
f_s	Sample frequency	100 MHz
s_1, s_2	Number of samples per symbol	2 samples
V_x, V_i	Number of symbols per signal	400 symbols
M_t	Total Number of samples per signal	800 samples
-	LEO ModCod	QPSK
-	p_{RC_x} and p_{RC_i} Roll-off factor	0.25

With this parameter set-up, Algorithm 2 generates two sets of data, the time-domain Signal dataset, and the frequency-domain Spectrum dataset as described in Section 2.3. The Signal dataset ($\mathbf{Y}_{\mathcal{A}}$) has

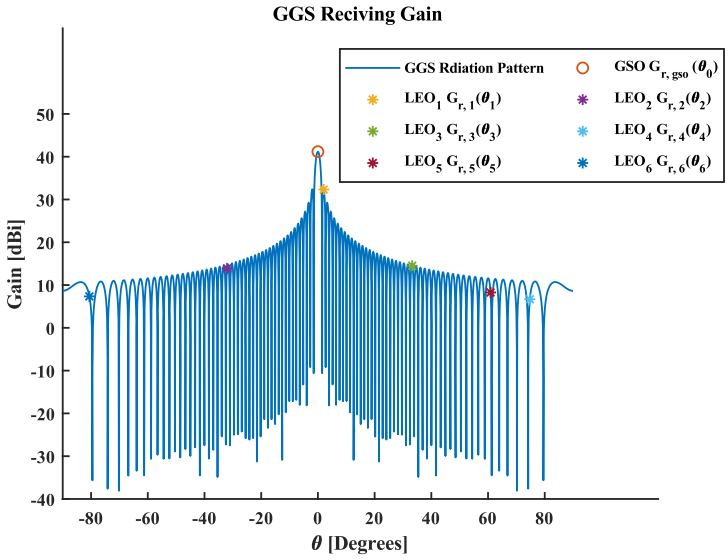


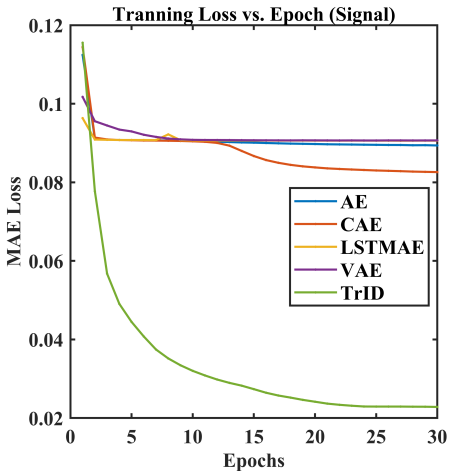
Figure 2.9: Visualization of the GGS receiving gain of each satellite accessing to GGS at 30-07-2023 11:44:30

Table 2.4: GSO ModCods

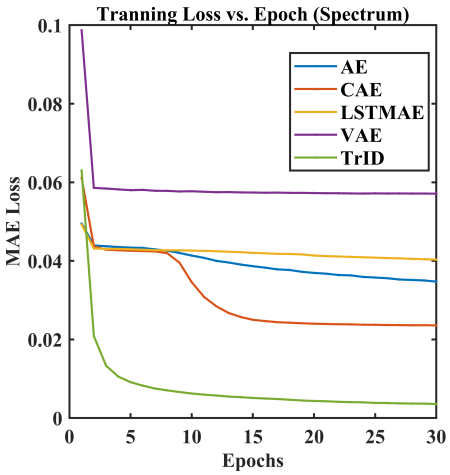
ModCod	CNR required [dB]
QPSK	≤ 6.6
8PSK	> 6.6 & ≤ 9.0
16APSK	> 9.0

dimensions of $N \times M_t = 17281 \times 800$ after excluding the label column $\alpha \in \mathbb{Z}_2^N$. Due to the fact that the FFT signal bandwidth covers the spectrum $[-\frac{f_s}{2}, \frac{f_s}{2}]$ in baseband, and the number of frequency bins in the frequency domain is equal to the number of samples in the time domain, thus the Spectrum dataset $\mathbf{Y}_{\mathcal{F}}$, has the dimensions of $N \times M_f = 17281 \times 800$ after excluding the label column $\alpha \in \mathbb{Z}_2^N$. In this case, both datasets have the same dimensions $N \times M$, where $M \in \{M_t, M_f\}$.

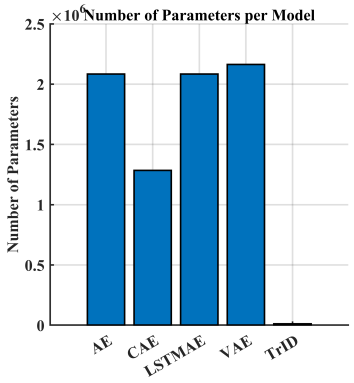
As mentioned in Section 2.4.1, the input layer in each model takes a vector (sequence) $\mathbf{y}_n$ with length M, where n indicates the sample index within N data points (sequences). The label α_n indicating the presence and absence of interference is only used to ensure that the models are trained only with the expected GSO signal. Consequently, the final data distribution used for training and testing is as follows: 1) The Training Set, composed exclusively of $10,397 \times M$ interference-free dats; 2) The Validation Set, containing $1,175 \times M$ interference-free data; and 3) The Testing Set, contains $2,907 \times M$ interference-free data and all $2,802 \times M$ interference data.



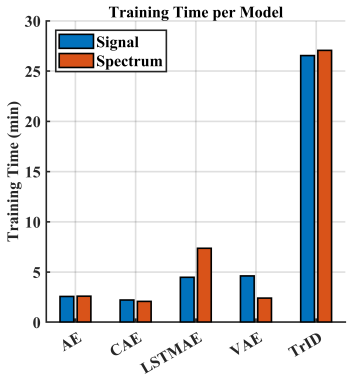
(a) Loss-Epochs (Signal)



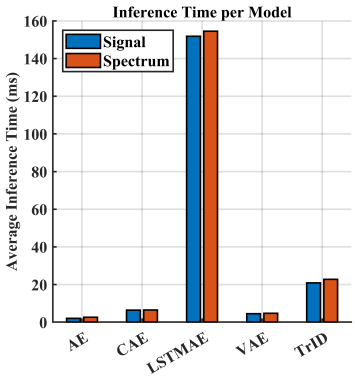
(b) Loss-Epochs (Spectrum)



(c) No. Parameters per model



(d) Training Time per model



(e) Inference Time per model

Figure 2.10: Training Phase Results

2.5.2 Models Training Phase

Tensorflow and Keras frameworks are used to build the models proposed in Section 2.4.2 in Python. All models are compiled with MAE as the main loss function, and Nesterov implemented Adam as the optimizer. The weight and base parameters were updated using the interference-free Training Set, and the results were validated using the Validation Set. The experiments in the following parts were carried outusing the HPC facilities of the University of Luxembourg [111]. Thanks to these facilities, 60-core CPU units with 3 TB RAM memory are used.

Models training

Each model inputs y_n, after a normalization step using the maximum and minimum values found on the Training Set as explained in (2.17). Each AE-based models, including VAE, reduced the

dimensionality of the input from $M = 800$ in y_n, to $M_z = 200$ in z_n, each layer parameters and structures can be seen in Fig. 2.4 and Fig. 2.5. For the TrID model, Fig. 2.6, in the Transformer Encoder we apply $h = 4$ parallel attention layers, $l = 2$ transformer encoder layers, and all the sub-layers, including the positional encodings, produce output of dimensions $\in \mathbb{R}^{\frac{M}{4} \times d_{TrID}}$, with $d_{TrID} = 16$.

The models were trained for 30 epochs with a batch size of 64. The model training phase is shown in Fig. 2.10. First, Fig. 2.10a shows the MAE loss over 30 epochs of training for the Signal dataset. The x-axis represents the epoch number, and the y-axis represents the MAE loss. A lower MAE indicates better reconstruction performance, as the error between the model predictions and the actual data is smaller. AE, LSTMAE, and VAE models seem to converge quickly, with most of the loss reduction occurring in the first few epochs, CAE converges after, and TrID converges at a significantly lower MAE value than the other models. This suggests that the TrID model learns the patterns in the time-domain data more efficiently. Except for TrID, all other models show a sharp decline in loss initially, which flattens as the epochs increase, indicating that they have quickly reached a point of minimal improvement in error reduction. Similarly, Fig. 2.10b shows the MAE loss over 30 epochs of training for the Spectrum dataset. The models training behavior is quite similar to that of the Signal dataset, with all models showing rapid convergence in the initial epochs, except TrID and CAE. Compared to the Signal dataset training, the loss values for the Spectrum dataset are lower overall, which may suggest that the models struggle a bit to capture the patterns in the data in the time-domain or that it is inherently more complex.

In Fig. 2.10c, the bar chart compares the number of trainable parameters across the models, which is the same for both Signal and Spectrum datasets. Generally, a model with more parameters can capture more complex patterns, but may also be prone to overfitting and may require more data to train effectively. AE, LSTMAE, and VAE models appear to have a similar number of parameters with their fully connected dense layers, while the models with convolutional layers seem to have a smaller number of parameters, with TrID being significantly the lowest. In satellite communication systems, where computing resources are often constrained, models with a large number of parameters can be impractical. They may require more memory and processing power, which could impact the efficiency of satellite systems.

Fig. 2.10d shows the training time for each model in minutes (min) for training both Signal and Spectrum datasets. Training time is important for practical consideration, since models that take longer to train can be more costly in terms of computational resources and time. Here, on both datasets, the TrID model trains the slowest compared to the other models, potentially due to the self-attention

mechanism within the transformers, which despite its computational complexity, is an important layer for improving the model accuracy. Other models, while having more trainable parameters than the TrID, were quicker to train.

Fig. 2.10e shows the inference time for each model in milliseconds (ms) for both Signal and Spectrum datasets. It can be seen that LSTMAE takes the longest time (up to 160 ms) to reconstruct an input data, which could be due to the LSTM unit complexity. Despite having a longer training time, TrID took less time (up to 20 ms) to reconstruct the input data. AE and CAE, VAE were the most efficient in terms of inference time. Satellite communications often require real-time or near-real-time response to maintain system integrity and performance. Interference detection models with faster inference times can quickly identify and respond to potential issues, preventing further complications or system failures.

Fig. 2.11 shows the reconstruction performance of the models, each figure depicts input data (cyan color) alongside the reconstructed output (navy color) obtained and the reconstruction error area between them (golden color), after being rescaled back to the original values of amplitude or dB/Hz. It is observed that the reconstruction error is more pronounced in the data with interference, as indicated by the larger golden area, which is expected since the models were trained in interference-free data and interference would naturally be harder to reconstruct and thus easier to detect. Despite the complexity of the training data [5], the TrID model generates an interference-free data with minimal MAE error, indicating the possibility of utilizing the model for future data generation for the purpose of training deep learning models.

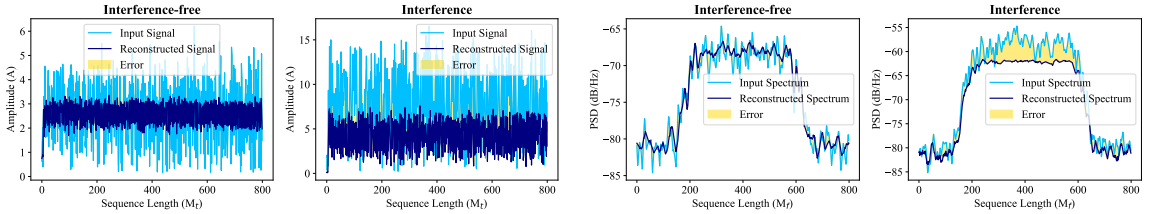
Threshold selection

As discussed in Section 2.4.1, by setting a threshold β on the training loss of each model and each dataset, it is possible to differentiate between interference-free and interference data. We propose to use an initial threshold value β_0 for each model and dataset, from the sum of the mean and two standard deviation of the MAE loss values on the training dataset $\mathcal{L}_{\mathrm{MAE,Train}}$, and it can be derived using this equation

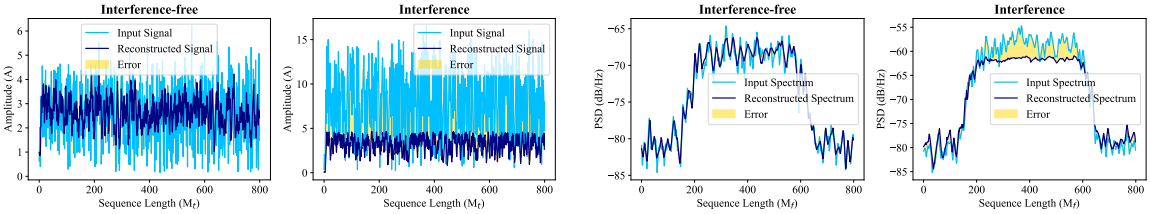
$$\beta_0 = \mu(\mathcal{L}_{\mathrm{MAE,Train}}) + 2 \times \sigma(\mathcal{L}_{\mathrm{MAE,Train}}) \tag{2.38}$$

The initial threshold value has been derived with the objective of achieving satisfactory perfor-

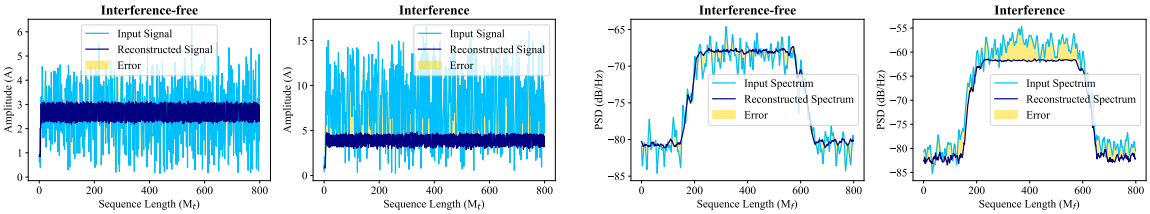
[5] For training data of a single NGSO satellite, single SNR, and single ModCod [97], all models demonstrated perfect reconstruction performance.



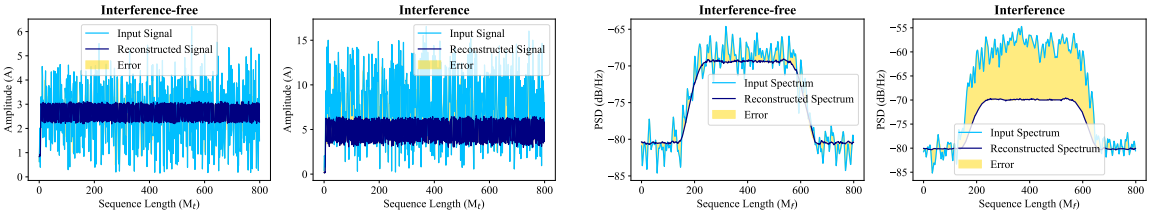
(a) AE



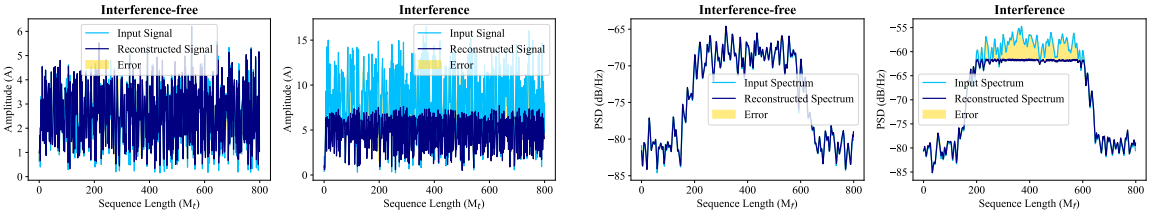
(b) CAE



(c) LSTMAE



(d) VAE



(e) TrID

Figure 2.11: Model input (cyan color), reconstructed output (navy color), and error area (golden color) for an interference-free and interference Signal data (sub-left figures) and Spectrum data (sub-right figures)

mance in the task of interference detection. However, as part of this chapter's contribution, we extended the threshold definition to an enhanced threshold value (β) by examination of interference segments (assuming that these are available and have been previously identified as such). In particular, we first evaluate the classification performance of each model on a Testing Set that includes interference and interference-free data, iterating over a series of threshold values that are derived from the MAE losses values of the training dataset $\mathcal{L}_{\text{MAE,Train}}$. Subsequently, we pinpoint the optimal threshold value that yields the maximum AUC score. The choice of the AUC score is due to its ability to be tuned to balance the detection of interference, or the recall, while avoiding false alarms.

Fig. 2.12 illustrate an example of the initial threshold β_0 and the enhanced threshold β within the MAE Loss values (thresholds series) specifically derived for the VAE model and the Signal dataset.

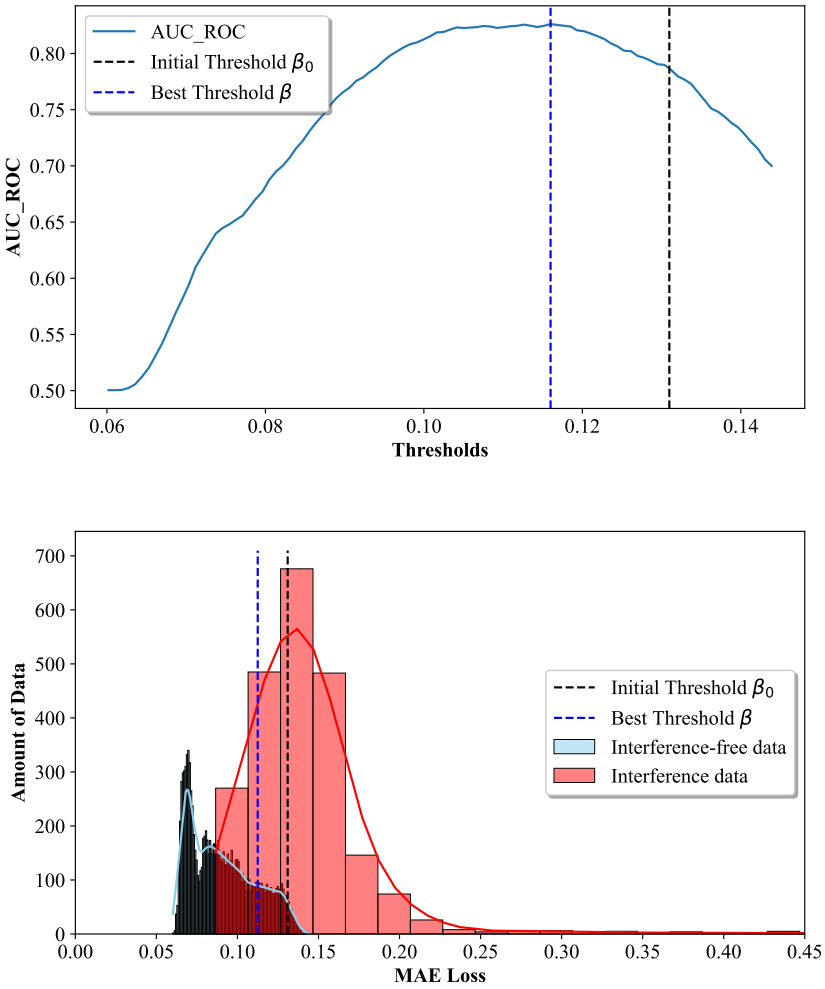


Figure 2.12: Threshold Selection Based On Optimal AUC Score Approach

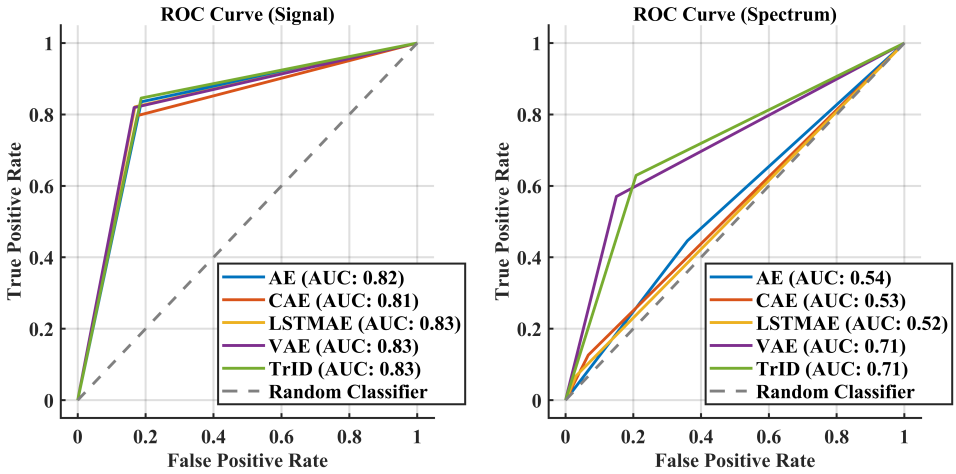


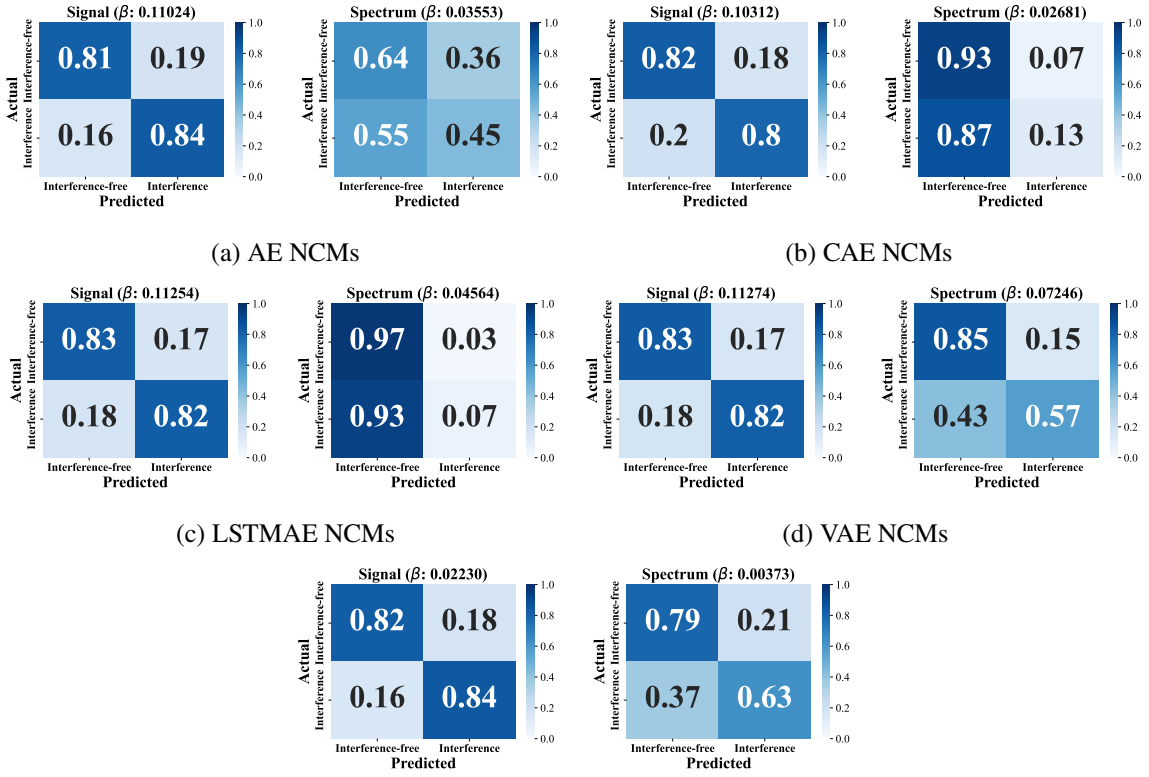
Figure 2.13: AUC_ROC plot per model for Signal data (left), and Spectrum data (right)

2.5.3 Models Evaluation Phase

After training and selecting the threshold for each model and each data representation, we can now evaluate the trained models with the data from the Testing Set. We analyze the performance of these models in detecting NGSO interference at GGS based on the key performance indicators described in Section 2.4.4. Evaluation encompasses two different representations of received signals: time domain (Signal data) and frequency domain (Spectrum data). We present some classification performance plots for each model: Fig. 2.13 presents the ROC curves per model for the Signal dataset (right), and the Spectrum dataset (left), as well as highlighting the AUC scores within the figure labels. These ROC curves show the trade-off between the true positive rate and false positive rate for each model. The closer the curve follows the left-hand border and then the top border of the ROC space, the more accurate the model. Hence, the closer AUC is to 1, the better the model is at predicting true interference-free instances while minimizing false alarms. The models' performances vary significantly between signal and spectrum data. For signal data, LSTMAE, VAE, and TrID perform equally well and slightly better than AE and CAE. For spectrum data, the TrID and VAE clearly outperform the other models, indicating that their architectures may capture the complexities of the spectrum data better. The CAE and LSTMAE models do not adapt as well to the spectrum data, possibly due to limitations in how they capture and utilize features in this type of data.

Fig. 2.14 shows the normalized confusion matrices CM for all models and data representations. In addition, Table 2.5 and Table 2.6 summarize the results from Fig. 2.13 and Fig. 2.14, for the Signal dataset and the Spectrum dataset, respectively.

Starting with Table 2.5, TrID tends to lead in all metrics compared to other models, it has the



(a) AE NCMs

(b) CAE NCMs

(c) LSTMAE NCMs

(d) VAE NCMs

(e) TrID NCMs

Figure 2.14: Normalized Confusion Matrices per model for Signal data (sub-left figures), and Spectrum data (sub-right figures)

highest Accuracy and AUC at 83. 18%, it also has a low false alarm rate or FPR at 17.63%, which is about 1% higher than VAE with the best value of 16.61%. On the other hand, LSTMAE and VAE show a closely identical performance with VAE being slightly better in Accuracy, FPR and AUC. AE and CAE while not leading in any specific category, they still perform reasonably well.

Regarding Table 2.6 for the Spectrum dataset, TrID and VAE models outperforms others, achieving the highest scores across all metrics, with +71% in AUC score, except FPR which LSTMAE and CAE were superior, however, this comes with a trade-off as their TPR are very low. VAE, although still performing well, falls slightly behind TrID in all metrics. All models show a marked decrease in performance metrics in the frequency-domain as compared to the time-domain, highlighting the complexity of detecting interference in the spectrum data.

As a conclusion for this evaluation, our proposed GenAI-based models (TrID and VAE) performed the best in both signal and spectrum data compared to the other models, with the highest Accuracy, F1Score, and AUC values. In applications where processing of both spectrum and signal data is required, VAE or TrID would be the preferable choice given their superior AUC scores. In real-

Table 2.5: Models performance summary on Signal test data

Model	β	**Accuracy** ↑	**TPR** ↑	**FPR** ↓	**F1 Score** ↑	**AUC** ↑
AE	0.1102	0.8239	0.8354	0.1874	0.8248	0.8240
CAE	0.1031	0.8107	0.7967	0.1754	0.8068	0.8106
LSTMAE	0.1125	0.8264	0.8215	0.1687	0.8244	0.8264
VAE	0.1127	0.8266	0.8192	**0.1661**	0.8242	0.8266
TrID	0.0223	**0.8318**	**0.8399**	0.1763	**0.8321**	**0.8318**

Table 2.6: Models performance summary on Spectrum test data

Model	β	**Accuracy** ↑	**TPR** ↑	**FPR** ↓	**F1 Score** ↑	**AUC** ↑
AE	0.0355	0.5441	0.4463	0.3597	0.4928	0.5433
CAE	0.0268	0.5327	0.1262	0.0671	0.2114	0.5296
LSTMAE	0.0456	0.5219	0.0681	**0.0311**	0.1238	0.5185
VAE	0.0725	**0.7112**	0.5703	0.1501	0.6621	0.7101
TrID	0.0037	**0.7112**	**0.6294**	0.2083	**0.6838**	**0.7106**

world applications, the choice between TrID and VAE, or another model, might also be influenced by computational constraints, training time, inference times, and reconstructing ability, which depends on the application requirements and the resources available. Given the critical nature of detecting NGSO interference in GGSs, where missed detections and false alarms may have significant implications, a model with a strong balance between TPR and FPR is essential. Overall, TrID was superior and also the best model in terms of reconstructing the input data. Thus, the TrID model on time-domain Signal data representation is recommended for further investigations. Here are some insights on possible reasons why the TrID architecture shows better results than the AE, CAE, LSTMAE, and VAE:

- **Multi-Head Self-Attention Mechanism:** As mentioned in the model description, the self-attention mechanism in TrID allows for a dynamic weighting of the significance of different parts of the signal. Moreover, the global receptive field of self-attention enables the model to capture long-term dependencies without being restricted by the vanishing gradient problem in typical LSTM.

- **Enhanced Accuracy:** The inclusion of convolutional layers for post-processing and skip connections within the TrID architecture helps maintain gradient flow and adjust dimensionality. This contributes to a more accurate signal reconstruction and guards against issues such as vanishing gradients that can hinder training in deep networks.

- **Better Data Generation Capabilities:** When generating data, TrID often outperform VAE as they can model complex distributions without being constrained by the need to match a specific prior distribution, leading to a higher fidelity in the generated data.
- **Adaptability:** The architecture of TrID is inherently flexible, allowing them to be adapted for a broad range of applications. This adaptability stems from the ability to process inputs of varying lengths and the ease of integrating additional information.
- **Computational Efficiency:** The potential for omitting the decoder in Transformers, along with the parallelization capabilities of Transformers, can lead to significant reductions in training time and computational complexity. This also paves the way for batch processing of signals, contributing to real-time performance in practical applications.

2.6 Comparison With Traditional Approach

In this section, we provide a comparison between our proposed GenAI-based models (TrID and VAE), and the traditional ED detector using only data in the time-domain.

2.6.1 Generation of Comparative Datasets

First, we examine the performance of the models in detecting the received LEO interference signals when its signal bandwidth: 1) 100% overlapped with GSO bandwidth, 2) 75% overlapped with GSO bandwidth, 3) 50% overlapped with GSO bandwidth and 4) 25% overlapped with GSO bandwidth. In other words, where the adjustment factor $B_{\text{adj},k}$ in (2.3) is 1, 0.75, 0.5 and 0.25 respectively. Therefore, to perform this comparison, we need to generate four new datasets, each referred to as the OVRLP% set representing the percentage of overlap within the data.

To generate these four OVRLP% sets, we considered only one LEO satellite pass ($k = \mathcal{K} = 1$). The simulation period is selected by experimental methods, where the LEO satellite is always visible to the GGS. The percentage of overlap between the GSO and LEO bandwidths is controlled by setting the GSO and LEO bandwidths at 50 MHz each and then adjusting the overlap bandwidth $B_{\text{overlap},k}$ in (2.3) according to the value that satisfies the target percentage, which will also require the change in the LEO carrier frequency $f_{c,k}$. The following steps outline the process of generating a single OVRLP% set:

- Initially, we fix GSO ModCod to QPSK, and the CNR values are selected within the range defined in Table 2.4 for the corresponding ModCod.
- The simulation runs with a single LEO satellite pass, "STARLINK-6173", starting at "01-Aug-2023 06:07:00", and a duration of $\mathcal{T}$ = 120 seconds, and it samples LEO coordination and INR value every $\Delta\tau$ = 5 ms, resulting in a total of $N = 2400$ samples from CNR and INR samples.
- We then repeat the simulation for other GSO ModCods listed in Table 2.4, i.e., 8PSK and 16APSK. This results in a total of three simulation rounds and a total of $N = 7200$ samples from CNR and INR values.
- Using simulation samples, we generate $N \times M_t$ time-domain interference data from (2.15). All N rows are then labeled as "1". In addition to the label, we also append the corresponding GSO ModCod scheme, the INR value, and off-axis angle to each row. This step forms the interference segment of 7200 data points to OVRLP% set.
- We also create interference-free data in the time-domain $N \times M_t$, from the magnitude of (2.14a), resulting in additional data points to the overall OVRLP% set. These data points are then labeled "0" and append the corresponding GSO ModCod, and two empty data columns to align with the other segment dimensions. This step forms the interference-free segment of 7200 data points to OVRLP% set.
- Finally, both segments are joined to form the full OVRLP% set, amounting in a total of $N = 14400$ time-domain data points and labels (i.e., $7200 \times M_t + 4$ interference-free data and $7200 \times M_t + 4$ interference data).

Four distinct OVRLP% sets are generated, each based on the varying degrees of overlap bandwidth B_{overlap}. By referring to equation (2.3), and with both B_x and B_i fixed to 50 MHz, the sets are created as in Table. 2.7.

Table 2.7: Overlapping Sets and Parameters

Set	**Overlap (%)**	B_{overlap} (MHz)	$f_{c,\text{leo}}$ (GHz)
OVRLP100	100	50	11.7500
OVRLP75	75	37.5	11.7625
OVRLP50	50	25	11.7750
OVRLP25	25	12.5	11.7875

Fig. 2.15 showcases an example of the LEO off-axis angles and INR values during single simulation round, particularly the GSO at QPSK within the OVRLP100 set.

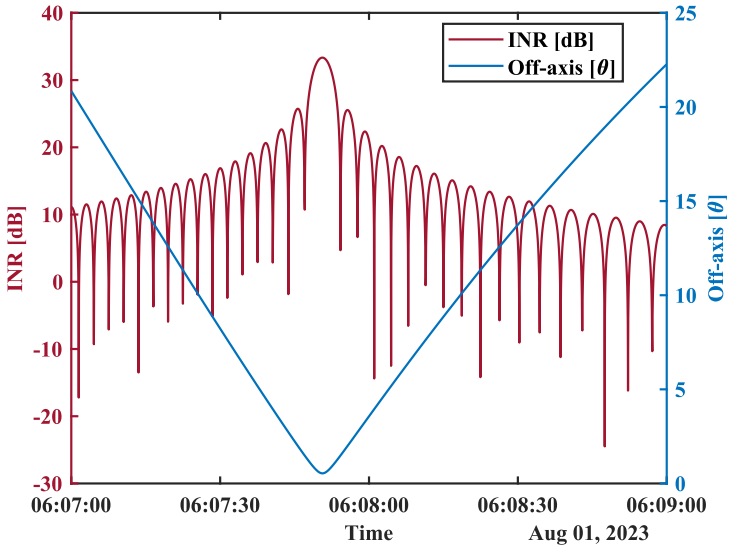


Figure 2.15: LEO pass vs INR and off-axis angles

2.6.2 Energy Detector Approach

An ED [112], is the optimal likelihood-ratio test for stochastic signals in white Gaussian noise (WGN) environments according to the classical detection theory [91]. ED is a fundamental tool for identifying the presence of interference signals in designated frequency bands. It functions by quantifying the energy content of received signal samples within a defined temporal window and comparing this value with a pre-established energy threshold. This mechanism enables the detector to effectively discern between GSO signals and scenarios encompassing both GSO and LEO signals.

Regarding the generated data, we know that the n^{th} data within N data points is a vector $\mathbf{y}_n \rightarrow y_n^{\mathcal{A}}$ of length M_t, and each vector contains the magnitude values of the corresponding received signal. Hence, the energy (magnitude squared) E_n of each data $\mathbf{y}_n$ is calculated by squaring the amplitude of its samples and summing them up.

$$E_n = \sum_{m=1}^{M_t} \mathbf{y}_n^2[m] \tag{2.39}$$

where $\mathbf{y}_n[m]$ is the amplitude of the m^{th} sample in the signal $\mathbf{y}_n$. An energy threshold β_E is set to determine whether a signal $\mathbf{y}_n$ contains an interference signal or not. This threshold is fixed and its

value is derived from the Testing Set based on the optimal AUC Score approach as for the threshold of the ML models explained in Section 2.5.2. In his case β_E = 86.03. The performance of the interference detector can be evaluated using the previously described interference detection performance metrics as in Table 2.5 and Table 2.6.

2.6.3 Comparison Results

Table 2.8: Performance Comparison of Models Across Bandwidth Overlap

Overlap (%)	Model	Accuracy ↑	TPR ↑	FPR ↓	F1 Score ↑	AUC ↑
100%	TrID	**0.8541**	**0.7867**	0.0785	**0.8435**	**0.8541**
	VAE	0.8442	0.7185	**0.0274**	0.8213	0.8442
	ED	0.8007	0.6754	0.0740	0.7721	0.8007
75%	TrID	**0.8431**	**0.7685**	0.0822	**0.8305**	**0.8431**
	VAE	0.8017	0.6369	**0.0336**	0.7626	0.8017
	ED	0.7578	0.5951	0.0794	0.7108	0.7578
50%	TrID	**0.8327**	**0.7571**	0.0812	**0.8227**	**0.8379**
	VAE	0.7526	0.5388	**0.0336**	0.6853	0.7526
	ED	0.7096	0.4999	0.0807	0.6325	0.7096
25%	TrID	**0.7936**	**0.6683**	0.0811	**0.7641**	**0.7936**
	VAE	0.6747	0.3817	**0.0324**	0.5398	0.6746
	ED	0.6378	0.3560	0.0786	0.4962	0.6387

Compare for difference overlapping factor

First, we compare the performance of TrID, VAE and ED using the aforementioned OVRLP% sets. Table 2.8 presents a comparative analysis of the three different models to detect NGSO-GSO interference in a time-domain representation of the signal $\mathbf{y}_n$ with varying degrees of bandwidth overlap between the NGSO and GSO signals.

In Table 2.8, TrID consistently outperforms the other models in all levels of bandwidth overlap. Its robustness to changes in overlap scenarios makes it a versatile model for different signal environments. VAE tends to minimize false alarms effectively, but struggles more than TrID with decreasing overlap in terms of accurately identifying interference. ED shows that traditional methods are less effective than the proposed GenAI-based approaches, especially as bandwidth overlap decreases, which likely introduces more complexity into the signal to which ED methods are not equipped to handle.

As a conclusion, in satellite communication systems, when choosing a model for interference detection across various environments constrains and possibilities of bandwidth overlaps, TrID may stand out as the most robust and high-performing model. Although VAE has merits, particularly in

environments where false alarms are highly undesirable, its performance drops with reduced overlap make it less reliable than TrID in diverse conditions. Traditional ED is significantly outclassed by the GenAI-based models, highlighting the potential benefits of GenAI-based in signal processing tasks.

Other comparisons

Based on the previous comparison, the models are more likely to detect interference in a fully overlap bandwidth scenarios than other scenarios. Therefore, we will focus on this next analysis only using the OVRLP100 set. In this section, we particularly investigate the impact of off-axis angles and INR values versus different GSO modulation schemes detection capabilities. The interference segment can be divided into three sub-segments based on GSO modulation schemes: [QPSK sub-segment, 8PSK sub-segment, and 16APSK sub-segment], each sub-segment contains 2400 data, and while different in GSO CNR values, each sub-segment contain the same LEO off-axis angles and the corresponding CNR values as in Fig. 2.15. The GSO CNR values range from 2.4 to 6.6 dB in the QPSK sub-segment, 6.7 to 9 dB for 8PSK, and 9.1 to 14 for 16APSK. The probability of detection $\mathrm{P_D}$ (or TPR) values are tested using coherent chunks of fixed sizes from each the sub-segments after sorted it out depending on the parameter of interest using the TrID, VAE, and ED.

The ability to maintain high interference detection performance across a range of off-axis angles is particularly important for systems that involve moving satellites, such as those in NGSO. We are comparing the models detection performance based on the LEO off-axis angles as seen from GGS. A small off-axis angle corresponds to a higher receive GSO ground station gain, therefore increasing the probability of detection. The previous hypothesis is validated with the results shown in Fig. 2.16, where the probability of detection is plotted with respect to the LEO link off-axis angle.

Based on the results in Fig. 2.16, we observed the following

- **Off-axis Angle Consideration**: When examining the probability detection with respect to the LEO off-axis angle, all models demonstrate a decreasing trend in $\mathrm{P_D}$ as the off-axis angle increases. This trend is expected because larger off-axis angles typically result in a weaker signal and more difficult detection. Thus, the models are more likely to detect LEO interference signals when their off-axis angles are close to the in-line interference scenario (i.e., LEO off-axis angle $\approx$ GSO boresight angle $\theta_0 = 0^\circ$).

- **Impact of GSO Modulation Schemes**: All models perform best in the 16APSK GSO modulation scheme, and the performance decreases as the GSO modulation scheme decreases in

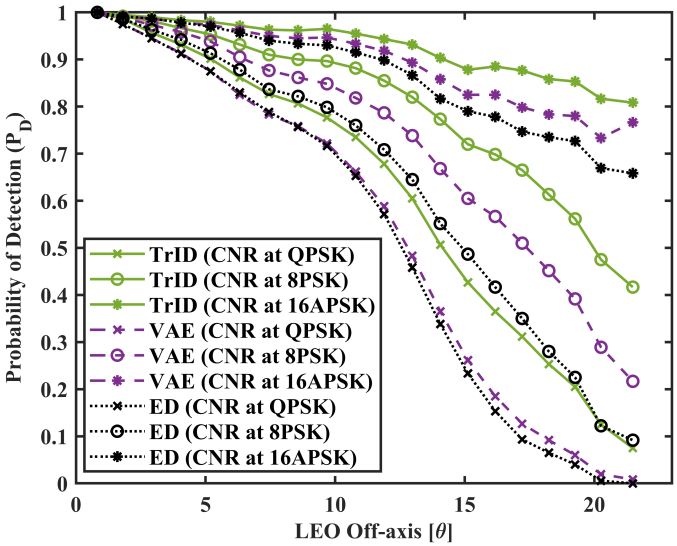


Figure 2.16: Detection vs LEO off-axis Angles for Various GSO ModCods

complexity. For the lower modulation scheme (i.e., GSO in QPSK), the models detection probability decreases to zero for LEO off-axis angles higher than 20° with TrID capturing interference in slightly higher angles. For GSO scenarios in 8PSK and 16APSK, TrID maintains its detection capability at superior performance compared to VAE and ED as well. We noticed that the model performance in detecting relatively higher off-axis angles (i.e., higher than 20°) increases for higher GSO modulation schemes.

- **TrID Performance**: TrID maintains the highest $\mathrm{P_D}$ over a larger range of off-axis angles, reinforcing its robustness. VAE and ED show a steeper decline in performance, with the ED being the most affected. This suggests that the TrID is better equipped to detect LEO interfering signals when they are not perfectly aligned with the GSO. Moreover, for different GSO modulation schemes data, TrID maintains a superior $\mathrm{P_D}$ across all modulation schemes compared to other models.

- **VAE Performance**: VAE detection performance also decreases with increasing off-axis angles, but at a faster rate than the TrID. This indicates that the VAE is somewhat sensitive to LEO off-axis angle, which could limit its effectiveness in operational environments where LEO usually does not perfectly align with GSO.

- **ED Performance**: The performance of the ED shows the most significant decline with increasing off-axis angles. This steep performance drop highlights the ED vulnerability to low levels of

interference. The ED performance gap drops more significantly with higher-order modulations (i.e., 16APSK).

Although the INR values are depending on LEO receiving off-axis angles at GGS, lower angles do not always lead to high INR, this due to the side lobes and nulls of the GGS beam pattern, as can be seen in Fig. 2.15. Higher INR values can provide a more distinct separation between the GSO desired signal and LEO interfering signals, which shall be exploited by the proposed models shall exploit to improve the detection performance. Fig. 2.17 shows the evolution of the probability of detection versus the INR values observed at the GSO ground station.

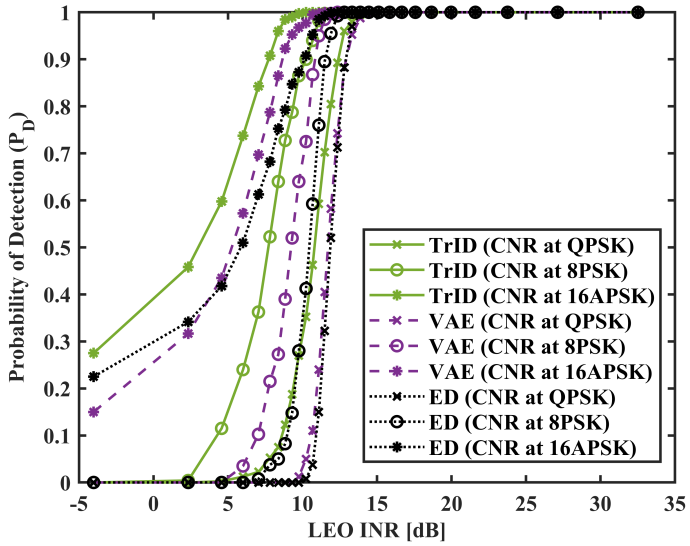


Figure 2.17: Detection vs LEO INR Values for Various GSO ModCods

Based on the results in Fig. 2.17, we observe the following

- **INR values Consideration**: All models' performance increases with higher INR values, they are capable of detecting LEO interference signals with INR value around 15 dB and higher. The ability of the TrID model to maintain high detection performance across a range of INR values is essential for practical applications, as it ensures reliability in various interference conditions.
- **Impact of GSO Modulation Schemes**: The model performance in detecting relatively small INR values increases for higher GSO modulation schemes. The models can still detect up to -5 dB INR values at the 16APSK sub-segment, 5 dB INR values at the 8PSK sub-segment, with TrID standing out across all the modulation schemes sub-segments and ED being the worse.

- **TrID Performance**: TrID consistently outperforms both VAE and ED across all GSO modulation schemes with respect to LEO INR values. Its performance is particularly notable at lower INR values, this implies that the TrID is more highly capable of distinguishing between the desired GSO signal and LEO interfering signals when the interference is within the noise level.
- **VAE Performance**: The VAE shows moderate detection performance, which is generally less than that of the TrID but superior to that of the ED. Its performance also degrades more gracefully compared to the ED as INR decreases, which can be advantageous in lower-quality signal environments. The VAE model also shows improved detection accuracy as INR increases, but to a lesser extent compared to the TrID.
- **ED Performance**: ED performance is less competitive compared to GenAI-based models, particularly at lower INR values. However, it shows a gradual increase in $\mathrm{P_D}$ with increasing INR, suggesting that it can still be somewhat effective in high interference scenarios.

TrID emerges as the superior model due to its high interference detection performance in comparison to other models, and it is also less sensitive to the complexity of the modulation scheme, making it a versatile and reliable choice for detecting NGSO to GSO interference. The VAE could serve as a fallback due to its moderate performance, while the ED could be considered for scenarios where computational simplicity is more critical than detection accuracy. Given these observations, the TrID is recommended as the best model for the task of NGSO to GSO interference detection due to its robustness to signal quality variations and its superior performance in both off-axis angles and INR values scenarios.

2.7 Chapter Conclusion

This chapter addressed the problem of interference detection in satellite communication, where signals from NGSO satellites have the potential to disrupt communications with GSO satellites when operating in the same spectral bands. We employ realistic simulations of satellite positions and trajectories, using actual system parameters to create interference scenarios. We proposed and evaluated different ML performance for the interference detection task. The proposed models are adeptly trained to discern interference in both the time and frequency domains of the received signals. The core contribution of this work is the development of GenAI-based models (TrID, and VAE) interference detectors designed to identify LEO interference by generating new samples of the original GSO signals.

The findings reveal that the models exhibits higher accuracy for detecting interference in the time-domain signal representations compared to the frequency-domain representations, with TrID being superior compared to VAE and other ML models. Moreover, TrID, VAE and ED were put in a comparison to explore the impact of varying GSO modulation schemes, bandwidth overlapping scenarios, LEO off-axis angles, and the interference power values (INR) on the detection accuracy, where TrID consistently outperforms both the VAE and ED across all the scenarios. Our research provides actionable insights for satellite communication operators. By understanding the efficacy of GenAI-based models in interference detection, they can make informed decisions and trade-off about integrating these technologies into existing and future satellite communication infrastructures.

Future work should focus on enhancing the models' capabilities in the frequency domain, potentially exploring hybrid models or advanced feature engineering techniques. Multiple models could be trained to detect interference in a single modulation scheme each, instead of training the models in all modulation schemes at once and see if that makes a difference. The data used in this work will be publicly available on the Smart-Space project website [84].

Chapter 3

Attention-based Blind Adaptive Receive Beamforming for NGSO Satellite Systems

This chapter presents an interference mitigation framework that can be applied on the user side for Non-Geostationary Satellite Orbit (NGSO) systems that share adjacent, overlapped frequencies to prevent unintentional co-frequency interference (CFI) scenarios. We introduce a novel Attention-based Beamformer (AttBF) model and explore its blind adaptive beamforming capabilities at the user terminals (UTs) side for spatial NGSO-to-NGSO downlink interference nulling, utilizing estimation-free data (e.g., received time-domain signals, frequency-domain representations, and sample covariance matrices (SCMs)) as direct inputs. We present a comprehensive performance evaluation of the proposed AttBF model against traditional deep learning (DL) models across various interference scenarios, encompassing both low spatial correlation (at UT's side-lobe) and high spatial correlation (at UT's main-lobe). To facilitate this research and future investigations into the interference management of NGSO systems, we implement innovative and extensive realistic satellite orbiting simulation and data generation methodologies, introducing new open datasets for the community. The results demonstrate that the proposed AttBF-based beamformer, particularly when employing SCMs input, achieves superior performance in mitigating interference compared to time- and frequency-domain inputs. Our findings highlight the enhanced nulling capabilities of the AttBF-based approach compared to DL-based models, such as convolutional neural networks (CNNs), and traditional methods, including zero forcing beamformer (ZFBF) and sample matrix inversion (SMI), underscoring the potential of advanced DL techniques for improving the reliability and efficiency of NGSO systems.

3.1 Introduction

3.1.1 Context and Motivation

Non-geostationary satellite orbits (NGSOs), particularly the rapidly growing low-Earth orbits (LEOs) mega-constellations, stand as the cornerstone of the global communication ecosystem led by Non-Terrestrial Networks (NTN), their importance constantly amplified by the ever-increasing demand for higher data throughput and the imperative for efficient spectrum utilization [3]. Given the congestion in the lower S and C bands, NGSO systems are increasingly leveraging higher frequency bands, including Ku, K, and Ka, to meet growing bandwidth demands [11]. These systems must manage co-existence strategies for sharing the limited spectrum [57]. Despite proactive efforts by the International Telecommunication Union (ITU) to manage and regulate radio emissions worldwide, the potential for unintentional co-frequency interference (CFI) remains a significant concern among NGSO operators [66]. Thus, advanced interference avoidance and mitigation techniques have become key points in the future NGSO ecosystem.

For many years, satellite user terminals (UTs) have relied on dish-type antennas that pointed to a fixed geostationary satellite in the sky [37]. With the advent of mega-LEO constellations, planar antenna arrays are gaining popularity due to their ability to electronically - without mechanical steering parts - steer the receiver main beam towards the moving satellite line of sight (LoS) [17]. This capability, known as beamforming, is a signal processing technique that leverages antenna arrays to spatially direct transmission or reception patterns [21]. By adjusting the complex weighting coefficients of each array element, BF enables precise beam control. Adaptive beamforming techniques (ABF) are those that allow for dynamically optimizing and tuning the antenna weights in real-time. In particular, ABF-based techniques are helpful in interference scenarios, as they can enhance the quality of the received signals, not only by focusing the main beam toward the desired direction of arrivals (DOAs), but they can also place low antenna gain values at unwanted DOAs [77].

Conventional blind ABF methods, such as the Capon beamformer, also known as the Minimum Variance Distortionless Response (MVDR) [113], exploit the inherent statistical properties of the desired signals or the knowledge of the covariance matrix of the received signal. The covariance matrix is typically estimated using a limited number of snapshots ”samples” of the received signal, and the observed matrix is called the sample covariance matrix (SCM); moreover, the traditional MVDR solution is replaced by a sample matrix inversion (SMI) algorithm. However, the SMI method requires a large number of signal snapshots to correctly estimate the original covariance

matrix and null interference locations, which is not desirable in fast-moving NGSO systems due to limited snapshots per coherent NGSO channel duration. Furthermore, the iterative nature and computational complexity in calculating the array weights (i.e, due to matrix inversion operations) are their main drawbacks [114]. Statistical ABF techniques, such as zero-forcing beamforming (ZFBF), provide optimal CFI interference nulling performance under perfect and full channel state information (CSI) knowledge, i.e., accurately knowing desired and interference DOAs and transmission channel characteristics. However, they usually rely on channel estimation for both desired and interference channels, which is typically difficult to achieve, especially in LEO systems, due to many factors such as: 1) fast time-variation of the LEO channels and the associated Doppler shifts [115], 2) high feedback overhead [116], 3) high computational complexity [117], and 4) imperfect synchronization & unknown interference sources [118]. This motivates the need for blind (estimation-free) beamforming solutions.

In response to these challenges, deep learning (DL)-based beamforming techniques have emerged as a potential solution to the drawbacks of traditional beamforming techniques [114]. DL-based beamforming typically replaces or augments classical weight calculation with a neural network that directly outputs beamforming weights [119–121]. Despite the significant time required to train a DL model in a satellite communications (SatCom) scenario, its fast temporal response (inference time) can be exploited for adaptive beamforming. After training, the DL model can perform complex operations in real-time, representing a promising solution for adaptive beamforming, where weights must be repeatedly calculated and conventional solutions are time-consuming.

3.1.2 Relevant Work

Achieving optimal beamforming in NGSOs presents more complex challenges compared to terrestrial network systems (TNs), including the need to adapt to highly dynamic environments characterized by moving satellites and UTs, the complex task of managing interference from various sources, and the continuous pursuit of enhanced performance under different operational constraints [22]. The satellite channel itself introduces impairments such as significant path losses, propagation delays, and Doppler shifts, further complicating the implementation of effective beamforming strategies [122]. Some state-of-the-art conventional ABF methods have been applied in the SatCom domain. In [123], and to mitigate the CFI of NGSOs, the authors propose a beamforming and power control-aided interference mitigation (BFPC-IM) scheme for uplink and downlink scenarios. In [124], the authors propose an iterative CFI null algorithm for NGSO systems that addresses an NP-hard unit modulus

least squares (UMLS) problem. These state-of-the-art approaches, among others, have an iterative manner and usually assume prior knowledge of the desired steering angle and/or the spatial locations of the interferer, which is typically not the case in CFI scenarios, where no information about the interference locations is available.

Considering that interferers' DOAs are unknown but the received signal carries an impact caused by interferers, DL-based beamforming approaches have been proposed for estimating the array weight vector to steer the antenna array towards the desired signal while nulling interference sources in TNs [125] and signal processing applications [126]. In [125], the authors introduced a deep neural network beamforming (NNBF) model for the TNs uplink sum-rate maximization problem (SRM). Here, the perfect and full CSI was used as input to the NNBF, but in the coexisting CFI case, only the channel component linked to the desired transmitter can be estimated. Furthermore, such a model might be sensitive to channel estimation errors. In [126], the SCM is used as input to a convolutional neural network beamformer (CNNBF). However, the approach in [126] assumes knowledge of the desired beamformer weights. Both [125] and [126] are based on a supervised learning approach, which requires input-output pairs by definition, and obtaining such labelled data can be challenging due to the unpredictable environments of NGSO systems, making the ground truth difficult to determine.

The Attention mechanism, introduced by [90], has been crucial in the development of Transformer-based large language model applications (LLM), which are now the backbone of many AI applications. Methods like convolution, dropout, and batch normalization have been essential for feature extraction and learning in DL models. The Attention mechanism provides a significant degree of interpretability. In particular, the model assigns attention weights to the features of the input that shall gather more focus, offering insights into the model's decision-making process. Transformer-based models have been introduced in the SatCom domain for various tasks, such as resource management [127], interference detection [118], and precoding [128]. In this chapter, we propose a novel self-supervised Attention-based beamformer (AttBF) model, which can be deployed on planar antenna arrays at the UT side. It does not rely on any CSI information, and it only uses the SCM of the received signal as an input. The results obtained are encouraging and highlight the potential of advanced GenAI-based techniques in improving conventional beamforming designs in NGSO systems.

3.1.3 Contribution

The key contributions of this work in the SatCom field, particularly in the area of NGSOs coexisting interference nulling via receive beamforming, can be stated as follows,

- We design and develop a novel AttBF-based adaptive beamformer for NGSOs-to-NGSO interference mitigation. We investigate the AttBF model capabilities to point towards the desired satellite while nulling interference locations without the need for any CSI. In particular, our proposed model works with the received signal's SCM, which is calculated within a coherence duration of an NGSO satellite pass.

- The proposed AttBF is a self-trained model, meaning that the learning is done based on Signal-to-Interference-plus-Noise Ratio (SINR) feedback measured at the UT output. Once it is trained, it is deployed in the customer UT, such deployment of the already-trained model ensures fast inference capable of working with short coherence duration and with UTs' power-limited devices.

- Due to the unavailability of real-world data, we implement extensive simulation and data generation methodologies to emulate a realistic NGSO scenario. We test the proposed blind beamformer method, considering interferences from different NGSO satellite orbits affecting the NGSO satellite user. Moreover, all datasets produced in this work are made publicly available at [84] to ensure research reproducibility.

- We present an evaluation of the proposed AttBF model against other beamforming methods for different interference scenarios (e.g., low spatial correlation in side-lobe scenarios and high spatial correlation main-lobe scenarios). In particular, we compare our proposed method with DL-based models [125, 126] and traditional non-learning methods such as ZFBF and SMI.

- The findings reveal that the proposed AttBF-based adaptive beamformer exhibits high performance in mitigating spatial interference instantaneously at the primary and side lobes of the UT, demonstrating superior null capabilities compared to other DL-based models and traditional methods.

3.1.4 Chapter Organization

The remainder of this chapter is organized as follows. Section 3.2. outlines the proposed system model. Section 3.3. describes the proposed AttBF-based model with SCMs input and its data preprocessing. Section 3.4. discusses the simulation setup for NGSO-to-NGSO interference scenarios and data generation, analyzes the results obtained from training the models as well as the interference mitigation performance, and provides a comprehensive comparison between the AttBF-based model

and traditional approaches. The chapter concludes in Section 3.5, which provides a summary, remarks, and suggested future improvements.

3.2 System Model

This section outlines the interference scenario between NGSO systems, along with the system model and link budget assumptions. It highlights the channel model, the signal model, and the concept of adaptive receive beamforming.

3.2.1 Interference Scenario

In Fig. 3.1 we illustrate the interference scenario, where an NGSO satellite system (green satellite icon) communicating with its UT may eventually and unintentionally be interfered with by other NGSO systems (red satellite icons), more specifically any other NGSO satellites that uses the same frequency bands and falls within the UT field of view (spherical cap) defined by a minimum elevation (θ_{min}) with respect to the local horizon of the UT, as shown in Fig. 3.1. Our scenario does not account for out-of-sight satellites (gray satellite icons) or those with different frequency bands within the spherical cap because they do not cause any significant CFI. Considering this scenario, we investigate a dynamic interference mitigation solution based on received beamforming that can be deployed on the UT side of the victim NGSO system.

3.2.2 Channel Model

In this chapter, we assume that the UT is equipped with a uniform planar array (UPA), as shown in Fig. 3.1. We consider a scenario in which the beam center of the desired satellite transmitters and interference satellite transmitters continuously track the UT location, resulting in worst-case interference scenarios at the UT. This is typically the case for many NGSO systems, where the satellite spot beams are Earth-fixed, meaning that they do not move during the satellite pass. We are only interested in the receiving beamforming at the UT side, and we focus on the downlink from satellites to the UT. By adopting the UPA, we aim to perform beamforming and achieve a high SINR.

Consider the UPA in the UT lying in the xy-plane with $M_x \times M_y$ antenna elements on the x and y axes, respectively, and the total number of antenna elements (antenna size) $M = M_x M_y$. Therefore, the UT array response vector can be written as [129],

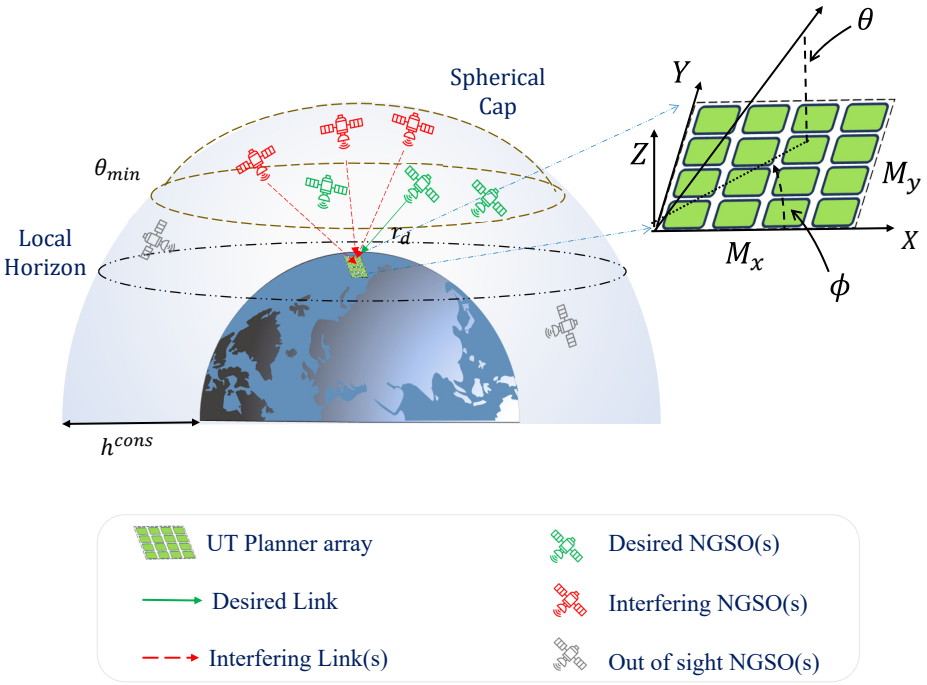


Figure 3.1: Considered scenario with a desired NGSO system (green) and an interfering NGSO system (red).

$$\mathbf{v}(\phi,\theta) = \frac{1}{\sqrt{M}}\left[1,\cdots,e^{j\frac{2\pi}{\lambda}d(m_x\sin\phi\cos\theta+m_y\sin\theta)},\cdots,\ e^{j\frac{2\pi}{\lambda}d((M_x-1)\sin\phi\cos\theta+(M_y-1)\sin\theta)}\right]^T \in \mathbb{C}^M, \tag{3.1}$$

where d is the inter-element spacing, $0 \leq m_x < M_x$ and $0 \leq m_y < M_y$ are the antenna indices in the xy plane, ϕ and θ are the azimuth and elevation angles, respectively, representing the DoAs of the desired satellite signal, and $\lambda = c/f_c$ is the carrier wavelength associated with the frequency carrier f_c. Note that the UT array response vector can be modeled as a plane wave; thus, for notational brevity, we define the pair angles of direction of arrival (DoA) as $\varphi \triangleq (\phi,\theta)$, i.e., the DOAs for the desired satellite (DS) are $\varphi_d \triangleq (\phi_d,\theta_d)$.

We are modeling a scenario where a DS transmits a signal ($s_d \in \mathbb{C}$) with $\mathbb{E}\{s_d s_d^H\} = 1$ to its UT, eventually, $\mathcal{K}(\mathcal{K} < M)$ NGSO satellites interfere with the desired downlink ($\text{IS}_k, \quad k \in 1,\cdots,\mathcal{K}$) and unintentionally transmit an interference signal ($s_{i,k} \in \mathbb{C}$) towards it. The number of main beam-pointing and nulling points should not exceed the number of antenna elements that satisfy the condition ($\mathcal{K}+1 < M$). A Rician fading channel can be assumed for NGSO communications [76]; however, we assume that the UT is placed in an obstacle-free elevated space, as recommended by

many operators (e.g., STARLINK [17]), the LoS component becomes dominant, thus the non-LoS (NLoS) component can be ignored. Doppler shift may introduce rapidly changing phase rotations in the received samples [130], thus, for the sake of simplicity, we assume that the DS Doppler shift is compensated for at the UT using system information (SI) [131]. We define the statistical time-varying channel state information (sCSI) model between the DS satellite and the UT at time instant t and frequency $f_{c,d}$ as follows,

$$\mathbf{h}_d = \chi_d \cdot \mathbf{v}_d(\varphi_d), \tag{3.2}$$

where χ_m is the desired channel gain, given by,

$$\chi_d = \sqrt{\frac{P_d^{sat} G_d^{ut}(\varphi_d)}{L_d}}, \tag{3.3}$$

where P_d^{sat} is the DS Equivalent Isotropic Radiated Power (EIRP), and $G_d^{ut}(\varphi_d)$ is the UT receives gain in the DS direction. L_d is the free-space path loss given by,

$$L_d[\text{dB}] = 20\log_{10} r_d + 20\log_{10} f_c + 20\log_{10}\frac{4\pi}{c}, \tag{3.4}$$

where r_d is the slant range between UT and DS and it can be expressed in terms of elevation angle as,

$$r_d = \left[(R_E + h^{\text{DScons}})^2 - (R_E + h^{\text{ut}})^2 \cdot \cos^2(\theta_d)\right]^{\frac{1}{2}} - (R_E + h^{\text{ut}}) \cdot \sin(\theta_d), \tag{3.5}$$

where R_E denotes the radius of the Earth ($R_E = 6371$km), h^{ut} is the altitude of the UT and h^{DScons} is the altitude of the desired constellation with respect to the Earth's surface, as shown in Fig. 3.1, the expression $(R_E + h^{\text{DScons}})$ is also known as the semi-major axis SM_d. The effective channel vector for the k^{th} interfering satellite IS_k to the UT receiver can be derived as follows,

$$\mathbf{h}_{i,k} = \chi_{i,k} \cdot \mathbf{v}_k(\varphi_k), \tag{3.6}$$

and,

$$\chi_{i,k} = \sqrt{\frac{P_k^{sat} G_k^{ut}(\varphi_k)}{L_k}}, \tag{3.7}$$

where P_k^{sat} is the IS transmit EIRP, and $G_k^{ut}(\varphi_k)$ is the UT receipt gain in k^{th} satellite IS direction. Similarly to (3.4) and (3.5), we can calculate the FSPL from the k^{th} interfering satellite, using the

slant range between the UT and IS_k denoted as $r_{i,k}$. The UT array receiving gain $G^{ut}(\varphi)$, at any DOAs φ can be obtained as follows [13],

$$G^{ut}(\varphi) = \eta^{ut}\Xi^{ut}(\varphi). \tag{3.8}$$

where η^{ut}, Ξ^{ut} are the UPA radiation efficiency and the directivity towards the φ direction. Directivity is the ratio of the radiation intensity in a given direction to the radiation intensity averaged in all directions, and can easily be calculated from the UPA array factor [132]. Intuitively speaking, the directivity should be as low as possible at interferences' DOA, leading to a gain value closer to zero (Ξ^{ut} at null locations $approx 0$). Note that the channel model adopted in (3.2) and (3.6) is applicable over a specific coherence time T_{samp}, as shown in Fig. 3.2, where the relative positions of the satellites and UT do not change significantly, and the physical channel parameters can be considered time invariant. In the next section, we explain the signal model for the entire pass of the desired satellite.

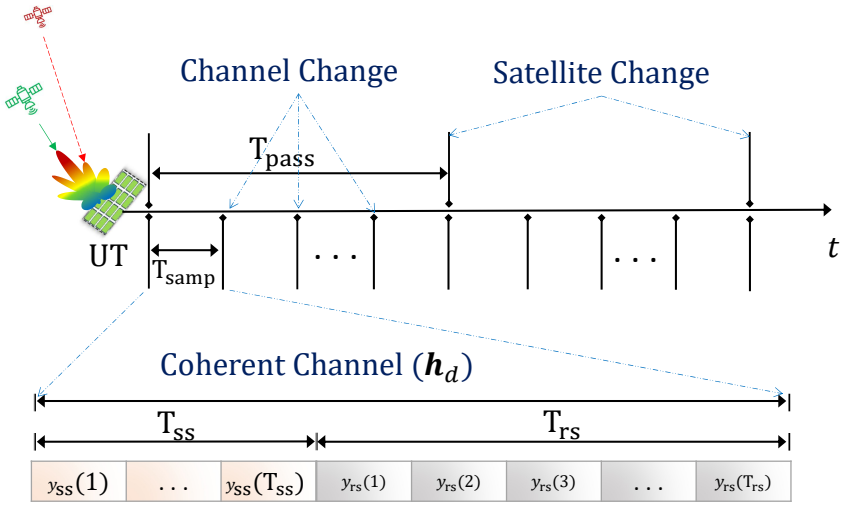


Figure 3.2: Time frame of the simulation scenarios

3.2.3 Signal Model

Let us assume the DS pass of duration T_{pass}, as shown in Fig. 3.2, which may encounter interference from the IS satellite. The satellite pass is divided into shorter time periods of duration T_{samp}, which corresponds to the channel coherence time. We assume that the UT array captures a total of T_{samp} snapshots within this coherence time. However, the UT must update the receive beamformer with $T_{\text{ss}} << T_{\text{samp}}$ so that the resulting beamforming weights can be applied for the remaining coherence

time $T_{\text{rs}} = T_{\text{samp}} - T_{\text{ss}}$.

The minimum value of T_{ss} that provides enough statistical information about the received signal is said to be at least M independent snapshots [133]. However, in many research articles, it is recommended to use at least double that, $2M$ snapshots, to achieve better beamforming results [134].

Let us now focus on a specific snapshot at a time instance t. In the presence of a single desired satellite and $\mathcal{K}$ interfering satellites, the received signal at the UT planar antenna array at a time instance t can be expressed as,

$$\mathbf{y}(t) = \mathbf{h}_d s_d(t) + \sum_{k=1}^{\mathcal{K}} \mathbf{h}_{i,k} s_{i,k}(t) + \mathbf{z}(t), \tag{3.9}$$

where $\mathbf{z}(t)$ is the additive white Gaussian noise (AWGN) at the UT receiver $\mathbf{z}(t) \in \mathbb{C}^M$ is i.i.d. $\mathcal{CN}(0, \sigma_z^2)$, with $\sigma_z^2 = \kappa T^{ut} BW_d$ where κ, T^{ut}, and BW_d are the Boltzmann constant, equivalent noise temperature of the UT, and DS signal bandwidth, respectively. Finally, $s_d(t)$ and $s_{i,k}(t)$ denote the independent information symbols transmitted from DS and ISs, respectively, whose average power is assumed to be normalized to one.

For the convenience of mathematical modeling, we will make use of the following matrix notation,

$$\mathbf{H}_i \triangleq [\mathbf{h}_{i,1}\ \mathbf{h}_{i,2}\ \ldots\ \mathbf{h}_{i,\mathcal{K}}] \in \mathbb{C}^{M \times \mathcal{K}}, \tag{3.10}$$

$$\mathbf{H} \triangleq [\mathbf{h}_d\ \mathbf{H}_i] \in \mathbb{C}^{M \times (\mathcal{K}+1)}, \tag{3.11}$$

$$\mathbf{S}_i(t) \triangleq [s_{i,1}(t)\ s_{i,2}(t)\ \ldots\ s_{i,\mathcal{K}}(t)] \in \mathbb{C}^{\mathcal{K} \times 1}. \tag{3.12}$$

3.2.4 Traditional Receive Beamforming Techniques

At the front-end of the UT receiver, a beamformer *weight* vector $\mathbf{w} \in \mathbb{C}^{M \times 1}$ is applied to steer the UT main beam towards φ_d direction and eliminating as much interference as possible from φ_k, $k = 1, \ldots, \mathcal{K}$ directions. The estimated signal after applying $\mathbf{w}$ is denoted as $\hat{s} \in \mathbb{C}$, as shown in Fig. 3.3, and is given as,

$$\hat{s}(t) = \mathbf{w}^H \mathbf{y}(t) = \mathbf{w}^H \mathbf{h}_d s_d(t) + \mathbf{w}^H \mathbf{H}_i \mathbf{S}_i(t) + \mathbf{w}^H \mathbf{z}(t). \tag{3.13}$$

Based on the above, the SINR after the receive beamforming procedure is expressed as,

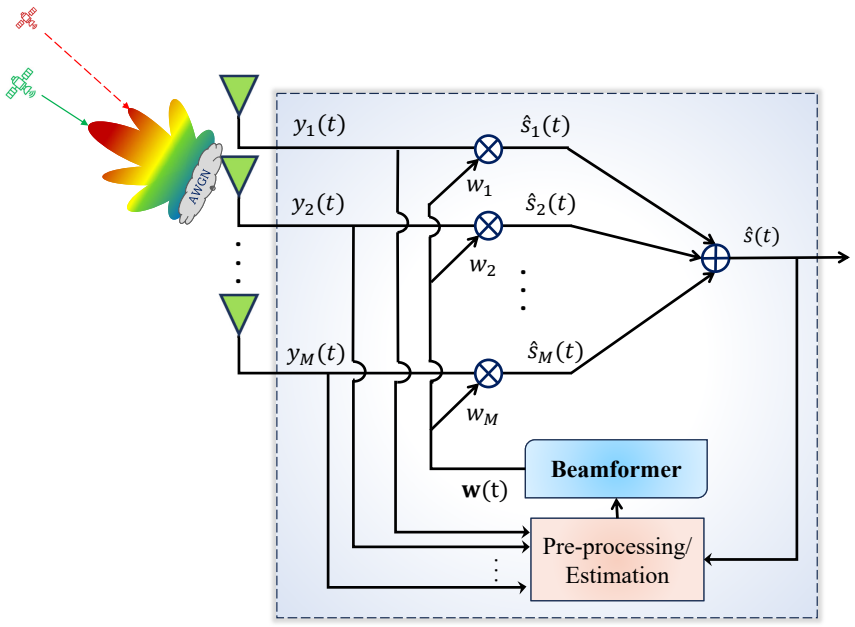


Figure 3.3: Typical structure of ABF

$$\gamma_{\text{out}} = \frac{\mathbf{w}^H \mathbf{R}_d \mathbf{w}}{\mathbf{w}^H \mathbf{R}_{i+z} \mathbf{w}} = \frac{\mathbf{w}^H (\mathbf{h}_d \mathbf{h}_d^H) \mathbf{w}}{\mathbf{w}^H (\mathbf{H}_i \mathbf{H}_i^H + \sigma_z^2 \mathbf{I}_M) \mathbf{w}} = \frac{|\mathbf{w}^H \mathbf{h}_d|^2}{\sum_{k=1}^{\mathcal{K}} |\mathbf{w}^H \mathbf{h}_{i,k}|^2 + \sigma_z^2 \mathbf{w}^H \mathbf{w}}, \tag{3.14}$$

where $\mathbf{R}_d = \mathbf{h}_d \mathbf{h}_d^H \in \mathbb{C}^{M \times M}$ and $\mathbf{R}_{i+z} = \mathbf{H}_i \mathbf{H}_i^H + \sigma_z^2 \mathbf{I}_M \in \mathbb{C}^{M \times M}$ are the covariance matrix of the desired signal and the interference-plus-noise covariance matrix, respectively. Note that we dropped the time index "t" here and in the next parts for simplicity.

The problem of maximizing (3.14) without knowledge of the interference DOA is mathematically equivalent to the MVDR beamforming problem [16]. In particular, the MVDR beamformer minimizes UT array input power while maintaining unity gain in DS direction,

$$\mathbf{w}_{\text{MVDR}} = \arg\min_{\mathbf{w}} \mathbf{w}^H \mathbf{R} \mathbf{w} \quad \text{subject to} \quad \mathbf{w}^H \mathbf{v}_d = 1, \tag{3.15}$$

where $\mathbf{v}_d$ has been used to denote $\mathbf{v}_d(\varphi_d)$ in a shorter way. The optimization problem in (3.15) leads to the following weights for the beamformer,

$$\mathbf{w}_{\text{MVDR}} = \frac{\mathbf{R}^{-1} \mathbf{v}_d}{\mathbf{v}_d^H \mathbf{R}^{-1} \mathbf{v}_d}. \tag{3.16}$$

Clearly, the covariance matrix $\mathbf{R} = \mathbb{E}\left[\mathbf{y}\mathbf{y}^H\right]$ serves as a fundamental tool in beamforming design,

providing a representation of the statistical relationships between the signals received at different elements of an antenna array. It contains information on the power of the signals received at each antenna element and the correlation between the signals received at different pairs of elements. This correlation structure is indicative of the spatial characteristics of the incoming waveforms, including the DOAs of desired and interfering signals. By analyzing the covariance matrix, beamforming algorithms, such as MVDR, can learn insights about the spatial distribution of signal sources and noise, which is essential for designing effective beamforming weights that enhance the reception of the desired signal while suppressing interference. Traditionally, $\mathbf{R}$ is not available and must be estimated from the receive signal by averaging the outer product of the receive signal vector over a finite number of time samples (L), often referred to as *snapshots* [77]. The covariance matrix can be estimated using the UPA snapshots by simply calculating the SCM matrix denoted as $\hat{\mathbf{R}}$, which is also called the autocorrelation matrix, and it is given as follows,

$$\hat{\mathbf{R}} = \frac{1}{L}\sum_{l=1}^{L}\mathbf{y}[l]\mathbf{y}^H[l] = \frac{1}{L}\mathbf{Y}\mathbf{Y}^H, \tag{3.17}$$

where $\mathbf{Y} \triangleq [\mathbf{y}[1];\mathbf{y}[2];\cdots;\mathbf{y}[L]] \in \mathbb{C}^{M\times L}$. When the SCM is used in the MVDR expression, the resulting beamformer is called the SMI beamformer, which solves the following minimum power distortionless response (MPDR) problem [113],

$$\mathbf{w}_{\text{SMI}} = \arg\min_{\mathbf{w}} \mathbf{w}^H\hat{\mathbf{R}}\mathbf{w} \quad \text{subject to} \quad \mathbf{w}^H\mathbf{v}_d = 1, \tag{3.18}$$

where $\mathbf{w}_{\text{SMI}}$ is the *SMI*-based minimum variance beamformer given by,

$$\mathbf{w}_{\text{SMI}} = \frac{\hat{\mathbf{R}}^{-1}\mathbf{v}_d}{\mathbf{v}_d^H\hat{\mathbf{R}}^{-1}\mathbf{v}_d}. \tag{3.19}$$

Remark 1. *As L increases, the SCM $\hat{\mathbf{R}}$ converges to the theoretical covariance matrix $\mathbf{R} = \mathbf{R}_d + \mathbf{R}_{i+z}$ and the corresponding* SINR *approximates the optimal value as $L \to \infty$. However, as the size of the available snapshots L decreases, the gap between $\hat{\mathbf{R}}$ and $\mathbf{R}$ increases, dramatically affecting the performance of SMI.*

In Fig. 3.4, we illustrate the traditional benchmark methods used in this work, including the SMI beamformer Fig. 3.4(a), alongside the intended DL-based beamformer, as shown in this figure. In

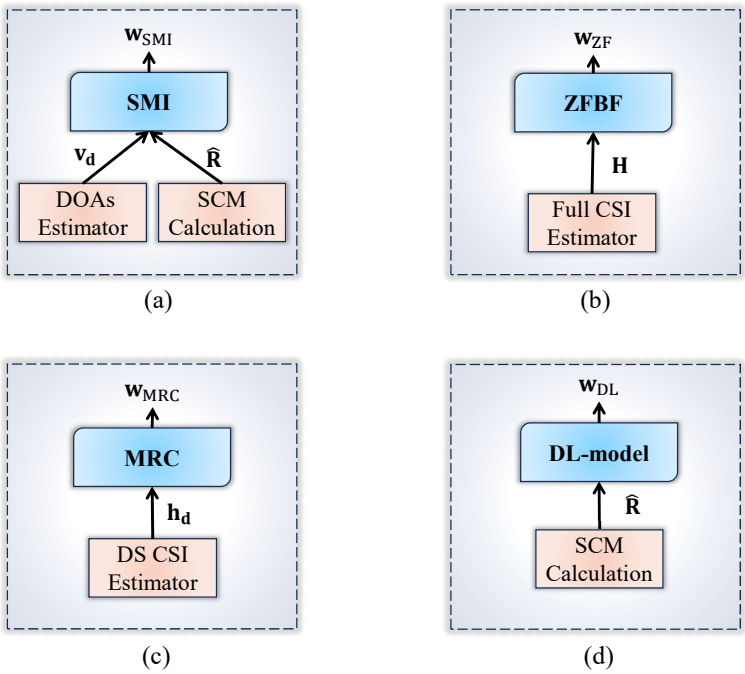


Figure 3.4: Receive Beamforming Techniques: (a) sample matrix inversion (SMI), (b) Zero forcing beamforming (ZFBF), (c) Maximum ratio combining (MRC), and (d) The intended DL-based beamformer

addition to the adaptive SMI beamformer $\mathbf{w}_{\text{SMI}}$, we will compare our DL-approach results with two famous statistical CSI-based beamforming benchmarks that are detailed below.

1) Zero forcing beamformer (ZFBF): Illustrated in Fig. 3.4(b), ZFBF represents the optimal/near-optimal scenario where UT can place a null towards DOAs of the interfering satellites φ_i. Clearly, ZFBF requires perfect full CSI estimation that includes both DS and ISs DOAs. In other words, the ZFBF uses the pseudoinverse of $\mathbf{H}$ as,

$$\mathbf{w}_{\text{ZF}} = \frac{\mathbf{H}(\mathbf{H}^H\mathbf{H})^{-1}\boldsymbol{\beta}}{\|\mathbf{H}(\mathbf{H}^H\mathbf{H})^{-1}\boldsymbol{\beta}\|}. \tag{3.20}$$

where $\boldsymbol{\beta} = [1; 0; \cdots; 0]^T \in \mathbb{N}^{\mathcal{K}+1}$.

2) Maximum ratio combining (MRC) beamformer: Illustrated in Fig. 3.4(c), MRC represents the worst-case nulling scenario, where the UT has only access to its own channel estimate corresponding to the desired DOA φ_d and thus focuses the UT main beam towards the DS satellite, without generating nulls towards DOAs of ISs satellites. Assuming perfect knowledge of $\mathbf{h}_d$, MRC is simply derived as,

$$\mathbf{w}_{\text{MRC}} = \frac{\mathbf{h}_d}{\|\mathbf{h}_d\|}. \tag{3.21}$$

MRC and ZFBF are sensitive to imperfect channel estimates (imCSI). Since we plan to evaluate the impact of the imCSI, we provide the model of CSI estimation errors herein.

The estimation error of the estimated DS channel $\hat{\mathbf{h}}_d$ is calculated as $\mathbf{e}_{d,\text{mrc}} = \hat{\mathbf{h}}_d - \mathbf{h}_d$ for MRC. When considering both the DS and the ISs channels, we model the error as $\mathbf{e}_{d,\text{zf}} = \hat{\mathbf{H}} - \mathbf{H}$, which will be used for ZFBF. Each error can be modeled as a complex Gaussian random variable $\mathbf{e}_d \sim \mathcal{CN}(\mathbf{0}, \sigma_e^2 \mathbf{I}_M)$. Note that perfect CSI (pCSI) is achieved for $\mathbf{e}_d = \mathbf{0}$. All beamformers $\mathbf{w}$ in this study are already or will be normalized, including SMI in (3.19), so that consistent and controlled beamforming weights are achieved independently of channel gains. In practice, UT might be able to estimate the CSI of the DS link, i.e., $\mathbf{h}_d$, using pilot signals, or at least have prior knowledge of the DS DOAs (to generate the steering vector $\mathbf{v}_d$), but cannot access any information about the ISs links. Estimation of DOA is usually performed using the MUSIC algorithm, where, in this case, the number of signal sources (desired and interference sources $\mathcal{K}+1$) is required. Furthermore, estimation stages and matrix inverse operations (e.g., SMI, ZFBF) add processing time and complexity to the UT design, making the temporal response of fast-moving NGSO satellites a critical concern.

In this work, we introduce a DL-based model that relies only on the available snapshots, specifically taking the SCM as input to instantly generate good beamformer weights, as illustrated in Fig. 3.4(d). The DL-based model does not depend on any CSI or is sensitive to its estimation errors, and provides acceptable performance in low and highly spatially correlated scenarios (e.g., in-line interference events).

3.3 Proposed Attention-Based Beamforming

In this work, we introduce a novel Attention-based beamformer DL-model, denoted as AttBF. The Attention mechanism, introduced by [90], is the main component behind our proposed AttBF model. This mechanism has been crucial in the development of Transformer-based LLM applications. In the following subsections, we provide a detailed explanation of the design of the proposed AttBF model and the processing carried out in its individual steps, as illustrated in Fig. 3.5. We also explain the training procedure, then outline other DL-based beamforming methods in the literature that will be used as benchmarks and their computational time complexity.

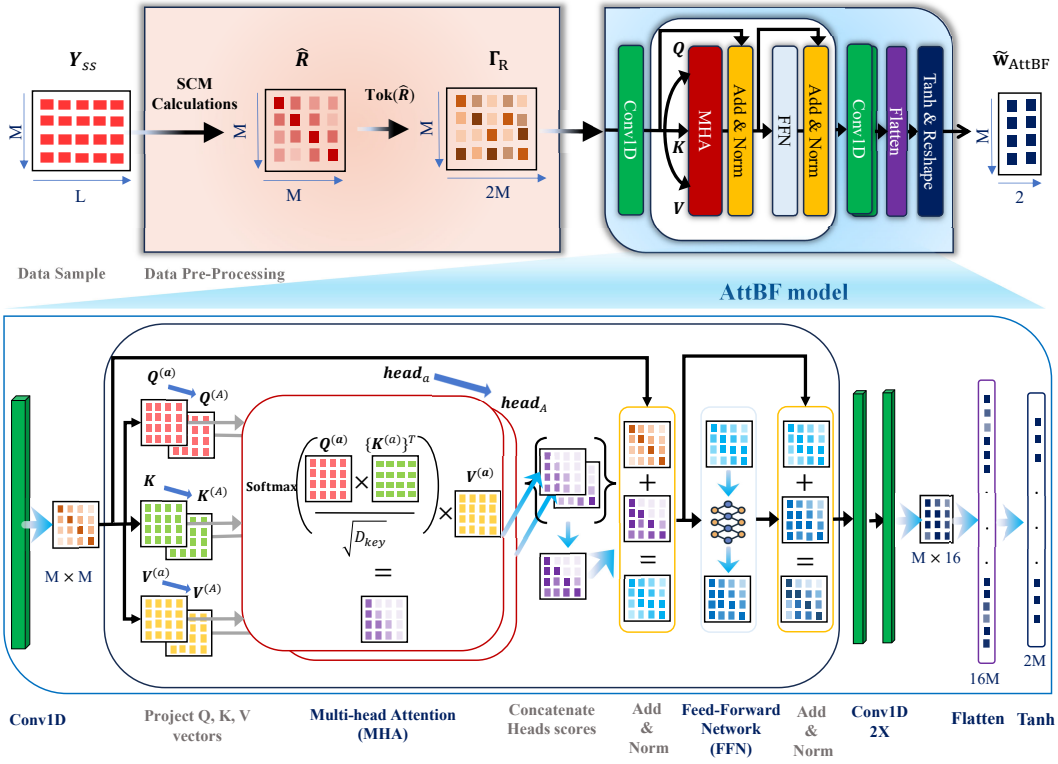


Figure 3.5: Illustration of the proposed AttBF beamformer.

3.3.1 Data Pre-processing

Our proposed AttBF model does not use the raw time-domain signal snapshot matrix $\mathbf{Y}(t)$ directly, so before feeding the proposed model with data, a few preprocessing steps are performed.

Sample Covariance Calculation

First, during the coherent duration of a satellite pass, the initial snapshots captured by UT during $L = T_{\text{ss}} << T_{\text{samp}}$ as in Fig. 3.2, and calculate the SCM, as in (3.17), more particularly,

$$\hat{\mathbf{R}} = \frac{1}{T_{ss}} \sum_{l=1}^{T_{ss}} \mathbf{y}_{\mathbf{ss}}[l] \mathbf{y}_{\mathbf{ss}}{}^{H}[l] = \frac{1}{T_{ss}} \mathbf{Y}_{\mathbf{ss}} \mathbf{Y}_{\mathbf{ss}}{}^{H}, \tag{3.22}$$

where $\mathbf{Y}_{ss} \triangleq [\mathbf{y}[1]; \mathbf{y}[2]; \cdots; \mathbf{y}[T_{ss}]] \in \mathbb{C}^{M \times T_{ss}}$. The AttBF model requires the SCMs' data to work in an adaptive way. SCMs represent spatial relationships and correlations within the received signal snapshots.

Data Tokenization

We define a tokenization operator,

$$\mathrm{Tok}(\cdot) : x \mapsto [\mathrm{Re}(x); \mathrm{Im}(x)]^T, \tag{3.23}$$

we simply transform the complex-valued $\hat{\mathbf{R}}$ matrix to a real-valued matrix of tokens $\mathbf{\Gamma}_R \in \mathbb{R}^{M \times 2M}$ as

$$\begin{aligned} \mathbf{\Gamma}_R &= \mathrm{Tok}\left(\hat{\mathbf{R}}\right) \\ &= \begin{bmatrix} \hat{r}_{1,1} & \hat{r}_{1,2} & \cdots & \hat{r}_{1,2M} \\ \hat{r}_{2,1} & \hat{r}_{2,2} & \cdots & \hat{r}_{2,2M} \\ \vdots & \vdots & \ddots & \vdots \\ \hat{r}_{M,1} & \hat{r}_{M,2} & \cdots & \hat{r}_{M,2M} \end{bmatrix}, \end{aligned} \tag{3.24}$$

where $\hat{r}_{i,j} \in \mathbb{R}$, each row in $\mathbf{\Gamma}_R$ represents a single input token (in this case an embedded vector $\in \mathbb{R}^{1 \times 2M}$), and M represents the total tokens. Each token corresponds to a row in the matrix, which we represent as a real-valued vector, meaning that there are always $2M$ features per token corresponding to the real and imaginary components of SCM. Unlike LLMs, where tokens represent linguistic units, here, tokens represent spatial relationships encoded in the SCM. This preserves the structural information of the array data while converting it into a form compatible with transformer-based architectures. Effectively, this tokenization step bridges signal processing representations with deep sequence models, enabling the network to learn embeddings that adaptively capture interference patterns for robust beamforming.

3.3.2 AttBF Model Architecture

The architecture of the AttBF model is a sequence of DL-based layers and matrix operations that process real-valued SCM $\mathbf{\Gamma}_R$ through successive transformations, as illustrated in Fig. 3.5, to predict beamforming weights $\mathbf{w}_{\text{AttBF}} \in \mathbb{C}^M$.The Attention mechanism, forming the core Transformer computation, enables the AttBF model to exploit the spatial relationships within the SCM tokens, which are crucial for effective beamforming. Instead of processing everything equally, the Attention mechanism works more dynamically; it efficiently weighs each token's contribution in improving the model's

beamforming performance by assigning weights to different parts of the input, and it then self-adjusts its learnable parameters to focus only on the token's parts that are most valuable to the model. We refer to the output of a DL layer as $\mathcal{X}_{\text{Layer Name}}$ and its learnable parameters as $\mathbf{\Theta}_{\text{Layer Name}}$.

Feature Extraction Layer

A single 1-dimensional (1D) convolution layer ($\mathrm{Conv1D}$) processes the AttBF model input using M filters, a single kernel, and Gaussian Error Linear Unit (GELU) activation. This layer acts as a dense layer applied independently to each of the $2M$ features per token along the first spatial dimension, reducing it back to M features per token. This can aid in feature extraction (FE) across the real and imaginary components of input data for each antenna element, thereby increasing the computational efficiency of the MHA block.

Multi-Head Attention Block

The next part of the AttBF model is the Multi-Head Attention (MHA) block, which consists of $a \in \{1, 2, \cdots, A\}$ Attention heads with key dimensions corresponding to the number of features extracted in each token ($i.e., D_{key} = M$). First, MHA performs a linear projection on the FE output to produce for each head three matrices as:

- Query (Q) matrix: Represents what an antenna element is "looking for" or a query about its correlation with other elements.
- Key (K) matrix: Represents the information an antenna element "holds" or what it has to offer to a query.
- Value (V) matrix: Contains the actual content or features that should be propagated forward if the corresponding key matches a query.

These matrices are formed as $Q^{(a)} = \mathcal{X}_{\text{FE}}\mathbf{\Theta}_Q^{(a)}, K^{(a)} = \mathcal{X}_{\text{FE}}\mathbf{\Theta}_K^{(a)}$, and $V^{(a)} = \mathcal{X}_{\text{FE}}\mathbf{\Theta}_V^{(a)}$, where these projections are able to learn parameter matrices $\mathbf{\Theta}_Q^{(a)}, \mathbf{\Theta}_K^{(a)}, \mathbf{\Theta}_V^{(a)} \in \mathbb{R}^{D_{key} \times D_{key}}$. Each head performs a scaled dot-product Attention with $\mathrm{Dropout}$ as in (3.25) to compute its Attention Score.

$$\text{head}_a = \text{Attention}(Q^{(a)}, K^{(a)}, V^{(a)}) = \text{Dropout}\left(\text{softmax}\left(\frac{Q^{(a)}{K^{(a)}}^\top}{\sqrt{D_{key}}}\right)\right) V^{(a)}. \tag{3.25}$$

In (3.25), for each token in the input, its Query matrix Q is multiplied by the Key matrix K of all other tokens (including itself). This produces a matrix of attention scores. A high score between a query from token i and a key from token j indicates a strong relationship. This is the mechanism by which the model "decides" which token features are most relevant to each other for the purpose of producing beamforming weights. For instance, it might learn that the correlations between certain token features are critical for identifying the desired signal or a strong interferer. The attention scores are then passed through a softmax function to normalize them into a probability distribution (where all weights sum to 1). These normalized weights are then multiplied by the Value matrix V. This step effectively creates a weighted sum of all Value matrices. Tokens with a high attention score (i.e., those deemed most important by the model) contribute more to the output of that attention head. The model thus "focuses" its attention on the most critical parts of the input SCM. For instance, if the SCM contains a strong interferer, the attention mechanism will learn to assign high weights to the correlations associated with that interferer, allowing the model to generate weights that nullify it.

The "multi-head" part of MHA means this entire process is performed multiple times in parallel, with each head using its own independent set of Q, K, and V projection matrices. Each attention head can learn to focus on different aspects of the tokenized SCM. For instance, one head might learn to focus on the desired signal's spatial signature, while another might learn to identify and focus on the spatial signature of a strong interferer. The outputs of all the individual heads are then concatenated and passed through a final linear projection layer as,

$$\begin{aligned} \mathcal{X}_{\text{MHA}} &= \text{MHA}(\mathcal{X}_{\text{FE}}) \\ &= \text{Concat}(\text{head}_1, \cdots, \text{head}_A)\boldsymbol{\Theta}_{\text{MHA}}, \end{aligned} \tag{3.26}$$

where $\boldsymbol{\Theta}_{\text{MHA}}$ are the output projection matrices in the MHA operation, and are also a learnable parameter that enables dimensional alignment and feature fusion between Attention heads.

The MHA block is then followed by a residual connection, and a normalization layer (LayerNorm) to stabilize training and improve generalization by normalizing activations across the M feature dimension,

$$\mathcal{X}_{\text{LN1}} = \text{LayerNorm}\left(\mathcal{X}_{\text{FE}} + \mathcal{X}_{\text{MHA}}\right). \tag{3.27}$$

Feed-forward network (FFN)

The FFN consists of a two-layer transformation with linear and Rectified Linear Unit (ReLU) activation, further processing the features learned by the MHA block, allowing for non-linear transformations of these features as,

$$\mathcal{X}_{\text{FFN}} = (\mathrm{ReLU}(\mathcal{X}_{\text{LN1}}\boldsymbol{\Theta}_{\text{F1}}))\boldsymbol{\Theta}_{\text{F2}}, \tag{3.28}$$

Afterwards a second residual connection and $\mathrm{LayerNorm}$ process layer follow to help stabilize the learning process,

$$\mathcal{X}_{\text{LN2}} = \mathrm{LayerNorm}\left(\mathcal{X}_{\text{LN1}} + \mathcal{X}_{\text{FFN}}\right). \tag{3.29}$$

Beamforming Weights Refining

In the rest of the AttBF architecture, we apply some basic DL-based layers to refine and extract the features that define the beamforming weights. First, two successive $\mathrm{Conv1D}$ layers are applied to the output of the second $\mathrm{LayerNorm}$, each with a single kernel, they progressively reduce the number of features and further refine the feature maps along their channel dimension, reducing the number of features from M to $\frac{M}{2}$ and then to 16. Here, the ReLU activation is chosen to introduce non-linearity to the AttBF model,

$$\mathcal{X}_{\text{CN}} = (\mathrm{ReLU}(\mathcal{X}_{\text{LN2}} * \boldsymbol{\Theta}_{\text{C1}}))\boldsymbol{\Theta}_{\text{C2}}. \tag{3.30}$$

The output tensor is flattened (FL) before a final Dense layer; this flattened vector contains the processed features.

$$\mathcal{X}_{\text{FL}} = \mathrm{vec}(\mathcal{X}_{\text{CN}}), \tag{3.31}$$

Finally, a Dense layer with $2M$ output units maps the learned features to the size of the complex beamforming weights. A hyperbolic tangent function (Tanh) activation function constrains the output values to the range $[-1, 1]$. The output is then reshaped to $(M \times 2)$, where the last dimension represents the real and imaginary components of the complex weight for each of the M antenna elements,

$$\mathcal{X}_{\text{out}} = \mathrm{Tanh}(\mathcal{X}_{\text{FL}})\boldsymbol{\Theta}_{\text{out}}, \tag{3.32}$$

$$\tilde{\mathbf{w}}^{(n)}_{\text{AttBF}} = \mathrm{Reshape}(\mathcal{X}_{\text{out}}). \in \mathbb{R}^{M\times 2} \tag{3.33}$$

The complex-valued beamforming weights $\mathbf{w}_{\text{AttBF}} \in \mathbb{C}^M$ can be constructed from the AttBF output matrix $\tilde{\mathbf{w}}_{\text{AttBF}}$ as,

$$\mathbf{w}_{\text{AttBF}}^{(n)} = \frac{\tilde{\mathbf{w}}_{\text{AttBF}}^{(n)}(:,1) + j \cdot \tilde{\mathbf{w}}_{\text{AttBF}}^{(n)}(:,2)}{\|\tilde{\mathbf{w}}_{\text{AttBF}}^{(n)}(:,1) + j \cdot \tilde{\mathbf{w}}_{\text{AttBF}}^{(n)}(:,2)\|}. \tag{3.34}$$

This final step preserves the phase and relative amplitude information needed for the beamformer weights.

3.3.3 AttBF Model Objective

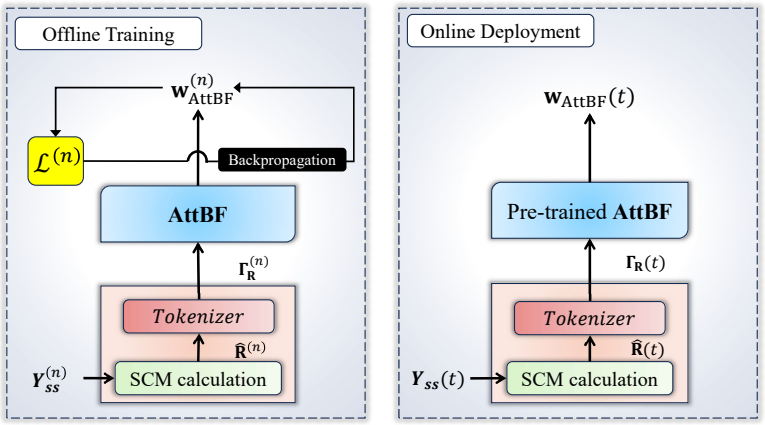


Figure 3.6: AttBF offline training, online deployment objectives.

The basic working concepts of the proposed AttBF design are illustrated in Fig. 3.6. The proposed learning procedure offers an offline, self-supervised training approach, or reward-like learning, as it learns without requiring explicit, human-labeled data. After training, the model can be used on new, unseen data to perform blind inference (Blind beamforming) without needing any prior knowledge or additional information about the environment. For the sake of notation specific to the proposed model, we add the index n as $\{\cdot\}^{(n)}$ to refer to the processed sample in the training datasets $n = 1, \ldots, \mathcal{N}_{Tr}$ or testing $n = 1, \ldots, \mathcal{N}_{Ts}$.

During the training phase, the model takes signal snapshots matrix $\mathbf{Y}_{ss}^{(n)}$, calculates the SCM $\hat{\mathbf{R}}_{ss}^{(n)}$, and transfers them into a DL-friendly form (i.e, tokens), then learns a beamformer design $\mathbf{w}_{\text{AttBF}}$ that is then fed back into the UT planar array to collect feedback from the environment in the form of a loss function $\mathcal{L}$, this loss function is customized to maximize SINR as,

$$\mathcal{L}_{\mathcal{B}} = -\frac{1}{\mathcal{B}} \sum_{n}^{\mathcal{B}} \gamma_{\text{out}}^{(n)}, \tag{3.35}$$

where $\mathcal{B}$ is the batch size. AttBF model modifies its learnable parameters according to the feedback of the loss function $\mathcal{L}_{\mathcal{B}}$ through the backpropagation process (Backprop).

Algorithm 3 summarizes the training process for the AttBF. First, the model parameters ($\boldsymbol{\Theta}_{\text{model}}$) are set to random values at the start. The model inputs a sample $\mathbf{Y}_{ss}^{(n)}$ from the processed mini batch of the training dataset $\mathcal{D}_{\text{Tr}}$, outputs the beamforming weights $\mathbf{w}_{\text{AttBF}}^{(n)}$ for that mini batch, and update the model parameter using the loss function feedback, the loss here is the negative SINR observation, and in this algorithm it is calculated per mini batch using $\mathbf{R}_{d}^{(n)}$ and $\mathbf{R}_{i+z}^{(n)}$ for each training sample. The gradients Gradients (∇_{Θ}) of the loss are calculated per mini batch; they are basically derivatives with respect to the model weights. An optimizer Ω uses these Gradients to update the model's parameters. This is the "learning" step where the model adjusts itself to produce a better beamformer in the next mini-batch. This loop continues until all mini-batches in an epoch are processed, and then it repeats for the next iteration ($epech$). Throughout training, the model keeps track of the best-performing set of parameters ($\boldsymbol{\Theta}_{\text{model}}^{(\text{best})}$), which is the final output of the training process after maximum iterations $E \rightarrow epoch$. The loss-per-epoch tensor $\mathbf{L}_{\text{epochs}}$ is used later on in the results section to compare the learning process performance with other DL-based benchmarks.

Algorithm 3: The Proposed Model Training Phase.

Input: Training dataset $\mathcal{D}_{\text{Tr}}$, Model f_{Θ}, Optimizer Ω
Output: Optimized model parameters $\boldsymbol{\Theta}_{\text{best}}$

Initialize: Model parameters $\boldsymbol{\Theta}_{\text{model}}$, B mini batches $\mathcal{B} \in \mathcal{D}_{\text{Tr}}$
for $epoch = 1$ **to** E **do**
  $\mathcal{L}_{\text{total}} \leftarrow 0$
  for $n = 1 : |\mathcal{B}|$ **do**
    $\mathbf{Y}_{ss}^{(n)}, \mathbf{R}_{d}^{(n)}, \mathbf{R}_{i+z}^{(n)} \leftarrow \mathcal{D}_{\text{Tr}}\{\mathcal{B}\}$ // Inputs
    $\boldsymbol{\Gamma}_{R}^{(n)} \leftarrow \mathbf{Y}_{ss}^{(n)}$ // Pre-process (3.23)
    $\mathbf{w}_{\text{AttBF}}^{(n)} \leftarrow f_{\Theta}(\boldsymbol{\Gamma}_{R}^{(n)})$ // Model outputs
    $\gamma_{\text{out}}^{(n)} \leftarrow \gamma_{\text{out}}(\mathbf{w}_{\text{AttBF}}^{(n)}; \mathbf{R}_{d}^{(n)}; \mathbf{R}_{i+z}^{(n)})$ // Calculate SINR (3.14)
    $\gamma_{\mathcal{B}} \leftarrow \gamma_{\mathcal{B}} + \gamma_{\text{out}}^{(n)}$// $\mathcal{B}$ SINR
  $\mathcal{L}_{\mathcal{B}} \leftarrow -\text{mean}(\gamma_{\mathcal{B}})$// $\mathcal{B}$ mean SINR (3.35)
  $\nabla_{\Theta} \leftarrow \text{Gradient}(\mathcal{L}_{\mathcal{B}}, \boldsymbol{\Theta}_{\text{model}})$ // Backprop
  $\boldsymbol{\Theta}_{\text{model}} \leftarrow \Omega(\Theta_{\text{model}}, \nabla_{\Theta})$ // Optimizer
  $\mathcal{L}_{\text{total}} \leftarrow \mathcal{L}_{\text{total}} + \mathcal{L}_{\mathcal{B}}$ // epoch loss
  $\boldsymbol{\Theta}_{\text{model}} = \text{Append}(\Theta_{\text{model}})$
  $\mathbf{L}_{\text{epochs}} = \text{Append}(\mathcal{L}_{\text{total}}/B)$
Return $\mathbf{L}_{epochs}$, $\boldsymbol{\Theta}_{model}^{(best)} \leftarrow \text{Best}(\boldsymbol{\Theta}_{model})$ // Return loss/epoch values and recall best parameters

Once the AttBF model is trained, it is deployed online, using the model's learned parameters, to

provide instant predictions of the beamforming weights $\mathbf{w}_{\mathrm{AttBF}}$ for any input sample (i.e., any $\mathbf{Y}_{ss}$), that focus the UT main beam towards the DS and null ISs directions.

3.3.4 Benchmark Models

The main objective of this work is to introduce a DL-based beamforming model that does not require any CSI or DOAs estimations. The AttBF model can learn to map the spatial correlation matrix $\hat{\mathbf{R}}$ into an appropriate beamforming weight vector $\mathbf{w}_{\mathrm{AttBF}}$ to maximize the received SINR.

Although our AttBF proposal works with the SCM $\hat{\mathbf{R}}$ as input, the same model can be adapted to work directly with the time and frequency domain representations of the received signal snapshots $\mathbf{Y}_{ss}$. We will consider these as benchmark approaches to strengthen the argument that the SCM provides more reliable performance in this context. To differentiate between the proposed model, which will also be referred to as $\mathrm{AttBF(R)}$ from hereafter, and the other models, we will denote the type of input data that will be used for each model. More particularly,

- $\mathrm{AttBF(Y)}$ model: Consider time-domain snapshots $\mathbf{Y}_{ss}$ as input after data normalization and tokenization preprocess (i.e., $\mathbf{\Gamma}_Y \in \mathbb{R}^{L\times 2M} \leftarrow \mathbf{Y}_{ss}$).

- $\mathrm{AttBF(FFT)}$ model: Consider the fast Fourier transform (FFT) representation of time-domain snapshots $\mathbf{Y}_{ss}$ as input after data tokenization preprocess (i.e., $\mathbf{\Gamma}_{FFT} \in \mathbb{R}^{L\times 2M} \leftarrow \mathrm{FFT}(\mathbf{Y}_{ss}) \leftarrow \mathbf{Y}_{ss}$).

We also compare our proposed model with other traditional DL-based beamformers available in the literature,

- $\mathrm{NNBF(H)}$ model: It assumes the NNBF model introduced [125], which relies on full CSI input data (i.e., inputs $\mathbf{H} \in \mathbb{C}^{M\times(\mathcal{K}+1)}$), thus, it is expected to be sensitive to CSI estimation errors.

- $\mathrm{CNNBF(R)}$ model: Inspired by the CNNBF model in [126], it uses the SCM inputs (i.e., the real-valued matrix $[\mathrm{Re}(\hat{\mathbf{R}}); \mathrm{Im}(\hat{\mathbf{R}})] \in \mathbb{C}^{M\times 2M}$). This is particularly useful for comparing the traditional CNN-based models with the proposed model using the same input data.

Note that the same loss function and training approach as in Algorithm 3 are used for all benchmark models for a fair comparison. Table 3.1 shows the difference between all traditional methods and train-based models benchmarks in terms of input type.

Table 3.1: Comparison between our proposed model and other benchmarks

Model/Method	**Input**	**CSI-Free?**
Proposed	SCMs ($\hat{\mathbf{R}} \in \mathbb{C}^{M\times 2M}$) (3.22)	Yes
AttBF(Y)	Time domain samples ($\mathbf{Y_{ss}} \in \mathbb{C}^{L\times 2M}$)	Yes
AttBF(FFT)	Frequency domain samples (FFT($\mathbf{Y_{ss}}$) $\in \mathbb{C}^{L\times 2M}$)	Yes
NNBF(H) [125]	Full CSI matrix ($\mathbf{H} \in \mathbb{C}^{M\times(\mathcal{K}+1)}$) (3.11)	No
CNNBF(R) [126]	SCMs ($\hat{\mathbf{R}} \in \mathbb{C}^{M\times 2M}$) (3.22)	Yes
ZFBF	Full CSI matrix ($\mathbf{H} \in \mathbb{C}^{M\times(\mathcal{K}+1)}$) (3.11)	No
MRC	Desired satellite CSI vector ($\mathbf{h}_d \in \mathbb{C}^{M}$) (3.2)	No
SMI	SCMs ($\hat{\mathbf{R}} \in \mathbb{C}^{M\times 2M}$) (3.22) and DS satellite response vector ($\mathbf{v}_d \in \mathbb{C}^{M}$)	Yes

3.3.5 AttBF Computational Time Complexity :

The time complexity of an off-line training DL model can be observed from the number of floating point operations (FLOPs) by each layer in inference [135], the complexity per layer for Conv1D: $\mathcal{O}(N_{seq} \cdot D_{hid}^2)$, Attention: $\mathcal{O}(D_{key} \cdot N_{seq}^2)$, and Dense: $\mathcal{O}(N_{in} \cdot N_{out})$, where N_{seq} is the size of the input sequence, D_{hid} is the hidden dimension, D_{key} is the attention key size [90], and N_{in}, N_{out} are the input and output neurons. Assuming the training data have been preprocessed, we can derive the per data sample time complexity for AttBF(Y) and AttBF(FFT) is $\mathcal{O}(L^2)$, and is equal to $\mathcal{O}(M^2)$ for other models for constant $D_{key} = D_{hid} = M$. However, only considering the number of FLOPs cannot be sufficient to draw a fair comparison between DL-based models and traditional methods, so we propose both end-to-end inference time complexity and the pure inference time in the following subsection as a performance indicator.

Table 3.2: Comparison of the End-to-end inference/latency time Complexity

Model/Method	**Time Complexity**
Proposed	$\tau_{\text{SCM}}^{\text{cal}} + \tau_{\text{SCM}}^{\text{Tok}} + \mathcal{O}(M^2)$
AttBF(Y)	$\tau_{\text{Y}}^{\text{Tok}} + \mathcal{O}(L^2)$
AttBF(FFT)	$\tau_{\text{Y}}^{\text{FFT}} + \tau_{\text{FFT(Y)}}^{\text{Tok}} + \mathcal{O}(L^2)$
NNBF(H) [125]	$\tau_{\text{fullCSI}}^{\text{est}} + \tau_{\text{fullCSI}}^{\text{Re/Im}} + \mathcal{O}(M^2)$
CNNBF(R) [126]	$\tau_{\text{SCM}}^{\text{cal}} + \tau_{\text{SCM}}^{\text{Re/Im}} + \mathcal{O}(M^2)$
ZFBF	$\tau_{\text{fullCSI}}^{\text{est}} + \mathcal{O}(M(\mathcal{K}+1)^2 + (\mathcal{K}+1)^3)$
MRC	$\tau_{\text{desCSI}}^{\text{est}} + \mathcal{O}(M)$
SMI	$\tau_{\text{desDOA}}^{\text{est}} + \tau_{\text{SCM}}^{\text{cal}} + \mathcal{O}(M^2L + M^3)$

In Table 3.2, we show the overall time complexity required by a model/method to perform an inference on a testing data sample. For the DL-based models, the Big-O notation written in the table refer to the model per data sample time complexity, in addition we notated the pre-precess steps time

complexity as "τ", for example, our proposed $\mathrm{AttBF(R)}$ model includes two data pre-processing steps, which are the SCM calculation time denoted as $\tau^{\mathrm{cal}}_{\mathrm{SCM}} = \mathcal{O}(M^2L)$ as in (3.17), and then its tokenization -a constant-time operation to separate the real/imaginary parts of SCM- step detonated as $\tau^{\mathrm{Tok}}_{\mathrm{SCM}} = \mathcal{O}(M^2)$ as in (3.23), finally, the proposed model per data sample inference complexity would be same as the training one, hence, it is equal to $\mathcal{O}(M^2)$.

The rest of the DL-based model pre-precess time complexity notations are as follows: 1) The snapshots matrix $\mathbf{Y_{ss}}$ tokenization $\tau^{\mathrm{tok}}_{\mathrm{Y}} = \mathcal{O}(L^2)$, 2) The standard FFT operation on $\mathbf{Y_{ss}}$ takes $\tau^{\mathrm{FFT}}_{\mathrm{Y}} = \mathcal{O}(ML\log L)$ and its tokenization $\tau^{\mathrm{tok}}_{\mathrm{FFT(Y)}} = \tau^{\mathrm{tok}}_{\mathrm{Y}}$, 3) The full CSI channel $\mathbf{H}$ estimation $\tau^{\mathrm{est}}_{\mathrm{fullCSI}}$ depends on the estimation algorithm used, for example a pilot based method will not be possible for the unknown $\mathcal{K}$ interference channels, overall $\tau^{\mathrm{est}}_{\mathrm{fullCSI}}$ would be significant without mentioning the additional complexity of knowing the number of $\mathcal{K}$ interference sources. Separating Real/Imaginary parts of full CSI channel $\mathbf{H}$ will equal to $\tau^{\mathrm{Re/Im}}_{\mathrm{fullCSI}} = \mathcal{O}(M(\mathcal{K}+1)$, 4) Separating Real/Imaginary parts of SMC is $\tau^{\mathrm{Re/Im}}_{\mathrm{fullCSI}} = \tau^{\mathrm{Tok}}_{\mathrm{SCM}}$.

Similarly, for the traditional methods, the Big-O notation listed in the table refers to the computational time complexity of the benchmark beamforming method per data sample as in (3.19), (3.20), and (3.21). In addition, we noted the time complexity of the pre-calculating/estimation steps as τ. The ZFBF method requires full CSI estimation $\tau^{\mathrm{est}}_{\mathrm{fullCSI}}$, while MRC only requires the desired CSI channel estimation, but also depends on the estimation algorithm (e.g., for least-square (LS) estimation with L pilot signals it will equal to $\mathcal{O}(ML)$). The SMI method involves an SMC calculation $\tau^{\mathrm{cal}}_{\mathrm{SCM}}$ and desired satellite DOA estimation $\tau^{\mathrm{est}}_{\mathrm{desDOA}}$ (e.g., using MUSIC algorithm) for calculating $\mathbf{v}_d$. Note that UT arrays shall be simple for NGSO applications (e.g., Direct to device (D2D)), reducing the overall complexity.

3.4 Simulation Results

In this section, we present the simulation setup, including details on data generation, the model training phase, and validation and comparison of our proposed model with the traditional techniques and different DL-based models.

3.4.1 Data and Simulation

We run a satellite simulation scenario with one desired NGSO satellite and multiple interfering NGSO satellites using MATLAB satellite toolbox [102]. We adopt a realistic approach to representing satellite

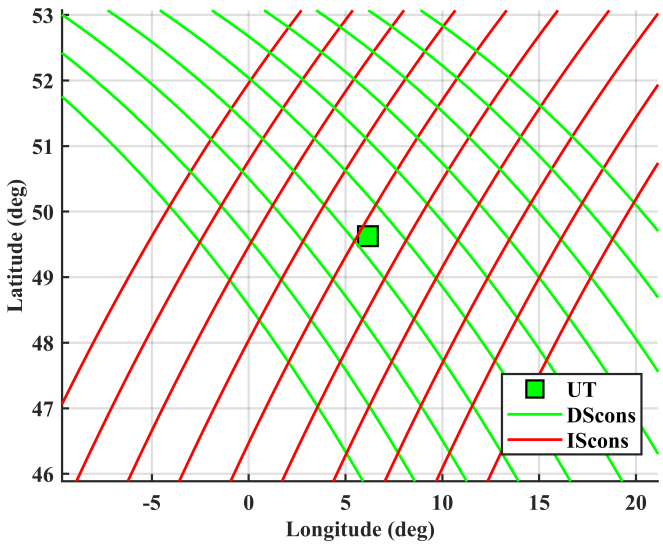


Figure 3.7: Proposed NGSO systems constellations

motion by assigning each satellite to a defined plane orbit through the six Kepler orbit elements: the semi-major axis, eccentricity, inclination, right ascension of the ascending node (RAAN), argument of perigee, and true anomaly. MATLAB built-in functions provide estimates of latitude, longitude, and altitude over time according to the satellite trajectory. Using this setup, we consider the physical environment (distances, angles, satellites' orbit propagation, etc.) and the operational conditions (frequency, bandwidth). With the correct adjustments of these simulation elements, we can alter SINR values. We can summarize this work simulation and the datasets generation phase in a few steps,

1. Using MATLAB built-in functions within the Satellite Communication Toolbox, we simulate two co-existing NGSOs constellations and a fixed UT location, as shown in Fig. 3.7, using parameters in Table 3.3 and Table 3.4. We then initiate two simulations $\mathcal{T}_{\text{Tr}}$ and $\mathcal{T}_{\text{Ts}}$ for training and testing datasets generation. Each simulation starts with one DS satellite from a fixed satellite plane in the DScons and one IS satellite ($\mathcal{K}$ = 1) that can be randomly selected from the IScons.

2. The DS satellite pass duration, where the DS is visible to the UT, is defined by the UT minimum elevation angle $\theta_{\text{min}} = 15°$, and in our simulation it equals $T_{\text{pass}} = 300$ seconds. We consider $T_{\text{samp}} = 1\ seconds, which leads$ to 300 coherent channels (samples/pass). The UT assumes knowledge of DOAs of the desired signal and thus apply an initial beamformer $\mathbf{w}_{\text{in}} = \mathbf{w}_{\text{MRC}}$ [1].

[1] In LoS scenarios, and when pCSI exist this yield to $\mathbf{w}_{\text{MRC}} = \frac{\mathbf{h}_d}{\|\mathbf{h}_d\|} \approx \mathbf{v}_d = \mathbf{w}_{\text{in}}$ and $\gamma_{\text{out}}(\mathbf{w}_{\text{MRC}}) \approx \gamma_{\text{in}}$ where γ_{in} is the measured SINR using the initial beamformer $\mathbf{w}_{\text{in}}$.

3. During each coherence time T_{samp}, we calculate the link budget for both DS and IS satellite links as in equations (3.1)-(3.8), using link budget parameters in Table 3.5, we also save the first $L = T_{ss}$ snapshots (3.9) and save the $\mathbf{Y}_{ss}$, γ_{out}, and $\mathbf{H}$, matrices in $\mathcal{D}_{\text{Tr}}$ tensor for training dataset generating phase, or $\mathcal{D}_{\text{Ts}}$ tensor for testing dataset generating phase. For the sake of evaluation, we apply a minimum interference-to-noise ratio (INR) threshold of -12 [dB], to only consider interference where the quality of service (QoS) of the desired link is affected [118].

4. The simulation is precisely configured to stop when reaching $\mathcal{N}_{\text{Tr}} = 9000$ training data samples (30 desired satellite passes) and $\mathcal{N}_{\text{Ts}} = 900$ testing data samples (3 desired satellite passes).

5. The lowest number of snapshots possible is what will make the SCM ($\hat{\mathbf{R}}$) a full rank, which requires at least $L = M$ independent data samples (snapshots) [133], in many research articles it is recommended to use at least $L = 2M$ snapshots when estimating the covariance matrix for better beamforming results [134]. We repeated the above data generation steps and generated three sets of data for when $L = M, 2M$, and $4M$.

The full datasets in this article are available with more details on the SmartSpace project web page [84]. That said, it will strengthen the proposed AttBF-based model, and possibly other AI-based solutions, if real-world datasets are made available by satellite operators. Authors are committed to disseminate the importance of this issue with relevant industrial partners.

Table 3.3: Constellations parameters

Parameters	DScons	IScons
Constellation Altitude (h^{cons})	550 [Km]	950 [Km]
Eccentricity	0.01	0.04
Inclination	55°	120°
RAAN	135°	35°
Argument of Perigee	20°	35°
True anomaly	82°	75°
Δh^{cons}	±50 [Km]	±50 [Km]
ΔRAAN	±12°	±12°

Fig. 3.8 shows the SINR measured on the UT side for a DS pass T_{pass} assuming that a fixed $\mathbf{w}_{\text{MRC}}$ is applied at the UT planar array for the entire pass of the satellite (non-adaptive beamforming). We can observe several SINR drops due to interference, particularly in the first half of the satellite pass.

Table 3.4: UT Parameters

Parameter	Value	**Parameter**	Value
Latitude	49.6257°	# Elements (M)	$8 \times 8 = 64$
Longitude	6.1598°	Noise Bandwidth	50 MHz
Altitude (h^{ut})	100 [m]	Temperature (T^{ut})	94°K
Min elevation (θ_{min})	15°	Efficiency (η^{ut})	0.99

Table 3.5: Satellite Link Budget Parameters

Parameters	DS Satellite	IS Satellite
Signal bandwidth (BW)	50 MHz	55MHz
Operational frequency (f_c)	11.75 GHz	11.75 GHz
Satellite EIRP (P^{sat})	34 dBW	45 dBW

3.4.2 Training Phase Results

The TensorFlow and Keras frameworks are used to build all DL models in Python. All models are compiled with $\mathcal{L}$ in (3.35) as the primary loss function, and Nesterov implemented Adam as the optimizer Ω. The model parameters were updated using the $\mathcal{N}_{\text{Tr}}$ training samples in the training dataset $\mathcal{D}_{\text{Tr}}$. The results were validated using the N_{Ts} testing samples in the testing dataset $\mathcal{D}_{\text{Ts}}$. All three AttBF models have $A = 2$ Attention heads, $D_{key} = D_{hid} = 64$, and $\mathrm{Dropout}$ layers (with rate 0.2) are applied to avoid training overfitting. The experiments in the following parts were carried out using an 8-core `AMD Ryzen 7 7700X CPU` unit with 12 GB RAM. During the training phase, as in Algorithm 3, we assume $E = 200$ epochs for all models, a training batch size $\mathcal{B} = 300$ includes all data samples per DS pass T_{pass}, leading to $B = 30$ training batches.

Fig. 3.9 plots the epochs versus the average SINR per epoch, that is, the negative loss/epochs ($-\mathbf{L}_{\text{epochs}}$) for each model on the $L = 2M$ datasets, demonstrating how beamforming performance quality improves (or stabilizes) as training progresses. Our $\mathrm{AttBF(R)}$ model, labeled as *Proposed*, achieves high convergence stability in early epochs and maintains a lead value throughout the rest of the epochs, indicating faster convergence and superior performance.

In Table 3.6, we compare the beamforming DL-based beamforming models in terms of their input, trainable parameters in their architectures, and training time efficiency.

- **Number of parameters**: The total trainable parameters (in thousands [$\times 10^3$]) is an indicator of the size of the model. The spatial sharing of weights in $\mathrm{Conv1D}$ and $\mathrm{Attention}$ drastically

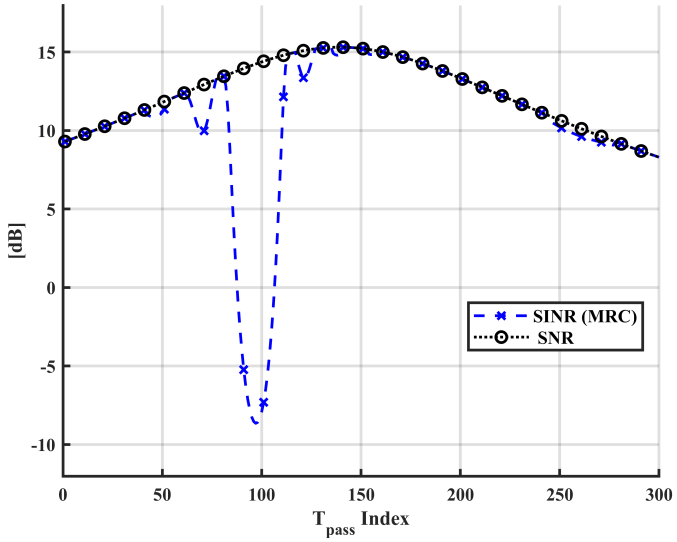


Figure 3.8: A representation link status from the $L = 2M$ test data of a desired satellite pass with nearby interference satellites as received by UT during T_{Pass}

Table 3.6: Comparison of models training (# $L = M \mid 2M \mid 4M$)

Model	**# Parameters** [$\times 10^3$]	**Train Time [min]**
AttBF(Y)	**184** | 315 | 577	**1.64** | 3.69 | 6.44
AttBF(FFT)	**184** | 315 | 577	1.81 | 3.42 | 6.95
Proposed	**184** | **184** | **184**	3.26 | 3.24 | 3.25
NNBF(H) [125]	203 | 203 | 203	1.75 | **1.77** | **1.74**
CNNBF(R) [126]	511 | 511 | 511	1.77 | **1.73** | **1.75**

reduces the number of parameters compared to Dense layers used in CNNBF(R). Furthermore, NNBF(H) input size is changing with the increment of $\mathcal{K}$, which may require a different architecture for each size of $\mathcal{K}$. With an increasing number of snapshots L, the proposed AttBF(R) model always has a fixed input token sequence M, compared to changing L tokens in AttBF(Y) and AttBF(FFT) models, making it the smallest model in terms of trainable parameters.

- **Train Time**: Our AttBF-based models fall behind conventional CNN models in terms of training time. However, the input size and the type of trainable layers used in each model may suggest that more time may be required for training. Moreover, overhead from operations like softmax, LayerNorm, or Dropout in all AttBF-based models may result in slower training[2], compared to CNNBF(R) and NNBF(H) models. Despite this, the training time is not very

[2]Backprop is typically implemented using matrix operations, which influence computational and memory requirements for each model.

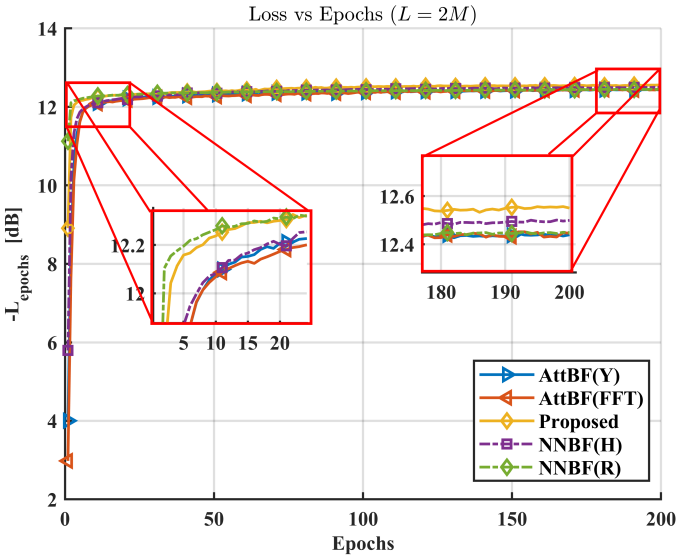


Figure 3.9: Loss vs Training Epoch ($L = 2M$ test data)

relevant for offline training as it usually depends on the model architecture, training environment, and hardware (e.g., CPU, GPU, accelerators) [96].

3.4.3 Beamforming Performance Results

During the testing phase (inference), a test batch size $\mathcal{B} = 1$ includes all data samples per DS T_{pass} pass, leading to $B = 900$ testing batches. In Fig. 3.10, we show histograms of the output SINR distribution per beamforming method (DL-based models and traditional methods) for the 900 instances in the testing dataset $\mathcal{D}_{\text{Ts}}$, the signal-to-noise (SNR) results are not realizable in real-time and serve as an upper bound for reference only (assuming no interference is present all the time). In each sub-figure, the X-axis (γ_{out} [dB]) represents the output SINR in decibels, a higher range of values, compared to the SNR plot, indicates a stronger desired satellite signal and better null performance in case of interference occurrence, as it means that the desired signal is relatively larger to the combined power of interference and noise. The Y-Axis (Count) shows the number of times a particular SINR value occurred across the entire test dataset. The height of the bars in each histogram indicates the frequency of the corresponding SINR range. Finally, the histograms are stacked and color-coded (i.e., "red" ($L = M$), "yellow" ($L = 2M$), and "cyan" $L = 4M$); other colors within the bars show the contribution of each condition stacked on top of each other. Here, the "Proposed" method's histogram, it can be seen that the majority of the instances are stacked on top of each other (the light green portion), indicating that this method performed similarly well under all L amounts, same as

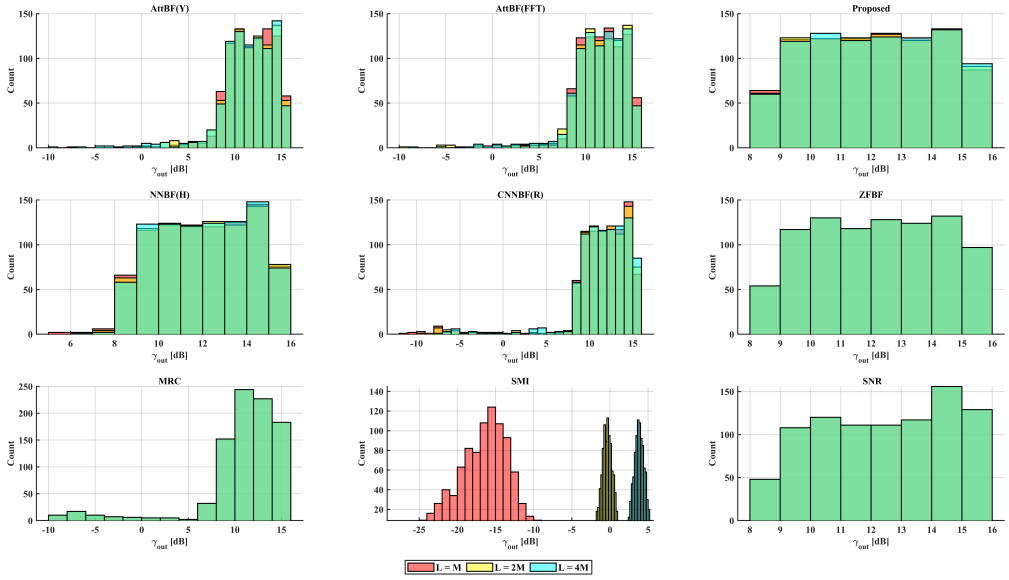


Figure 3.10: SINR distribution per beamforming method (when $L = M \mid 2M \mid 4M$)

ZFBF, compared to other model/methods which have some wider and some negative γ_{out} values. In Table 3.7 we summarize the key insights of Fig. 3.10 results, along with the pure inference time:

Table 3.7: Comparison of models/methods beamforming performance (# $L = M \mid 2M \mid 4M$)

Model/Method	**Pure Inference Time** [μs]	γ_{out} [dB]		
		Min	**Max**	**Mean**
AttBF(Y)	6.21 | 6.95 | 7.38	-7.04 | -6.46 | -9.23	15.26 | 15.25 | 15.25	11.69 | 11.60 | 11.44
AttBF(FFT)	6.74 | 6.99 | 7.73	-0.75 | -9.49 | -8.14	15.25 | 15.24 | 15.26	11.68 | 11.55 | 11.52
Proposed	**4.36** | 4.70 | **4.57**	**8.00** | **8.03** | **8.06**	**15.29** | **15.30** | **15.30**	**12.09** | **12.11** | **12.13**
NNBF(H) [125]	6.54 | 6.53 | 6.56	5.07 | 7.25 | 6.72	**15.29** | 15.28 | 15.29	12.05 | 12.08 | 12.07
CNNBF(R) [126]	4.67 | **4.50** | 4.71	-11.48 | -9.01 | -7.27	15.27 | 15.28 | 15.28	11.40 | 11.47 | 11.62
ZFBF (optimalBF)	2.14 | 2.80 | 2.77	**8.10** | **8.10** | **8.10**	**15.31** | **15.31** | **15.31**	**12.18** | **12.18** | **12.18**
MRC	**1.31** | **1.16** | **1.08**	-8.65 | -8.65 | -8.65	15.31 | 15.31 | 15.31	10.80 | 10.80 | 10.80
SMI	133.02 | 132.65 | 134.33	-30.65 | -2.53 | 1.88	-9.64 | 1.53 | 5.96	-16.40 | -0.37 | 3.83
SNR	- | - | -	8.30 | 8.30 | 8.30	15.31 | 15.31 | 15.31	12.42 | 12.42 | 12.42

- **Pure Inference Time :** Inference time is particularly crucial for fast adaptive beamforming in high-mobility NGSOs, where real-time processing is essential. The pure interface time here is observed without considering the pre-processing duration per model (i.e., for the proposed AttBF(R) model, we assume SCM is calculated and tokenized), and only observes the per-sample model processing time and the calculation time for the traditional methods (e.g., for the ZFBF method we assume full CSI is already estimated). The proposed AttBF(R) model offers the fastest inference time "average on all test data" among learning-based methods ($\sim 4.5\ \mu s$), CNNBF(R) has similar time performance ($\sim 4.6\ \mu s$). Other DL-based models have slightly

slower inference ($\sim 6-7\ \mu s$). Regarding classical methods, MRC offer the fastest inference ($\sim 1.2\ \mu s$) but without interference nulling ability, ZFBF comes slightly after ($\sim 2.5\ \mu s$). Still, the SMI method is the slowest among all metrics ($\sim 133\ \mu s$), making it not preferable for real-time deployments.

- **Min/Max SINR Stability :** The Min/Max values show the minimum and maximum γ_{out} in the results distribution achieved from each test dataset. The proposed model shows stable values for minima ($sim8$ [dB]) and maximum (~ 15.30 [dB]), similar to the optimal beamformer ZFBF method. NNBF(H) model shows competitive results. In contrast, other DL models and traditional methods fall behind, especially on minimum SINR, indicating limitations on interference nulling performance in high INR scenarios (i.e., In-Line scenarios).

- **Mean SINR Performance :** The Mean value calculated from the distribution of the results indicates the average γ_{out} achieved from each test dataset. The proposed model demonstrates the highest mean SINR "γ_{out}" in the test data, which is almost aligned with the optimal ZFBF results. NNBF(H) with full CSI inputs (both desired and interference channels) has slightly lower average γ_{out} values compared to the proposed model. All other DL-based models show moderate average γ_{out} values due to wider distribution spread, implying less stable beamforming performance. The classic MRC method falls short under interference conditions; it only indicates the initial average γ_{out}, which is improved by all other methods except SMI, with worse performance due to an insufficient number of snapshots.

- **Impact of Snapshots:** As explained in the data generation steps Section 3.4.1, we have three main datasets, each with a different snapshot amount ($L = M, 2M, 4M$). The amount of snapshots has no noticeable effects on inference time, except for the AttBF(Y) and AttBF(FFT) models, where it increases with more snapshots, probably because of the model architecture changes. The proposed model and the CNNBF(R) model show some performance improvement in Min/Max/Mean results with more snapshots. The SMI shows noticeable improvements with more snapshots (see Remark. 1).

Robustness to high Correlation

It is well-known that the presence of high spatial correlation between desired and interference signals (similar DOAs) makes it harder to separate them, even with accurate channel information. The *mutual coherence* measures how "similar" or "aligned" the normalized steering vectors of two signals are.

For a desired steering vector $\mathbf{v}_d$ and $\mathcal{K}$ interfering vectors, mutual coherence measures the highest correlation as [136],

$$\rho_{\max} = \max_{1 \leq k \leq \mathcal{K}} \left| \mathbf{v}_d^H \mathbf{v}_{i,k} \right| . \tag{3.36}$$

When $\rho_{\max} = 0$, it means they are perfectly orthogonal (and thus completely uncorrelated). At the same time, a small value $\rho_{\max} \to 0$ shows that they are nearly orthogonal, meaning that they can generally distinguish between the corresponding signals. When $\rho_{\max} \to 1$, the channel matrix $\mathbf{H}$ becomes *poorly conditioned*, posing challenges to methods that involve matrix inversion. A good beamformer should be able to null interfering DOAs while reserving power toward desired DOAs under correlation conditions up to $\rho_{\max} \approx 0.9$ [136].

In Fig. 3.11 and Fig .3.12, we present a comparative evaluation of beamforming methods, we show a single DS satellite pass duration T_{pass} from the testing data set $\mathcal{D}_{\text{Ts}}$, containing only 300 testing samples, as shown in the left-upper part of this two figures, this highlights all methods SINR performance per data sample (except AttBF(Y), AttBF(FFT), as proposed AttBF(R) model shows better results than these Attention-based models already, and also to save space). Here, perfect CSI is assumed for the benchmark models/methods.

In each figure, we zoomed in on a specific part of that pass, representing an interfering case, and indicated it with a red box. For each zoomed-in part, we plot six sub-figures representing each model/method beam patterns visualization as seen from the UT side for a specific data sample n (assuming that method/model was applied to the UT at that particular sample), in these beam patterns, x-axis: azimuth angle ϕ°, y-axis: elevation θ°, and z-axis: directivity Ξ^{ut}, the DS satellite is highlighted with a black circle ($\circ$), while the IS satellite is indicated by black crosses ($\times$). The observations of the two cases are as follows,

- **Case 1 - High Mutual Coherence between desired and interference**

  Looking at the UT array beam pattern obtained from MRC, we can see that the interferer satellite power is captured in the *main-lobe*, thus suffering a severe interference impact (i.e., extremely low SINR level). The DOAs of the DS satellite are $\varphi_d = \left[-27.92^\circ; 19.97^\circ\right]$ and the DOAs of the IS satellite are $\varphi_i = \left[-20.94^\circ; 15.53^\circ\right]$, leading to very high mutual coherence of $\rho_{\max} = 0.67$. Here, the proposed AttBF(R) model creates a well-formed beam pattern and gives the highest γ_{out} compared to other DL-based methods despite the high spatial correlation. NNBF(H) with full CSI input follows behind, and CNNBF(R) seem to have weak nulling capabilities for high $\rho_{\max}$ values. ZFBF has the optimal interference nulling with pCSI, and

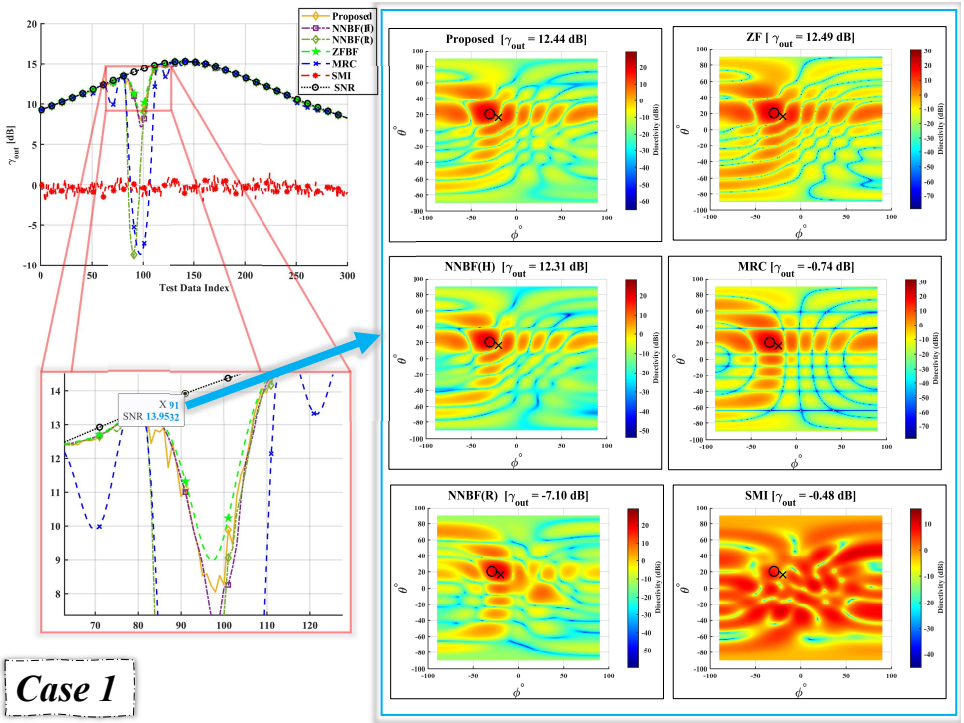


Figure 3.11: Case1: a main-lobe correlation ($\rho_{\max} = 0.67$)

SMI has the worst performance among all methods, as expected, because with low snapshots, it only reduces power "null" in the DOAs of the IS satellite direction without focusing the power towards the DOAs of the DS satellite.

- **Case 2 - Low Mutual Coherence between desired and interference**

  Noting that both satellites are moving, and we can see with the MRC beamformer, the interferer satellite power is now moved to the *side-lobe*, thus the system suffered a lower interference compared to Case 1. In this instant, the DOAs of the DS satellite are $\varphi_d = \left[-9.56°; 12.38°\right]$ and the DOAs of the IS satellite are $\varphi_i = \left[-31.17°; 7.78°\right]$, which leads to a low mutual coherence of $\rho_{\max} = 0.19$. Here, the proposed AttBF(R) model still provides a well-formed beam pattern, focusing the power toward the DOAs of the DS satellite and reducing the power "null" in the DOAs of the IS satellite direction, which achieves the highest γ_{out} compared to other DL-based methods. NNBF(H) and CNNBF(R) models show competitive SINR and nulling performance with the proposed model in side-lobe instances. ZFBF always has the optimal interference nulling with pCSI, and SMI continues to give the worst performance among all methods.

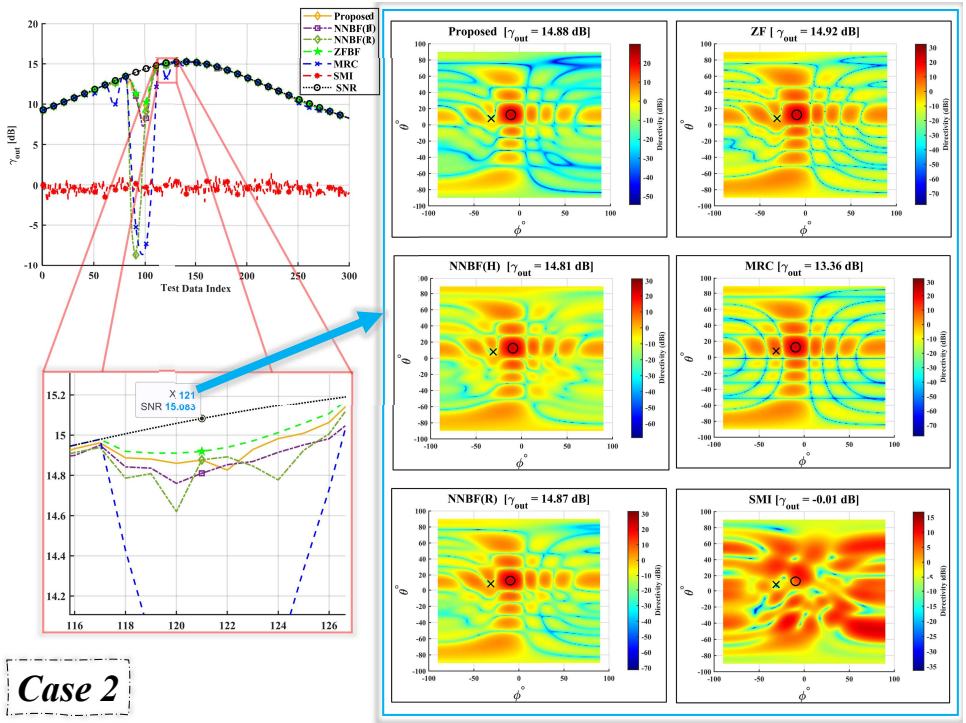


Figure 3.12: Case2 : a side-lobe correlation ($\rho_{\max} = 0.19$).

Robustness to imCSI

To analyze our model in contrast to CSI-dependent methods, we chosen an interference case in the satellite pass (i.e., a main-lobe instant ($\rho_{\max} = 0.78$)), then show how the γ_{out} value varies with increasing variance of imCSI estimation error (σ_e^2), observed from 500 MontyCarlo realizations, as in Fig. 3.13. The proposed model $\mathrm{AttBF(R)}$ is clearly the most robust and effective, maintaining a high SINR without the need for CSI estimation quality. $\mathrm{CNNBF(R)}$ and SMI offer very low but consistent performance, due to their input of the SCM and their lack of reliance on any CSI information. $\mathrm{NNBF(H)}$ performs well at small estimate error, but its performance degrades with higher error levels. ZFBF and MRC are not reliable under imperfect practical CSI conditions, as γ_{out} performance gradually degrades with increasing error.

Avoiding CSI estimation and its errors, especially when unknown spatial interference is present, is desirable in NGSO systems, where fast mobility and Doppler effects make CSI acquisition costly and/or inaccurate. This makesDL modes, such as our proposed $\mathrm{AttBF(R)}$ model, promising for co-existing NGSO system users. In conclusion, Table 3.8 provides a comprehensive summary and the expected trade-off for each beamforming approach discussed in this work.

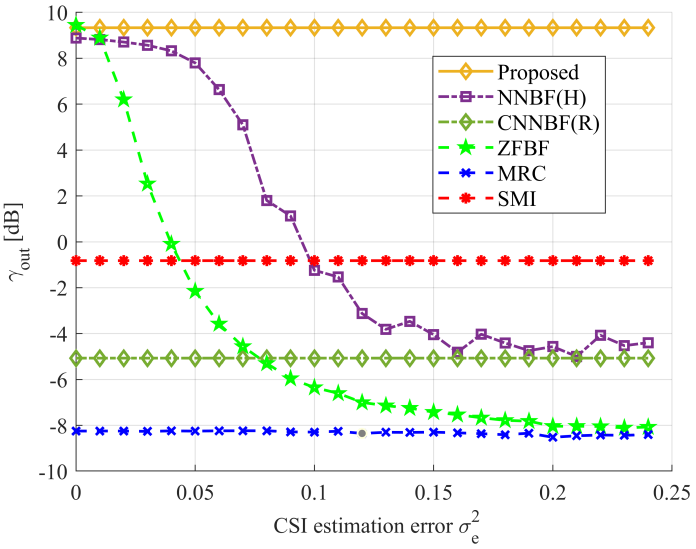


Figure 3.13: SINR vs CSI estimation error ($\rho_{\max} = 0.78$)

Table 3.8: Summary Comparison of Beamforming Methods for NGSOs Interference Mitigation

Method	**Advantages**	**Trade-offs**
Proposed	• No CSI knowledge required, • High SINR maximization performance, • Fast inference ($\sim 4.5\mu s$).	• Needs SCM $\hat{\mathbf{R}}$ calculation.
AttBF(Y)	• No CSI knowledge required, • Generate a beamformer from time-domin signals inputs.	• Moderate SINR maximization performance.
AttBF(FFT)	• No CSI knowledge required, • Generate a beamformer from frequency-domain inputs.	• Moderate SINR maximization performance. • Requires FFT transformation.
NNBF(H) [125]	• High SINR performance with pCSI.	• Requires full CSI knowledge, • Performance degrades with imCSI errors.
CNNBF(R) [126]	• No CSI estimation required, • Fast inference ($\sim 4.5\ \mu s$).	• Moderate SINR maximization performance, • Largest model in terms of trainable parameters, • Needs SCM calculation.
ZFBF	• High SINR maximization performance with pCSI.	• Requires full CSI knowledge, • Performance degrades with imCSI estimation error, • Complex (contain matrix inversion operations).
MRC	• Lowst latency ($\sim 1.1\ \mu s$ inference), • Low complexity.	• Requires desired channel CSI knowledge, • Performance degrades with imCSI errors, • Not suitable for interference nulling tasks.
SMI	• No CSI knowledge required.	• Sensitive to the low accuracy of the estimated $\hat{\mathbf{R}}$, • Requires lots of snapshots ($L \leftarrow T_{\text{samp}}$) to perform optimally, • Highest latency ($\sim 133\ \mu s$), • Needs SCM $\hat{\mathbf{R}}$ calculation.

3.5 Chapter Conclusion

In this work, we have presented the model $\mathrm{AttBF(R)}$, a self-supervised DL beamforming method that learns a nonlinear mapping from the SCM to the complex beamforming weights. The goal is for this mapping to implicitly learn to identify the spatial characteristics of the desired signal and the interfering signals from the SCMs. By learning to produce appropriate complex weights, the beamformer can steer the main lobe towards the desired user and create nulls in the direction of the interference sources, thus mitigating CFI interference in the NGSOs co-existing environment with latency. The proposed $\mathrm{AttBF(R)}$ model appears to be a promising beamforming technique that balances fast interference null performance, CSI-free requirements, and DL models' computational efficiency, achieving the highest SINR among other DL-based techniques, while traditional methods such as SMI that use the same input as the $\mathrm{AttBF(R)}$ model had the worst performance among all methods due to their sensitivity to the SCM estimation accuracy. Future works may investigate UT mobility scenarios, complex channel model (with NLOS, Doppler effect, etc.), various interfering sources (terrestrial, jamming CFI signals), and real hardware scenarios, which are critical topics for integrating SatComs with the 6G communication systems. In this context,there is a need for collaborations with satellite operators to provide real measurements and generalized datasets, which currently limits the real-world validations for our method (and similar AI-based techniques). It's important to making such data publicly available in future work to accelerate research in this domain.

Chapter 4

Federated Learning–Enabled Beamforming for NGSO Direct-to-Vehicle Systems

Non-geostationary satellite orbit (NGSO) systems are expected to play a central role in enabling direct satellite-to-vehicle (DS2V) connectivity. However, dense spectrum reuse and the coexistence of multiple NGSO constellations introduce severe co-frequency interference (CFI). In this chapter, we propose a federated learning (FL)–enabled collaborative receive beamforming framework (FedSatBF) for DS2Vs. In FedSatBF, a serving satellite aggregates locally trained beamforming models at a subset of vehicular user terminals (VUTs) using federated averaging, and broadcasts a global model that can be directly applied by both participating and non-participating VUTs experiencing similar CFI conditions. An attention-based beamforming architecture is adopted as the base model to train local models at each VUT, using estimation-free sample covariance matrices as input data, thereby eliminating the need for explicit estimation of the interference channel or direction of arrival. We investigate the impact of key FL hyperparameters, including per-coherent block communication rounds, per-round training data, per-VUT local epochs, VUT participation, and geographical VUT clustering, on convergence speed, interference nulling capability, and computational efficiency. Simulation results demonstrate that FedSatBF achieves near-optimal signal-to-interference-plus-noise ratio (SINR) performance, within 0.1 [dB] of an optimal zero-forcing beamformer (ZFBF), and significantly outperforms conventional maximum-ratio combining (MRC), all while using only a moderate FL hyperparameter settings. Moreover, the global model exhibits strong generalization to non-participating VUTs and remains effective under reduced settings.

4.1 Introduction

4.1.1 Context and Motivation

Non-geostationary satellite orbit (NGSO) systems in low-Earth orbits (LEO) hold great promise for meeting the demanding requirements of Fifth Generation (5G)/Sixth Generation (6G) systems through non-terrestrial networks (NTN) due to their low latency compared to other satellite orbits [11]. Given congestion in lower S- and C-band allocations, NGSO systems are increasingly transitioning to higher-frequency bands, such as Ku-, K-, and Ka-band, to meet escalating broadband capacity demands. This shift necessitates sophisticated coexistence and coordination strategies to ensure efficient sharing of limited spectrum resources [3, 137]. Modern NGSO networks are characterized by the simultaneous operation of multiple large-scale constellations, each consisting of hundreds or thousands of fast-moving satellites. The resulting spatial and temporal overlap of satellite beams leads to a high probability of co-frequency interference (CFI), even when coordination mechanisms and regulatory constraints are in place [29, 66]. As NGSO constellations continue to increase, CFI becomes a fundamental system-level impairment rather than a rare edge case.

Vehicular users represent a particularly attractive and growing market for NGSO systems. Vehicles frequently traverse rural regions, national borders, and areas with limited or inconsistent terrestrial coverage, where satellite connectivity can provide service continuity. These factors have driven increasing interest in direct satellite-to-vehicle (DS2V) communications as a key extension of future 5G/6G networks [18]. Emerging automotive vehicle applications such as *real-time road monitoring*, *collision avoidance*, *autonomous driving assistance*, and *high-definition map updates*, impose stringent requirements on global continuity and seamless TN/NTNs switching with high reliability and low latency, which align well with LEO-based satellite architectures [138]. The CFI presents a critical concern for DS2V systems, as it may increase traffic accidents, congestion, and quality of service (QoS) degradations [18, 138]. Consequently, advanced CFI interference management techniques are becoming critical to the design and improvement of the overall DS2V ecosystems.

Unlike handheld user equipment, vehicular platforms offer sufficient physical space and power resources to support multi-antenna transceivers and allow the practical integration of planar phased-arrays on vehicle rooftops [139, 140]. This enables spatial signal processing techniques that are infeasible for conventional omnidirectional antennas, such as the electronic beam steering technique (i.e., without the need for any tilting mechanical parts) known as beamforming [16]. In particular, adaptive beamforming (ABF) enables real-time steering of the vehicle receive beams toward time-

varying NGSO satellite links, while effectively suppressing the CFI effect [123, 141].

Conventional adaptive beamforming techniques rely heavily on explicit interference channel structure and signal statistics [113]. In fast-varying NGSO environments, short channel coherence times, and unknown interferers severely limit the availability of reliable channel state information (CSI) and sufficient signal snapshots, leading to degraded performance and slow adaptation [142]. In contrast, deep learning (DL)–based beamforming approaches can implicitly learn robust mappings from available observation data, such as raw received signals or sample covariance matrices (SCMs), to beamforming weights, without requiring explicit estimation of interference channels, directions of arrival, or analytical interference models [44]. As a result, DL-based methods exhibit improved adaptability to nonstationary propagation conditions, unknown or time-varying interference sources, and modeling uncertainties inherent to dense NGSO constellations [118]. However, such techniques are based on centralized DL (CDL), in which the main DL model on the centralized server is trained on user-collected training data. This process requires transmitting each user's data to the server. Therefore, the data collection and transmission introduce significant overhead. Moreover, training a generalized DL-based beamforming model for multiple users using offline training or CDL requires extensive dataset collection that includes all possible CFI-interfering scenarios. This will raise concerns about data security, misuse, and privacy, especially under strict regulations such as the European General Data Protection Regulation (GDPR). Because collecting raw data from vehicle users is neither secure nor compliant with these regulations, a centralized training framework is impractical [143]. Furthermore, this is well-suited for multiple distributed vehicles with the same tasks to be trained collaboratively using distributed learning paradigms [9].

Federated learning (FL) is a distributed learning paradigm introduced by Google that enables edge devices to exchange their locally trained model parameters with a central server that aggregates a global model. In contrast, the devices never share their locally trained data [144]. This significantly reduces the amount of data exchanged over the network, improving communication efficiency. The size of model updates is often much smaller than the raw data, which is particularly advantageous for reducing network traffic and latency [145]. Furthermore, FL enhances privacy by keeping sensitive data on local vehicles, minimizing the risk of data theft or breaches during transmission [146]. To the best of the authors' knowledge, the collaborative beamforming for NGSO's users remains unexplored, and this is primarily due to several main fundamental challenges, such as:

- **Energy constraints**: the individual user terminals (UTs) are often compact devices with limited battery life and transmission power (e.g., consumer devices). Locally training and then sending

local model updates from such users to the NGSO satellite may be expensive and impractical.

- **Channel coherence**: the satellite communication latency and the relatively fast NGSO mobility induce fast channel condition changes, and the local model parameters may become outdated before FL's global convergence completes, and this degrades local performance.

- **Non-IID conditions**: each user obtains a distinct non-IID (non-independent and identically distributed) data and channel statistics arising from the varying satellite-user link geometries, the local beam steering, and service demands. Training DL models locally under these conditions can fit a local mapping from local data. Still, the global model produced by standard FL averaging may yield incompatible gradients and suboptimal global models that perform worse for each user.

Motivated by the discussion above, we consider the use of vehicular user terminals (VUTs) in FL-based collaborative beamforming, as they offer significant advantages over compact devices [143,147]. This shift moves the system towards Vehicular Edge Computing (VEC) integrated with satellite communications. The enhanced capabilities of VUTs have the potential to directly address most FL-based collaborative beamforming challenges by

- **Mitigating Energy Constraints**: drawing power from their engine or a substantial battery system, VUTs can afford to locally train and transmit full model updates more frequently and reliably to the NGSO satellite without draining a small battery.

- **Compensating for Channel coherence**: modern VUTs possess substantial computing capabilities in comparison to unmodified handheld devices (e.g., CPU, GPU, dedicated AI/ML accelerators), which is critical for reducing the local processing time in each FL round. Moreover, VUTs also have the space to accommodate multi-antenna systems (e.g., phased arrays on the roof [139]). This allows for higher antenna gain, compensates for path loss, and enables more reliable high-rate uplink communication, reducing transmission time.

- **Strategies for Non-IID Condition:** The greater capabilities of VUTs enable the personalized FL (pFL), where each user can perform a few fine-tune for the global model based on the available local data when needed. The serving satellite can also cluster its VUTs geographically when few VUTs with pFL capabilities can participate in the learning process, and this enables a generalized global model for other users within the same geographical cluster.

4.1.2 Related Work

Recent studies have extensively explored FL in several applications in satellite communications, including resource allocation [148], Inter-Satellite Links (ISLs) [149], and traffic forecasting [150], among others. Most of these articles considered image classification tasks to evaluate their proposed FL frameworks using IID, and Non-IID labelled image datasets, such as MNIST, CIFAR, and fMoW [45, 46, 151]. The term beamforming has been associated with FL and NGSO satellite systems in several research articles [152–154]. Authors in [152] introduced a synchronized FL technique across multiple LEO satellites to select the appropriate codebook for the distributed precoding technique, thereby improving the achievable rate at a terrestrial user. A ResNet-18 model was integrated on-board to train localized data, and a target-rate-constrained joint beamforming design was formulated. In [155], the authors presented a distributed multi-agent DRL framework for downlink precoding in LEO mega-constellations, in which each satellite serves as an autonomous learning client and periodically exchanges model updates via FL without relying on a centralized server. The task was to jointly optimize communication throughput and navigation accuracy by enabling satellites to learn cooperative precoding vectors from local observations, with a shared global reward signal. Dakkak et al. [154] investigated cell-free Multiple-Input Multiple-Output (CF-MIMO) beamforming in NTNs composed of multiple swarms of NGSO satellites, where each swarm acts as a distributed client performing local digital beamforming while collaboratively contributing to a federated CF-MIMO architecture without relying on a centralized server. The task focuses on mitigating Co-channel Interference (CCI) under full frequency reuse (FFR) by combining CSI-based and position-based beamforming strategies and introducing a limited field-of-view (LFoV) subarray design that enhances onboard antenna directivity and interference suppression. Most papers in the context of FL-based beamforming in NGSO satellite systems have been mainly employed for on-board precoding (satellite-to-users beamforming), where multiple satellites are assumed to collaboratively train local models. Moreover, these papers considered the central server to orchestrate the learning process from outside the constellation, either at a ground station (GS) or on a satellite at a higher orbital altitude. There are only a few articles investigated ground user participation in FL training as edge devices and an onboard LEO satellite server, particularly optimizing uplink energy efficiency of satellite Direct-to-device (SD2D) via selective device participation in FL [156, 157]. Still, the collaborative beamforming from the NGSO users' side (users-to-satellite beamforming) remains unexplored.

4.1.3 Contribution

The main contributions of our work can be summarized as follows:

- We introduce FedSatBF, a novel FL framework that enables collaborative receive ABF beamforming among VUTs served by an NGSO satellite, without sharing raw signal data or requiring explicit interference channel knowledge.
- An attention-based beamforming model (AttBF) is employed to train local models at each VUT using raw sample covariance matrices (SCMs) as inputs, enabling blind ABF and mitigating interference from NGSO space-to-Earth links.
- We analyze how the number of participating users, user clustering, communication rounds, local training intensity, and data availability affect convergence and performance within a single coherence interval.
- We demonstrate that the broadcast global model generalizes effectively to non-participating VUTs experiencing similar CFI interference conditions, as shown in Fig. 4.1, where it achieves near-optimal SINR without personalization or retraining.
- Through simulations with realistic NGSO orbital dynamics, we quantify the trade-off between beamforming performance and computational overhead, showing that near-optimal interference mitigation can be achieved with lightweight FL configurations suitable for real-time operation.

4.1.4 Chapter Organization

The remainder of this chapter is organized as follows. Section 4.2 introduces the NGSO direct-to-vehicle system model, including the channel and signal models. Section 4.3 briefly discusses the traditional ABF techniques utilized in this work. Section 4.4 presents the proposed FedSatBF framework, detailing the federated learning procedure, evaluation protocol, and attention-based beamforming architecture. Section 4.5 describes the simulation setup and provides a comprehensive performance evaluation, including convergence behavior, generalization capability, and sensitivity to key FL hyperparameters under both channel coherence-time and serving satellite visibility-time. Finally, Section 4.6 concludes the work and outlines promising directions for future research.

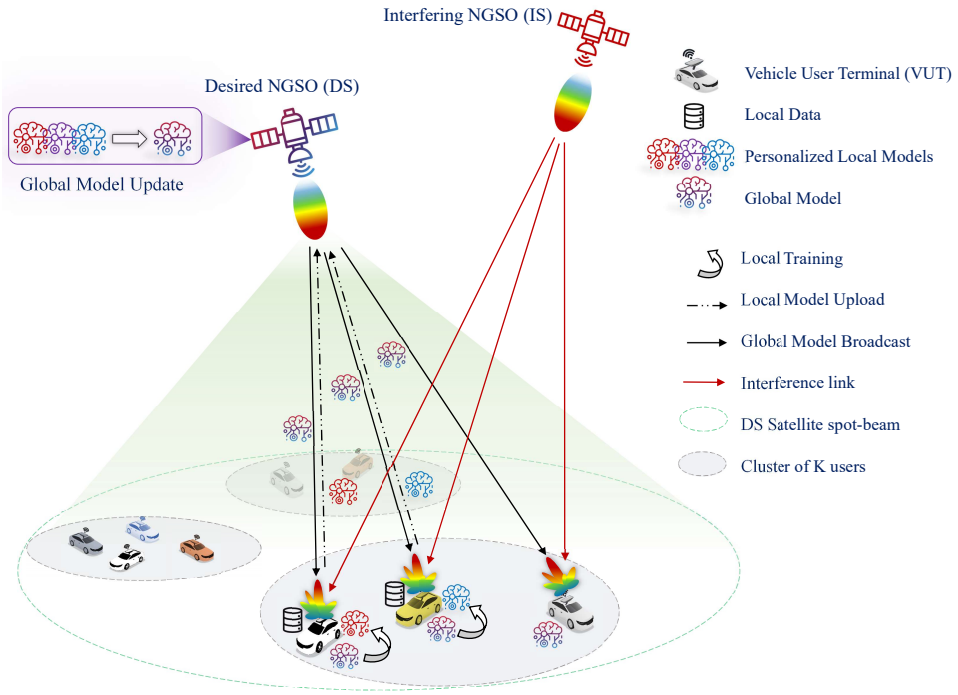


Figure 4.1: Illustration of the proposed FedSatBF Framework.

4.2 System Model

As depicted in Fig. 4.1, we consider an NGSO downlink coexistence scenario, where a desired NGSO system (DS) is transmitting data to a set of VUTs $\mathcal{K} \triangleq \{1, \ldots, k, \ldots, K\}$. Still, they simultaneously experience downlink CFI from a nearby interfering NGSO system (IS). We assume that the VUTs are equipped with a uniform planar array (UPA) for receiving the DS signal, as shown in Fig. 4.2. The uplink channel is assumed to be interference-free and operating on Frequency-Division Duplexing (FDD). Throughout this work, the terms *VUTs* and *users* are used interchangeably. Likewise, the terms *model parameters* and *model gradients* are used interchangeably to refer to the quantities exchanged during FedSatBF learning.

4.2.1 Channel Model

Modern constellations increasingly employ Quasi-Earth fixed beams, in which coverage is steered toward fixed footprints [158], thereby simplifying mobility for VUTs within the coverage area. The half-power beamwidth (HPBW) of a satellite antenna can be used to approximate the radius of a

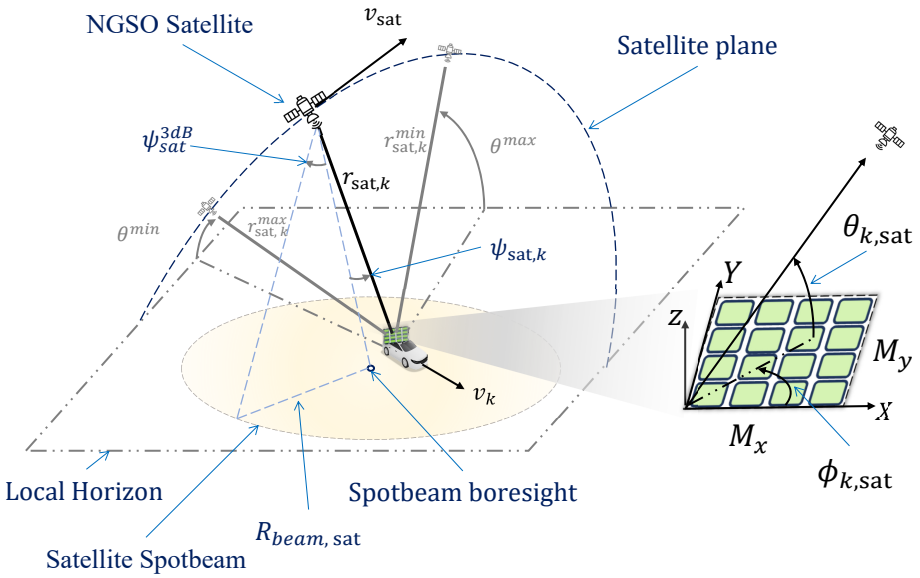


Figure 4.2: An illustration of a Sat-VUTs link geometry.

spotbeam on the Earth's surface $R_{\text{beam, d}}$, as shown in Fig 4.2. Considering the DS satellite,

$$R_{\text{beam, d}} = r_{\text{d, bore}} \tan\left(\frac{\texttt{HPBW}_{\text{d}}}{2}\right) = r_{\text{d, bore}} \tan\left(\psi_{\text{d}}^{\text{3dB}}\right), \tag{4.1}$$

where $\psi_{\text{d}}^{\text{3dB}}$ is the off-axis angle of the DS satellite boresight and the edge of the 3-dB beamwidth, $r_{\text{d, bore}}$ is the DS slant range from its beam boresight.

In this work, we focus on the receiving beamforming at the VUTs side and the link between the satellites and the VUTs. By adopting the UPA, we aim to steer VUT's beam towards the DS direction continuously, place nulls at the IS direction, and achieve a high SINR. Consider the UPA in a VUT lying in the xy-plane with $M_{\text{x}} \times M_{\text{y}}$ antenna elements on the x and y axes, respectively, and the total number of antenna elements (antenna size) $M = M_{\text{x}} M_{\text{y}}$. Therefore, the normalized array response vector at the k^{th} VUT user towards the DS can be written as in (4.2),

$$\begin{aligned}\bar{\mathbf{a}}_k(\phi_{k,\text{d}}, \theta_{k,\text{d}}) = \frac{1}{\sqrt{M}} \Big[1, \cdots, &\texttt{exp}[j\frac{2\pi}{\lambda_{\text{d}}}\rho(m_{\text{x}} \sin\phi_{k,\text{d}} \cos\theta_{k,\text{d}} + m_{\text{y}} \sin\theta_{k,\text{d}})], \cdots, \\ &\texttt{exp}[j\frac{2\pi}{\lambda_d}\rho((M_{\text{x}}-1) \sin\phi_{k,\text{d}} \cos\theta_{k,\text{d}} + (M_{\text{y}}-1) \sin\theta_{k,\text{d}})]\Big]^T \in \mathbb{C}^M,\end{aligned} \tag{4.2}$$

where ρ is the inter-element spacing, and λ_{d} is the carrier wavelength associated with the frequency carrier f_{d}, and the speed of light $c_{\mathrm{l}} = 3 \times 10^8$ [m/s] as $\lambda_{\mathrm{d}} = \frac{c_{\mathrm{l}}}{f_{\mathrm{d}}}$. Moreover, $0 \leq m_{\mathrm{x}} < M_{\mathrm{x}}$ and $0 \leq m_{\mathrm{y}} < M_{\mathrm{y}}$, $\phi_{k,\mathrm{d}} \in [-\pi, \pi]$ and $\theta_{k,\mathrm{d}} \in [\theta^{\min}, \theta^{\max}]$ are the azimuth and elevation angles, respectively, representing the direction of arrivals (DoAs) of the DS signal and driven from a Earth-Centered Earth-Fixed (ECEF) coordinate system where the three-dimensional (3D) position and velocity vectors of the satellite at a certain moment are prior known by the network [159], $\theta^{\min}$ is the minimum elevation angle predefined by 3GPP or VUT operator e.g., (10° [158]), which beyond communication is not possible, and $\theta^{\max} \leq \frac{\pi}{2}$ depends on the k^{th} VUT and DS geometry. Note that the VUT array response vector can be modeled as a plane wave; thus, for convenient expression, we define $\varphi \triangleq (\phi, \theta)$, i.e., at a k^{th} VUT, DOAs for the DS will be denoted as $\varphi_{k,\mathrm{d}} \triangleq (\phi_{k,\mathrm{d}}, \theta_{k,\mathrm{d}})$. Rician fading channel model can be assumed for NGSO communications [76]; however, we assume that the UPA are placed on top of each vehicle in a rural area where no obstacles exist between the VUTs and the satellite, and with negligible foliage reflections. Here, the LoS component becomes dominant; thus, the non-LoS (NLoS) component can be ignored due to UPA directivity. We define the statistical time-varying channel model between the DS and the k^{th} VUT at time instant t and frequency f_{d} as follows,

$$\mathbf{h}_{\mathrm{d},k} = \chi_{\mathrm{d},k} \cdot \bar{\mathbf{a}}_k(\varphi_{k,\mathrm{d}}), \tag{4.3}$$

where $\chi_{\mathrm{d},k}$ is the desired channel gain, given by,

$$\chi_{\mathrm{d},k} = \sqrt{\frac{G_{\mathrm{d}}(\psi_{\mathrm{d},k}) G_k(\varphi_{k,\mathrm{d}})}{L_{\mathrm{d},k}}}, \tag{4.4}$$

where $\psi_{\mathrm{d},k}$ is the off-boresight angle from the DS satellite's bore-sight to the k^{th} VUT, $G_{\mathrm{d}}(\psi_{\mathrm{d},k})$ is the DS transmit gain towards k^{th} VUT directions expressed as $G_{\mathrm{d}}(\psi_{\mathrm{d},k}) = G_{\mathrm{d}}^{\max}\left(\frac{J_1(\alpha_{\mathrm{d},k})}{2\alpha_{\mathrm{d},k}} + 36\frac{J_3(\alpha_{\mathrm{d},k})}{\alpha_{\mathrm{d},k}^3}\right)$, where $G_{\mathrm{d}}^{\max}$ denotes the maximum antenna gain, $J_n(\cdot)$ denotes the nth-order Bessel function and $\alpha_{\mathrm{d},k} = \frac{\pi D_{\mathrm{d}}}{\lambda_{\mathrm{d}}} \sin(\psi_{\mathrm{d},k})$, where D_{d} is the dimeter of the DS antenna [118]. The term $G_k(\varphi_{k,\mathrm{d}})$ is the VUT receives gain towards the DS direction related to the UPA's radiation efficiency η_k and its directivity towards a φ direction $\Xi_k(\varphi_{k,\mathrm{d}})$ as $G_k(\varphi_{k,\mathrm{d}}) = \eta_k \Xi_k(\varphi_{k,\mathrm{d}})$, and the directivity can be calculated from the UPA array factor [132]. Finally, $L_{\mathrm{d},k}$ is the large-scale free-space path loss given by,

$$L_{\mathrm{d},k} = \left(\frac{4\pi r_{\mathrm{d},k}}{\lambda_{\mathrm{d}}}\right)^2, \tag{4.5}$$

where $r_{\mathrm{d},k}$ is the slant range between k^{th} VUT and DS, and it can be derived from the spherical law

of cosines in terms of elevation angle as [159],

$$r_{\mathrm{d},k} = \sqrt{(R_{\mathtt{E}} + A_{\mathtt{DScons}})^2 - (R_{\mathtt{E}} + A_k)^2 \cdot \cos^2(\theta_{k,\mathrm{d}})} - (R_{\mathtt{E}} + A_k) \cdot \sin(\theta_{k,\mathrm{d}}), \tag{4.6}$$

where $R_{\mathrm{E}} = 6371$ [km] indicate the radius of the Earth, A_k is the altitude of the VUT and $A_{\mathtt{DScons}}$ is the altitude of the desired constellation with respect to the Earth's surface, as shown in The expression $(R_{\mathrm{E}} + A_{\mathtt{DScons}})$ is also known as the semi-major axis $\mathtt{SM}_{\mathrm{d}}$.

The equations for the IS interferer link follow the same form as those in equations (4.1)-(4.2) , but with a superscript "d" replaced by "i", e.g., the channel vector of the IS satellite at the k^{th} VUT user is $\mathbf{h}_{\mathrm{i},k} = \chi_{\mathrm{i},k} \cdot \bar{\mathbf{a}}_k(\varphi_{k,\mathrm{i}})$, where the IS channel gain $\chi_{\mathrm{i},k} = \sqrt{\frac{G_i(\psi_{\mathrm{i},k}) G_k(\varphi_{k,\mathrm{i}})}{L_{\mathrm{i},k}}}$. Intuitively speaking, the directivity should be as low as possible at IS's DOAs, leading to a gain value closer to zero ($\Xi_k(\varphi_{k,\mathrm{i}})$ at null locations $\approx$0). For the sake of simplicity, we assume that the Doppler shift for the DS satellite is assumed to be perfectly compensated at the VUT side using ephemerids and GPS(Global Positioning System) VUT location [131].

We assume that a DS remains visible to the VUTs for a duration $T_{\mathtt{VIS}}$ before communication is handed over to the next DS satellite. During $T_{\mathtt{VIS}}$, VUTs may encounter interference from the IS direction. The channel model adopted in (4.3) is applicable over a specific coherence time $T_{\mathtt{COH}}$, where the relative positions of the satellites do not change significantly, and the physical channel parameters can be considered time invariant [43]; thus, a total of $N_{\mathtt{COHs}}$ coherent channels can be observed by VUTs $N_{\mathtt{COHs}} = \left\lfloor \frac{T_{\mathtt{VIS}}}{T_{\mathtt{COH}}} \right\rfloor$.

4.2.2 Signal Model

We model a scenario in which the DS transmits signals to its k^{th} VUT, and that VUT eventually receives interference signals arriving from the IS direction. Let us now focus on a specific snapshot at a time instance "t", the k^{th} VUT received signal can be expressed as,

$$\mathbf{y}_k[t] = \mathbf{h}_{\mathrm{d},k} \sqrt{P_{\mathrm{d}}} s_{\mathrm{d},k}[t] + \mathbf{h}_{\mathrm{i},k} \sqrt{P_{\mathrm{i}}} s_{\mathrm{i},k}[t] + \mathbf{z}_k[t], \tag{4.7}$$

where $\mathbf{z}_k[t] \sim \mathcal{CN}(0, \sigma_{\mathrm{z}}^2)$ is the additive white Gaussian noise (AWGN) at the k^{th} VUT receiver, with $\sigma_{\mathrm{z}}^2 = \kappa \mathtt{Tem}_k \mathtt{BW}_{\mathrm{d}}$ where $\kappa = 1.380649 \times 10 - 23$ [J/K] is the Boltzmann constant, $\mathtt{Tem}_k$, and $\mathtt{BW}_{\mathrm{d}}$ are the equivalent noise temperature of the k^{th} VUT, and DS signal bandwidth, respectively. P_{d} is the transmit power from the DS, P_{i} is the overlapped transmit power from IS. Finally, $s_{\mathrm{d},k}[t] \in \mathbb{C}$ and

$s_{\mathrm{i},k}[t] \in \mathbb{C}$ denote the independent information symbols transmitted from DS and IS, respectively, whose average power is assumed to be normalized to one, i.e., $\mathbb{E}\{s_{\mathrm{d},k}s_{\mathrm{d},k}^H\} = \mathbb{E}\{s_{\mathrm{i},k}s_{\mathrm{i},k}^H\} = 1$. We assume orthogonal resource block allocation for VUTs, thus, the intra-beam interference is omitted for simplicity, i.e., $\Sigma_{q\neq k}^{\mathcal{K}}\mathbf{h}_{\mathrm{d},q}\sqrt{P_{\mathrm{d}}}s_{\mathrm{d},q}[t] = 0$. We define the received signal matrix at the k^{th} VUT as,

$$\mathbf{Y}_k \triangleq \left[\mathbf{y}_k[1], \mathbf{y}_k[2], \ldots, \mathbf{y}_k[L]\right] \in \mathbb{C}^{M\times L}, \tag{4.8}$$

where L denotes the number of received snapshots in (4.7). The minimum snapshot length required to provide sufficient statistical information is typically at least M independent snapshots [133]. However, in this work, we assume $L = 2M$ snapshots to achieve improved beamforming performance [134]. The total number of snapshot matrices within one coherence block T_{COH} is determined by the coherence time and the sampling interval T_{SR} of the k^{th} VUT, i.e., $N_{\mathbf{Y}} = \left\lfloor \frac{T_{\mathrm{COH}}}{T_{\mathrm{SR}}} \right\rfloor$.

4.3 Traditional ABF Techniques

At each VUT, a receive beamforming weight vector $\mathbf{u}_k \in \mathbb{C}^M$ is applied to steer the main beam of the UPA toward the desired DS direction $\varphi_{k,\mathrm{d}}$, while ideally suppressing interference arriving from the IS direction $\varphi_{k,\mathrm{i}}$. The resulting beamformed output signal at the k^{th} VUT, denoted by $\hat{s}_k[t] \in \mathbb{C}$, is given by

$$\begin{aligned}\hat{s}_k[t] &= \mathbf{u}_k^H\mathbf{y}_k[t] \\ &= \mathbf{u}_k^H\mathbf{h}_{\mathrm{d},k}\sqrt{P_d}\, s_{\mathrm{d},k}[t] \\ &\quad + \mathbf{u}_k^H\mathbf{h}_{\mathrm{i},k}\sqrt{P_i}\, s_{\mathrm{i},k}[t] + \mathbf{u}_k^H\mathbf{z}_k[t].\end{aligned} \tag{4.9}$$

Based on the beamformed received signal in (4.9), the resulting output SINR at the k^{th} VUT is expressed as

$$\begin{aligned}\gamma_k &= \frac{\mathbf{u}_k^H\mathbf{Q}_{\mathrm{d},k}\,\mathbf{u}_k}{\mathbf{u}_k^H\mathbf{Q}_{\mathrm{iz},k}\,\mathbf{u}_k} \\ &= \frac{\mathbf{u}_k^H\left(P_{\mathrm{d}}\mathbf{h}_{\mathrm{d},k}\mathbf{h}_{\mathrm{d},k}^H\right)\mathbf{u}_k}{\mathbf{u}_k^H\left(P_{\mathrm{i}}\mathbf{h}_{\mathrm{i},k}\mathbf{h}_{\mathrm{i},k}^H + \sigma_{\mathrm{z}}^2\mathbf{I}_M\right)\mathbf{u}_k} \\ &= \frac{P_{\mathrm{d}}\left|\mathbf{u}_k^H\mathbf{h}_{\mathrm{d},k}\right|^2}{P_{\mathrm{i}}\left|\mathbf{u}_k^H\mathbf{h}_{\mathrm{i},k}\right|^2 + \sigma_{\mathrm{z}}^2\,\mathbf{u}_k^H\mathbf{u}_k},\end{aligned} \tag{4.10}$$

where $\mathbf{Q}_{\mathrm{d},k} = P_{\mathrm{d}}\mathbf{h}_{\mathrm{d},k}\mathbf{h}_{\mathrm{d},k}^H$ and $\mathbf{Q}_{\mathrm{iz},k} = P_{\mathrm{i}}\mathbf{h}_{\mathrm{i},k}\mathbf{h}_{\mathrm{i},k}^H + \sigma_{\mathrm{z}}^2\mathbf{I}_M$ denote the desired-signal covariance and interference-plus-noise covariance, respectively. The full covariance matrix $\mathbf{Q}_k = \mathbb{E}[\mathbf{y}_k\mathbf{y}_k^H]$ captures the spatial statistics of the received array data and plays a central role in ABF, e.g., Minimum Variance

Distortionless Response (MVDR) [74]. In practice, $\mathbf{Q}_k$ is unknown and must be estimated from the L temporal snapshots using the sample covariance matrix (SCM),

$$\hat{\mathbf{Q}}_k = \frac{1}{L}\sum_{l=1}^{L}\mathbf{y}_k[l]\mathbf{y}_k^H[l] = \frac{1}{L}\mathbf{Y}_k\mathbf{Y}_k^H. \tag{4.11}$$

When the SCM is used in the MVDR expression, the resulting beamformer is called the SMI beamformer, which solves the following minimum power distortionless response (MPDR) problem [113]. The problem with SMI is that it requires a large number of snapshots $L \to \infty$ to perform as well as MVDR, making it less preferable for real-time deployments in NGSO systems [44].

With the maximum ratio combining (MRC) beamformer at the VUT array, it can only access its own channel estimate corresponding to the desired DOA φ_d and thus focus the VUT main beam towards the DS, without generating nulls towards DOAs of IS. Assuming perfect knowledge of $\mathbf{h}_k$, MRC is simply derived as,

$$\mathbf{u}_{k,\text{MRC}} = \frac{\mathbf{h}_k}{\|\mathbf{h}_k\|}. \tag{4.12}$$

The statistical, CSI-based, zero forcing beamformer (ZFBF) is considered as an upper bound benchmark,

$$\mathbf{u}_{k,\text{ZF}} = \frac{\mathbf{H}_k(\mathbf{H}_k^H\mathbf{H})^{-1}\boldsymbol{\beta}}{\|\mathbf{H}_k(\mathbf{H}_k^H\mathbf{H}_k)^{-1}\boldsymbol{\beta}\|}. \tag{4.13}$$

where $\boldsymbol{\beta} = [1;0]^T \in \mathbb{N}^2$, and $\mathbf{H}_k \triangleq [\mathbf{h}_{\text{d},k}\ \mathbf{h}_{\text{i},k}] \in \mathbb{C}^{M\times 2}$ is the full CSI matrix at the k^{th} VUT. ZFBF represents the optimal/near-optimal beamformer under perfect CSI (pCSI) conditions, i.e., we explicitly calculate ZFBF with accurate desired and interference channel vectors. In reality, the interference channel $\mathbf{h}_{\text{i},k}$ is difficult to obtain because the user has no information about the IS interfering channel available at the VUT side. Although pCSI is assumed for MRC as well, both ZFBF and MRC are sensitive to imperfect channel estimates (imCSI). Furthermore, estimation stages and matrix inversion operations (e.g., SMI, ZFBF) increase processing time and complexity in VUT antenna design, making the temporal response of fast-moving NGSO satellites a critical concern. Note that any beamformer $\mathbf{u}$ in this study is assumed to be normalized, so that consistent and controlled beamforming weights are achieved independently of channel gains.

4.4 Proposed FedSatBF framework

In this section, we introduce the FedsatBF framework, where the DS satellite utilizes FL and assists its VUTs (clustered within its spot-beam footprint that face similar CFI conditions) to collaboratively train an ABF global model capable of generating beamforming weights locally at the VUTs' side, enabling effective blind ABF and spatial nulling of CFI interference from NGSO space-to-Earth links. In Table 4.1, we categorized the parameter notation utilized in our FedSatBF framework.

Table 4.1: Key Notation of the FedSatBF Framework

Notation	Description
$\mathcal{K}$	The set of all VUTs served by the DS.
$\mathcal{K}^{\texttt{Fed}}$	Subset of VUTs participating in the FL learning.
$T_{\texttt{COH}}$	Duration over which a channel is assumed coherent.
$N_{\texttt{COHs}}$	Number of coherent channels within $T_{\texttt{VIS}}$.
$T_{\texttt{CR}}$	Duration of a single communication round (indexed as τ).
$N_{\texttt{CRs}}$	Number of rounds within $T_{\texttt{COH}}$ ($\tau \in \{1, \ldots, N_{\texttt{CRs}}\}$).
$\mathcal{D}^{\text{tr}}_{k,\tau}, N^{\text{tr}}_{k,\tau}$	Local training dataset per VUT per round and its size.
$\mathcal{D}^{\text{ts}}_{k,\tau}, N^{\text{ts}}_{k,\tau}$	Local evaluation dataset per VUT per round and its size.
$T_{\texttt{LE}}$	Duration of a single local epoch (indexed as ϵ).
$N_{\texttt{LEs}}$	Number of local epochs within $T_{\texttt{CR}}$ ($\epsilon \in \{1, \ldots, N_{\texttt{LEs}}\}$.
B	Training mini-batch size.
$N_{\texttt{Bs}}$	Number of mini-batches per local epoch.
Ω	Local training optimizer.
$\mathbf{\Theta}^{\tau}_{g}$	Global model gradients broadcast by the DS at τ.
$\mathbf{\Theta}^{\tau}_{k}$	Personalized local model by k^{th} VUT k at τ.
$\mathcal{L}^{\tau}_{k}$	Local loss function of k^{th} VUT at τ.
$\mathbf{u}^{\tau}_{k,\texttt{gFL}}$	UPA weights generated by k^{th} VUT via $\mathbf{\Theta}^{\tau}_{g}$ at τ.
$\mathbf{u}^{\tau}_{k,\texttt{pFL}}$	UPA weights generated by k^{th} VUT via $\mathbf{\Theta}^{\tau}_{k}$ at τ.
Γ^{τ}_{gFL}	Global SINR value resulting from $\mathbf{\Theta}^{\tau}_{g}$ evaluation at τ.
Γ^{τ}_{pFL}	Global SINR value resulting from $\mathbf{\Theta}^{\tau}_{k}$ evaluation at τ.
$\mathbf{\Theta}^{\tau+1}_{g}$	Optimized Global model by the DS at τ for $\tau + 1$.

4.4.1 Base Model Architecture

In this work, for local model training at each VUT, we use the attention-based beamformer (AttBF) as the base model for our FedsatBF framework, with the raw SCMs data with limited snapshots $L = 2M$ as direct input [44]. AttBF does not depend on any CSI or is sensitive to its estimation errors, and provides acceptable performance in low and highly spatially correlated interference scenarios (e.g., in-line interference events). The architecture of the AttBF model is summarized in Table 4.2, consists of a sequence of DL-based layers and matrix operations, such as, 1) 1-dimensional (1D) convolution

Table 4.2: Summary of the AttBF Model Architecture

Stage	Layer / Operation	Output Shape
Projection	`Input`$(2M,\ M)$	$(B,\ M,\ 2M)$
	`Conv1D`(M) + `GeLU`	$(B,\ M,\ M)$
Attention Block	`MHA` (heads=2)	$(B,\ M,\ M)$
	`Dropout`(rate= 0.2)	$(B,\ M,\ M)$
	`Add` & `LayerNorm`	$(B,\ M,\ M)$
FFN Block	`Dense`(M) + `GeLU`	$(B,\ M,\ M)$
	`Dense`(M)	$(B,\ M,\ M)$
	`Add` & `LayerNorm`	$(B,\ M,\ M)$
Beamformer	`Conv1D`$(\frac{M}{2})$ + `GeLU`	$(B,\ M,\ \frac{M}{2})$
	`Conv1D`$(\frac{M}{4})$ + `GeLU`	$(B,\ M,\ \frac{M}{4})$
	`Flatten`	$(B,\ \frac{M}{2} \times M)$
	`Dense`$(2M)$ + `Tanh`	$(B,\ 2M)$
	`Reshape`$(M, 2)$	$(B,\ M,\ 2)$

layers (`Conv1D`), 2) Gaussian Error Linear Unit (`GeLU`) activations, 3) Multi-Head Attention (`MHA`) block, which consists of two attention heads with key dimensions corresponding to the number of features extracted in each token (*i.e.*, $D_{key} = M$), 4) `Dense` layers, 5) Hyperbolic tangent function (Tanh) activation function constrains the output values to the range $[-1, 1]$. These layers process a real-valued SCM as tokens data (i.e., $[\mathrm{Re}(\hat{\mathbf{Q}}_k); \mathrm{Im}(\hat{\mathbf{Q}}_k)] \in \mathbb{C}^{M \times 2M}$ through features extractions, and the complex-valued beamforming weights can be constructed from the AttBF real-valued output matrix as $\mathbf{u}_{k,\mathtt{FL}} \in \mathbb{C}^M = \widetilde{\mathbf{U}}_{k,\mathtt{FL}}(:,2) + j\,\widetilde{\mathbf{U}}_{k,\mathtt{FL}}(:,2)$, where $\widetilde{\mathbf{U}}_{k,\mathtt{FL}} \in \mathbb{C}^{M \times 2}$ is the AttBF output matrix [44].

It is important to note that FedSatBF does not learn a single beamforming solution. Instead, the AttBF model learns a mapping from SCMs $\{\mathbf{\Theta}_k^\tau\}_{k=1}^{K^{\text{Fed}}}$ to beamforming weights $\{\mathbf{u}_{k,\mathtt{gFL}}^\tau\}_{k=1}^{K^{\text{Fed}}}$. By aggregating updates from multiple VUTs experiencing diverse but related interference conditions, the global model $\{\mathbf{\Theta}_g^\tau\}_{\tau=1}^{N_{\text{CRs}}}$ captures a generalized beamforming policy that can be applied to unseen users without retraining. Table 4.3 shows the difference between MRC, ZFBF benchmarks, and the AttBF model in terms of input type.

Table 4.3: Comparison of benchmarks Input type

Method	Input	CSI-Free?
AttBF	SCMs ($\hat{\mathbf{Q}}_k \in \mathbb{C}^{M \times 2M}$) (4.11)	Yes
MRC	Desired satellite CSI vector ($\mathbf{h}_d \in \mathbb{C}^M$) (4.12)	No
ZFBF	Full CSI matrix ($\mathbf{H}_k \in \mathbb{C}^{M \times 2}$) (4.13)	No

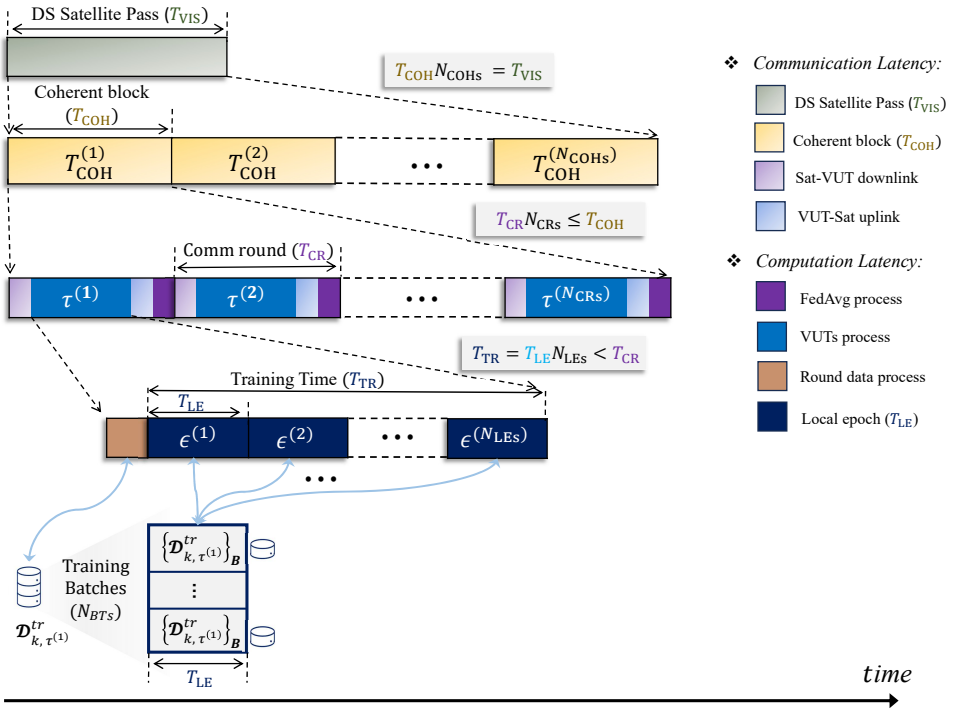


Figure 4.3: Per-VUT training time frame.

4.4.2 Learning Procedure

We assume that during a coherent channel duration T_{COH}, DS-VUTs can communicate for N_{CRs} rounds, each round lasts for a duration T_{CR} including the DS-VUTs transmission round-trip time (i.e., a few ms), and processing time, as shown in Fig. 4.3. Note that we assume a dedicated signaling channel for model exchange, where even with Low SINR, the link is still utilizable. Algorithm 4 summarizes the FedSatBF learning framework, and it can be outlined in three main parts as,

1) Initial Global model broadcast: The DS satellite selects a set of VUTs with training capabilities to participate in the FedsatBF learning, particularly $\mathcal{K}^{\text{Fed}} \subseteq \mathcal{K}$. At the first round $\tau = 1$, the DS satellite broadcasts an initial global model gradient to all VUTs $\mathbf{\Theta}_g^1$. This can be a previous DS plane's global model shared via ISLs/handover techniques [150], a pre-trained base model [44], or totally random gradients. This initialization ensures that subsequent local updates remain aligned, enabling coherent model aggregation in later rounds. Note that at rounds $\tau > 1$, the DS satellite broadcasts an optimized global model.

2) VUTs local training: After the DS satellite broadcasts a global model $\mathbf{\Theta}_g^\tau$ to all $\mathcal{K}$ users (initial at $\tau = 1$, and optimized for rounds $\tau > 1$). Each user $k \in K^{\text{Fed}}$ is capable of collecting their own fresh, real-time raw SCMs data for online fine-tuning (personalization) and evaluation $\mathcal{D}_{k,\tau}^{\text{tr}} \triangleq$

Algorithm 4: FedSatBF learning

Input: Set of VUTs $\mathcal{K}$, participating set $\mathcal{K}^{\texttt{Fed}}$, $T_{\texttt{COH}}$, $N_{\texttt{CRs}}$, $N_{\texttt{LEs}}$, batch size B, optimizer Ω
Output: Final global ABF model $\mathbf{\Theta}_g^*$

Initialization:
DS initializes global model gradients $\mathbf{\Theta}_g^1$
Set communication round index $\tau \leftarrow 1$.
for $\tau \leftarrow 1$ **to** N_{CRs} **do**
  Global model broadcast: DS broadcasts $\mathbf{\Theta}_g^\tau$ to all $k \in \mathcal{K}^{\texttt{Fed}}$.
  Local training at each VUT (in parallel):
  forall $k \in \mathcal{K}^{Fed}$ **do**
    Collect local datasets $\mathcal{D}_{k,\tau}^{\text{tr}}$ and $\mathcal{D}_{k,\tau}^{\text{ts}}$.
    Initialize local model $\mathbf{\Theta}_k^\tau \leftarrow \mathbf{\Theta}_g^\tau$.
    for $\epsilon \leftarrow 1$ **to** N_{LEs} **do**
      Partition $\mathcal{D}_{k,\tau}^{\text{tr}}$ into mini-batches of size B.
      Compute loss $\mathcal{L}_k^\tau$ over each mini-batch.
      Update local model using SGD: $\mathbf{\Theta}_k^\tau \leftarrow \Omega(\mathbf{\Theta}_k^\tau, \mathcal{L}_k^\tau, \mathcal{D}_{k,\tau}^{\text{tr}})$.
  Uplink transmission: Each $k \in \mathcal{K}^{\texttt{Fed}}$ sends its $\mathbf{\Theta}_k^\tau$ to the DS.
  Global aggregation at DS: DS computes the federated average:

$$\mathbf{\Theta}_g^{\tau+1} = \frac{1}{K^{\texttt{Fed}}} \sum_{k \in \mathcal{K}^{\texttt{Fed}}} \mathbf{\Theta}_k^\tau.$$

  Broadcast updated model: DS broadcasts $\mathbf{\Theta}_g^{\tau+1}$ to all VUTs.
Output:
Set final global model $\mathbf{\Theta}_g^* \triangleq \mathbf{\Theta}_g^{N_{\text{CRs}}+1}$.
Store $\mathbf{\Theta}_g^*$ for the next coherence block.

$\big[\hat{\mathbf{Q}}_{k,\tau}^{(1)}, \hat{\mathbf{Q}}_{k,\tau}^{(2)}, \ldots, \hat{\mathbf{Q}}_{k,\tau}^{(N_{k,\tau}^{\text{tr}})}\big]$ and $\mathcal{D}_{k,\tau}^{\text{ts}} \triangleq \big[\hat{\mathbf{Q}}_{k,\tau}^{(1)}, \hat{\mathbf{Q}}_{k,\tau}^{(2)}, \ldots, \hat{\mathbf{Q}}_{k,\tau}^{(N_{k,\tau}^{\text{ts}})}\big]$, respectively. Local training is executed independently by refining $\mathbf{\Theta}_g^\tau$ into a personalized model $\mathbf{\Theta}_k^\tau$ over $N_{\texttt{LEs}}$ epochs, using mini-batches of size B (yielding $N_{\texttt{Bs}}$ batches per epoch). The local training main objective is to minimize the per-epoch negative SINR loss function $\mathcal{L}_k^{\tau(\epsilon)} = -\frac{1}{\mathcal{B}} \sum_{b=1}^{\mathcal{B}} \gamma_k^{\tau(b)}$[1] using stochastic gradient descent (SGD) optimizer Ω expressed as $\mathbf{\Theta}_k^\tau \leftarrow \Omega(\mathbf{\Theta}_k^\tau, \mathcal{L}_k^\tau, \mathcal{D}_{k,\tau}^{\text{tr}})$. After $N_{\texttt{LEs}}$ epochs, the participating VUTs send their individual personalized models' gradients $\{\mathbf{\Theta}_k^\tau\}_{k=1}^{K^{\text{Fed}}}$ gradients to the DS through their uplink channel.

3) DS perform global model optimization: The DS satellite receives and directly aggregates the local models $\{\mathbf{\Theta}_k^\tau\}_{k=1}^{K^{\text{Fed}}}$ using federated averaging (`FedAvg`) algorithms [144]. We assume that all $k \in \mathcal{K}^{\texttt{Fed}}$ utilize the same amount of training data in each round $N_{k,\tau}^{\text{tr}}$, and this leads to the simplified `FedAvg` formula based on a simple arithmetic mean at the end of round τ as,

[1] Using γ_k here as an online loss function is due to its availability as a terminal-measured QoS indicator [14].

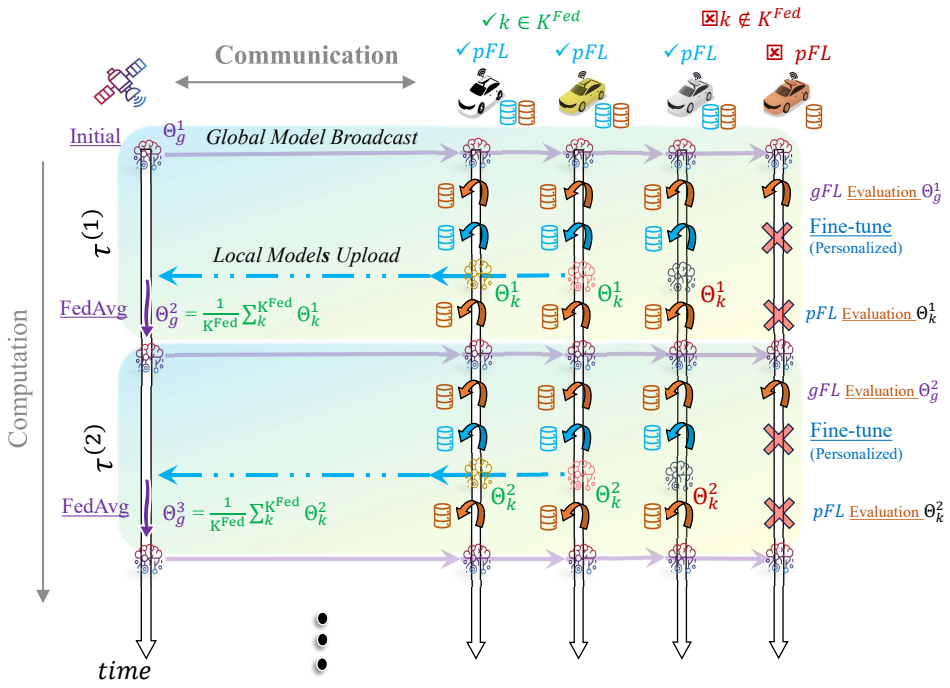


Figure 4.4: FedSatBF leaning diagram and assessment strategies (pFL: personalized FL, gFL: global FL).

$$\mathbf{\Theta}_g^{\tau+1} = \frac{1}{K^{\text{Fed}}} \sum_{k \in \mathcal{K}^{\text{Fed}}} \mathbf{\Theta}_k^{\tau}. \tag{4.14}$$

where $\mathbf{\Theta}_g^{\tau+1}$ is the optimized (averaged) global model gradients at round τ, that intended for $\tau+1$ or as a final global model by the end of the communication rounds $\mathbf{\Theta}_g^{N_{\text{CRs}}+1} \triangleq \mathbf{\Theta}_g^*$. This simple average ensures that the contributions of the local models, which are equally informed by data quantity, are equally weighted in refining the global interference nulling strategy. The DS then broadcasts the optimized (averaged) global model gradients back to all K VUTs for round $\tau+1$ evaluation. This global aggregation is performed for N_{CRs} rounds until performance convergence or T_{COH} expires. Note that the DS should memorize the last global model to be used as new initial model for the next coherence block $T_{\text{COH}}^{(t+1)}$ of future interference instances, e.g., $\mathbf{\Theta}_g^*(T_{\text{COH}}^{(t)}) \rightarrow \mathbf{\Theta}_g^1(T_{\text{COH}}^{(t+1)})$.

4.4.3 Evaluation Protocol and Performance Metrics

The evaluation procedure at each communication round τ depends on the adopted FL assessment strategy, as illustrated in Fig. 4.4,

- In general, the broadcast global model $\mathbf{\Theta}_g^{\tau}$ can be directly used to generate beamforming vectors

$\mathbf{u}^{\tau}_{k,\mathtt{gFL}}$, which are then evaluated on the local test dataset $\mathcal{D}^{\mathrm{ts}}_{k,\tau}$ at each VUT $k \in \mathcal{K}$. This pre-personalization evaluation reflects the global model's performance across participating users.

- Alternatively, VUTs may locally personalize the received global model, yielding personalized parameters $\mathbf{\Theta}^{\tau}_{k}$ and corresponding beamforming vectors $\mathbf{u}^{\tau}_{k,\mathtt{pFL}}$. The resulting performance, evaluated on $\mathcal{D}^{\mathrm{ts}}_{k,\tau}$, captures the benefits of personalization and applies only to VUTs that can personalize the global model, including VUTs that did not participating in the FL ($k \notin \mathcal{K}^{\mathtt{Fed}}$) but own local training capabilities.

- A more general FL setting considers non-participating VUTs ($k \notin \mathcal{K}^{\mathtt{Fed}}$) that do not support local personalization and rely solely on the broadcast global model $\mathbf{\Theta}^{\tau}_{g}$. Evaluating $\mathbf{\Theta}^{\tau}_{g}$ at these VUTs highlights the generalization capability of the proposed FedSatBF framework without requiring personalized models at all users.

For clarity of exposition, the primary evaluation in this work focuses on the *pre-personalization performance of the broadcast global model* $\mathbf{\Theta}^{\tau}_{g}$ measured at participating VUTs ($k \in \mathcal{K}^{\mathtt{Fed}}$), i.e., using $\mathbf{u}^{\tau}_{k,\mathtt{gFL}}$.

Since no centralized hold-out dataset is maintained by the DS, in this work, the global SINR, denoted as $\Gamma^{\tau}_{\mathtt{gFL}}$, is adopted as the pre-personalized global KPI and defined as,

$$\Gamma^{\tau}_{\mathtt{gFL}} = \frac{1}{|\mathcal{K}^{\mathtt{Fed}}|} \sum_{k \in \mathcal{K}^{\mathtt{Fed}}} \bar{\gamma}^{\tau}_{k}(\mathbf{\Theta}^{\tau}_{g}), \tag{4.15}$$

where $\bar{\gamma}^{\tau}_{k}(\mathbf{\Theta}^{\tau}_{g})$ denotes the average per-user SINR computed over the local test samples $\mathcal{D}^{\mathrm{ts}}_{k,\tau}$ using the global-model beamforming vectors $\mathbf{u}^{\tau}_{k,\mathtt{gFL}}$. Importantly, at the initial communication round $\tau = 1$, the global model $\mathbf{\Theta}^{1}_{g}$ corresponds to the initial model and has not yet incorporated any federated aggregation. Consequently, any performance observed at $\tau = 1$ reflects purely initial inference behavior, and no global generalization is applicable at this stage. For this reason, results at $\tau = 1$ are interpreted as initial model performance, while rounds $\tau > 1$ capture the evolution of the global model through `FedAvg`.

To summarize global performance over all communication rounds, a single KPI is defined as

$$\Gamma_{\mathtt{gFL}} = \frac{1}{N_{\mathtt{CRs}}} \sum_{\tau=1}^{N_{\mathtt{CRs}}} \Gamma^{\tau}_{\mathtt{gFL}}. \tag{4.16}$$

Furthermore, to assess generalization to non-participating VUTs, the following KPI is employed:

$$\Gamma^{\tau}_{\texttt{genFL}} = \frac{1}{K - |\mathcal{K}^{\texttt{Fed}}|} \sum_{k \notin \mathcal{K}^{\texttt{Fed}}} \bar{\gamma}^{\tau}_{k}(\mathbf{\Theta}^{\tau}_{g}), \tag{4.17}$$

which quantifies the general performance of the broadcast global model without local personalization at non-participating VUTs. In a single figure later on, we will show the performance of personalized models, which can be evaluated using $\Gamma^{\tau}_{\texttt{pFL}} = \frac{1}{|\mathcal{K}^{\texttt{Fed}}|} \sum_{k \in \mathcal{K}^{\texttt{Fed}}} \bar{\gamma}^{\tau}_{k}(\mathbf{\Theta}^{\tau}_{k})$ for participating VUTs[2].

4.5 Simulation Results

In this section, we present the simulation setup, including details on data generation, the effects of the hyperparameters of FedSatBF, and the evaluation and comparison of our proposed model with the traditional MRC and ZFBF techniques.

4.5.1 Data and Simulation

We run a satellite simulation scenario with one desired NGSO satellite and multiple interfering NGSO satellites using MATLAB satellite toolbox by assigning each satellite to a defined plane orbit through the six Kepler orbit elements: the semi-major axis, eccentricity, inclination, right ascension of the ascending node (RAAN), argument of perigee, and true anomaly [44]. We apply a minimum interference-to-noise ratio (INR) threshold of -12 [dB] to only consider interference where the QoS of the desired link is affected [118]. Tables 4.4 and 4.5 summarize the constellation parameters, link budget parameters, and VUT parameters, respectively.

During simulation, the DS satellite steered a quasi-Earth fixed beam toward a ground location centered at (49.6257°, 6.1598°) in latitude, longitude, respectively, and the IS satellite steered a quasi-Earth fixed beam toward a ground location centered at (49.6307°, 6.1648°). The DS and IS generates a spot-beam ground radius as $R_{\text{beam, d}} = 50$[km], $R_{\text{beam, i}} = 60$[km]. We assume that K VUTs are distributed randomly within a clustered cell around the DS boresight coordinates; the cluster radius (R_{cluster}) is adjustable by the DS. The users have varying altitude ($\triangle A_k = 100 \pm 50$[m]). The full datasets in this work will be made available with more details on our SmartSpace project web page [84].

[2]For context, although not covered in this work, if non-participating assumed to have pFL capabilities, the performance of personalized models can be evaluated by $\frac{1}{K-|\mathcal{K}^{\texttt{Fed}}|} \sum_{k \notin \mathcal{K}^{\texttt{Fed}}} \bar{\gamma}^{\tau}_{k}(\mathbf{\Theta}^{\tau}_{k})$ for non-participating VUTs, or $\frac{1}{|\mathcal{K}|} \sum_{k \in \mathcal{K}} \bar{\gamma}^{\tau}_{k}(\mathbf{\Theta}^{\tau}_{k})$ for all users.

Table 4.4: Satellite Parameters

Parameters	**DS Satellite**	**IS Satellite**
Altitude (A)	550 [Km]	650 [Km]
Eccentricity	0.01	0.04
Inclination	55°	120°
RAAN	134°	34°
Argument of Perigee	20°	35°
True anomaly	82°	75°
Signal bandwidth (BW)	50 MHz	55MHz
Signal Power (P)	10 dBW	15 dBW
Operational frequency (f_c)	11.5 GHz	11.5 GHz
Satellite Gain (G)	30 dBi	35 dBi

Table 4.5: Per-VUT Parameters

Parameter	**Value**
# Elements (M)	$8 \times 8 = 64$
Temperature ($\texttt{Tem}_k$)	290°K
Efficiency (η_k)	0.99
Maximum Directivity ($\Xi_k^{\max}$)	M
Min elevation ($\theta^{\min}$)	10°

4.5.2 FedSatBF Performance Analysis for $T_{\texttt{COH}}$

In this subsection, we investigate the impact of key FL hyperparameters on the performance of the proposed FedSatBF framework. The objective is to identify flexible parameter configurations that allow a sufficient number of communication rounds within the channel coherence block $T_{\texttt{COH}}$, while preserving acceptable beamforming performance. For clarity, in this subsection the horizontal axis is indexed by the ***Global Model Index***, refers to the beamforming model parameters broadcast by the DS satellite, where index 1 corresponds to the initial model evaluation, and indices 2 through 10 correspond to the global models evaluation after successive FL aggregation (FedAvg). Thus, the final round global model is not evaluated here; instead, it is assumed to be memorized by DS for future use as an initial model, as explained in Section 4.4.2. This convention emphasizes that the first assessment reflects pre-FL behavior, while meaningful global FL performance emerges only for $\tau > 1$. Unless otherwise stated, the parameters in Table 4.6 are used throughout our evaluation.

For reference, at the selected $T_{\texttt{COH}}$, the employed MRC per-VUT achieves a global SINR per-round ($\Gamma^{\tau}_{\texttt{MRC}}$) of $\mathbf{6.2352}$ [dB] across the participating VUTs. At the same time, the theoretical zero-forcing

Table 4.6: FL Fixed Parameters

Parameter	**Value**
Total VUTs K	14
Participating VUTs K^{Fed}	7 (with pFL)
Non-participating VUTs	7 (without pFL)
Cluster radius R_{cluster}	5 km
Training samples $N_{k,\tau}^{\text{tr}}$	12 (per VUT per round)
Testing samples $N_{k,\tau}^{\text{ts}}$	20 (per VUT per round)
Local epochs N_{LEs}	10
Batch size B	1
Mini-batches N_{Bs}	12
Communication rounds N_{CRs}	10

beamforming ZFBF benchmark attains ($\Gamma_{\mathsf{ZFBF}}^{\tau}$) $\mathbf{14.8165}$ [dB]. Since ZFBF represents an upper bound on interference mitigation, it is included only as a performance reference, whereas MRC represents the worst-case assumption and is used as the initial instance of our approach, and it is omitted from most subsequent discussions.

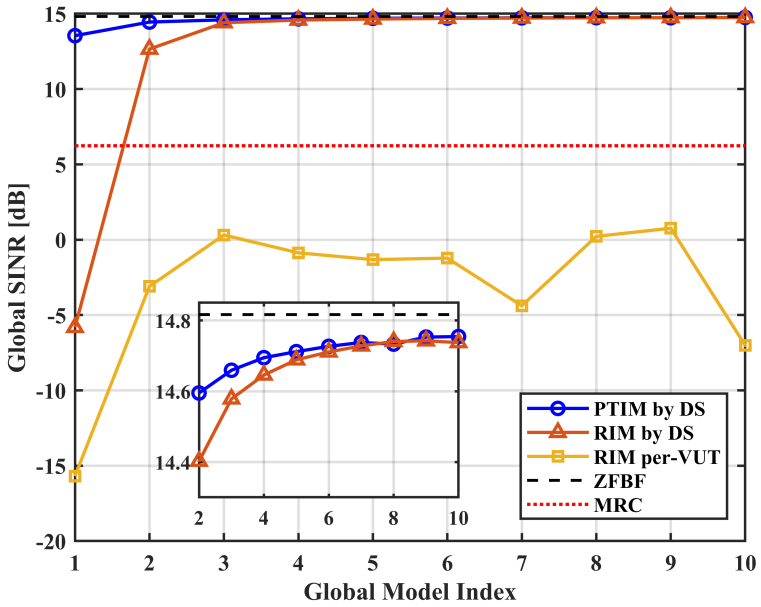


Figure 4.5: Impact of model initialization on $\Gamma_{\mathsf{gFL}}^{\tau}$ performance.

Fig. 4.5 presents the global SINR performance of the proposed FedSatBF under three different initialization strategies ($\tau = 1$) over nine global model updates ($\tau = 2 \rightarrow 10$). The curve labeled "PTIM by DS" corresponds to the FedSatBF initialization using a pre-trained transfer initialization

model parameters (PTIM) [44], whereas "RIM by DS" indicates reuse of a shared random initialized model across VUTs, and "RIM per-VUT" denotes independent random initialization per VUT. The dashed and dotted lines represent the ZFBF and MRC benchmarks, respectively. Results show that PTIM achieves near-optimal global SINR performance from the earliest rounds, converging rapidly close to the ZFBF benchmark (within 0.1 [dB]). The shared random initialization (RIM by DS) also converges toward PTIM performance, but with a lower global SINR in the early rounds. In contrast, per-VUT random initialization exhibits greater variability and generally lower global SINR across rounds, with fluctuations difference exceeding 15 [dB]. These results demonstrate that a shared initial global model is critical for stabilizing early fine-tuning by VUT, ensuring coherent aggregation, and achieving near-optimal global performance in the proposed FedSatBF framework for beamforming tasks.

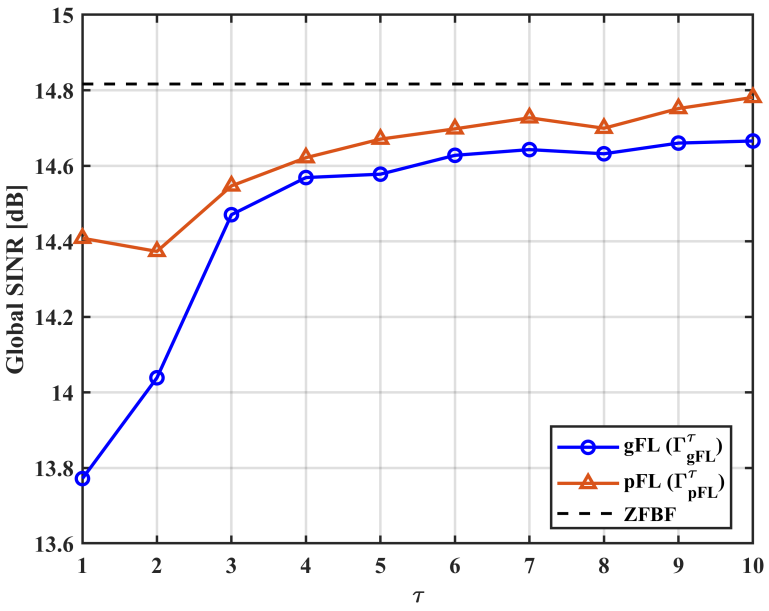


Figure 4.6: Impact of global model personalization on global SINR performance.

Fig. 4.6 compares the global FL beamformer performance Γ^{τ}_{gFL} and the personalized FL beamformer performance Γ^{τ}_{pFL} on the same per-round test datasets $\mathcal{D}^{\text{ts}}_{k,\tau}$. The personalized model consistently outperforms the global model across all communication rounds, demonstrating effective adaptation to user-specific channel and interference statistics within their local SCMs data. The observed global SINR remains modest due to the proximity of the global model to the ZFBF benchmark, indicating that the global model already captures most interference suppression capabilities while personalization provides fine-grained local refinements.

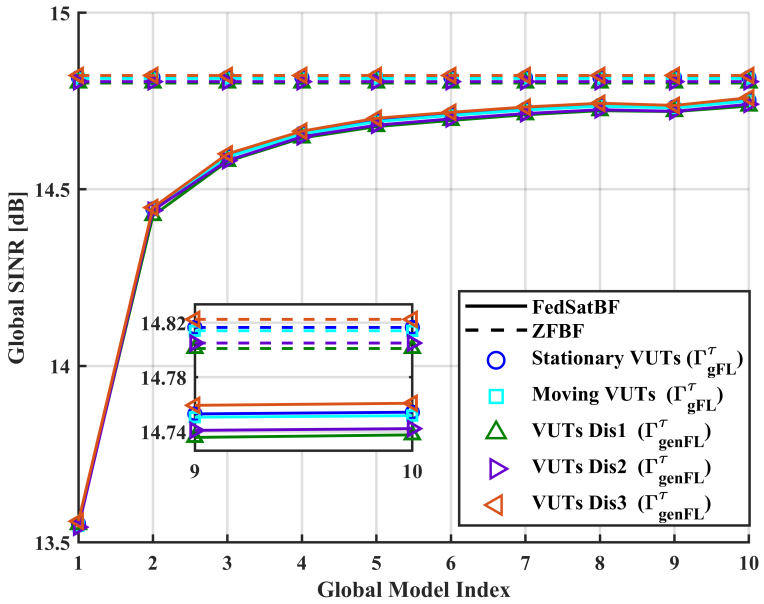


Figure 4.7: Generalization performance of FedSatBF on non-participating VUTs in terms of global SINR.

In Fig. 4.7, we evaluate the generalization capability of the proposed FedSatBF framework to unseen VUTs that do not participate in FL training. For participating VUTs ($k \in \mathcal{K}^{\texttt{Fed}}$), the global model maintains nearly identical SINR evolution for both stationary and moving participating VUTs (i.e., VUT moving at 10-50 km/h per round), indicating robustness to participating VUT mobility[3]. More importantly, the proposed FedSatBF framework demonstrates strong generalization to non-participating VUTs ($k \notin \mathcal{K}^{\texttt{Fed}}$), this can be observed when evaluate the performance of aggregated FedAvg global model on three unseen spatial user distributions within the cluster radius $R_{\texttt{cluster}}$ (Dis1, Dis2, Dis3), the global model achieves performance that closely tracks the ZFBF benchmark, with a final global SINR gap below 0.1 [dB] (calculated as $\triangle(\Gamma^{\tau}_{\texttt{gFL}} - \Gamma^{\tau}_{\texttt{ZFBF}})$ per scenario). This confirms that the learned global model effectively generalizes across other VUT locations and channel realizations without requiring personalization or retraining.

In Fig. 4.8, we show the evolution of the global SINR Γ^{τ}_{g} versus the global model index for different communication rounds $N_{\texttt{CRs}}$. A clear increasing trend is observed during the first few model updates, after which the performance saturates and converges near 14.8 [dB]. Increasing the number of communication rounds generally has no noticeable impact on this convergence, where $N_{\texttt{CRs}} = 5$ already achieves performance close to the asymptotic levels attained with $N_{\texttt{CRs}} = 10$ and $N_{\texttt{CRs}} = 20$.

[3]This shows that the learned global beamforming policy is robust to moderate mobility, assuming Doppler effects are compensated at VUT.

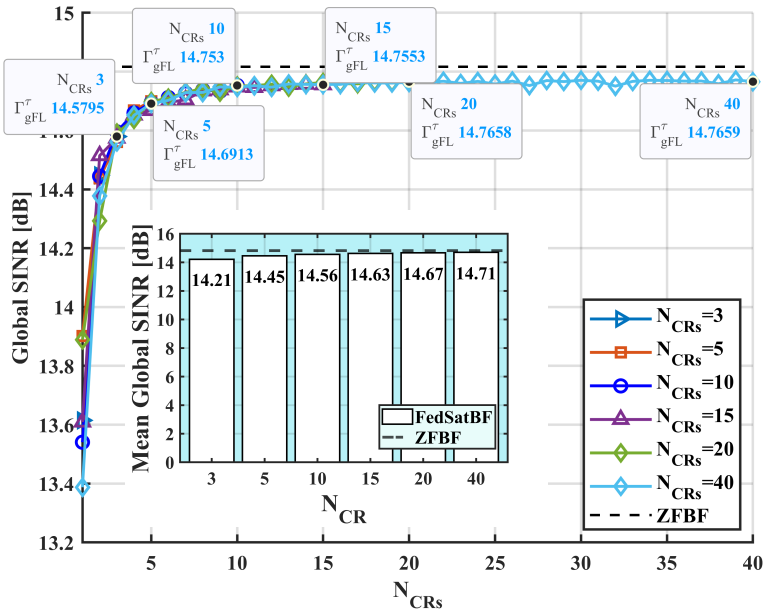


Figure 4.8: Impact of $N_{\mathtt{CRs}}$ on global SINR performance. The bars highlight the mean global SINR from all rounds ($\Gamma_{\mathtt{gFL}}$).

The dashed line indicates the ZFBF optimal benchmark, showing that the FedSatBF model rapidly approaches near-optimal SINR levels. Notably, using only a moderate number of communication rounds (e.g., $N_{\mathtt{CRs}} = 5 - 10$) is sufficient to converge close to the ZFBF performance, while still offering a significant improvement over the MRC beamformer, which attains only 6.2352 [dB] averaged SINR.

Fig. 4.9 shows how the number of participating VUTs $K^{\mathtt{Fed}}$ influences the convergence behavior of FedSatBF, as a relative performance gap with ZFBF. Increasing $|\mathcal{K}^{\mathtt{Fed}}|$ accelerates early-rounds convergence toward the ZFBF baseline, whereas smaller participation yields slower improvement. Nonetheless, all configurations converge to within approximately $0.06 - 0.08$ [dB] of the ZFBF baseline after nine global updates. Notably, even moderate participation levels (e.g., $K^{\mathtt{Fed}} = 5$–10) are sufficient to achieve near-optimal performance, indicating that FedSatBF does not require full VUTs participation to approach acceptable beamforming performance, even when all VUTs hold local training capabilities.

Fig. 4.10 illustrates the effect of varying the geographical clustering radius R_{cluster} on the global performance gap relative to the ZFBF baseline. Smaller clustering radii (e.g., $R_{\text{cluster}} \leq 5$ [km]) lead to faster convergence and reduced performance loss, since participating users experience more similar interference conditions. As the clustering radius increases, especially approaching the spot-beam

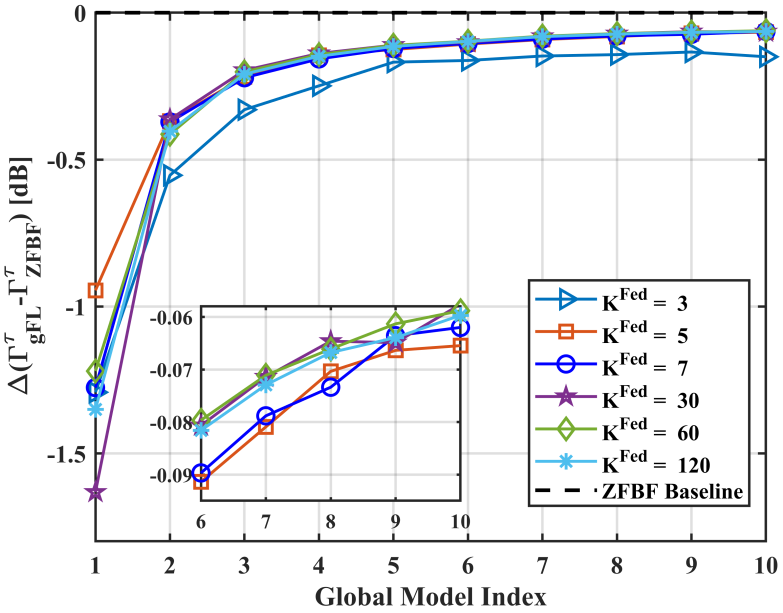


Figure 4.9: Effect of K^{Fed} on Global SINR.

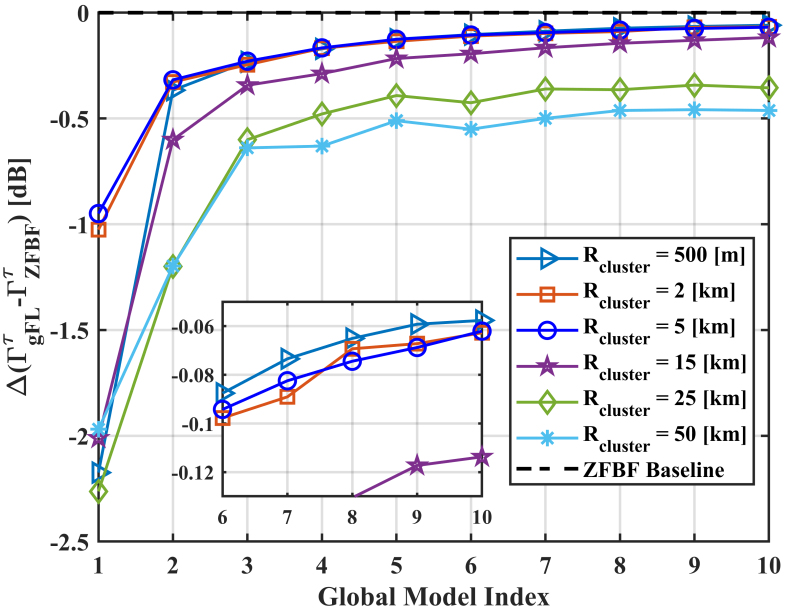
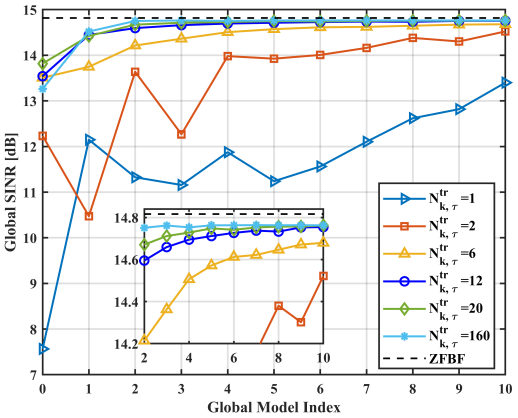
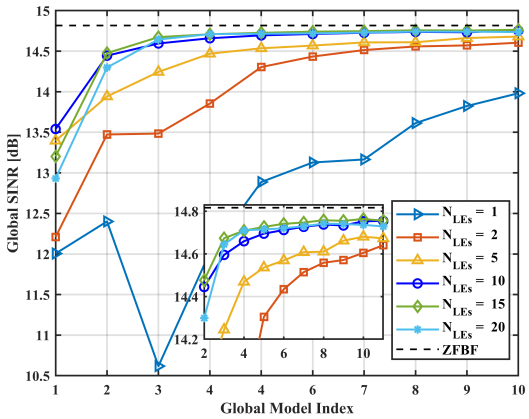


Figure 4.10: Effect of R_{cluster} on Global SINR.

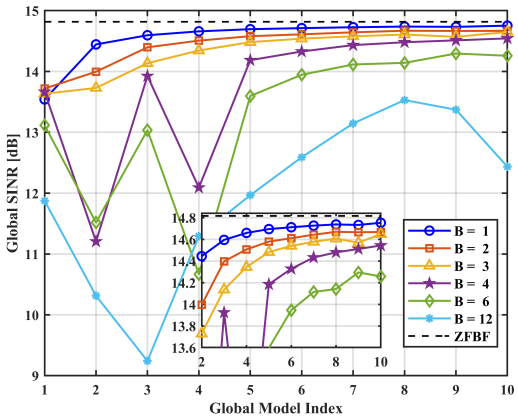
footprint radius ($R_{\text{cluster}} \rightarrow R_{\text{beam, b}} = 50[\text{km}]$), the performance degrades slightly due to higher channel heterogeneity within each round. Nevertheless, for all considered radii, the gap remains bounded within approximately 0.4–0.6 [dB] at convergence, confirming that FedSatBF remains robust even when user groups span large spatial separations.



(a) $N^{\text{tr}}_{k,\tau}$ vs Global SINR



(b) N_{LEs} vs Global SINR



(c) N_{Bs} vs Global SINR

Figure 4.11: Comparison of different training parameters on the FedSatBF conformance: (a) Impact of the amount of training data per round; (b) Impact of the number of local epochs per round; (c) Impact of batch size.

Figs. 4.11 show a comparison of key FL training parameters on FedSatBF convergence. Fig. 4.11a demonstrates that larger training data points per round ($N^{\text{tr}}_{k,\tau}$) yield significantly more stable learning and faster convergence. In contrast, fewer points per round lead to fluctuating model behavior and degraded performance. Once a modest number of samples is collected (e.g., 8-12), convergence stabilizes, and the final SINR remains close to the ZFBF benchmark. Fig. 4.11b indicates that the more local epochs VUT executes (N_{LEs}), the better results in the form of robust improvements per

round and smoother convergence. However, beyond roughly 10 epochs, additional local training yields only marginal improvement, indicating an efficient operating point that balances computational cost with global SINR performance. Finally, in Fig. 4.11c we show that the smallest batch size possible (i.e., $B = 1$) leads to faster and more stable gains in SINR, whereas larger batches (i.e., $B = N_{k,\tau}^{\mathrm{tr}}$) introduce higher instability and slower convergence. This highlights that lightweight local updates outperform large-batch training within constrained coherence intervals, improving responsiveness to interference variations.

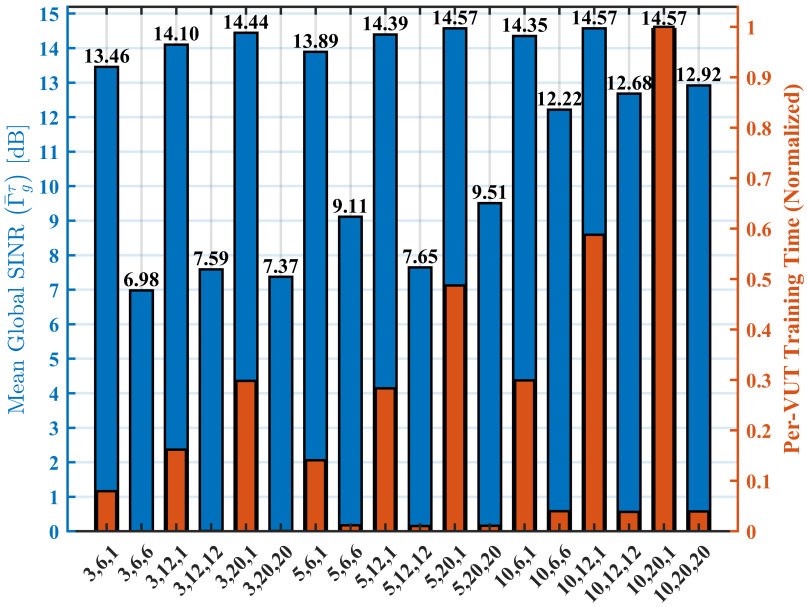


Figure 4.12: Training parameters' performance bars ($N_{\mathrm{LEs}}, N_{k,\tau}^{\mathrm{tr}}, B$).

Fig. 4.12 illustrates the impact of the local training parameters on the achieved SINR and per-VUT training time, and it can be outlined as follows,

Impact of local epochs N_{LEs}: Increasing N_{LEs} improves the achieved SINR by enabling more refined local optimization, but this improvement saturates beyond $N_{\mathrm{LEs}} = 10$. In contrast, the per-VUT normalized training time increases nearly linearly with N_{LEs}, indicating that excessive local iterations primarily increase computational cost rather than improving SINR performance (i.e., interference mitigation).

Impact of training data size $N_{k,\tau}^{\mathrm{tr}}$: Expanding the training dataset improves the achieved SINR up to a moderate regime; However, once $N_{k,\tau}^{\mathrm{tr}} \gtrsim 12$, further SINR improvements become marginal, while the training time grows significantly, making it the dominant contributor to training latency.

Impact of batch size B: As batches get smaller $1 \leftarrow B$, they slightly stabilize the learning process,

achieving better SINR performance, but substantially increase the per-round processing time. In contrast, as batches get bigger, $B \rightarrow N_{k,\tau}^{\mathrm{tr}}$, they tend to significantly lower training time, but also degrade SINR performance.

These results indicate that convergence can be achieved under lightweight local training settings (e.g., $N_{\mathtt{LEs}} = 5, N_{k,\tau}^{\mathrm{tr}} = 6, B = 1$), thereby reducing the computational burden at each VUT and ultimately supporting real-time adaptation within a single coherence interval $T_{\mathtt{COH}}$.

From a computational perspective, a lower number of training data per round $N_{k,\tau}^{\mathrm{tr}}$, Local epochs $N_{\mathtt{LEs}}$, number of batches $N_{\mathtt{Bs}}$, and communication rounds $N_{\mathtt{CRs}}$, translates into shorter per-VUT processing time and lower processing latency per coherence interval $T_{\mathtt{COH}}$. Since each round includes back-and-forth signaling, local training, and aggregation, achieving convergence within fewer rounds, local epochs, and training data per round substantially reduces per-VUT local computation cycles and central aggregation workload, enabling real-time adaptation within practical operational time budgets.

4.5.3 FedSatBF Performance Analysis for $T_{\mathtt{VIS}}$

In this subsection, we evaluate the performance of the proposed FedSatBF framework in two representative coherent-block windows within the DS pass period $T_{\mathtt{VIS}}$.

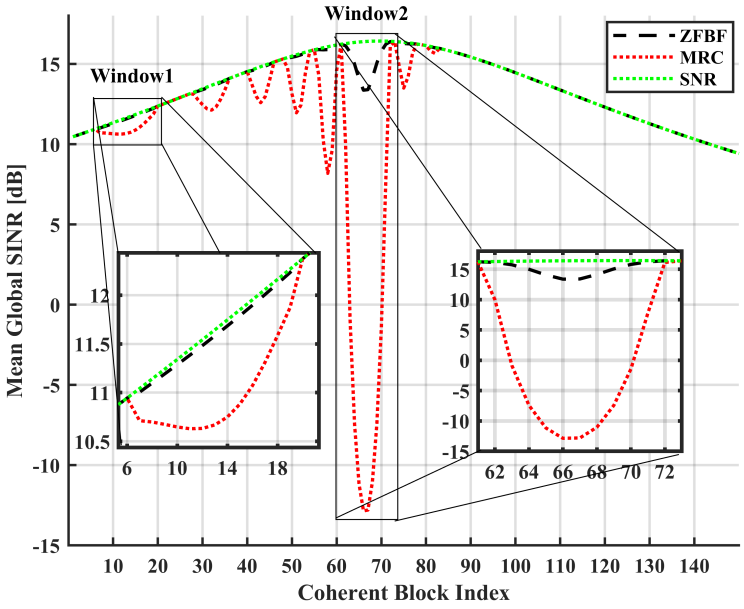


Figure 4.13: Mean global SINR of $T_{\mathtt{VIS}}$ across coherent blocks under MRC and ZFBF, and highlighted representative windows of interest.

Fig. 4.13 illustrates the simulated DS pass and the selected windows of interest (zoomed views),

Window 1 and Window 2, as the mean global SINR in each coherent-block $T_{\mathtt{COH}}$ and a total of $N_{\mathtt{COHs}} = 150$. Similar to the results in Section 4.5.2, the ZFBF and MRC benchmarks characterize the corresponding optimal-interference-aware and non-interference-aware beamforming performance, respectively. The Signal-to-Noise (SNR) curve here reflects the theoretical interference-free MRC beamforming performance. Here, **Window 1** corresponds to moderate interference conditions with gradually varying link quality, whereas **Window 2** captures a severe interference and in-line event where the MRC benchmark experiences a pronounced SINR collapse. These windows are selected to generate representative interference patterns and channel realizations used in subsequent FedSatBF performance evaluation.

In the next part, we evaluate the sensitivity of the proposed FedSatBF framework to key FL hyperparameters by comparing two representative configurations,

- **Config.1**: $N_{\mathtt{CRs}} = 10, N_{\mathtt{LEs}} = 12, N_{k,\tau}^{\mathrm{tr}} = 12, B = 1,$
- **Config.2**: $N_{\mathtt{CRs}} = 3, N_{\mathtt{LEs}} = 5, N_{k,\tau}^{\mathrm{tr}} = 6, B = 1.$

Config. 1 represents a relatively high training budget per coherence block, with more communication rounds and more extensive local training per-VUT. This setup is expected to yield near-optimal beamforming performance at the cost of increased computation. Second, Config. 2 reduces both the number of communication rounds and the amount of local computation per round per-VUT, approximating a lightweight training regime that better aligns with practical constraints on per-VUT processing time and limited coherence block duration.

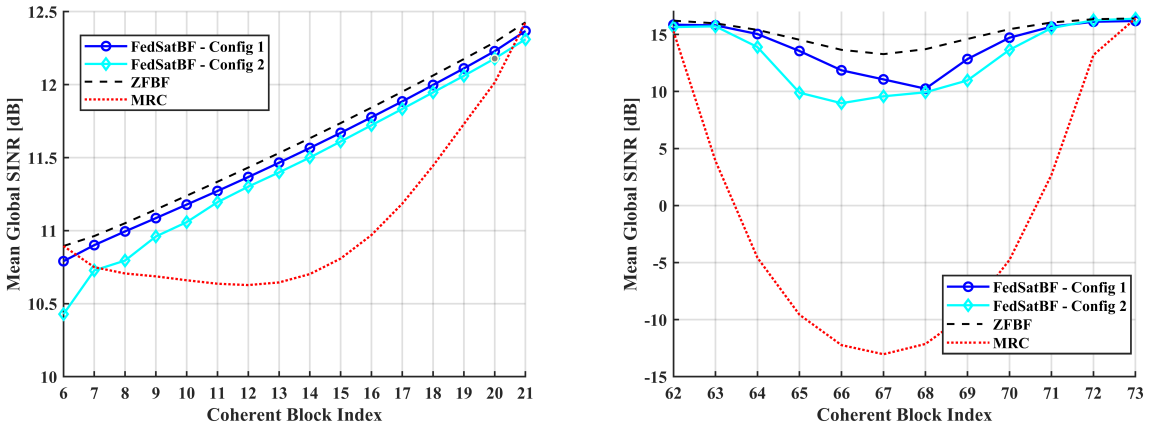


Figure 4.14: FedSatBF performance on $T_{\mathtt{VIS}}$ comparison within: (a) Window 1; (b) Window 2.

Figs. 4.14 show the FedSatBF performance comparison within representative $T_{\mathtt{VIS}}$ windows

(cases), Window 1, and Window 2, as in the zoomed-in views of Fig. 4.13. The proposed FedSatBF framework consistently achieves mean SINR performance comparable to ZFBF across both windows, demonstrating robustness in moderate-to-severe CFI cases. Config 1, which employs more communication rounds and local training updates, more closely tracks the ZFBF benchmark. In contrast, Config 2 incurs a modest SINR loss (e.g., 1-3 dB) due to its reduced training budget, yet it still significantly outperforms MRC in both coherent-block windows (cases). The studied configurations allowed us to investigate the performance–complexity trade-off inherent in the FedSatBF framework. By comparing the high-budget (Config. 1) versus a low-budget setting (Config. 2) within the same coherence interval $T_{\mathtt{COH}}$, we quantify how reductions in training data, local updates per-round per-VUT, and round count impact the convergence behavior and resulting SINR performance of FedSatBF. This result indicates that reducing the number of communication rounds does not significantly degrade performance, provided that local training intensity remains sufficient. This observation confirms that FedSatBF can operate within short coherence intervals without sacrificing interference suppression capability.

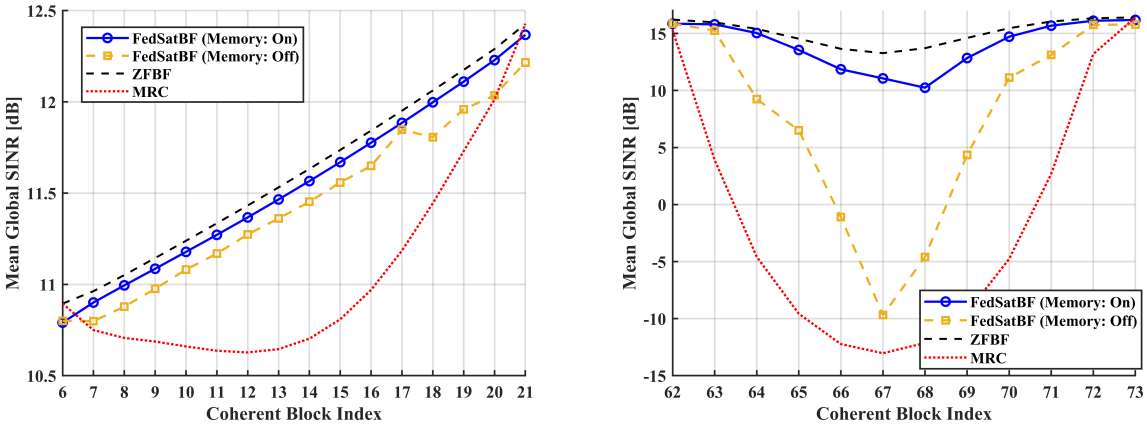


Figure 4.15: The effect of global model sharing (Memory: On) between Coherent-blocks: (a) Window 1; (b) Window 2.

It worth mentioning that during both windows we assume the DS memorizes the last global model and used it as an initial model for the next coherence block $T_{\mathtt{COH}}^{(t+1)}$ of future interference instances, e.g., $\mathbf{\Theta}_g^*(T_{\mathtt{COH}}^{(t)}) \rightarrow \mathbf{\Theta}_g^1(T_{\mathtt{COH}}^{(t+1)})$, as explained in Algorithm 4. Otherwise, the performance would not be consistent, as we show in Fig. 4.15 using Config.1, sharing the last global model between coherent-blocks tends to give better and consistent results than starting from a shared initial model.

4.6 Chapter Conclusion

In this work, we propose FedSatBF, a federated learning–enabled collaborative beamforming framework for NGSO direct-to-vehicle communications. By leveraging local training at vehicular user terminals and federated aggregation at the serving satellite, FedSatBF enables effective blind adaptive beamforming and spatial nulling of co-frequency interference without sharing raw data or requiring explicit interference channel state information. Simulation results show that FedSatBF achieves near-optimal SINR performance compared to zero-forcing beamforming, while significantly outperforming conventional maximum-ratio combining. Importantly, we demonstrated that near-optimal performance can be attained with a limited number of communication rounds and lightweight local training settings, enabling real-time adaptation within practical channel coherence constraints. Moreover, the global model exhibits strong generalization to non-participating vehicular terminals, highlighting the scalability and robustness of the proposed framework.

Future work may investigate hierarchical federated learning architectures to mitigate further data heterogeneity across large coverage areas, as well as asynchronous and resource-aware user selection strategies. Additional directions include integrating predictive features based on satellite ephemeris and vehicular mobility, hybrid AI-classical beamforming designs, and large-scale evaluations under more realistic NGSO channel impairments such as Doppler residuals, handovers, and intentional/jamming interference.

Chapter 5

Conclusions and Future Research

This thesis establishes a unified, data-driven framework for interference detection and mitigation in next-generation satellite communication systems (SatComs). It demonstrates that Artificial Intelligence (AI)-enabled techniques can overcome the fundamental limitations of conventional model-based methods, particularly under highly dynamic non-geostationary satellite orbits (NGSOs) orbital conditions compared to Earth synchronous geostationary satellite orbits (GSOs). This chapter presents the main conclusions of the thesis and suggests potential directions for future research.

5.1 Main Conclusions

By introducing generative-AI (GenAI) detectors, attention-based adaptive beamformers, and federated learning (FL) frameworks, this thesis shows that co-frequency interference (CFI) management in SatComs can be made robust, scalable, and largely estimation-free, paving the way toward more autonomous and intelligent SatCom operation.

- Chapter 1 presented a comprehensive introduction on SatComs from general overview, link budget analysis, radio spectrum, its role in the 6-th generation (6G) mobile communication era, and a summary of AI and its applications in SatComs. This chapter also discusses interference problems in SatComs and their management strategies. Then it presented the motivation and limitations of existing studies, research gap, research questions, thesis methodologies, and an overview of the thesis contributions and overall structure.

- Chapter 2 introduced GenAI-based interference detection models for NGSO-to-GSO coexistence. By leveraging variational autoencoders (VAEs) and a transformer-based interference detector (TrID), interference was identified through reconstruction errors of the expected

interference-free GSO signal. Using realistic orbital dynamics and signal models, the proposed approach significantly outperformed conventional energy detectors and classical autoencoder baselines, showing an increase of up to 31.23% in interference detection accuracy, demonstrating that GenAI models provide a powerful and flexible mechanism for anomaly-based interference detection in non-stationary satellite environments.

- Chapter 3 proposed an attention-based blind adaptive beamformer (AttBF) for NGSO-to-NGSO interference mitigation at user terminals (UTs). The model operates directly on estimation-free sample covariance matrices and is trained in a self-supervised manner using Signal-to-Interference-plus-Noise Ratio (SINR) feedback. The results showed that AttBF achieves superior interference suppression compared to classical beamforming techniques, such as zero-forcing beamforming (ZFBF) and sample matrix inversion (SMI), and deep learning baselines, which offer near-optimal SINR performance with the fastest inference ($\sim 4.5\mu s$), validating the effectiveness of attention mechanisms for spatial interference mitigation in NGSO systems.

- Finally, Chapter 4 developed FedSatBF, a FL–enabled collaborative beamforming framework for direct satellite-to-vehicle communications (DS2V). This work is also related to the previous chapter, as it addresses the AttBF model generalization aspects and the various users' training capabilities. By distributing the learning process across vehicular user terminals (VUTs) and aggregating models at the serving satellite, FedSatBF enabled scalable and privacy-preserving interference mitigation without sharing raw signal data or requiring explicit interference channel knowledge. The framework achieved near-optimal performance, within 0.1 [dB] SINR difference of ZFBF, and strong generalization to non-participating users, and favorable performance versus complexity trade-offs, demonstrating the practicality of federated intelligence for large-scale NGSO deployments.

5.2 Future Work

Each study in this thesis establishes a building block toward fully intelligent satellite interference management: Chapter 2 addresses interference awareness, Chapter 3 enables local interference mitigation, and Chapter 4introduces collaborative intelligence. Building on the foundations established here, future research can be divided into two complementary directions: (i) *possible extensions*, which naturally build upon and enhance the proposed frameworks, and (ii) *open research directions*, which explore more visionary and long-term challenges toward fully autonomous SatCom systems.

5.2.1 Possible Extensions

These extensions aim to strengthen the proposed methodologies in this thesis and bring them closer to real operational deployment.

- **Enhanced interference detection robustness**: In Chapter 2, the interference detection frameworks were developed under ideal synchronization assumptions. Future work should extend these models to practical receiver conditions by incorporating time misalignment, synchronization errors, and Doppler-induced distortions, which may otherwise be falsely interpreted as interference [160, 161]. Moreover, integrating cyclostationarity-based features (e.g., Cyclic Autocorrelation Function (CAF) and Spectral Correlation Function (SCF) [162]) into the detection pipeline can further improve discrimination between desired signals, interference, and noise under non-ideal conditions.

- **Lightweight AI-based beamformer**: While Chapter 3 focused on blind adaptive beamforming, an alternative extension is to formulate beam selection as a supervised classification problem over a predefined beamforming codebook [163], but at the UTs side. Such an approach could reduce offline training complexity and enable faster online deployment (inference) on low-power UTs while maintaining acceptable interference suppression performance.

- **System-aware and scalable federated learning**: The FedSatBF framework in Chapter 4 was based on cluster-based FL (CFL) and federated averaging (FedAvg) aggregation. The framework scalability can be further enhanced by incorporating,

    1. *Resource-aware FL*: where optimization-based FL methods, such as FedProx [164], improve upon the standard FedAvg by adding a proximal terms, making global aggregation robust to data heterogeneity (different data types/amounts per-user) and system constraints (users varying in power/availability).
    2. *Asynchronous FL*: schemes that handle communications delayed and irregular model updates [165], which allow users to participate in global model updates without waiting for global synchronization, enabling faster convergence and better resilience to stragglers.
    3. *Hierarchical FL (HFL)*: a multi-tier learning architecture where high-power UTs assist lower-power UTs by forming hierarchical aggregation levels [166]. This structure can significantly improve scalability and reduce communication overhead.

4. *Security-aware aggregation*: by developing global aggregation strategies beyond the physical layer, FL can become more resilient to unreliable, faulty, or malicious local models. This includes Byzantine-resilient aggregation, anomaly detection on model updates, and trust-aware weighting mechanisms [167], to ensure the integrity and reliability of collaborative learning in large-scale NGSO deployments.

- **End-to-end AI-based interference-aware receivers**: This thesis addressed detection and mitigation through separate models. A natural extension is an integrated end-to-end receiver capable of jointly detecting, classifying, localizing, and suppressing interference, as well as identifying any information about their origin (e.g., which system is causing interference). Such receivers would enable fully autonomous interference management pipelines.

- **Toward operational deployment**: While this thesis relies on highly realistic simulations and orbital dynamics, the transition toward practical deployment requires a progressive validation pipeline. Future work may include:

  1. *Improved simulation fidelity*: extending the current simulation assumptions to incorporate additional real-world constraints such as residual Doppler shifts [130], Non-Line-of-Sight (NLoS) propagation [76], and hardware impairments [168]. This will further narrow the gap between synthetic and operational conditions.

  2. *Real-world validation*: validating the proposed frameworks using over-the-air measurements from antenna testbeds, software-defined radio (SDR) platforms, or operational satellite terminals. For instance, real antenna data from a dual Ku/Ka-band tracking antenna [169] can be leveraged to experimentally evaluate the GenAI detector of Chapter 2. Such validation is essential to assess robustness under practical hardware impairments and environmental conditions.

  3. *Collaboration with satellite operators*: establishing partnerships with satellite operators and research institutions to access real satellite telemetry, antenna measurements, and interference logs. This would enable large-scale experimental validation, facilitate dataset curation for the community, and accelerate the translation of AI-based interference management techniques into operational SatCom systems.

5.2.2 Open Research Directions

Building on the proven capability of AI to manage interference, longer-term research can explore its role in more complex, system-level challenges.

- **Hybrid AI–classical interference management**: Combining AI with classical signal processing remains a promising extension of the proposed interference management frameworks. Hybrid designs, such as using AI to estimate the number of interference sources and/or interference direction of arrival (DoA) followed by classical beamformer [170], offer a compromise between robustness and computational efficiency, although latency constraints must be carefully addressed. Model-driven deep unfolding methods can also be utilized to embed DoA estimation algorithms (e.g., MUSIC-based) into trainable networks, yielding physics-aware and interpretable models [171].

- **Next Generation Satcom-TNs integration**: In this thesis, we focus on interference between satellite operators, but the integrated frameworks can be extended to manage co-existence interference in the future integration of non-terrestrial and terrestrial networks (NTNs–TNs). For instance, both systems could collaboratively implement AI-based dynamic spectrum management (DSM) [172], where intelligent agents (at satellite gateways, or TNs base stations) use federated or reinforcement learning (RL) to predict spectrum occupancy and proactively adapt spectrum access to avoid interfering with each other. This approach aligns as well with emerging Open-Radio Access Network (O-RAN) architectures [173] as it would enable proactive cross-domain spectrum sharing, improved spectral efficiency, and intelligent coexistence under highly dynamic, heterogeneous conditions.

- **AI-based anti-jamming and adversarial resilience**: While this thesis focused on unintentional CFI, intentional interference poses a fundamentally different threat [32]. Researchers already investigated AI-based anti-jamming methods for Global Navigation Satellite Systems (GNSS) [174], but there is a need for advanced AI-based methods capable of detection, classification, localization, and suppression of jammers in SatCom systems. Generative adversarial networks (GANs) could be used to model adversarial interference, train robust detectors, and reconstruct legitimate signals [175]. Federated intelligence could further enable the rapid dissemination of anti-jamming strategies across users and satellites [176]. Deep reinforcement learning (DRL) can also be used to learn optimal anti-jamming policies in environments where the jammer's behavior is unknown and time-varying [177].

- **Semantic Reasoning for Network Autonomy**: Future satellite networks can benefit from semantic intelligence and foundation models, such as large language models (LLMs), to enable high-level reasoning, decision making, and autonomous control [178]. These models can operate on semantic information extracted from system telemetry, signals metadata, regulatory constraints, and network feedback to orchestrate spectrum access, federated learning configurations, and interference management strategies, enabling autonomous and self-optimizing satellite communication systems.

Bibliography

[1] Y. Xiao, Z. Ye, M. Wu, H. Li, M. Xiao, M.-S. Alouini, A. Al-Hourani, and S. Cioni, "Space-Air-Ground Integrated Wireless Networks for 6G: Basics, Key Technologies, and Future Trends," *IEEE Journal on Selected Areas in Communications*, vol. 42, no. 12, pp. 3327–3354, 2024.

[2] M. M. Azari, S. Solanki, S. Chatzinotas, O. Kodheli, H. Sallouha, A. Colpaert, J. F. Mendoza Montoya, S. Pollin, A. Haqiqatnejad, A. Mostaani, E. Lagunas, and B. Ottersten, "Evolution of Non-Terrestrial Networks From 5G to 6G: A Survey," *IEEE Communications Surveys & Tutorials*, vol. 24, no. 4, pp. 2633–2672, 2022.

[3] E. Lagunas, S. Chatzinotas, and B. Ottersten, "Low-Earth Orbit Satellite Constellations for Global Communication Network Connectivity," *Nature Reviews Electrical Engineering*, vol. 1, no. 10, pp. 656–665, 2024.

[4] I. Leyva-Mayorga, B. Soret, M. Röper, D. Wübben, B. Matthiesen, A. Dekorsy, and P. Popovski, "LEO Small-Satellite Constellations for 5G and Beyond-5G Communications," *IEEE Access*, vol. 8, pp. 184 955–184 964, 2020.

[5] H. Al-Hraishawi, H. Chougrani, S. Kisseleff, E. Lagunas, and S. Chatzinotas, "A survey on nongeostationary satellite systems: The communication perspective," *IEEE Communications Surveys & Tutorials*, vol. 25, no. 1, pp. 101–132, 2023.

[6] J. Heo, S. Sung, H. Lee, I. Hwang, and D. Hong, "MIMO Satellite Communication Systems: A Survey From the PHY Layer Perspective," *IEEE Communications Surveys & Tutorials*, vol. 25, no. 3, pp. 1543–1570, 2023.

[7] A. Bakambekova, N. Kouzayha, and T. Al-Naffouri, "On the Interplay of Artificial Intelligence and Space-Air-Ground Integrated Networks: A Survey," *IEEE Open Journal of the Communications Society*, vol. 5, pp. 4613–4673, 2024.

[8] S. Mahboob and L. Liu, "Revolutionizing Future Connectivity: A Contemporary Survey on AI-Empowered Satellite-Based Non-Terrestrial Networks in 6G," *IEEE Communications Surveys& Tutorials*, vol. 26, no. 2, pp. 1279–1321, 2024.

[9] A. Adam, E. Lagunas, M. Samy, A. Saifaldawla, and S. Chatzinotas, "Generative AI for non-terrestrial networks: design, applications, and challenges," *EURASIP Journal on Wireless Communications and Networking*, 2025.

[10] N. Heydarishahreza, T. Han, and N. Ansari, "Spectrum sharing and interference management for 6G LEO Satellite-Terrestrial network integration," *IEEE Communications Surveys & Tutorials*, vol. 27, no. 5, pp. 2794–2825, 2025.

[11] O. Kodheli, E. Lagunas, N. Maturo, S. K. Sharma, B. Shankar, J. F. M. Montoya, J. C. M. Duncan, D. Spano, S. Chatzinotas, S. Kisseleff, J. Querol, L. Lei, T. X. Vu, and G. Goussetis, "Satellite Communications in the New Space Era: A Survey and Future Challenges," *IEEE Communications Surveys & Tutorials*, vol. 23, no. 1, pp. 70–109, 2021.

[12] M. Giordani and M. Zorzi, "Non-terrestrial networks in the 6G era: Challenges and opportunities," *IEEE Network*, vol. 35, no. 2, pp. 244–251, 2021.

[13] W. L. Stutzman and G. A. Thiele, *Antenna theory and design*. John Wiley & Sons, 2012.

[14] A. Goldsmith, *Wireless communications*. Cambridge university press, 2005.

[15] K.-B. Yu, "Adaptive beamforming for satellite communication with selective earth coverage and jammer nulling capability," *IEEE Transactions on Signal Processing*, vol. 44, no. 12, pp. 3162–3166, 1996.

[16] L. C. Godara, *Smart Antennas*. CRC Press, 2004.

[17] Starlink, *Starlink Standard Kit Installation Guide*, SpaceX, 2024. [Online]. Available: https://api.starlink.com/public-files/installation_guide_standard_kit.pdf

[18] Z. M. Bakhsh, Y. Omid, G. Chen, F. Kayhan, Y. Ma, and R. Tafazolli, "Multi-Satellite MIMO systems for direct Satellite-to-device communications: A survey," *IEEE Communications Surveys & Tutorials*, vol. 27, no. 3, pp. 1536–1564, 2025.

[19] Thales, "Earth fixed vs. Earth moving cells in NTN LEO," 3rd Generation Partnership Project (3GPP), Reno, USA, 3GPP TSG-RAN WG2 Meeting #108 Contribution R2-1916351, November 2019. [Online]. Available: https://www.3gpp.org/ftp/tsg_ran/WG2_RL2/TSGR2_108/Docs/R2-1916351.zip

[20] A. I. Perez-Neira, M. A. Vazquez, M. B. Shankar, S. Maleki, and S. Chatzinotas, "Signal processing for high-throughput satellites: Challenges in new interference-limited scenarios," *IEEE Signal Processing Magazine*, vol. 36, no. 4, pp. 112–131, 2019.

[21] B. Van Veen and K. Buckley, "Beamforming: a versatile approach to spatial filtering," *IEEE ASSP Magazine*, vol. 5, no. 2, pp. 4–24, 1988.

[22] M. Fakharzadeh, S. H. Jamali, P. Mousavi, and S. Safavi-Naeini, "Fast Beamforming for Mobile Satellite Receiver Phased Arrays: Theory and Experiment," *IEEE Transactions on Antennas and Propagation*, vol. 57, no. 6, pp. 1645–1654, 2009.

[23] Q. Li, M. El-Hajjar, K. Cao, C. Xu, H. Haas, and L. Hanzo, "Holographic metasurface-based beamforming for multi-altitude leo satellite networks," *IEEE Transactions on Wireless Communications*, vol. 24, no. 4, pp. 3103–3116, 2025.

[24] H. Friis, "A note on a simple transmission formula," *Proceedings of the IRE*, vol. 34, no. 5, pp. 254–256, 1946.

[25] E. Cianca, T. Rossi, A. Yahalom, Y. Pinhasi, J. Farserotu, and C. Sacchi, "Ehf for satellite communications: The new broadband frontier," *Proceedings of the IEEE*, vol. 99, no. 11, pp. 1858–1881, 2011.

[26] R. Kreutel, D. DiFonzo, W. English, and R. Gruner, "Antenna technology for frequency reuse satellite communications," *Proceedings of the IEEE*, vol. 65, no. 3, pp. 370–378, 1977.

[27] International Telecommunication Union, *Radio Regulations, Edition of 2024*. ITU, 2024, contient les textes adoptés par la Conférence Mondiale des Radiocommunications (WRC-95) et révisés par les conférences ultérieures (WRC-97, WRC-03, WRC-07, WRC-12, WRC-15, WRC-19, WRC-23). [Online]. Available: https://www.itu.int/pub/R-REG-RR

[28] Y. Ahmed and D. Grace, "Overview of dynamic spectrum sharing between leo satellites and mobile networks: Enabling seamless connectivity and coexistence in 6g," *IEEE Access*, vol. 13, pp. 162 681–162 695, 2025.

[29] F. Ortiz, E. Lagunas, A. Saifaldawla, M. Jalali, L. Emiliani, and S. Chatzinotas, "Emerging ngso constellations: spectral coexistence with gso satellite communication systems," *Frontiers in Communications and Networks*, vol. 7, 2026.

[30] F. Fourati and M.-S. Alouini, "Artificial intelligence for satellite communication: A review," *Intelligent and Converged Networks*, vol. 2, no. 3, pp. 213–243, 2021.

[31] F. Ortiz, E. Lagunas, J. Querol, and S. Chatzinotas, "Chapter 15 - artificial intelligence in non-terrestrial networks: innovations, challenges, and the road ahead," in *Non-Terrestrial Networks*, M. Z. Shakir and A. Kaushik, Eds. Academic Press, 2026, pp. 353–371.

[32] P. Henarejos, M. A. Vazquez, and A. I. Perez-Neira, "Deep learning for experimental hybrid terrestrial and satellite interference management," in *2019 IEEE 20th International Workshop on Signal Processing Advances in Wireless Communications (SPAWC)*. IEEE, Jul. 2019.

[33] S. Semanjski, I. Semanjski, W. De Wilde, and A. Muls, "Use of supervised machine learning for gnss signal spoofing detection with validation on real-world meaconing and spoofing data—part i," *Sensors*, vol. 20, no. 4, p. 1171, 2020.

[34] L. Yang, X. Gu, and H. Shi, "A noval satellite network traffic prediction method based on gcn-gru," in *2020 International Conference on Wireless Communications and Signal Processing (WCSP)*, 2020, pp. 718–723.

[35] Y. Zhang, Y. Wu, A. Liu, X. Xia, T. Pan, and X. Liu, "Deep learning-based channel prediction for leo satellite massive mimo communication system," *IEEE Wireless Communications Letters*, vol. 10, no. 8, pp. 1835–1839, 2021.

[36] A. Guidotti and A. Vanelli-Coralli, "Clustering strategies for multicast precoding in multibeam satellite systems," *International Journal of Satellite Communications and Networking*, vol. 38, no. 2, pp. 85–104, 2020.

[37] A. Saifaldawla, F. Ortiz, E. Lagunas, and S. Chatzinotas, "Convolutional autoencoders for non-geostationary satellite interference detection," in *2024 IEEE International Conference on Communications Workshops (ICC Workshops)*, 2024, pp. 1334–1339.

[38] F. G. Ortiz-Gomez, L. Lei, E. Lagunas, R. Martinez, D. Tarchi, J. Querol, M. A. Salas-Natera, and S. Chatzinotas, "Machine learning for radio resource management in

multibeam geo satellite systems," *Electronics*, vol. 11, no. 7, 2022. [Online]. Available: https://www.mdpi.com/2079-9292/11/7/992

[39] G. Fontanesi, F. Ortíz, E. Lagunas, L. M. Garcés-Socarrás, V. M. Baeza, M. Á. Vázquez, J. A. Vásquez-Peralvo, M. Minardi, H. N. Vu, P. J. Honnaiah *et al.*, "Artificial intelligence for satellite communication: A survey," *IEEE Communications Surveys & Tutorials*, 2025.

[40] X. Hu, Y. Zhang, X. Liao, Z. Liu, W. Wang, and F. M. Ghannouchi, "Dynamic beam hopping method based on multi-objective deep reinforcement learning for next generation satellite broadband systems," *IEEE Transactions on Broadcasting*, vol. 66, no. 3, pp. 630–646, 2020.

[41] X. Zhang, J. Liu, R. Zhang, Y. Huang, J. Tong, N. Xin, L. Liu, and Z. Xiong, "Energy-efficient computation peer offloading in satellite edge computing networks," *IEEE Transactions on Mobile Computing*, vol. 23, no. 4, pp. 3077–3091, 2024.

[42] D. Zhao, H. Qin, N. Xin, and B. Song, "Flexible resource management in high-throughput satellite communication systems: A two-stage machine learning framework," *IEEE Transactions on Communications*, vol. 71, no. 5, pp. 2724–2739, 2023.

[43] A. Saifaldawla, E. Lagunas, F. Ortiz, A. B. M. Adam, and S. Chatzinotas, "Smartut: Receive beamforming for spectral coexistence of NGSO Satellite systems," in *2025 28th International Workshop on Smart Antennas (WSA)*, 2025, pp. 195–200.

[44] A. Saifaldawla, F. Ortiz, E. Lagunas, and S. Chatzinotas, "Attention-based blind adaptive receive beamforming for interference limited NGSO Satellite systems," *IEEE Open Journal of the Communications Society*, vol. 6, pp. 8946–8964, 2025.

[45] A. Farajzadeh, A. Yadav, and H. Yanikomeroglu, "Federated learning in NTN: Design, architecture, and challenges," *IEEE Communications Magazine*, vol. 63, no. 6, pp. 26–33, 2025.

[46] B. Matthiesen, N. Razmi, I. Leyva-Mayorga, A. Dekorsy, and P. Popovski, "Federated learning in Satellite constellations," *IEEE Network*, vol. 38, no. 2, pp. 232–239, 2024.

[47] 3GPP, "Summary of Rel-18 Work Items," 2023. [Online]. Available: https://www.3gpp.org/specifications-technologies/releases/release-18

[48] ——, "Release 19 Advancing 5G towards 6G," 2025. [Online]. Available: https://www.3gpp.org/specifications-technologies/releases/release-19

[49] A. Stroescu and A. Franchi, "Converging Earth and Space: AI-Driven TN/NTN Connectivity," European Space Agency (ESA), Tech. Rep., May 2025, Space for 5G/6G and Sustainable Connectivity. [Online]. Available: https://connectivity.esa.int/wp-content/uploads/2026/01/AI-Driven-TN-NTN-Connectivity-1.pdf

[50] ITU, "Rules of procedure," ITU, Geneva, Switzerland, Tech. Rep., 2009.

[51] R. Acharya, "Chapter 8 - noise, multipath and interference," in *Satellite Signal Propagation, Impairments and Mitigation*, R. Acharya, Ed. Academic Press, 2017, pp. 247–278. [Online]. Available: https://www.sciencedirect.com/science/article/pii/B9780128097328000089

[52] ITU, "Radio regulations," ITU, Geneva, Switzerland, Tech. Rep., 2020.

[53] R. Morales-Ferre, P. Richter, E. Falletti, A. de la Fuente, and E. S. Lohan, "A survey on coping with intentional interference in satellite navigation for manned and unmanned aircraft," *IEEE Communications Surveys & Tutorials*, vol. 22, no. 1, pp. 249–291, 2020.

[54] E. Younesian, E. Fettes, P. G. Madoery, J. Hosek, and H. Yanikomeroglu, "Guardians of connectivity: Navigating and mitigating nonmalicious disruptions in satellite networks," *IEEE Aerospace and Electronic Systems Magazine*, vol. 40, no. 3, pp. 20–32, 2025.

[55] F. Öztürk, E. Aydın, and A. Kara, "Comparative assessment and performance analysis of interference mitigation techniques for co-existent non-geostationary and geostationary satellites," *International Journal of Communication Systems*, vol. 37, no. 18, p. e5956, 2024.

[56] J. P. Wonjae Shin and H. Lee, "Survey on interference management for multibeam leo satellite networks: Technology, challenges, and solutions," *Journal of Space Security*, vol. 1, no. 1, pp. 19–26, 2024. [Online]. Available: https://cdn.apub.kr/journalsite/sites/JOSS/2024-001-01/N0670010102/N0670010102.pdf

[57] Y. He, Y. Li, and H. Yin, "Co-frequency interference analysis and avoidance between NGSO constellations: Challenges, techniques, and trends," *China Communications*, vol. 20, no. 7, pp. 1–14, 2023.

[58] M. T. Nguyen and L. B. Le, "Adjacent channel interference cancellation for robust spectrum sharing in satellite communications systems," in *2017 IEEE 28th Annual International Symposium on Personal, Indoor, and Mobile Radio Communications (PIMRC)*, 2017, pp. 1–5.

[59] J. Yun, B.-J. Ku, D. Oh, and C. Joo, "Hierarchical learning for interference management in multi-user leo satellite networks," *Journal of Communications and Networks*, vol. 27, no. 2, pp. 119–126, 2025.

[60] J. Winters, "Differential detection with intersymbol interference and frequency uncertainty," *IEEE Transactions on Communications*, vol. 32, no. 1, pp. 25–33, 1984.

[61] M. Jia, X. Zhang, X. Gu, Q. Guo, Y. Li, and P. Lin, "Interbeam interference constrained resource allocation for shared spectrum multibeam satellite communication systems," *IEEE Internet of Things Journal*, vol. 6, no. 4, pp. 6052–6059, 2019.

[62] International Telecommunication Union, *Final Acts: World Radiocommunication Conference (WRC-23)*. Geneva: International Telecommunication Union, 2023. [Online]. Available: http://handle.itu.int/11.1002/pub/8225d4fb-en

[63] W. Wiltshire, "Application for fixed satellite service by space exploration holdings, LLC," SAT-LOA20200526-00055 / SATLOA2020052600055, 2020.

[64] Weimer, Brian D., "Application for fixed satellite service by worldvu satellites limited, debtor-in-possession," SAT-MPL-20200526-00062 / SATMPL2020052600062, 2023.

[65] M. Jalali, F. G. Ortiz-Gomez, E. Lagunas, S. Kisseleff, L. Emiliani, and S. Chatzinotas, "Radio regulation compliance of NGSO constellations' interference towards GSO ground stations," in *2022 IEEE 33rd Annual International Symposium on Personal, Indoor and Mobile Radio Communications (PIMRC)*, 2022, pp. 1425–1430.

[66] C. Braun, A. M. Voicu, L. Simić, and P. Mähönen, "Should We Worry About Interference in Emerging Dense NGSO Satellite Constellations?" in *2019 IEEE International Symposium on Dynamic Spectrum Access Networks (DySPAN)*, 2019, pp. 1–10.

[67] S. Tonkin and J. P. De Vries, "Newspace spectrum sharing: Assessing interference risk and mitigations for new satellite constellations," in *TPRC 46: The 46th Research Conference on Communication, Information and Internet Policy 2018*, 2018.

[68] FCC, "FCC Proposes Innovative Small Cell Use in 3.5 GHz Band," Online, 2012. [Online]. Available: http://www.fcc.gov/document/fcc-proposes-innovative-small-celluse-35-ghz-band

[69] E. Lagunas, S. K. Sharma, S. Maleki, S. Chatzinotas, and B. Ottersten, "Resource allocation for cognitive satellite communications with incumbent terrestrial networks," *IEEE Transactions on Cognitive Communications and Networking*, vol. 1, no. 3, pp. 305–317, 2015.

[70] C. Wang, D. Bian, S. Shi, J. Xu, and G. Zhang, "A novel cognitive satellite network with GEO and LEO broadband systems in the downlink case," *IEEE Access*, vol. 6, pp. 25 987–26 000, 2018.

[71] C. Politis, S. Maleki, C. Tsinos, S. Chatzinotas, and B. Ottersten, "On-board the satellite interference detection with imperfect signal cancellation," in *2016 IEEE 17th International Workshop on Signal Processing Advances in Wireless Communications (SPAWC)*, 2016, pp. 1–5.

[72] L. Xie, Y. Zhuang, X. Zhuang, and X. Zeng, "Satellite interference signal classification using improved mlp model," in *2022 IEEE International Conference on Unmanned Systems (ICUS)*, 2022, pp. 635–640.

[73] C. Hao, D. Feng, Q. Zhang, and X.-G. Xia, "Interference geolocation in satellite communications systems: An overview," *IEEE Vehicular Technology Magazine*, vol. 16, no. 1, pp. 66–74, 2021.

[74] S. K. Sharma, S. Chatzinotas, J. Grotz, and B. Ottersten, "3d beamforming for spectral coexistence of satellite and terrestrial networks," in *2015 IEEE 82nd Vehicular Technology Conference (VTC2015-Fall)*, 2015, pp. 1–5.

[75] A. U. Makarfi and K. A. Hamdi, "Interference analysis of energy detection for spectrum sensing," *IEEE Transactions on Vehicular Technology*, vol. 62, no. 6, pp. 2570–2578, 2013.

[76] L. You, K.-X. Li, J. Wang, X. Gao, X.-G. Xia, and B. Ottersten, "Massive MIMO Transmission for LEO Satellite Communications," *IEEE Journal on Selected Areas in Communications*, vol. 38, no. 8, pp. 1851–1865, 2020.

[77] A. B. Gershman, N. D. Sidiropoulos, S. Shahbazpanahi, M. Bengtsson, and B. Ottersten, "Convex Optimization-Based Beamforming," *IEEE Signal Processing Magazine*, vol. 27, no. 3, pp. 62–75, 2010.

[78] L. Zhang, Z. Wei, L. Wang, X. Yuan, H. Wu, and W. Xu, "Spectrum sharing in the sky and space: a survey," *Sensors*, vol. 23, no. 1, p. 342, 2022.

[79] L. Pellaco, N. Singh, and J. Jalden, "Spectrum prediction and interference detection for satellite communications [international communications satellite systems conference]," in *Advances in Communications Satellite Systems. 37th International Communications Satellite Systems Conference (ICSSC-2019)*. Institution of Engineering and Technology, 2019.

[80] M. A. Vazquez, P. Henarejos, I. Pappalardo, E. Grechi, J. Fort, J. C. Gil, and R. M. Lancellotti, "Machine learning for satellite communications operations," *IEEE Communications Magazine*, vol. 59, no. 2, pp. 22–27, Feb. 2021.

[81] R. De Silva, S. R. Pokhrel, J. Kua, and S. Kandeepan, "Intelligent spectrum management in satellite communications," *arXiv preprint arXiv:2509.00286*, 2025.

[82] NewSpace, "Newspace index: Concise original overview of commercial satellite constellations," https://www.newspace.im/, 2024.

[83] SES Astra, "Response to ofcom's spectrum review: Annex 4 - satellite spectrum issues," Office of Communications (Ofcom), Consultation Response, 2004. [Online]. Available: https://www.ofcom.org.uk/siteassets/resources/documents/consultations/uncategorised/8137-spectrum-review/responses/ses_annex_4.pdf

[84] E. Lagunas, "FNR SmartSpace Project: Leveraging AI to Empower the Next Generation of Satellite Communications." [Online]. Available: https://fnr-smartspace-project.uni.lu/datasets/

[85] M. Jalali, F. Ortiz, E. Lagunas, S. Kisseleff, L. Emiliani, and S. Chatzinotas, "Joint power and tilt control in satellite constellation for NGSO-GSO interference mitigation," *IEEE Open Journal of Vehicular Technology*, vol. 4, pp. 545–557, 2023.

[86] ITU, "ITU member states agree on new global treaty to advance digital transformation." [Online]. Available: https://www.itu.int/en/mediacentre/Pages/PR-2023-12-15-WRC23-closing-ceremony.aspx

[87] D. Peng, D. He, Y. Li, and Z. Wang, "Integrating terrestrial and satellite multibeam systems toward 6G: Techniques and challenges for interference mitigation," *IEEE Wireless Communications*, vol. 29, no. 1, pp. 24–31, 2022.

[88] I. Goodfellow, J. Pouget-Abadie, M. Mirza, B. Xu, D. Warde-Farley, S. Ozair, A. Courville, and Y. Bengio, "Generative adversarial nets," *Advances in neural information processing systems*, vol. 27, 2014.

[89] D. P. Kingma and M. Welling, "Auto-encoding variational bayes," *arXiv preprint arXiv:1312.6114*, 2013.

[90] A. Vaswani, N. Shazeer, N. Parmar, J. Uszkoreit, L. Jones, A. N. Gomez, L. Kaiser, and I. Polosukhin, "Attention is All You Need," *Advances in neural information processing systems*, vol. 30, 2017.

[91] S. Kay, *Fundamentals of Statistical Signal Processing: Detection theory*, ser. Fundamentals of Statistical Si. Prentice-Hall PTR, 1998.

[92] J. Font-Segura, G. Vazquez, and J. Riba, "Nonuniform Sampling Walls in Wideband Signal Detection," *IEEE Transactions on Signal Processing*, vol. 62, no. 1, pp. 44–55, 2014.

[93] M. Lipski, S. Kompella, and R. Narayanan, "Practical Implementation of Adaptive Threshold Energy Detection using Software Defined Radio," *IEEE Transactions on Aerospace and Electronic Systems*, vol. 57, no. 2, pp. 1227–1241, 2021.

[94] ETSI, "ETSI: EN 302 307-2 digital video broadcasting (DVB)," *Second generation framing structure, channel coding and modulation systems for Broadcasting, Interactive Services, News Gathering and other broadband satellite applications Part II: S2-Extensions (DVB-S2X)*, pp. 13–24, 2014.

[95] F. Dimc, G. Baldini, and S. Kandeepan, "Experimental detection of mobile satellite transmissions with cyclostationary features," *International Journal of Satellite Communications and Networking*, vol. 33, no. 2, pp. 163–183, 2015.

[96] F. Ortiz, V. M. Baeza, L. M. Garces-Socarras, J. A. Vásquez-Peralvo, J. L. Gonzalez, G. Fontanesi, E. Lagunas, J. Querol, and S. Chatzinotas, "Onboard Processing in Satellite Communications Using AI Accelerators," *Aerospace*, vol. 10, no. 2, p. 101, Jan. 2023.

[97] A. Saifaldawla, F. G. Ortiz-Gomez, E. Lagunas, S. Daoud, and S. Chatzinotas, "NGSO-To-GSO satellite interference detection based on autoencoder," in *2023 IEEE 34th Annual International Symposium on Personal, Indoor and Mobile Radio Communications (PIMRC)*, 2023, pp. 1–7.

[98] J. D. Kraus and R. J. Marhefka, *Antennas for all applications*. SAO/NASA Astrophysics Data System, 2002.

[99] G. N. Watson, *A treatise on the theory of Bessel functions*. The University Press, 1922, vol. 2.

[100] S. Daoud, G. Eappen, F. Ortiz, E. Lagunas, W. Martins, and S. Chatzinotas, "CNN-Based on-board interference detection in satellite systems: An analysis of dataset impact on performance," in *2023 IEEE International Conference on Acoustics, Speech, and Signal Processing Workshops (ICASSPW)*, 2023, pp. 1–5.

[101] P. Welch, "The use of fast fourier transform for the estimation of power spectra: A method based on time averaging over short, modified periodograms," *IEEE Transactions on Audio and Electroacoustics*, vol. 15, no. 2, pp. 70–73, Jun. 1967.

[102] M. Inc., "Interference from satellite constellation on communications link - MATLAB & Simulink - MathWorks Benelux." [Online]. Available: https://nl.mathworks.com/help/satcom/ug/interference-from-satellite-constellation-on-comms-link.html

[103] CelesTrak, "Celestrak: Current GP element sets." [Online]. Available: https://celestrak.org/NORAD/elements/

[104] M. Sakurada and T. Yairi, "Anomaly detection using autoencoders with nonlinear dimensionality reduction," in *Proceedings of the MLSDA 2014 2nd Workshop on Machine Learning for Sensory Data Analysis*, ser. MLSDA'14. NY, USA: Association for Computing Machinery (ACM), 2014, p. 4–11.

[105] S. Kullback, *Information theory and statistics*. Courier Corporation, 1997.

[106] A. Tharwat, "Classification assessment methods," *Applied Computing and Informatics*, vol. 17, no. 1, p. 168–192, Jul. 2020. [Online]. Available: http://dx.doi.org/10.1016/j.aci.2018.08.003

[107] S. Schmidl, P. Wenig, and T. Papenbrock, "Anomaly detection in time series: a comprehensive evaluation," *Proceedings of the VLDB Endowment*, vol. 15, no. 9, pp. 1779–1797, 2022.

[108] SES, "SES Network Map." [Online]. Available: https://www.ses.com/sites/default/files/network_map/SES_NetworkMap_RGB_180827_Rise_BlueVersion-p.pdf

[109] ESA, "ESA - satellite frequency bands." [Online]. Available: https://www.esa.int/Applications/Connectivity_and_Secure_Communications/Satellite_frequency_bands

[110] ITU, "Allowable short-term error performance for a satellite hypothetical reference digital path." [Online]. Available: https://www.itu.int/dms_pubrec/itu-r/rec/s/R-REC-S.2099-0-201612-I!!PDF-E.pdf

[111] S. Varrette, H. Cartiaux, S. Peter, E. Kieffer, T. Valette, and A. Olloh, "Management of an Academic HPC & Research Computing Facility: The ULHPC Experience 2.0," in *Proc. of the 6th ACM High Performance Computing and Cluster Technologies Conf. (HPCCT 2022)*. Fuzhou, China: Association for Computing Machinery (ACM), July 2022.

[112] H. Urkowitz, "Energy detection of unknown deterministic signals," *Proceedings of the IEEE*, vol. 55, no. 4, pp. 523–531, 1967.

[113] H. L. Van Trees, *Optimum array processing: Part IV of detection, estimation, and modulation theory*. John Wiley & Sons, 2002.

[114] H. A. Kassir, Z. D. Zaharis, P. I. Lazaridis, N. V. Kantartzis, T. V. Yioultsis, and T. D. Xenos, "A Review of the State of the Art and Future Challenges of Deep Learning-Based Beamforming," *IEEE Access*, vol. 10, pp. 80 869–80 882, 2022.

[115] Y. Omid, M. Aristodemou, S. Lambotharan, M. Derakhshani, and L. Hanzo, "Reinforcement learning-based downlink transmit precoding for mitigating the impact of delayed CSI in satellite systems," *arXiv preprint arXiv:2410.21489*, 2024.

[116] M. S. Rahman, E. Onggosanusi, H. Si, and J. Cho, "CSI feedback based on space-frequency compression," in *2020 IEEE 17th Annual Consumer Communications & Networking Conference (CCNC)*, 2020, pp. 1–6.

[117] S. Lin, J. An, L. Gan, M. Debbah, and C. Yuen, "Stacked Intelligent Metasurface Enabled LEO Satellite Communications Relying on Statistical CSI," *IEEE Wireless Communications Letters*, vol. 13, no. 5, pp. 1295–1299, 2024.

[118] A. Saifaldawla, F. Ortiz, E. Lagunas, A. B. M. Adam, and S. Chatzinotas, "GenAI-Based Models for NGSO Satellites Interference Detection," *IEEE Transactions on Machine Learning in Communications and Networking*, vol. 2, pp. 904–924, 2024.

[119] H. Yang, K.-Y. Lam, J. Nie, J. Zhao, S. Garg, L. Xiao, Z. Xiong, and M. Guizani, "3D Beamforming Based on Deep Learning for Secure Communication in 5G and Beyond Wireless Networks," in *2021 IEEE Globecom Workshops (GC Wkshps)*, 2021, pp. 1–6.

[120] G. Konstantopoulos and Y. Louët, "Deep Learning Aided Beamforming for Downlink Non-Orthogonal Multiple Access Systems," *IEEE Open Journal of the Communications Society*, vol. 5, pp. 4337–4353, 2024.

[121] J. Kim, H. Lee, S.-E. Hong, and S.-H. Park, "Deep Learning Methods for Universal MISO Beamforming," *IEEE Wireless Communications Letters*, vol. 9, no. 11, pp. 1894–1898, 2020.

[122] K.-X. Li, L. You, J. Wang, X. Gao, C. G. Tsinos, S. Chatzinotas, and B. Ottersten, "Downlink Transmit Design for Massive MIMO LEO Satellite Communications," *IEEE Transactions on Communications*, vol. 70, no. 2, pp. 1014–1028, 2022.

[123] X. Xie, X. Ding, and G. Zhang, "Interference Mitigation via Beamforming for Spectrum-Sharing LEO Satellite Communication Systems," *IEEE Systems Journal*, vol. 17, no. 4, pp. 5822–5830, 2023.

[124] Z. Chen, L. Kuang, B. Liu, and Z. Ni, "Fast and Efficient Phase-Only Beam Nulling for NGSO Satellite Communication Systems," *IEEE Wireless Communications Letters*, vol. 13, no. 12, pp. 3261–3265, 2024.

[125] C. Vahapoglu, T. J. O'Shea, T. Roy, and S. Ulukus, "Deep learning based uplink multi-user simo beamforming design," in *2024 IEEE International Conference on Machine Learning for Communication and Networking (ICMLCN)*, 2024, pp. 329–333.

[126] P. Ramezanpour and M.-R. Mosavi, "Two-Stage Beamforming for Rejecting Interferences Using Deep Neural Networks," *IEEE Systems Journal*, vol. 15, no. 3, pp. 4439–4447, 2021.

[127] R. Giuliano, E. Innocenti, F. Mazzenga, A. Vizzarri, L. Di Nunzio, P. B. Divakarachari, and I. Habib, "Transformer Neural Network for Throughput Improvement in Non-Terrestrial Networks," in *2023 International Conference on Network, Multimedia and Information Technology (NMITCON)*, 2023, pp. 1–6.

[128] S. Zhang, S. Zhang, W. Yuan, and T. Q. S. Quek, "Transformer-Empowered Predictive Beamforming for Rate-Splitting Multiple Access in Non-Terrestrial Networks," *IEEE Transactions on Wireless Communications*, vol. 23, no. 12, pp. 19 776–19 788, 2024.

[129] O. E. Ayach, S. Rajagopal, S. Abu-Surra, Z. Pi, and R. W. Heath, "Spatially Sparse Precoding in Millimeter Wave MIMO Systems," *IEEE Transactions on Wireless Communications*, vol. 13, no. 3, pp. 1499–1513, 2014.

[130] W. Zhang, "Two-ray channel models with doppler effects for LEO satellite communications," *ITU Journal on Future and Evolving Technologies*, vol. 5, no. 2, pp. 243–259, 2024.

[131] 3GPP, "NR; Radio Resource Control (RRC); Protocol Specification," 3GPP, Tech. Rep., September 2020.

[132] J. Andrés Vásquez-Peralvo, J. Querol, F. Ortíz, J. Luis González Rios, E. Lagunas, L. Manuel Garcés-Socorrás, J. Carlos Merlano Duncan, M. O. K. Mendonça, and S. Chatzinotas, "Multi-beam Beamforming for Direct Radiating Arrays in Satellite Communications Using Genetic Algorithm," *IEEE Open Journal of the Communications Society*, vol. 5, pp. 2343–2357, 2024.

[133] H. Cox, R. Zeskind, and M. Owen, "Robust Adaptive Beamforming," *IEEE Transactions on Acoustics, Speech, and Signal Processing*, vol. 35, no. 10, pp. 1365–1376, 1987.

[134] D. Brooker, K. L. Gemba, and L. T. Fialkowski, "Overcoming snapshot-deficient measurements with knowledge-aided approaches," *JASA Express Letters*, vol. 2, no. 5, 2022.

[135] P. Zhang, L. Pan, T. Laohapensaeng, and M. Chongcheawchamnan, "Hybrid Beamforming Based on an Unsupervised Deep Learning Network for Downlink Channels With Imperfect CSI," *IEEE Wireless Communications Letters*, vol. 11, no. 7, pp. 1543–1547, 2022.

[136] C. Lu, H. Li, and Z. Lin, "Optimized projections for compressed sensing via direct mutual coherence minimization," *Signal Processing*, vol. 151, pp. 45–55, 2018. [Online]. Available: https://www.sciencedirect.com/science/article/pii/S0165168418301464

[137] A. D. Panagopoulos, P.-D. M. Arapoglou, and P. G. Cottis, "Satellite communications at KU, KA, and V bands: Propagation impairments and mitigation techniques," *IEEE Communications Surveys & Tutorials*, vol. 6, no. 3, pp. 2–14, 2004.

[138] J. Mu, J. Zhu, Y. Xiong, and X. Jing, "Multi-user communication-assisted sensing via direct Satellite-to-Vehicle communications," *IEEE Communications Magazine*, vol. 63, no. 11, pp. 83–89, 2025.

[139] R. Correia, T. Varum, J. N. Matos, A. Oliveira, and N. B. Carvalho, "User terminal segments for low-earth orbit satellite constellations: Commercial systems and innovative research ideas," *IEEE Microwave Magazine*, vol. 23, no. 10, pp. 47–58, 2022.

[140] A. V. Shishlov, "Vehicular antennas for satellite communications," in *2011 VIII International Conference on Antenna Theory and Techniques*, 2011, pp. 34–39.

[141] G. Foreman-Campins, L. Pallarés-Rodríguez, S. Locubiche-Serra, G. Seco-Granados, and J. A. López-Salcedo, "Methodologic assessment of beamforming techniques for interference mitigation on GNSS handheld devices," in *2023 International Conference on Localization and GNSS (ICL-GNSS)*, 2023, pp. 1–7.

[142] X. Wang, Y. He, Z. Dou, C. Zhao, and C. Zhu, "3-D fast adaptive beamforming method for Satellite uniform planar array based on improved transformers," *IEEE Internet of Things Journal*, pp. 1–1, 2025.

[143] V. P. Chellapandi, L. Yuan, C. G. Brinton, S. H. Żak, and Z. Wang, "Federated learning for connected and automated vehicles: A survey of existing approaches and challenges," *IEEE Transactions on Intelligent Vehicles*, vol. 9, no. 1, pp. 119–137, 2024.

[144] B. McMahan, E. Moore, D. Ramage, S. Hampson, and B. A. y Arcas, "Communication-efficient learning of deep networks from decentralized data," in *Artificial Intelligence and Statistics*. PMLR, 2017, pp. 1273–1282.

[145] T. Yin, L. Li, W. Lin, T. Ni, Y. Liu, H. Xu, and Z. Han, "Joint client scheduling and wireless resource allocation for heterogeneous federated edge learning with non-IID data," *IEEE Transactions on Vehicular Technology*, vol. 73, no. 4, pp. 5742–5754, 2024.

[146] L. Tian, F. Lin, J. Gan, J. Qi, R. Jia, Z. Zheng, M. Li, and X. Shen, "Enhancing security in parallel federated learning with sharded blockchain for Internet of Vehicles," *IEEE Transactions on Vehicular Technology*, pp. 1–16, 2025.

[147] S. Bhardwaj and D. Kim, "Federated learning mmWave beamforming for V2X communications with imperfect CSI and doppler shift," in *2024 Fifteenth International Conference on Ubiquitous and Future Networks (ICUFN)*, 2024, pp. 410–415.

[148] Z. Lin, Z. Chen, Z. Fang, X. Chen, X. Wang, and Y. Gao, "FedSN: A federated learning framework over heterogeneous LEO Satellite networks," *IEEE Transactions on Mobile Computing*, vol. 24, no. 3, pp. 1293–1307, 2025.

[149] N. Razmi, B. Matthiesen, A. Dekorsy, and P. Popovski, "On-board federated learning for Satellite clusters with inter-Satellite links," *IEEE Transactions on Communications*, vol. 72, no. 6, pp. 3408–3424, 2024.

[150] M. Alsenwi, E. Lagunas, J. Querol, M. Al-Ansi, and S. Chatzinotas, "Flexible synchronous federated learning approach for LEO Satellite constellation networks," in *2024 IEEE International Mediterranean Conference on Communications and Networking (MeditCom)*. IEEE, 2024, pp. 7–12.

[151] Y. Wang, C. Zou, D. Wen, and Y. Shi, "Federated learning over LEO Satellite," in *2022 IEEE Globecom Workshops (GC Wkshps)*, 2022, pp. 1652–1657.

[152] T. Hou, Z. Song, J. Wang, W. Gong, A. Li, and A. Nallanathan, "Federated learning aided LEO Satellite communications: A distributed beamforming approach," *IEEE Internet of Things Journal*, vol. 12, no. 16, pp. 33 155–33 166, 2025.

[153] S. Pala, K. Singh, C.-P. Li, O. A. Dobre, and T. Q. Duong, "Joint beamforming design and sensing in Satellite and RIS-enhanced terrestrial networks: A federated learning approach," *IEEE Transactions on Cognitive Communications and Networking*, vol. 11, no. 5, pp. 3397–3411, 2025.

[154] M. R. Dakkak, D. G. Riviello, A. Guidotti, and A. Vanelli–Coralli, "Federated beamforming with subarrayed planar arrays for B5G/6G LEO Non-Terrestrial Networks," in *2024 IEEE Wireless Communications and Networking Conference (WCNC)*, 2024, pp. 01–06.

[155] M. Wang, R. Ma, and G. Liu, "Federated multi-agent reinforcement learning for interference-aware precoding in LEO integrated communication and navigation," *Wireless Networks*, pp. 1–11, 2025.

[156] A. Zhou, Y. Wang, and Q. Zhang, "Energy-efficient resource management for federated learning in LEO Satellite IoT," in *2024 IEEE Wireless Communications and Networking Conference (WCNC)*, 2024, pp. 1–6.

[157] X. Pei, Z. Zhang, and Y. Zhang, "Cost-efficient hierarchical federated edge learning for Satellite-Terrestrial Internet of Things," *Mobile Networks and Applications*, vol. 29, no. 3, pp. 922–934, 2024.

[158] 3GPP, "Solutions for NR to support Non-Terrestrial networks (NTN)," 3rd Generation Partnership Project (3GPP), Technical Report 38.821, 2018, under Change Control; initial Release: Rel-16. [Online]. Available: https://portal.3gpp.org/desktopmodules/Specifications/SpecificationDetails.aspx?specificationId=3525

[159] J. Cheng, P. Yi, Q. Du, R. Wang, W. Deng, and Y. Huang, "Interference mitigation optimization for Satellite-Terrestrial spectrum sharing," in *2025 IEEE/CIC International Conference on Communications in China (ICCC)*, 2025, pp. 1–6.

[160] J. Grotz, B. Ottersten, and J. Krause, "Signal detection and synchronization for interference overloaded satellite broadcast reception," *IEEE Transactions on Wireless Communications*, vol. 9, no. 10, pp. 3052–3063, 2010.

[161] M. Huang, J. Chen, and S. Feng, "Synchronization for ofdm-based satellite communication system," *IEEE Transactions on Vehicular Technology*, vol. 70, no. 6, pp. 5693–5702, 2021.

[162] F. Dimc, G. Baldini, and S. Kandeepan, "Experimental detection of mobile satellite transmissions with cyclostationary features," *International Journal of Satellite Communications and Networking*, vol. 33, no. 2, pp. 163–183, 2015.

[163] J. Palacios, N. González-Prelcic, C. Mosquera, and T. Shimizu, "A dynamic codebook design for analog beamforming in mimo leo satellite communications," in *ICC 2022 - IEEE International Conference on Communications*, 2022, pp. 1–6.

[164] N. S. Gaikwad, L. Heublein, N. L. Raichur, T. Feigl, C. Mutschler, and F. Ott, "Federated learning with mmd-based early stopping for adaptive gnss interference classification," in *NOMS 2025-2025 IEEE Network Operations and Management Symposium*, 2025, pp. 01–10.

[165] M. Elmahallawy and T. Luo, "Asyncfleo: Asynchronous federated learning for leo satellite constellations with high-altitude platforms," in *2022 IEEE International Conference on Big Data (Big Data)*, 2022, pp. 5478–5487.

[166] L. Li, L. Zhu, and W. Li, "Hisatfl: A hierarchical federated learning framework for satellite networks with cross-domain privacy adaptation," *Electronics*, vol. 14, no. 16, p. 3237, 2025.

[167] S. Salim, N. Moustafa, M. Hassanian, D. Ormod, and J. Slay, "Deep-federated-learning-based threat detection model for extreme satellite communications," *IEEE Internet of Things Journal*, vol. 11, no. 3, pp. 3853–3867, 2024.

[168] K. Guo and K. An, "On the performance of ris-assisted integrated satellite-uav-terrestrial networks with hardware impairments and interference," *IEEE Wireless Communications Letters*, vol. 11, no. 1, pp. 131–135, 2022.

[169] E. Lagunas, "Ku/ka band tracking antenna," Personal Website of Dr. Eva Lagunas. [Online]. Available: https://sites.google.com/view/evalagunas/home/research/kuka-tracking-antenna

[170] Y. Li, Y. Huang, J. Ren, Y. Liu, G. F. Pedersen, and M. Shen, "Robust doa estimation in satellite systems in presence of coherent signals subject to low snr," *IEEE Access*, vol. 10, pp. 109 983–109 993, 2022.

[171] L. Pellaco, M. Bengtsson, and J. Jaldén, "Matrix-inverse-free deep unfolding of the weighted mmse beamforming algorithm," *IEEE Open Journal of the Communications Society*, vol. 3, pp. 65–81, 2022.

[172] A. F. Mirza, M. Umer, and S. A. Hassan, "Ai-driven dynamic spectrum management in integrated tn-ntn networks," in *Artificial Intelligence for Integrated Terrestrial and Non-terrestrial Networks*. Springer, 2026, pp. 169–195.

[173] J. Deng, F. Hassan, H. Zhou, S. Al-Ahmadi, M.-S. Alouini, and D. B. Da Costa, "Ai-native open ran for non-terrestrial networks: An overview," *arXiv preprint arXiv:2507.11935*, 2025.

[174] J. Rijnsdorp, A. van Zwol, and M. Snijders, "Satellite navigation signal interference detection and machine learning-based classification techniques towards product implementation," *Engineering Proceedings*, vol. 54, no. 1, 2023. [Online]. Available: https://www.mdpi.com/2673-4591/54/1/60

[175] H. Mansourifar, A. Moskovitz, B. Klingensmith, D. Mintas, and S. J. Simske, "Gan-based satellite imaging: A survey on techniques and applications," *IEEE Access*, vol. 10, pp. 118 123–118 140, 2022.

[176] M. Deng, R. Luo, and Z. Yao, "Gnss interference signal classification based on federated learning," in *2024 IEEE 100th Vehicular Technology Conference (VTC2024-Fall)*, 2024, pp. 1–7.

[177] Y. Cho, W. Yang, D. Oh, and H.-S. Jo, "Multi-agent deep reinforcement learning for interference-aware channel allocation in non-terrestrial networks," *IEEE Communications Letters*, vol. 27, no. 3, pp. 936–940, 2023.

[178] P. Jiang, C.-K. Wen, X. Li, S. Jin, and G. Y. Li, "Semantic satellite communications based on generative foundation model," *IEEE Journal on Selected Areas in Communications*, vol. 43, no. 7, pp. 2431–2445, 2025.